2020

Single-cell pump probe imaging of intrinsic chromophores identifies diagnostic marker and therapeutic target of diseases

BOSTON UNIVERSITY

GRADUATE SCHOOL OF ARTS AND SCIENCES

Dissertation

SINGLE-CELL PUMP PROBE IMAGING OF INTRINSIC CHROMOPHORES IDENTIFIES DIAGNOSTIC MARKER AND THERAPEUTIC TARGET OF DISEASES

by

PUTING DONG

B.A., University of Science and Technology of China, 2014

Submitted in partial fulfillment of the

requirements for the degree of

Doctor of Philosophy

2020

Approved by

First Reader

Ji-Xin Cheng, Ph.D.
Moustakas Chair Professor in Photonics and Optoelectronics
Professor of Biomedical Engineering
Professor of Electrical and Computer Engineering
Professor of Materials Science and Engineering
Professor of Chemistry
Professor of Physics

Second Reader

Qiang Cui, Ph.D.
Professor of Chemistry
Professor of Biomedical Engineering

Third Reader

Lawrence D. Ziegler, Ph.D.
Professor of Chemistry
Professor of Materials Science and Engineering

Fourth Reader

Ahmad S. Khalil, Ph.D.
Associate Professor of Biomedical Engineering

Fifth Reader

Michael K. Mansour, M.D., Ph.D.
Assistant Professor of Medicine
Massachusetts General Hospital

DEDICATION

I would like to dedicate this work to my parents, Huiming Dong and Meiling Cheng, my grandparents, Fucang Dong and Qiurong Dong.

ACKNOWLEDGMENTS

First and foremost, I would like to thank my major professor, Dr. Ji-Xin Cheng, for his passion and curiosity for science, precise scientific training, continuous support, and guidance on my research throughout my whole PhD study. His enthusiasm to science, dedication to push everything to perfect, sharp creativity, curiosity and breadth of knowledge set an excellent example for me about how to be a scientist. I deeply appreciate his encouragement, his support on my way to becoming an independent scientist. I feel so honored and lucky to have him as my Ph.D. advisor. I would also like to thank the members of my advisory committee, Dr. Ahmad Khalil, Dr. Qiang Cui, Dr. Lawrence Ziegler, and Dr. Michael Mansour, for their insightful suggestions and constructive criticisms over my PhD study.

I would like to thank Dr. Mohamed N. Seleem, and his postdoc, Dr. Haroon Mohammad, for their suggestions and help on developing the utilization of blue light on MRSA-infected skin infection model. I would like to thank Dr. Tianhong Dai, and his postdoc, Dr. Leon G. Leonse, for their help on IVIS imaging of mice abrasion study. I would also like to thank Dr. Zeina Dagher, Dr. Michael Mansour for their wonderful help and suggestions for the antifungal therapy project and amphotericin B imaging project.

In addition, I'd like to thank all the current and some former Cheng group members, who I have had great pleasure to work with. In particular, I am very grateful to Dr. Junjie Li, Dr. Jie Hui, Dr. Lijia Liang, Dr. Chien-Sheng Liao, Dr. Hyeon Jeong Lee, Dr. Andy Jing Chen, Kai-Chih Huang, Haonan Lin, Dr. Cheng Zong, Dr. Meng Zhang, Jiabao Xu, Yuewei Zhan, Sebastian Jusuf, Yimin Huang, Xiaojie Li, Peng Lin, for their insightful

comments or significant contributions to my research.

In the end, I would like to dedicate this dissertation to my parents, Huiming Dong and Meiling Cheng, for their endless love, support, and encouragement. I also deeply appreciate my grandma, Qiurong Dong, who always teaches me the value of love, diligence and persistence. I also cherish every moment with my siblings, my sister, Pujie Dong, who always sets an excellent example of being brave and optimistic towards dream, and my brother, Zhenyu Dong, who shares the pains and joys of life as we grow up. I also would like to dedicate my great appreciation to my fiancé and colleague, Jie Hui, who always provides solid strengths, console and encouragement for me to enjoy science, relish life, to overcome any challenges in the past and future.

SINGLE-CELL PUMP PROBE IMAGING OF INTRINSIC CHROMOPHORES IDENTIFIES DIAGNOSTIC MARKER AND THERAPEUTIC TARGET OF DISEASES

PUTING DONG

Boston University Graduate School of Arts and Sciences, 2020

Major Professor: Ji-Xin Cheng, Moustakas Chair Professor in Photonics and Optoelectronics, Professor of Biomedical Engineering, Professor of Electrical and Computer Engineering, Professor of Materials Science and Engineering, Professor of Chemistry, Professor of Physics

ABSTRACT

When photons transport inside the biological samples, the interaction between photons and biological analytes enable us to map a specific diagnostic biomarker for disease. However, biological media are composed of discrete scattering particles. Propagation of photons are highly attenuated due to scattering and absorption, which makes it challenging for clinical diagnosis.

There is a need for identifying biomarkers for precision medicine and diagnosis. Chromophores exists endogenously in various organisms and cells; however, their potential of precision diagnosis and treatment still remain under-explored. Note that lots of research has been harnessed, for example, autofluorescence from FAD and NADH has been used for cancer diagnosis, but the potential of this area needs to be further mined, as most of the intrinsic chromophores has considerably low fluorescent quantum yield.

This thesis illustrates how we came with an absorption-based chemical microscopy approach to study these chromophores at single cell level, and that these opens new discoveries for diagnosis and treatment. It first outlines how transient absorption

microscopy is utilized to diagnose diabetes at single cell level, and then this technique enabled the discovery of a molecular signature, staphyloxanthin photolysis, for efficacious treatment of methicillin-resistant *Staphylococcus aureus* (MRSA)-caused infections through photo-disassembling its cell membrane microdomains. Besides staphyloxanthin, we also uncovered that catalase, which exists in most of the microbes (*Candida auris,* and drug-resistant gram-negative pathogens included), can be efficiently photo-inactivated, thus enabling these catalase-positive pathogens to be sensitive to exogenous antimicrobial agents. We also utilized stimulated Raman scattering microscopy to map the orientation amphotericin B, a golden standard antifungal agent, in a single fungal cell membrane to reveal its working mechanism. Collectively, nonlinear chemical imaging offers a profound tool to visualize *in situ* microbial metabolic dynamics, and discover molecular markers for precision treatment and diagnostic purposes.

TABLE OF CONTENTS

LIST OF TABLES

LIST OF FIGURES

CHAPTER 1 INTRODUCTION

1.1 Interaction Between Photons and Cells, Tissues

When light penetrates tissues or cells, the optical characteristics of analytes endow photons with both diagnostic and therapeutic applications[1,2]. As shown in **Figure 1.1**, three processes may happen during this interaction, that is scattering, absorption, and fluorescence emission[1]. Generated through the interrogation between photons and biological analytes, these physical processes enable us to achieve disease diagnosis or treatments.

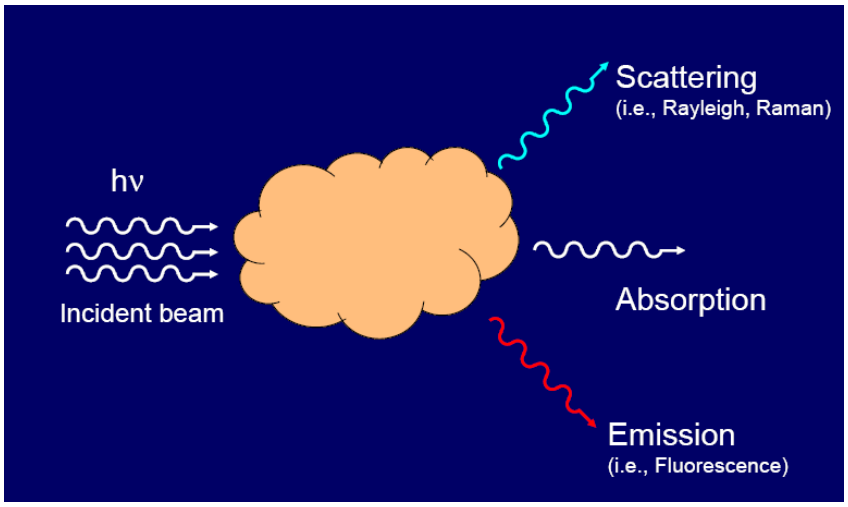

Figure 1.1. Interaction between photons and biological cells or tissues.

1.1.1 Spontaneous Raman Scattering

For optical scattering, it happens when molecules or atoms which are exposed to light absorb the light energy, and then re-emit light in various directions with variable energies[3]. Optical scattering is composed of elastic scattering and inelastic scattering. Especially, Raman scattering, which was discovered and explained by Indian Scientist C. V. Raman in 1928[4], has been widely harnessed to address lots of important biomedical problems, and

it is an inelastic scattering process. Briefly, when photons encounter with polarizable electrons are always within molecules or a cell, Raman scattering signal is directly related to the polarizability of the analytes, which is the ability to form instantaneous dipole[5]. For example, conjugated C=C double bonds can be relatively easier polarized, thus a predominant Raman shift ~1500-1600 cm^{-1} arising from the stretching vibrations[6]. This process can be described as following induced dipole (μ) formula[5]:

$$\mu = \alpha E \qquad (1)$$

, where α is the polarizability of the molecule: $\alpha_0 + \beta \sin(2\pi\nu_R t)$, where ν_R is the vibrational frequency of the molecule; E is the applied field, and β is a constant. When the applied field is traveling at frequency ν and magnitude of E_0, then μ becomes the following equation:

$$\mu = (\alpha_0 + \beta \sin(2\pi\nu_R t))E_0 \sin(2\pi\nu t) \qquad (2)$$

Given trigonometric relations, Equation (2) becomes:

$$\mu = \alpha_0 E_0 \sin(2\pi\nu t) + \frac{1}{2} E_0\beta * \{cos2\,\pi(\nu - \nu_R)t - cos2\,\pi(\nu + \nu_R)t\} \quad (3)$$

, where the term $cos2\,\pi(\nu - \nu_R)t$ is the Stoke's Raman band, which has lower energy than the incident light, and the term $cos2\,\pi(\nu + \nu_R)t$ is the anti-Stoke's Raman band, which has higher energy compared with the incident light. Noteworthy, the anti-Stokes band is temperature dependent[7]. It is also interesting to notice that for Raman-active molecular chemical bonds, their electron clouds are prone to being polarized by the excitation laser field. As shown in the Jablonski diagram in **Figure 1.2**, the excited laser field usually excites ground-state molecules to a virtual state, then generating Stoking scattering and anti-Stokes scattering.

Since each chemical bond has its specific vibrational frequency, thus, the generating Raman spectrum can be deciphered as a 'molecular fingerprint', which not only provides information about the structure, conformation and identity of the sample, but also the dynamics and interactions between targeted analytes and its surrounding environment. Moreover, Raman spectrum of cancer cells, bacteria or tissue slices also enable us to have new discovery, which provides us important clues to solve the cutting-edge medical and health problems.

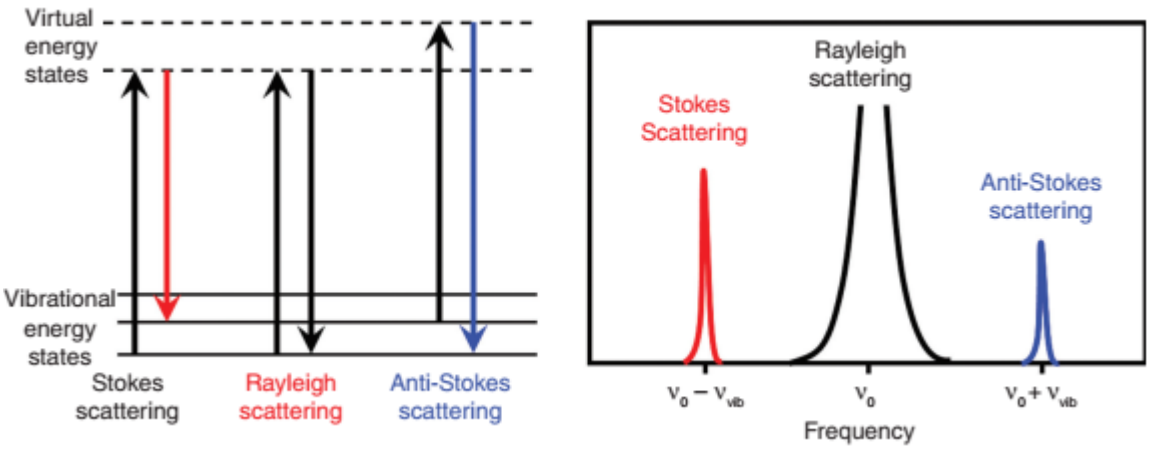

Figure 1.2. Schematics of vibrational Raman process. Figure adapted from paper[8].

Nonetheless, the radiant power of Raman scattering is closely related to Raman scattering cross section, which is in the range of $10^{-30} cm^2 sr^{-1}$ [9], thus it takes at least tens of minutes per frame to get a whole mapping of targeted chemical from cells or tissue slices.

Since Raman scattering is a weak physical process, typically less than one in a million excitation photons give rise to a single Raman photon. To improve the detection sensitivity, one prevalent Raman spectroscopy is called resonance Raman spectroscopy[10], where

incident photon energy is close in energy to an electronic transition of a molecule, resulting in greatly enhanced intensity of Raman scattering. Another widely used approach is called surface-enhanced Raman spectroscopy (SERS), where Raman scattering is enhanced through amplification of electromagnetic fields on rough metal surfaces[11,12]. Sensitivity of SERS is theoretically calculated to have a 10^{10} – 10^{11} times enhancement[13], which significantly broadens the feasibility and application of Raman spectroscopy.

1.1.2 Coherent Raman Scattering

Coherent Raman Scattering (CRS) microscopy is an emerging technique that overcomes the slow image acquisition speed of spontaneous Raman scattering microscopy. As shown in **Figure 1.3[14]**, two excitation fields are used, denoted as pump (ω_p) and Stokes (ω_s). When the beating frequency ($\omega_p - \omega_s$) is resonant with a Raman-active chemical bond, four major CRS processes occur simultaneously, coherent anti-Stokes Raman scattering (CARS) at a new frequency of $(\omega_p + (\omega_p - \omega_s))$, coherent Stokes Raman scattering at a new frequency of $\omega_s - (\omega_p - \omega_s)$), stimulated Raman gain (SRG) at ω_s, and stimulated Raman loss (SRL) at ω_p. Both SRG and SRL belong to the process of stimulated Raman scattering (SRS). Here, we will focus SRS only as SRS is free of non-resonant background, spectral distortion, and SRS signal is linearly dependent on molecular concentration[15].

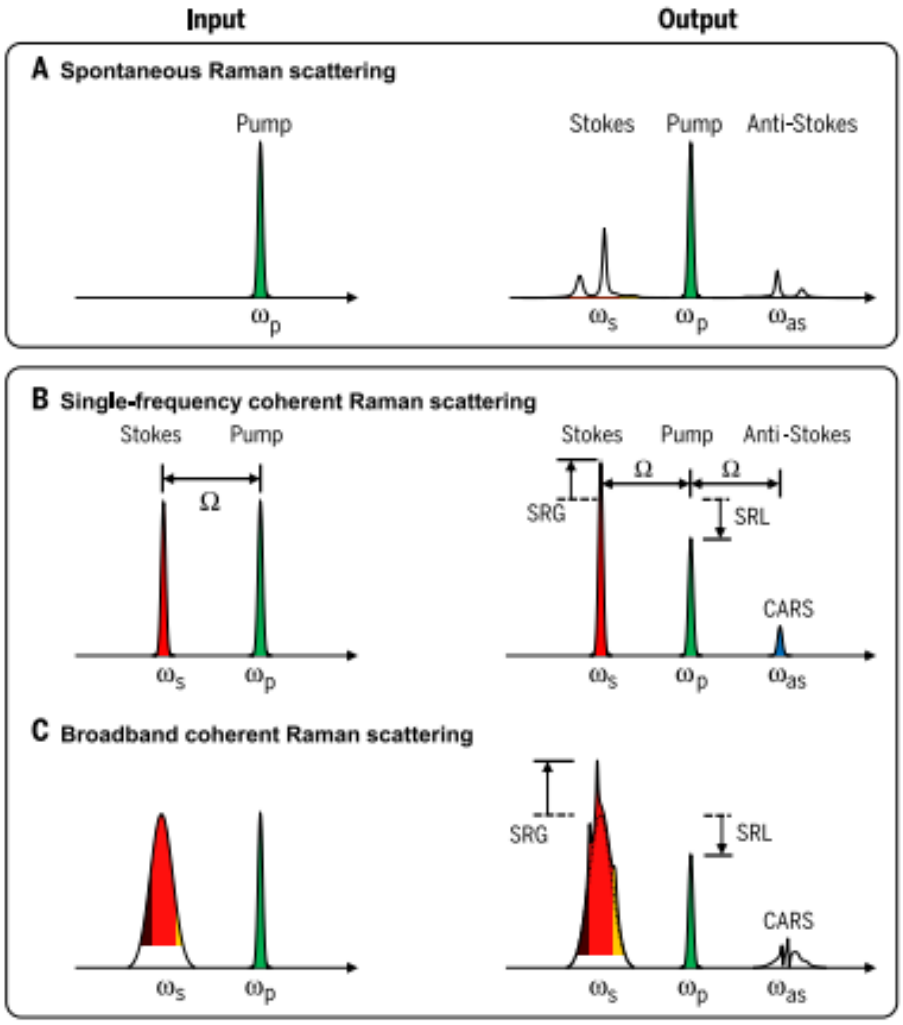

Figure 1.3. Spontaneous versus Coherent Raman Scattering process. (a). A pump laser with narrowband generates non-coherent spontaneous Raman scattering signal. (b). Pump laser, Stokes laser with narrowband generate a resonant frequency matching that of the vibrational frequency of a chemical bond inside the analyte. (c). A narrowband laser and a broadband laser simultaneously excite multiple Raman transitions. SRG: stimulated Raman gain; SRL: stimulated Raman Loss; CARS: coherent anti-Stokes Raman scattering. Figure is adapted from paper[14]. Copyright to AAAS.

Compared to incoherent spontaneous Raman scattering, SRS microscopy gains speed through signal amplification by the presence of a local oscillator at the detection wavelength[14]. Moreover, with all modes oscillating in unison, the resulting SRS radiation is highly directional and strong, offering signal detection efficiencies that are many orders of magnitude higher[16]. SRS techniques also enable the direct observation of the coherent

molecular motions at ultrafast time scales which can't be inferred from Raman spectrum analysis alone. Moreover, SRS is a nonlinear imaging technique with excellent optical sectioning property[14,17], which enables us to obtain 3D imaging of tissue slices.

Besides single-frequency (at a fixed Raman shift) SRS imaging, when encountering chemical bonds who have overlapping Raman bands, hyperspectral SRS (hSRS) microscopy offers better chemical specificity. Frame-by-frame hSRS imaging records a 3D stack of SRS images at multiple Raman shifts[18]. To obtain hSRS imaging stacks, wavelength scanning is a straightforward approach. Utilization of two tunable picosecond lasers, the wavelength can be tuned over a continuous range to cover multiple Raman shifts[19]. With the broad bandwidth, femtosecond lasers can also be used for hSRS imaging in multiple ways. Spectral focusing[20,21] by chirping two femtosecond laser beams with NSF57 glass rods to picosecond range, a relatively simple and robust method, improves the spectral resolution. By tuning the time delay between the two chirped pulses, the frequency difference is subsequently translated to excite different Raman shifts. This robust method could record hSRS images within a minute over a 270-cm^{-1} spectral window. Moreover, the spectral resolution obtained through method is positively related to the number of chirping glass rods, a spectral resolution of ~ 7 cm^{-1} can be achieved by chirping with 6 glass rods. Another approach is through a pulse shaper to filter and scan a narrow spectral component out of a broadband femtosecond spectrum[18,22,23]. By coupling with a customized fiber amplifier, a spectral resolution of ~ 10 cm^{-1} can be achieved[24]. Detailed applications of SRS microscopy and hyperspectral SRS imaging techniques will be illustrated in **Chapter 1.2**.

1.1.3 Fluorescence Microscopy

Due to its intrinsic selectivity, fluorescence imaging has become the mainstay of microscopy to solve numerous biological problems. Fluorescence is the emission of light that occurs within nanoseconds after the absorption of light that is typically of shorter wavelength[25,26]. As shown in **Figure 1.4**, the difference between exciting and emitted wavelengths is called Stokes shift[25]. Through completely filtering out the exciting light without blocking the emitted fluorescence, thus fluorescence microscopy is a background-free imaging technique.

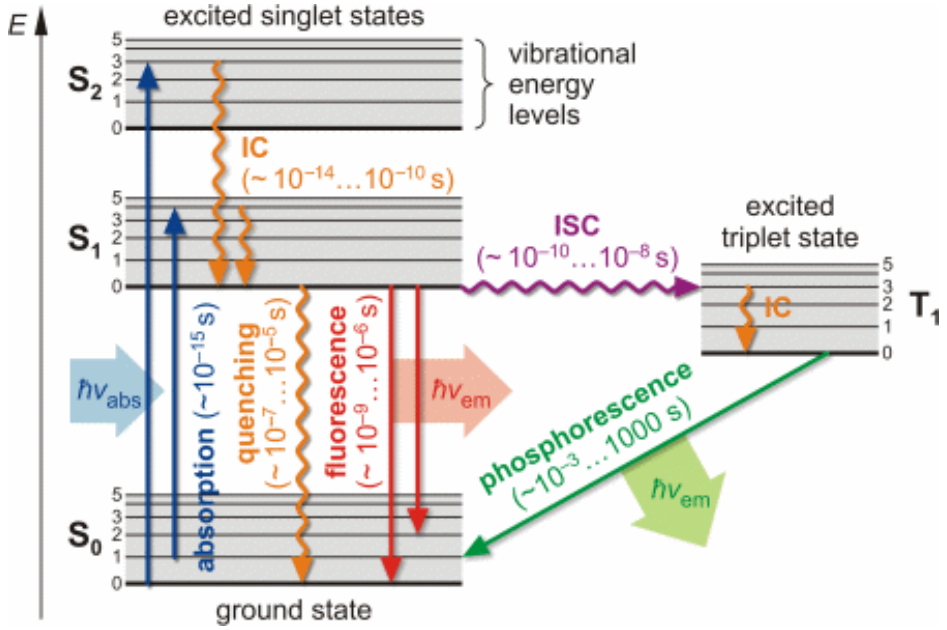

Figure 1.4 Jablonski energy diagram illustrating the transitions between electronic state of a molecule for the physical process of fluorescence and phosphorescence. Waved lines represent the non-radiative transitions. IC means internal conversion, ISC stands for intersystem crossing. Figure adapted from diploma thesis of Steve Pawlizak, 2009.

Molecules which have fluorescent properties are called fluorophores. As shown in **Figure 1.5**, the outermost electron orbitals in the fluorophore molecule determine both its efficiency as a fluorescent compound and the wavelengths of absorption and emission. When fluorescent compounds in their ground state absorb photons, the absorbed energy

moves electron into a different orbital that is farther way from the nucleus (happens in femtoseconds).

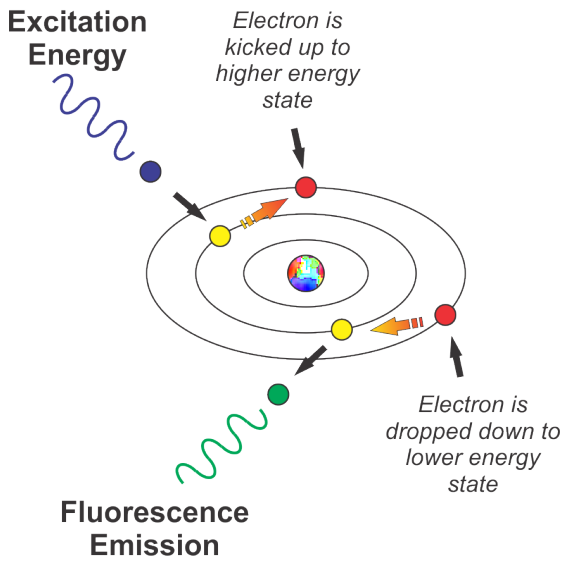

Figure 1.5. Schematic illustration of how the excited photons interact with electron orbitals to generate fluorescence signals. Copyright to FIIREDIVEGEAR.COM.

Fluorescence microscopy takes great advantage of synthesized compounds that have conjugated double bonds as these chemicals have ring structures with π bonds that easily distribute outer orbital electrons over a wide area. Usually, these compounds are optimal for fluorescence microscopy because the energy differences between excited state and ground states are small enough that relatively low-energy photons in the visible part of the electromagnetic spectrum can be used to excite electrons into excited states. Interestingly, the more conjugated bonds in the molecule, the lower the excited energy requirement, and the longer the wavelength (redder) the exciting light can be.

Besides synthesized compounds, genetically encoding fluorescent protein, such as green fluorescent protein (GFP)[27] or yellow fluorescent protein (YFP), which is an imidazolidone ring with conjugated double bonds and planar structure in the center of the

barrel-shaped protein as shown in **Figure 1.6**.

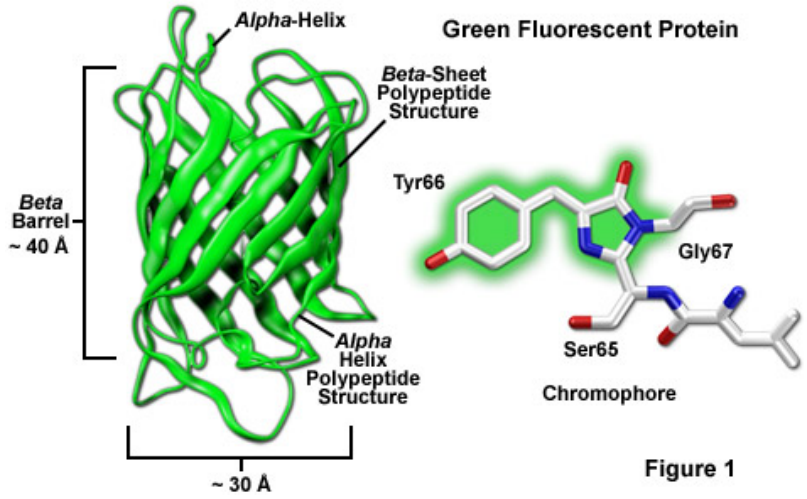

Figure 1.6. Structure of jellyfish green fluorescent protein (GFP) with the chromophore, Tyr66-Gly67-Ser65 in the center of β-barrel. Copyright to ZEISS.

Cells or bacteria encoded with those fluorescent proteins enable us to visualize the metabolite dynamics under fluorescence microscope. Detailed applications will be illustrated in **Chapter 1.2**.

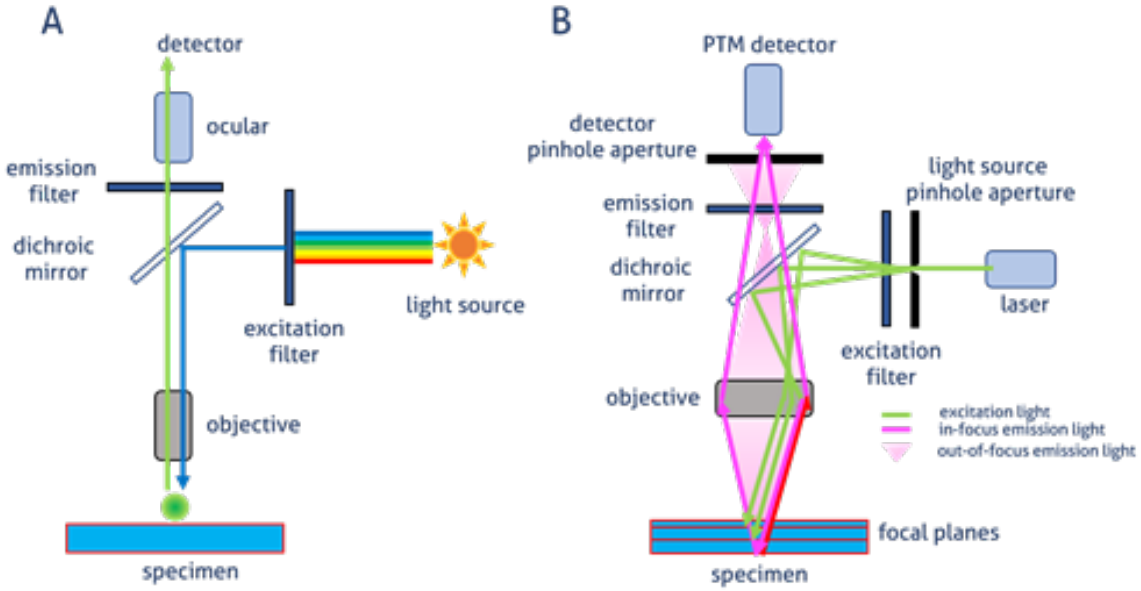

Figure 1.7. Comparison between conventional wide-field microscope and confocal microscope. PMT: photon-multiplier tube. Figure adapted from proteintech®.

As shown in **Figure 1.7**., confocal laser scanning microscope (CLSM) takes the advantage of the pinhole aperture to eliminate the out-of-focus photons, thus having increase in both lateral and axial resolution[28,29].

However, fluorescent microscopy is still limited by relatively low spatial resolution because of the diffraction of light, which is about 200-300 nm in the lateral direction and 500-700 nm in the axial direction, and this is larger than many subcellular structures[30,31]. To improve resolution, many super-resolution fluorescence microscopy methods, such as stimulated emission depletion microscopy[32], structured-illumination microscopy[33], stochastic optical reconstruction microscopy[34], photoactivated localization microscopy[35] have been developed to reach a resolution of 20-50 nm. Images from these super-resolution techniques enable scientists to visualize biological samples at nanometer scale, significantly expanding the understanding of molecular interactions and metabolic dynamic processes in living systems.

1.1.4 Absorption Spectroscopy and Transient Absorption Microscopy

Not all the biological samples could emit fluorescence, however, everything could absorb. Lots of biological endogenous chemicals have substantial absorption at specific wavelength. For example, hemoglobin (oxy-form, or reduced form) has strong absorption at 400 nm, lipid has a prominent absorption peak at around 900 nm (**Figure 1.8)**. According to Beer-lambert law:

$$\boldsymbol{A = \varepsilon * b * C}$$

$$\boldsymbol{A = -\log\left(\frac{I_1}{I_0}\right)}$$

, where A is the absorbance, $\boldsymbol{\varepsilon}$ is the molar extinction coefficient, and $\boldsymbol{C}$ is the concentration of analyte, $\boldsymbol{I_0}$ and $\boldsymbol{I_1}$ are the original photon intensity and intensity after passing sample. Since linear absorption is proportional to the concentration of analyte, thus it can be widely used to quantify the amount of analyte given a standard calibration curve.

Besides linear absorption, nonlinear absorption-based approached have drawn increasing attention during past years. For example, two-photon absorption, where ground state molecules absorb two photons of identical or different frequencies to a higher energy state (excited electronic state)[36]. Laurdan, a popular fluorescence marker utilized to quantify the cell membrane rigidity, is commonly excited at 770 nm[37] aiming at reducing photobleaching.

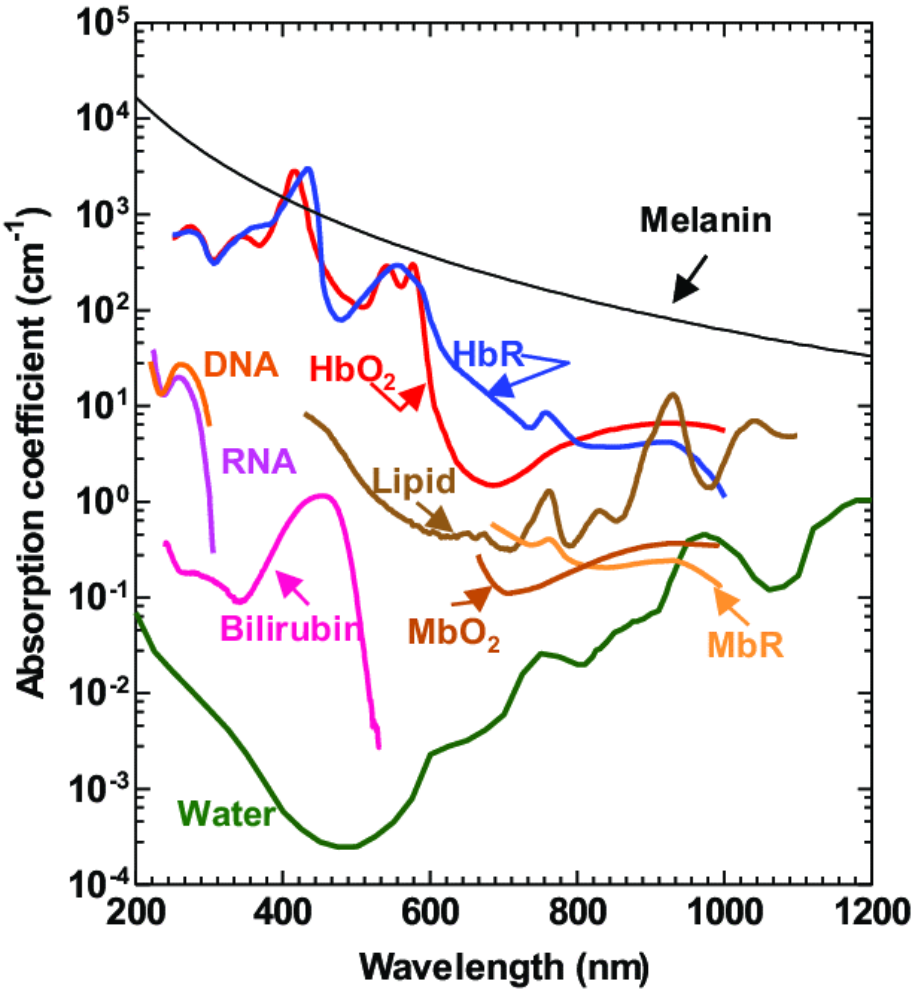

Figure 1.8. Absorption spectra of major endogenous contrast in biological tissue at normal concentration. HbO_2: oxy-hemoglobin. HbR: deoxy-hemoglobin. MbR: reduced myoglobin. MbO_2: oxy-myoglobin. Figure adapted from paper[38].

Another powerful nonlinear absorption-based approach is transient absorption, different to the conventional linear absorption spectroscopy, transient absorption measures the absorbance at a wavelength or a range of wavelengths of a sample as a function of time after excitation by a pump laser field.

As shown in **Figure 1.9**, An optical parametric oscillator pumped by a high-intensity mode-locked laser generates synchronous pump and probe pulse trains. The Ti:sapphire oscillator is split to separate pump and probe pulse trains. Temporal delay between the

pump and probe pulses is achieved by guiding the pump beam through a computer-controlled delay line. Pump beam intensity is modulated with an acousto-optic modulator (AOM), and the intensity of both beams is adjusted through the combination of a half-wave plate and polarizer. Subsequently, pump and probe beams are collinearly guided into the microscope. After the interaction between the pump beam and the sample, the modulation is transferred to the unmodulated probe beam. Computer-controlled scanning galvo mirrors are used to scan the combined lasers in a raster scanning manner to create microscopic images. The transmitted light is collected by the oil condenser.

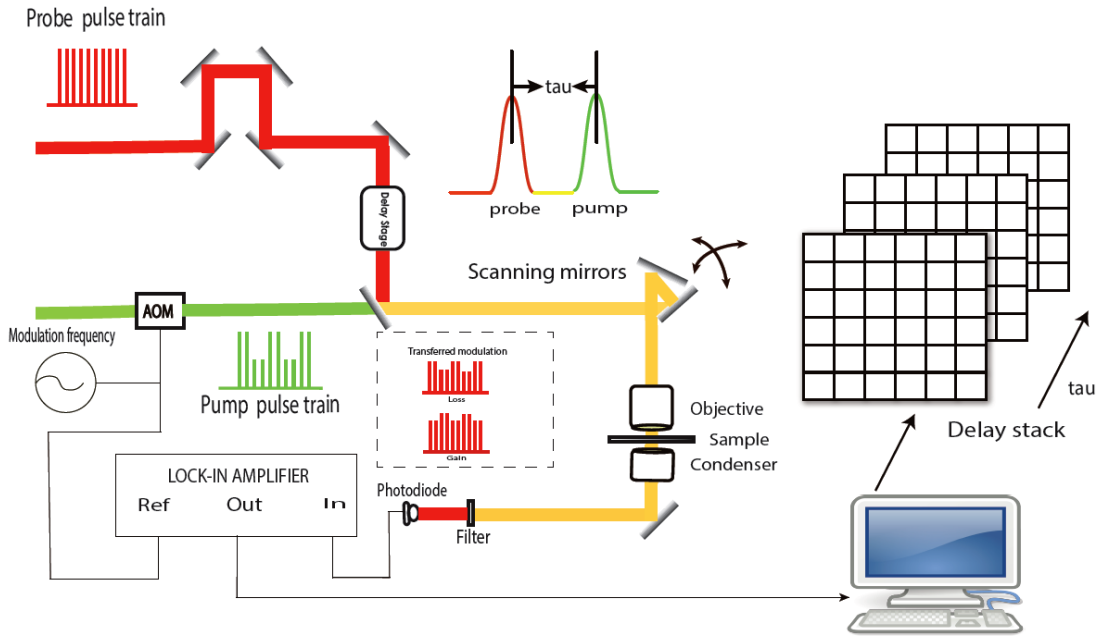

Figure 1.9. Schematic illustration of a transient absorption microscope. Figure adopted with permission from paper[39].

Subsequently, the pump beam is spectrally filtered by an optical filter, and the transmitted probe intensity is detected by a photodiode. A phase-sensitive lock-in amplifier then demodulates the detected signal. Therefore, pump-induced transmission

changes of the sample versus time delay can be measured from the focus plane. This change over time delay shows different decay signatures from different chemicals, thus offering the origin of the chemical contrast. This time-resolved decay signature provides molecular specificity.

Three processes could happen during transient absorption process, that is, excited state absorption (ESA), stimulated emission (SE), and ground state depletion (GSD) (**Figure 1.10**). The first step is that ground state molecules always absorb the light energy from pump laser, ESA happens when excited state continues to absorb probe photons to even higher electronic state, GSD occurs when pump laser beam is absorbed by the ground state molecules as well, SE happens when photons in the excited states are stimulated down to the ground state[40].

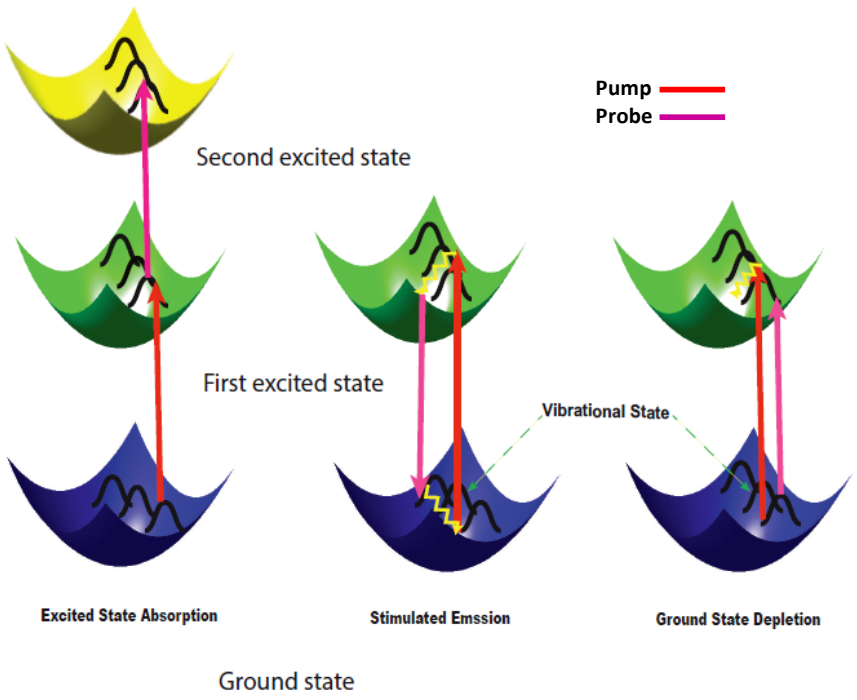

Figure 1.10. Three processes in a transient absorption experiment. Figure adapted from paper[39].

Since transient absorption microscopy owns the advantage of molecular specificity as each molecule has unique excited state dynamics, high sensitivity (single molecule detection has been achieved[41]), high spatial resolution[42], and fast image acquisition speed[43], it has been widely used for disease diagnosis[44], identification of artificial natural pigments[45], quantification of oxyhemoglobin[46] etc. More applications are illustrated in **Chapter 1.2**.

1.2 Applications of Biomedical Optics

1.2.1 Applications of Raman Spectroscopy

Since Raman spectroscopy provides molecular vibrational fingerprint for molecules, thus we could differentiate various species, detection of biomarker for disease, and diagnosis of stages of disease or even for forensic purpose.

1.2.1.1 Cancer diagnosis

Cancer is the second-leading cause of death worldwide[47]. Therefore, there is an urgent need to achieve accurate and timely diagnosis. Alfano and coworkers were the first to adapt Raman spectroscopy to distinguish healthy breast tissues from malignant ones[48]. Feld and coworkers attained a 96% specificity and 94% sensitivity to diagnose benign and malignant lesions in human breast tissues based on their chemical composition[49]. Many others also achieved discrimination of malignant cancer tissues from that of healthy ones[50] based on the differences of spectroscopic profiles arising from Raman-active functional groups of nucleic acids, proteins, lipids and carbohydrates.

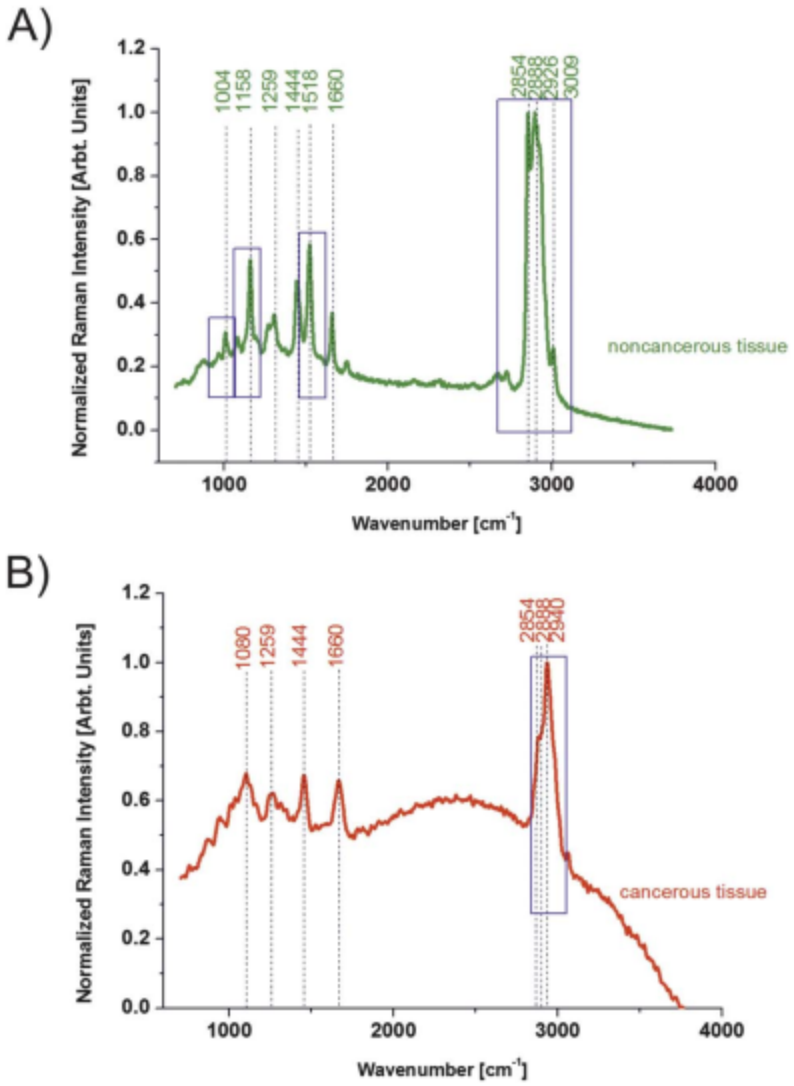

Figure 1.11. Comparison of the Raman spectra of the non-cancerous (a) and the cancerous (b) tissues. Figure adapted from[51].

Take the diagnosis of breast cancer[51] as an example, Raman spectrum of noncancerous tissue was dominated by peaks at 1004, 1158, 1259, 1444, 1660, 2854, 2888, and 2926 cm^{-1}, while that of the cancerous tissue shows prominent peaks at 1080, 1259, 1444, 1660, and 2940 cm^{-1}. The peaks at 1004, 1158, and 1518 cm^{-1} of the noncancerous tissue correspond to vibrations typical for the C–C and C=C stretching modes of carotenoids

(polyene), and the peak at 1259 cm^{-1} arises from the asymmetric stretching mode of the -PO_2 group. Other apparent vibrations characteristic for the C–H groups of lipids are 1444 (scissoring mode), 1660 (C=C stretching mode), 2854 (symmetric stretching mode), 2888 (stretching mode), and 2926 cm^{-1} (asymmetric stretching mode), and the peak at 3009 cm^{-1} corresponds to the (C=C)–C–H asymmetric stretching mode. The cancerous breast tissue shows strong peaks at 1080, 1259, 1444, 1660, 2854, and 2940 cm^{-1}, the peak at 1080 cm^{-1} corresponds to phospholipids, and the vibrations at 2854 cm^{-1} are typical for the C-H group of lipids, while the vibrations at 2940 cm^{-1} can be defined as a combination of the vibrations of lipids and proteins[52]. It was also worth noting that the ratio of Raman intensity between carotenoid and C-H vibration in cancerous tissues is higher from that of noncancerous tissues, suggesting that there are more carotenoids in the cancerous tissues as carotenoids could scavenge the intracellular reactive oxygen species and correlate with a high cholesterol level[53].

1.2.1.2 Detection of Bacteria

Besides cancer diagnosis, detection of bacteria in a turbid and complex environment is essential for late-stage bacteremia patients. Popp and coworkers have utilized Resonant Raman spectroscopy to visualize intracellular *Staphylococcus aureus* (*S. aureus*)[54], however, this paper measured the metabolites change revealed by Raman spectroscopic profile change. Later, Popp and coworkers directly visualized an intracellular pathogen by resonant Raman imaging at around Raman shifts around 1449 and 1660 cm^{-1} [55] as intracellular *Mycobacterium gordonae* has distinctive Raman peak due to the existence of carotenoids[56].

Apart from resonant Raman spectroscopy, SERS has also widely used for detecting bacteria[57,58]. Popp and others demonstrated the efficient discrimination of different *Escherichia coli* (*E. coli*) strains by means of a microfluidic chip chamber[59]. Ziegler and coworkers showed the efficient feasibility of detecting single *Bacillus anthracis* (*B. anthracis*) by SERS[12]. Later they also demonstrated that SERS provided important metabolic profiling of bacteria cellular activity under starvation[60]. Xu and coworkers demonstrated the potential of SERS on the detection of foodborne pathogens such as by tagging with a Fe_3O_4@Au@PEI substrate[61]. Srivastava *et al.* employed metallic nano sculptured thin films to achieve highly sensitive and specific detection of *E. coli* in 10 µl volume of the sample[62]. Doty *et al*. demonstrated the utilization of Raman spectroscopy for forensic analysis, for example, the gunshot residues[63].

With the merits of spectroscopic profiles and molecular specificity, Raman spectroscopy still holds great potential for more biomedical applications.

1.2.2 Applications of Stimulated Raman Scattering

As it takes hours to get a desired Raman images, SRS solved this image acquisition speed issue. Thus, it has been drawing increasing attention in the field of biomedical applications, especially, SRS imaging could drive the discovery of novel signature for disease diagnosis, and further treatment.

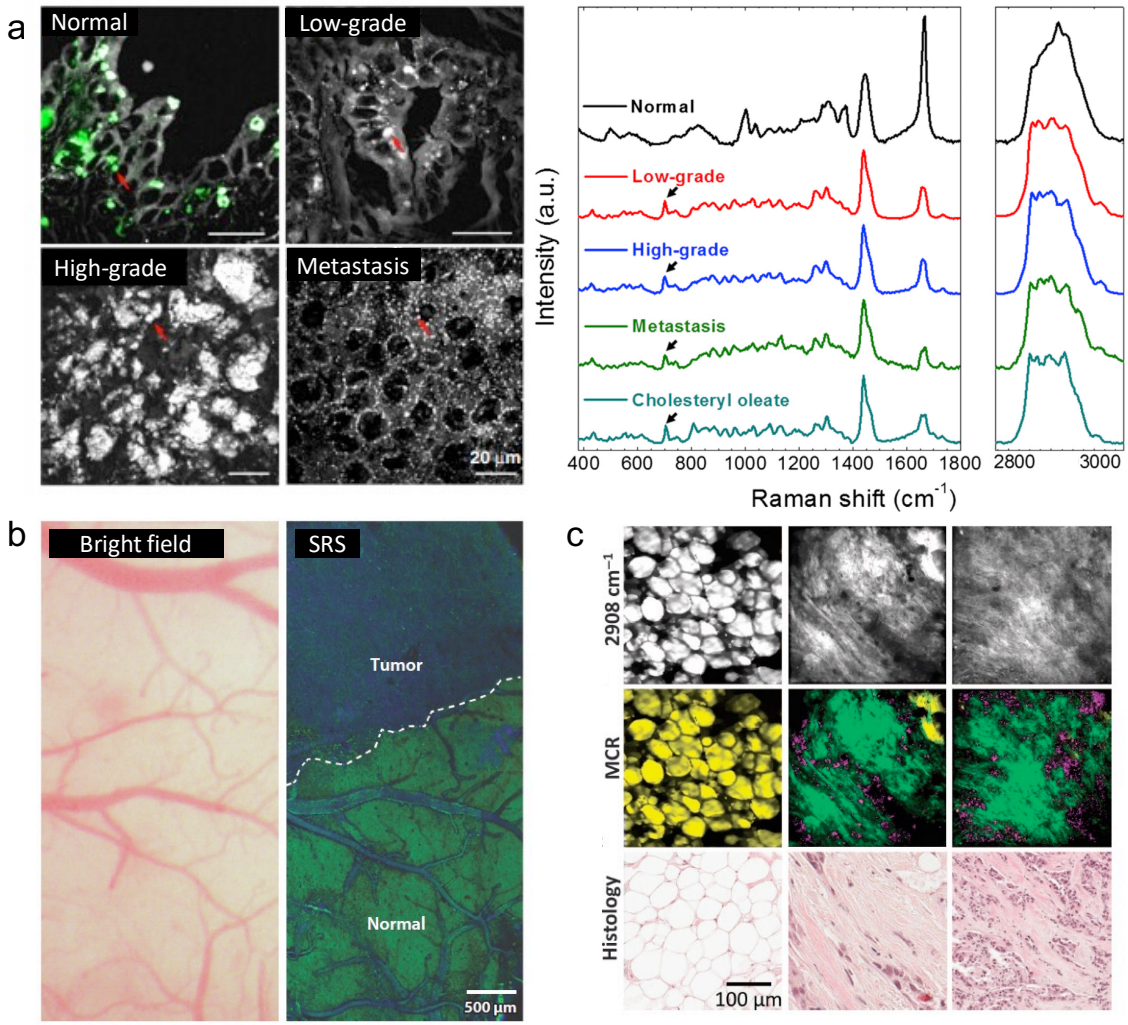

Figure 1.12. Chemical contents mapping by SRS in cells and tissues. (a). SRS (grey) and two-photon fluorescence (Green) images of normal prostate, low-grade, high-grade, and metastatic prostate cancer tissue slices, respectively. Raman spectra of auto-fluorescent granules in normal prostate, low-grade, high-grade, metastatic prostate cancer tissue slices, and cholesterol oleate. Black arrows stand for the cholesterol rings at 702 cm^{-1}. Figure adapted from paper [64]. (b). Bright-field image (left) and SRS image (right) showing the brain tumor interface. Figure adapted from paper[65]. (c). SRS images of a cancerous human breast tissue slice after MCR analysis and H&E stained histologic results of the same tissue slice. Figure adapted from paper[66].

Through coupling confocal Raman microscopy with SRS microscopy together, it enabled identification of metabolic signature of aggressive human prostate cancer and quantitative analysis of lipid content at single cell level in human patient cancerous tissue[64]. The spectroscopic imaging data (**Figure 1.12a**) showed the aberrant accumulation of

cholesteryl ester (702 cm^{-1}) in lipid droplets of high-grade prostate cancer and metastases (**Figure 1.12**), which was shown to be a consequence of loss of tumor suppressor PTEN and subsequent activation of PI3K/AKT pathway in prostate cancer cells[64]. Depleting cholesteryl ester storage significantly suppressed tumor growth in mouse xenograft models and impaired cancer invasion. This work opens opportunities for using altered cholesterol metabolism for treating aggressive prostate cancer metastases.

In vivo SRS imaging of mouse brain after craniotomy was performed to locate brain tumor margin [65] (**Figure 1.12b**) due to the sharp contrast between lipids and proteins SRS signals. A recent development of spectrometer-free multiplex SRS microscopy further enabled the *in-situ* label-free histological analysis of highly scattered, 5-mm thick human breast cancer tissues [66] (**Figure 1.12c**). This work opens opportunities to perform in vivo clinical imaging using label-free SRS microscopy for cancer diagnosis and tumor margin detection during the surgery.

By combining SRS and iso-tope labelling, many researchers harnessed the deuterated-glucose, deuterated water (D_2O), to study the *de novo* synthesis of lipids or protein and to achieve fast antimicrobial susceptibility test [67,68].

1.2.3 Applications of Transient Absorption Microscopy

Responsible for transporting oxygen, hemoglobin is a metalloprotein in the red blood cells of vertebrates. It is an assembly of four globular protein subunits. Each subunit is composed of a protein tightly associated with a heme group[69]. A heme group consists of an iron ion in a porphyrin. It is well known that the heme group portrays strong absorption yet weak fluorescence. These properties make label free transient absorption microscopy

imaging of hemoglobin an ideal approach. Fu and colleagues[70] demonstrated label free deep tissue imaging of micro vessels in nude mouse ear. They chose a pump beam of 775 nm and a probe beam of 650 nm, and successfully harvested two-color two photon absorption images of microvasculature at different depths with a penetration depth of ~70 μm. In their following-up study, they chose a longer probe beam of 810 nm to differentiate oxyhemoglobin and oxyhemoglobin[70]. Later Fu and coworkers achieved quantification of oxyhemoglobin in single red blood cells level by pumping at 1040 nm and probing at 700 nm[46]. Min and colleagues conducted stimulated emission imaging of microvasculature network in a mouse ear based on the endogenous hemoglobin contrast by choosing the pump beam as 830 nm (two-photon excitation of Soret band) and probe beam as 600 nm[71].

Transient absorption microscopy could also be used to differentiate different melanin. Melanin generally come in two polymeric forms: eumelanin (black) and pheomelanin (red/brown)[72]. Their biosynthetic pathways involve the oxidation of tyrosine leading to the formation of indoles and benzothiazines[72]. Pheomelanin is reddish yellow, and it exhibits phototoxic and pro-oxidant behavior[72]. Eumelanin is a brown–black pigment that is substantially increased in melanoma. Therefore, imaging the microscopic distribution of eumelanin and pheomelanin could be used to separate melanomas from benign nevi in a highly sensitive manner[44].

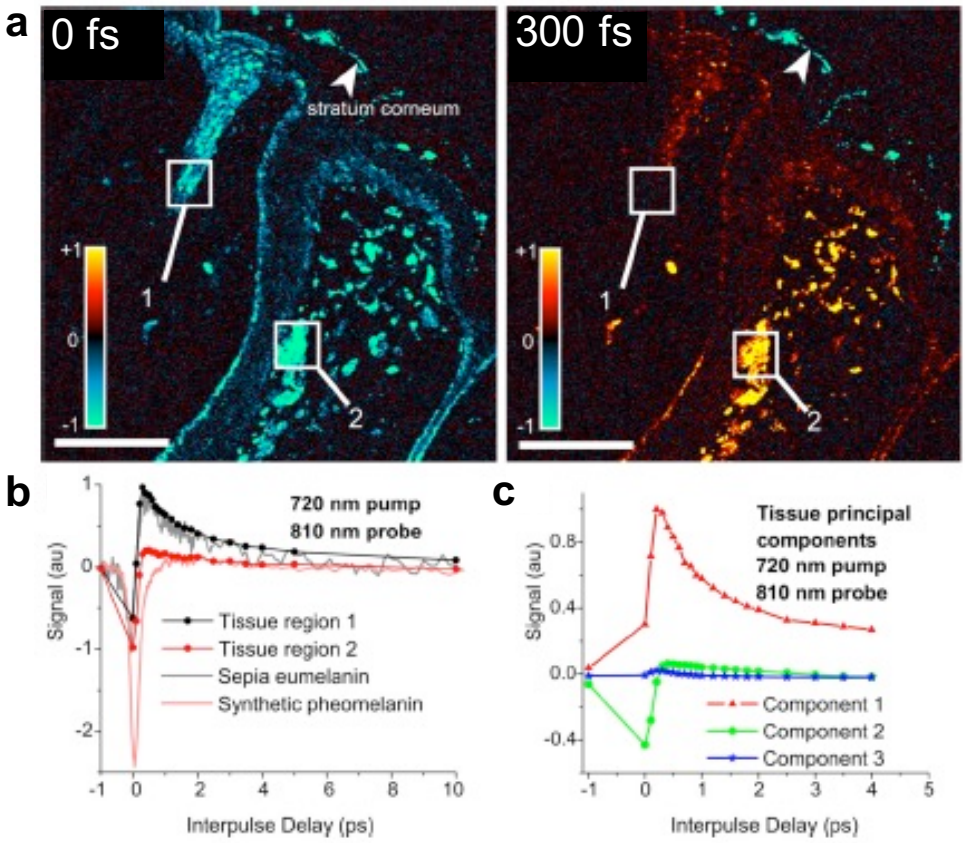

Figure 1.13. Transient absorption microscopy imaging melanocyte tissues. (a) Pump-probe image of a mixture nevi at 0-fs inter-pulse delay (left) and 300-fs inter-pulse delay (right). Scalar bar=100 μm. (b). Time-resolved delay traces of regions of interest 1 and 2 from 0-fs images, and pure melanin solutions. (c). The first three principal components found from time-resolved traces of melanocyte tissues. Component 1 and component 2 account for more than 98% of the variance. Figure is adapted from paper[44].

The differences of the signals of this two melanin are shown in **Figure 1.13**. Eumelanin has an abrupt positive absorption corresponding to excited-state absorption or two-photon absorption, the same as hemoglobin, whereas pheomelanin gives a negative bleaching signal. Their difference arises from stimulated emission or ground-state bleaching, respectively[44]. Through principal component analysis, we could know that the time-resolved delay traces are mainly composed of that of pure eumelanin and that of pheomelanin (**Figure 1.12c**), which provides valuable guidance for detecting melanocyte nevi.

Since biological have many endogenous chromophores, and many of which don't emit fluorescence, transient absorption microscopy offers an excellent imaging approach to visualize these molecules, thus holding great potential for disease diagnosis and further treatment.

CHAPTER 2 LABEL-FREE IMAGING OF GLYCATED HEMOGLOBIN BY TRANSIENT ABSORPTION MICROSCOPY

This work presented in this chapter was published in Science Advances[73]. Copyright© American Association for the Advancement of Science. Prof. Ji-Xin Cheng conceived the idea of imaging HbA1c by transient absorption microscopy. Pu-Ting conducted all the experiments. Haonan contributed to the mathematical modelling of HbA1c distribution in single red blood cells. Kai-Chih and Pu-Ting built the 520-nm pump, 780 nm- probe transient absorption microscope.

As a stable and accurate biomarker, glycated hemoglobin (HbA1c) is clinically used to diagnose type 2 diabetes with a threshold of 6.5% HbA1c among total hemoglobin (Hb). Current methods such as boronate affinity chromatography or enzymatic assay involve complex processing of large-volume blood samples, which inhibits real-time measurement in clinic. Moreover, these methods cannot measure the HbA1c fraction at single red blood cells level, thus unable to separate the contribution by diabetes from other factors such as diseases related to lifetime of red blood cells. Here, we demonstrate a spectroscopic transient absorption imaging approach that is able to differentiate HbA1c from Hb based on their distinct excited state dynamics. HbA1c fraction inside a single red blood cell is derived quantitatively through phasor analysis. HbA1c fraction distribution of diabetic blood is found apparently different from that of healthy blood. A mathematical model is developed to derive the long-term blood glucose concentration. Our technology provides a new way to study heme modification and to derive clinically important information avoid of glucose fluctuation in the bloodstream.

2.1 Introduction

According to the Centers for Disease Control and Prevention diabetes statistics report in 2017, around 30.3 million people (~9.4% of the U.S. population) have diabetes, and this disease is responsible for 4.6 million deaths each year [74]. Diabetes mellitus is a group of metabolic diseases characterized by hyperglycemia resulting from defects in insulin secretion, insulin action or both [75]. Long-term type 2 diabetes induces severe complications such as retinopathy with potential loss of vision [76], nephropathy leading to renal failure [77], and peripheral neuropathy with risk of foot ulcers or even limb amputations [78]. Being cost-effective and convenient, blood glucose measurement has been widely utilized as the golden standard to monitor type 2 diabetes [79]. However, glucose level fluctuates [80] and blood glucose measurement often produces false positive results [81].

As a marker of long-term glucose level, glycated hemoglobin (HbA1c) presents a valuable target for long-term type 2 diabetes monitoring [82,83]. HbA1c is formed by an irreversible non-enzymatic glycosylation of hemoglobin (Hb) exposed to glucose in the bloodstream [84]. Specifically, through the Maillard reaction, glucose attaches to the NH2-terminal valine of the β-chain of Hb [85]. HbA1c concentration in the blood depends on two parameters, the lifespan of red blood cells (RBCs) (~ 120 days) and the glucose concentration in the blood [86]. Therefore, a strong correlation exists between HbA1c concentration and the average glucose concentration in the bloodstream over the past three months. Thus, HbA1c concentration could be utilized to monitor long-term glucose levels [87]. HbA1c fraction among total hemoglobin has been approved for screening for diabetes

(HbA1c $\geq$ 6.5%) and prediabetes (5.7% $\leq$ HbA1c $\leq$6.4%) according to the American Diabetes Association [88].

Multiple methods have been developed to detect HbA1c fraction [89]. Boronate affinity chromatography, for example, was employed to differentiate HbA1c from Hb [90]. Based on the polarity difference between HbA1c and Hb, capillary electrophoresis was also utilized to separate these two molecules [91]. Through conjugating upconversion nanoparticles such as NaYF4: Yb^{3+}, Er^{3+} with anti-HbA1c monoclonal antibody, HbA1c concentration is negatively proportional to the luminescence signal from the conjugated nanoparticle [92]. Anti-HbA1c antibody-functionalized gold nanoprobe provides another clue for the determination of HbA1c based on a one-step colorimetric immunoassay [93]. Surface enhanced Raman spectroscopy was reported to achieve selective detection of HbA1c as a characteristic Raman band around 770-830 cm^{-1} was found in the case of HbA1c [94]. Drop coating Raman technique was used to locally enrich and quantify HbA1c concentration [95]. Mass spectrometry in combination with high-performance liquid chromatography was also utilized to detect HbA1c from other Hb species [96]. One major limitation of the above methods lies in the poor detection specificity [91]. Moreover, none of those methods can provide HbA1c fraction at single RBCs level, thus unable to separate the contributions by glucose and by lifetime of RBCs.

Here, through transient absorption microscopy, we found that HbA1c and Hb possess different excited state dynamics. This spectroscopic signature triggered us to apply

transient absorption microscopy, an advanced label-free imaging technique for non-fluorescent chromophores [40,97-105], to study this heme modification process and to quantify the Hb1Ac percent in single RBCs. At a pixel dwell time of 10 μs, we obtained a time-resolved whole blood image stack within two minutes. Through quantitative phasor analysis, we harvested the standard calibration curve for HbA1c fraction quantitation. Subsequently, combined with the time-resolved whole blood image stacks, we obtained the HbA1c fraction in single RBCs. We show that HbA1c fraction distribution behaves differently between diabetic whole blood and healthy whole blood. Single-cell Hb1Ac fraction distribution could offer long-term monitoring of type 2 diabetes void of the interference from the lifespan of RBCs. Moreover, we utilized a mathematical model to interpret this distribution, and derived the averaged glucose concentration which monitors the bloodstream glucose concentration over the past three months.

2.2 Experimental Section

2.2.1 Chemicals and reagents

Healthy human whole blood and diabetic human whole blood (Lee Biosolutions, Inc.). Fresh human whole blood samples (Boston Children's Hospital Blood Donor Center). Lyphochek Hemoglobin A1c linearity set (BIO-RAD). Poly-Prep slides (P0425-72 EA, Sigma Aldrich). Pure hemoglobin (H7379-1G, Sigma Aldrich). Pure hemoglobin A1c (Lee Biosolutions, Inc.). 0.17 mm cover glass (VWR® Micro Cover Glasses, 48393-048). Double-side tape (Scotch).

2.2.2 Transient absorption microscope

An optical parametric oscillator synchronously pumped by a femtosecond pulsed laser generates the pump (1040 nm) and probe (780 nm) pulse trains (Fig. S2). The pump (1040 nm) is then frequency-doubled via the second harmonic generation (SHG) process to 520 nm through a barium borate (BBO) crystal. Temporal delay between the pump and probe pulses is controlled through a motorized delay stage. The pump beam intensity is modulated with an acousto-optic modulator (AOM). The intensity of each beams is adjustable through the combination of a half-wave plate (HWP) and a polarization beam splitter (PBS). Thereafter, pump and probe beams are collinearly combined and directed into a lab-built laser-scanning microscope. Through the nonlinear process in the sample, the modulation of pump beam is transferred to the un-modulated probe beam. Computer-controlled scanning galvo mirrors are used to scan the combined laser beams in a raster scanning approach to create microscopic images. The transmitted light is collected by an oil condenser. Subsequently, the pump beam is spectrally filtered by an optical filter and the transmitted probe intensity is detected by a photodiode. A phase-sensitive lock-in amplifier (Zurich Instruments) then demodulates the detected signal. Therefore, pump-induced transmission changes in probe beam versus the temporal delay can be measured. This change over time delay shows different time-domain signatures of a chromophore, thus offering the origin of the chemical contrast.

2.2.3 Phase determination from lock-in amplifier

As reported previously[106], the modulated component of an input signal to a lock-in amplifier is $I_{in}\sin(\Omega t + \phi_{in})$, the two channels of the lock-in amplifier output signals are proportional to $I_{in}\cos(\phi_{in} - \phi_R)$ and $= I_{in}\sin(\phi_{in} - \phi_R)$. Here, I_{in}, Ω, ϕ_{in}, ϕ_R are the amplitude of modulated signal, modulation frequency, phase of input signal, and reference phase of lock-in amplifier, respectively. To calibrate the reference phase, we send the modulated pump (520 nm) field in the form of $I_{pump}\sin(\Omega t + \phi_{pump})$. Then the output signals of lock-in amplifier are proportional to $I_{pump}\cos(\phi_{pump} - \phi_R)$ and $I_{pump}\sin(\phi_{pump} - \phi_R)$. Here, ϕ_{pump} is the phase of the modulated pump field, and ϕ_R is the reference phase of lock-in amplifier. By setting ϕ_R to ϕ_{pump}, the output signal from the cosine channel and the sine channel becomes maximum and zero, respectively. We define the cosine channel as in-phase-channel (X channel) and sine channel (Y channel) as quadrature-channel of the lock-in amplifier. When a modulated probe signal at a modulation frequency of Ω, $I_{probe}\sin(\Omega t + \phi_{probe})$, is detected by the lock-in amplifier, the in-phase channel and quadrature-channel output signals are $X = I_{probe}\cos(\phi_{probe} - \phi_{pump})$ and $Y = I_{probe}\sin(\phi_{probe} - \phi_{pump})$, respectively. Here, phase $= \phi_{probe} - \phi_{pump}$. If the analyte behaves as excited state absorption, then phase = 180°; if the analyze abides by stimulated emission or ground state depletion, then phase = 0°. Here, in the case of Hb and HbA1c, they abide by excited state absorption under our current settings (pump: 520 nm, probe: 780 nm).

2.2.4 Multi-exponential fitting

The time-resolved intensity is regarded as the convolution between the instrument response function R(t) and the response from the sample S(t):

$$\mathrm{I(t)} = \int R(t-t')S(t')dt' \qquad (1)$$

The instrument response function is modeled by a Gaussian function with a full width half maximum σ:

$$R(t) = A_1 \exp\left(-\frac{t^2}{2*\sigma^2}\right) \qquad (2)$$

, where A_1 is the constant. Here, in the case of hemoglobin solution, pump-probe decay is modeled by a double-exponential decay with decay constants τ_1, τ_2:

$$S(t) = A_2 \exp\left(-\frac{t}{\tau_1}\right) + A_3 \exp\left(-\frac{t}{\tau_2}\right) \qquad (3)$$

, where A_2 and A_3 are the constants. Then the convolution signal can be derived as the following function:

$$I(t) = I_0 + A * \exp\left(\frac{\sigma^2 - 2*t*\tau_1}{2*{\tau_1}^2}\right) * \left(1 - \mathrm{erf}\left(\frac{\sigma^2 - t*\tau_1}{\sqrt{2}*\sigma*\tau_1}\right)\right) + B$$
$$* \exp\left(\frac{\sigma^2 - 2*t*\tau_2}{2*{\tau_2}^2}\right) * \left(1 - \mathrm{erf}\left(\frac{\sigma^2 - t*\tau_2}{\sqrt{2}*\sigma*\tau_2}\right)\right) \qquad (4)$$

, where I_0, A and B are the constants. All the time-resolved decay curves showed in this manuscript are fitted by the above equation (4).

2.2.5 Preparation of whole blood samples on the poly-prep slides

Whole blood samples were diluted by a hundred times with sterile 1×PBS. Then the diluted whole blood samples were kept bubbling with oxygen gas or air for two hours at 4°C. Then 1.5 μL of the whole blood was pipetted onto a poly-lysine coated cover slide, and sandwiched between a cover slide (0.17-mm thickness, VWR® Micro Cover Glasses, 48393-048) and poly-lysine coated cover slide (P0425-72 EA, Sigma Aldrich). Wait for at least 30 min so that the RBC could adhere to the surface of poly-lysine coated cover slide because of the electrostatic force.

2.2.6 Data analysis

The crystal protein structure of HbA1c and Hb were analyzed by PyMOL (Schrödinger). The time-resolved curves were analyzed by OriginPro2017. Quantitative phasor analysis combined with mean shift theory, HbA1c fraction distribution of whole blood samples were analyzed by Matlab (Mathworks).

2.2 Results

2.3.1 Structure difference between HbA1c and Hb revealed by PyMOL simulation

Similar to Hb, HbA1c is a tetramer, in which glucose is covalently linked to the N-terminal of β-chain of Hb [107]. This modification not only confers HbA1c with different polarity from Hb [91,108], but also alters the secondary structure of Hb [109]. To have a direct

visualization of the protein structure of HbA1c and Hb, we utilized PyMOL to analyze the protein structure of Hb and HbA1c. As shown in **Figure 2.1**, the heme ring in Hb is hidden inside the hydrophobic pocket, whereas the porphyrin ring become more exposed to the outside environment in the case of HbA1c (**Fig. 2.1**, **a** and **b**).

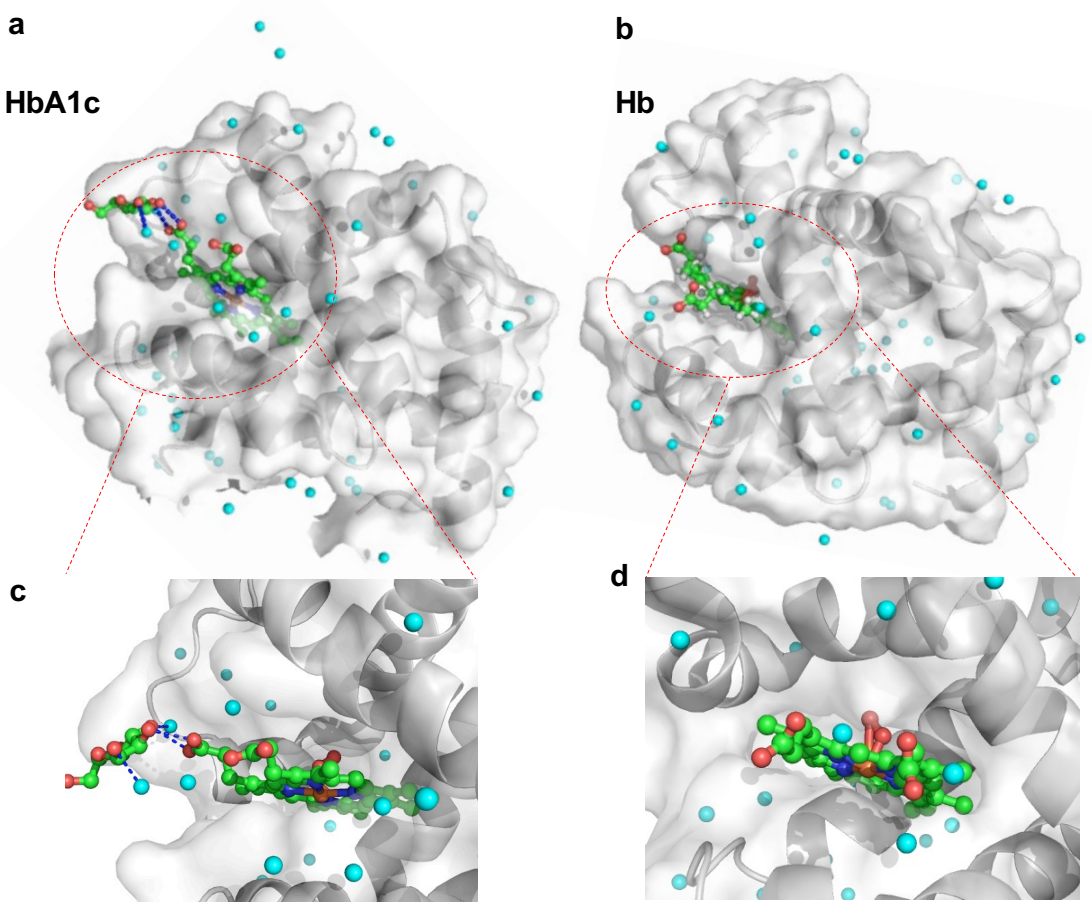

Figure 2.1. PyMOL simulation of the N-terminal of the β chain in HbA1c (a) and Hb (b). The crystal structure of HbA1c (3B75) and Hb (1LFZ) are from Protein Data Bank. Cyan sphere: water molecule; Red sphere: oxygen atom; Green sphere: carbon atom; blue sphere: nitrogen atom. In (a), the polar force between glucose and heme and surrounding water is highlighted by dashed blue lines. Region of interests (ROIs) are highlighted by red dashed circles. (c-d) Zoom-in view of the interaction between glucose and porphyrin ring from glycated hemoglobin (c) and normal hemoglobin (d).

And there is indeed some difference in the secondary structure between HbA1c (**Fig. 2.1**, **a** and **c**) and Hb (**Fig. 2.1**, **b** and **d**). Interestingly, the glucose at the N-terminal has a polar interaction with the heme ring in the case of HbA1c, shown by dashed blue lines in

Fig. 2.1c. This interaction indicates that the excited dynamics of heme might be altered after glycation, which can be measured by transient absorption spectroscopy.

2.3.2 Characterization of HbA1c and Hb by fluorescence, time-resolved photoluminescence, and linear absorption spectroscopy

To identify the spectral difference between HbA1c and Hb, we first measured their fluorescence emission spectra. Due to the poor quantum yield of Hb [110], the fluorescence emission spectra for Hb (**Fig. 2.2a**) and HbA1c (**Fig. 2.2b**) were recorded with an integration time of 1000 seconds. Both HbA1c and Hb exhibit a fluorescence emission peak at 492 nm (**Fig. 2.2**, **a**-**b**), whereas HbA1c has a weaker shoulder peak (**Fig. 2.2b**). This finding confirms the structural difference between Hb and HbA1c. Then, we employed time-resolved photoluminescence to understand this emission difference. It turned out that Hb demonstrates a longer fluorescence lifetime (**Fig. 2.2c**) compared with HbA1c (**Fig. 2.2d)**. We further measured their absorption spectra. Consistent with previously documented literature [94,111], we observed the absorption difference between Hb and HbA1c as well. In the Soret band (~ 400 nm) region, Hb shows a strong absorption at 405 nm (**Fig. 2.2e**), whereas HbA1c shows a characteristic peak at 411 nm, around 6-nm red shift (**Fig. 2.2f**). In the Q bands region, Hb shows peaks at 498 nm, 538 nm, 630 nm, and 677 nm (**Fig. 2.2e**) while HbA1c has only two peaks at 540 nm, and 575 nm (**Fig. 2.2f**). These data altogether consolidate the fact that HbA1c and Hb are spectrally distinct from each other. However, Fourier-transform Raman spectroscopy and linear spectroscopy, either fluorescence emission or electronic absorption, do not have the sensitivity to determine the fraction of HbA1c inside single RBCs. Transient absorption microscopy

circumvents such difficulty, as shown in the following sections.

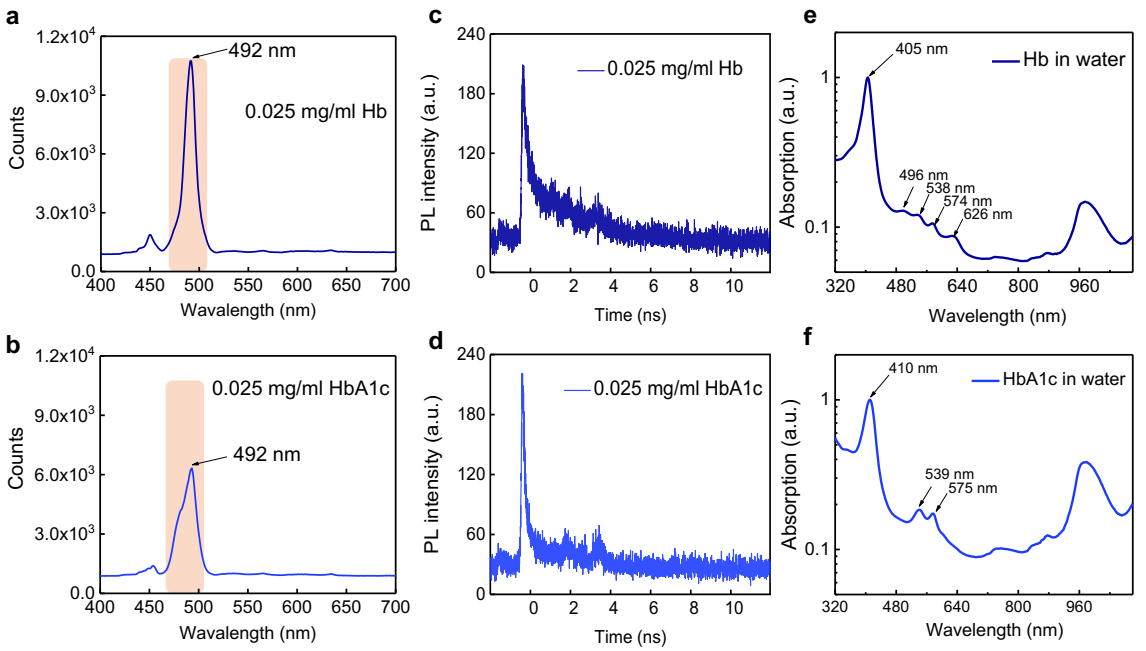

Figure 2.2. Comparative characterization of Hb and HbA1c by fluorescence, time-resolved photoluminescence, and absorption spectroscopy. (a-b) Fluorescence spectra of 0.025 mg/ml Hb (a) along with 0.025 mg/ml HbA1c (b), respectively. Excitation wavelength: 447 nm. Integration time: 1000 s. Bandpass filter: 488±10 nm. Power on the sample: 150 µW. 20× air objective. (c-d) Time resolved photoluminescence measurements of 0.025 mg/ml Hb (c) and 0.025 mg/ml HbA1c (d), respectively. (e-f) Absorption spectra (normalized) of Hb (e) and HbA1c (f), respectively.

2.3.3 Time domain signature of HbA1c and Hb unveiled by transient absorption microscopy

Given the weak fluorescence quantum yield of HbA1c and Hb, we turned to a pump-probe approach to detect the transient absorption of HbA1c in the time domain. By pumping at 520 nm and probing at 780 nm, a time-resolved curve was obtained for Hb (**Fig. 2.3a**) and HbA1c (**Fig. 2.3b**), respectively. Then, we fitted these curves with an equation accounting for the convolution between a Gaussian function and multi-exponential decay function [112]. Through fitting, Hb exhibits two decay constants, with $\tau 1$ = 439 fs and $\tau 2$ = 3.14 ps. In the case of HbA1c, we obtained $\tau 1$ = 577 fs and $\tau 2$ = 3.61 ps. Thus, HbA1c has

a slower excited state decay compared with Hb (**Fig. 2.3c**). It is known that Hb in whole blood has two main forms, deoxy-form hemoglobin (deoxyHb) and oxy-form hemoglobin (oxyHb)[113]. Moreover, oxyHb and deoxyHb show different time-resolved decays [104]. To alleviate the interference from oxygen, we applied a protocol [114] to transfer all deoxy-form Hb or HbA1c to oxy-form by saturating HbA1c or Hb solution with oxygen balloon. Interestingly, OxyHb decays faster compared to Hb (**Fig. 2.3d**) and oxyHbA1c decays faster compared to HbA1c as well (**Fig. 2.3e**). Nevertheless, the decay constants of oxyHbA1c stay larger compared to oxyHb (**Fig. 2.3f**). In the following experiments, we treated the samples in the same manner to ensure that the Hb and Hb1Ac molecules stay in the oxy-form.

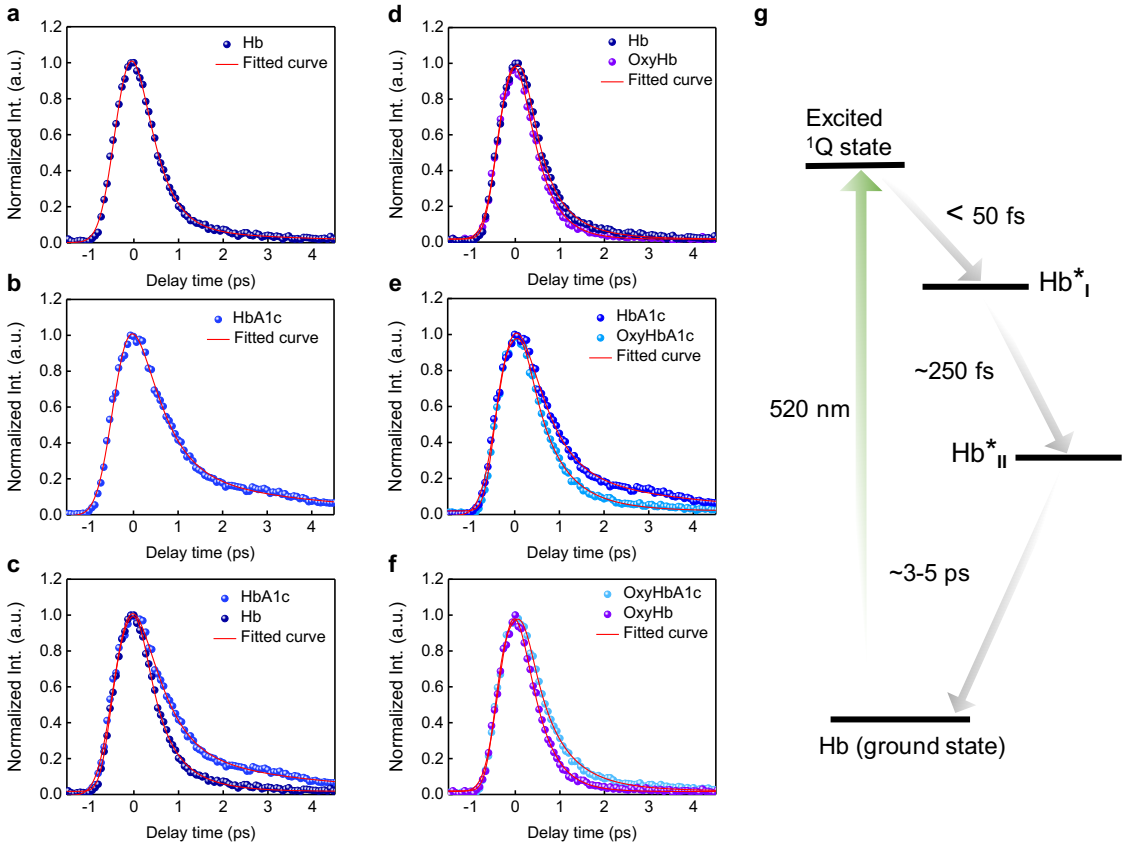

Figure 2.3. Comparison of transient absorption decay signatures between Hb and HbA1c. (a-b) Time-resolved decay curves (normalized) of Hb (a) and HbA1c (b), respectively. (c) Merged time-resolved curves (normalized) of Hb and HbA1c. (d-e) Time-resolved decay curves (normalized) of oxyHb (d) and oxyHbA1c (e), respectively. (f) Merged time-resolved curves (normalized) of oxyHb and oxyHbA1c. (g) Proposed excited state dynamic pathway of Hb when pumped at 520 nm and probed at 780 nm.

The transient absorption signal comes from three major processes, that is, excited state absorption, ground state depletion, and stimulated emission[102]. To identify the dominant mechanism in the case of Hb and HbA1c under our transient absorption settings, we adopted a method developed by Jung *et al.* [106] and retrieved the intensity and phase information of both the X-channel and Y-channel from a lock-in amplifier. The lock-in amplifier detects the in-phase channel (X channel, $\frac{\Delta I_{probe}}{I_{probe}}\cos(\phi_{probe}-\phi_{pump})$), and quadrature channel (Y channel, $\frac{\Delta I_{probe}}{I_{probe}}\sin(\phi_{probe}-\phi_{pump})$), where phase is given by

$\phi_{probe} - \phi_{pump}$. We found that at a phase of 180°, the intensity from X channel has a maximal positive signal, whereas that of Y is the same as background, indicating the sign of $\frac{\Delta I_{probe}}{I_{probe}}$ is negative. Altogether, this means under our transient absorption settings, we observed a gain in absorption. Thus, both Hb and HbA1c abide by excited state absorption. The difference in decay constants between oxyHb and oxyHbA1c led us to explore intramolecular dynamics. Laser at 520 nm in this study pumps Hb or HbA1c from the ground state to the excited ^{1}Q state (**Fig. 2.3g**). Due to ring-to-metal charge transfer [115], the excited ^{1}Q state would relax to the Hb*$_I$ state (~ 50 fs). Then the Hb*$_I$ state would jump to Hb*$_{II}$ state because of ring-to-iron charge transfer (~ 300 fs) [115], and finally, Hb*$_{II}$ relaxes back to the ground state (~ 3-5 ps [115]). Based on the difference in linear absorption in the Q-band region (**Figs 2.2, e-f**), it is reasonable to elucidate that HbA1c and Hb exhibit different excited state dynamics. This difference provides a foundation for mapping the fraction of HbA1c in single RBCs.

2.3.4 Quantitation of HbA1c fraction by transient absorption imaging and phasor analysis

The excited state dynamic difference between Hb and HbA1c allows for differentiation of these two molecules. We first obtained time-resolved decay curves (normalized) of a series of standard HbA1c solutions (**Fig. 2.4a**). However, very small difference between 14% HbA1c solution and 9.9% solution is found (**Fig. 2.4b**). Thus, to accurately quantitate HbA1c fraction in a mixed solution, we turned to a phasor approach [116] that convert a pump-probe decay curve into a vector in the phasor domain.

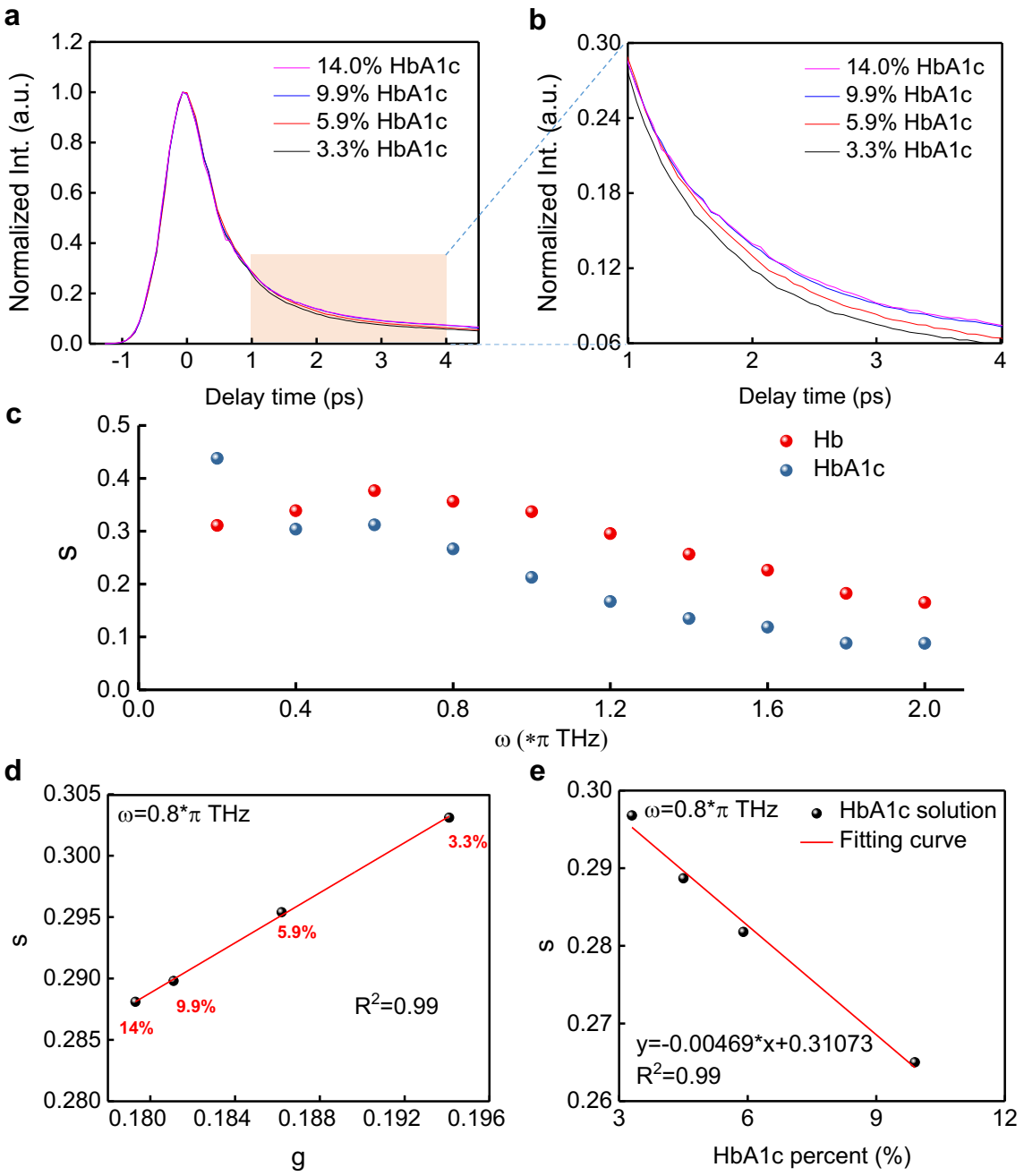

Figure 2.4. Quantitation of HbA1c in a series of solutions by phasor analysis of transient absorption traces. (a) Time-resolved decay curves (normalized) of standard HbA1c solutions (human whole blood based) at different concentrations. (b) Zoom-in view of (a) from delay time of 1 ps to 4 ps. (c) Component *s* versus different ω from 0 THz to 2π THz for pure HbA1c and Hb. (d) Phasor plot of standard HbA1c solutions of different concentrations when ω = 0.8π THz. (e) Calibration curve of standard HbA1c solution at different concentrations (component *s* versus HbA1c%).

Phasor analysis provides an intuitive and efficient method for analyzing transient absorption images as it is void of dependence upon the analyte concentration and initial parameters [116]. In this method, time-resolved signals at each pixel are decomposed into two components, *g* and *s*, representing the real and imaginary parts of the time-resolved signal's Fourier transformation at a given frequency [116], respectively. Components *g* and *s* are defined as the following equations: $g(\omega) = \frac{\int I(t)*\cos(\omega t)dt}{\int |I(t)|dt}$, $s(\omega) = \frac{\int I(t)*\sin(\omega t)dt}{\int |I(t)|dt}$, where $I(t)$ is the time-resolved signal and ω is the given frequency which is a free parameter depending on the separation efficiency. The algorithm transformed the initial time-resolved image stacks into clusters of dots in the phasor domain, where the cluster location of HbA1c is different from that of Hb. To maximize the separation efficiency between Hb and HbA1c, we scanned the component *s* of HbA1c and Hb at different frequencies (**Fig. 2.4c**). It turned out that separation efficiency reaches the maximum in the range of 0.6π THz to 1.2π THz (**Fig. 2.4c**). Therefore, in the following experiments, we set the value of ω as 0.8π THz.

Because hemoglobin depicts as a unipolar signal in the phasor plot [40], we predict that different HbA1c fractions linearly align between the clusters of pure Hb and pure HbA1c in the phasor domain. To validate this hypothesis, we calculated component *s* and component *g* from time-resolved curves of standard HbA1c solutions at different concentrations and then plot *s* versus *g*. As expected, *s* is indeed proportionally linear to *g* at different HbA1c fractions (**Fig. 2.4d**).

To obtain the calibration curve for quantitation of HbA1c fraction in single RBCs, we transferred the focused 1600 pixels from each time-resolved stack of a certain HbA1c fraction to the phasor domain. Subsequently, we utilized an algorithm based on mean-shift theory to find the most aggregated spot. Then, we plotted the coordinate of this spot versus HbA1c fractions and get the standard calibration curve (**Fig. 2.4e**). This curve allows us to determine the HbA1c fraction from single RBC in a real blood specimen.

2.3.5 Transient absorption mapping of Hb1Ac fraction in diabetic versus healthy whole blood

For mapping HbA1c fraction in single RBCs, we first coated the glass substrate with poly-L-lysine so that a single layer of blood cells could adhere to the substrate. Then, we obtained time-resolved image stacks from whole blood under the transient absorption microscope. The RBCs exhibit strong intensity when pump and probe beams are spatially and temporally overlapped with each other (**Fig. 2.5a**). Different RBCs exhibit distinct decay time constants, as observed in region of interest ROI 1 (**Fig. 2.5b**) and ROI 2 (**Fig. 2.5c**), suggesting that HbA1c fraction varies from cell to cell.

By combining the time-resolved decay curves from RBCs along with the standard calibration curve obtained from whole blood samples with known HbA1c percent, we calculated HbA1c fraction for each RBCs. Then, we compiled the HbA1c fractions from seven diabetic whole blood samples (at least 150 RBCs for each sample) and seven healthy whole blood samples (at least 150 RBCs for each sample). Strikingly, the distributions of HbA1c fraction in the diabetic whole blood samples (**Figs. 2.5**, **d-f**) are significantly different from those of healthy whole blood samples (**Figs. 2.5**, **g-i**).

2.3.6 Modeling of hemoglobin glycation

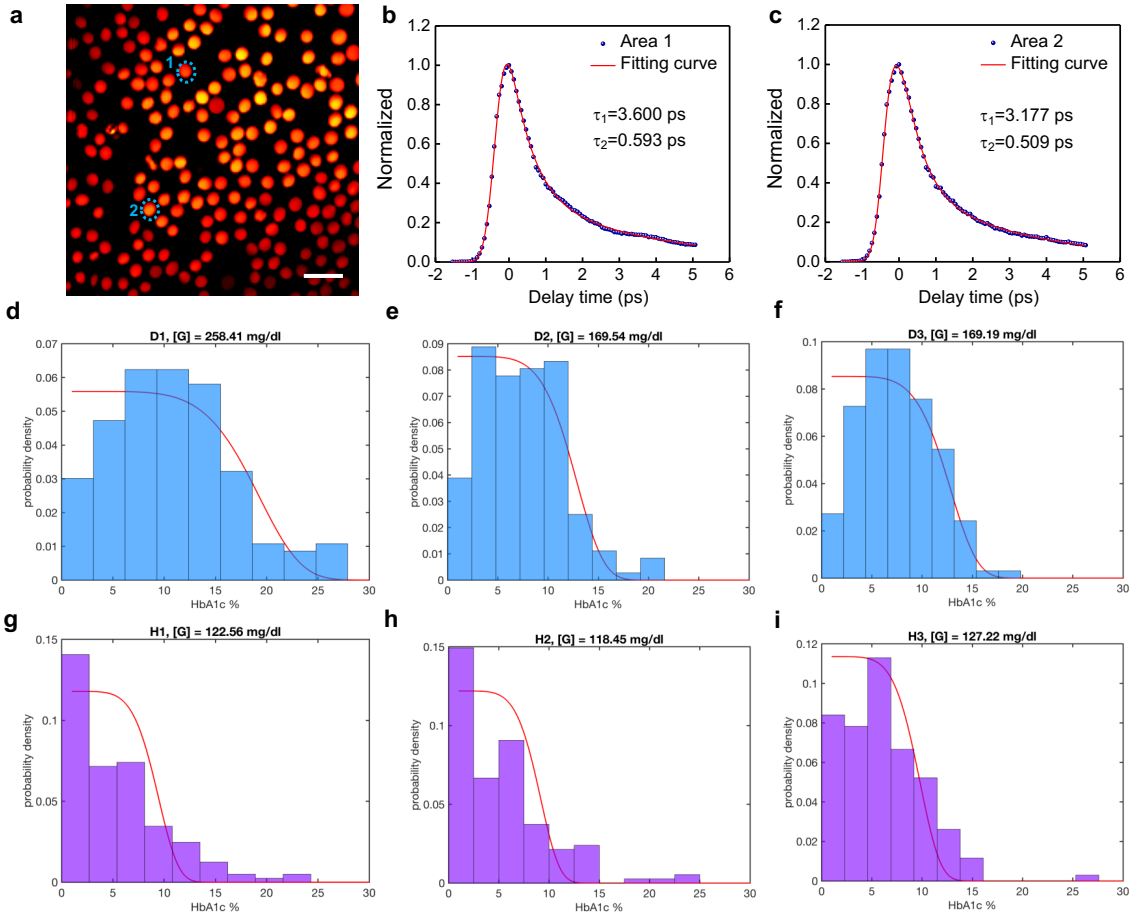

Figure 2.5. Transient absorption imaging of diabetic whole blood and healthy whole blood. (a) Pseudo-color transient absorption image (delay time = 0 ps) of single RBCs with ROIs are highlighted by blue dashed circle. Scalar bar, 10 μm. Pump: 520 nm, 2 mW on the sample; probe = 780 nm, 10 mW on the sample. (b-c) Time-resolved decay curves (normalized) of ROIs shown in (a). (d-f) HbA1c fraction (in single RBCs) distribution along with the fitted glucose concentration from three diabetic whole blood samples. (g-i) HbA1c fraction (in single RBCs) distribution along with the derived glucose concentration from three healthy whole blood samples. Curve fitted by equation (8).

2.4 Discussion and conclusion

Type 2 diabetes mellitus have become an expanding global health problem which is closely linked to the epidemic of obesity [117]. Moreover, patients with type 2 diabetes are at

high risk of microvascular complications and macro-vascular complications because of hyperglycemia and insulin resistance [118]. Conventional method to diagnose type 2 diabetes mellitus is to monitor the bloodstream glucose concentration [79]. However, blood glucose measurement often causes false positives due to fluctuation [81]. As a stable biomarker, HbA1c has drawn increasing attention to be a new target to diagnose type 2 diabetes mellitus [119]. Multiple methods such as boronate affinity chromatography, surface enhanced Raman spectroscopy have been developed to detect HbA1c [91,94]. Nevertheless, none of the above methods could provide HbA1c fraction from single RBCs. Moreover, they couldn't separate the HbA1c fraction contributed by other factors such as diseases related to lifetime of RBCs. Therefore, other innovative methods are highly needed to provide accurate HbA1c fraction in single RBCs.

Here, through high-speed label-free transient absorption microscopy, we showed that HbA1c and Hb have different excited state dynamics, thus possessing distinct time-resolved signatures. Then, quantitative phasor analysis generated the standard calibration HbA1c fraction curve without any priori information input. Subsequently, combined with the standard calibration curve from whole blood samples with known HbA1c percent, HbA1c fraction in single RBCs is derived. And we found that HbA1c fraction distribution in the diabetic whole blood is significantly different from that in healthy whole blood. A mathematical model is further developed to convert such distribution into clinically relevant information for diagnosis of type 2 diabetes stage.

Noteworthy, both Hb and HbA1c have poor fluorescence quantum yield yet strong absorption due to the existence of heme ring [110]. Transient absorption microscopy is an

absorption-based imaging technique which is able to image chromophores with undetectable fluorescence [105]. Herein, both Hb and HbA1c present strong intensity under the transient absorption microscope. Moreover, Hb and HbA1c have distinct time-resolved decay signatures, which allows for the quantitation of Hb1Ac at single RBCs level. The approach reported here can be extended to study heme modification in other conditions, such as detection of hemozoin in malaria infection.

Phasor analysis has been widely used to interpret the fluorescence signal of relevant biological fluorophores by using their phasor fingerprints [120]. Compare with other methods, such as principal component analysis, phasor analysis doesn't need any priori information [121]. Moreover, phasor analysis is not dependent upon the concentration of analyte, thus eliminating fluctuation caused by intensity [122]. Through normalization, phasor analysis could also amplify the molecular contrast, especially when the concentration of analyte is low in a mixture. For example, the time-resolved curves of HbA1c at 3.3% and 5.9% look similar (**Fig. 2.4a**), however, they demonstrate significant difference in the phasor plot. Therefore, combined with mean-shift theory, phasor analysis provides an optimal method to quantify the HbA1c fraction in single RBCs.

It is worth noting that the HbA1c fraction distribution in the diabetic whole blood samples is significantly different from that of healthy whole blood samples. Most of the diabetic RBCs have high HbA1c fraction. Even for the healthy whole blood samples, there is still quite a portion of RBCs whose HbA1c fraction is higher than 6.5%. Through modelling, we derived that the stable average glucose concentration from the past three months in the diabetic whole blood sample is higher compared with that of healthy whole

blood, which is consistent with the real condition in type 2 diabetes. Moreover, this method only needs ~ μL of whole blood samples other than ~ mL of the whole blood sample. In the future, a portable fiber-laser based transient absorption microscope can be developed to achieve noninvasive diagnosis of type 2 diabetes through imaging the artery whole blood. In summary, work reported here underlies the profound potential of utilizing label-free transient absorption microscopy to study heme modification process and to determine the accurate long-term glucose level in the clinic.

CHAPTER 3 PHOTOLYSIS OF STAPHYLOXANTHIN IN METHICILLIN-RESISTANT STAPHYLOCOCCUS AUREUS POTENTIATES KILLING BY REACTIVE OXYGEN SPECIES

The work presented in this chapter was published in Advance Science[123]. Copyright © Wiley online library. Pu-Ting made the accidental discovery of staphyloxanthin photobleaching, and conducted the experiments. Prof. Cheng conceived the concept of photobleaching therapy. Haroon and Pu-Ting conducted the mice infection experiment together under the guidance of Prof. Seleem. Jie contributed to the illustration of photobleaching mathematical model. Leon and Pu-Ting conducted the IVIS imaging of luminescent MRSA-caused skin infection under the guidance of Dr. Dai.

Confronted with the severe situation that the pace of resistance acquisition is faster than the clinical introduction of new antibiotics, health organizations are calling for effective approaches to combat methicillin-resistant *Staphylococcus aureus* (MRSA) infections. Here, we report an approach to treat MRSA through photolysis of staphyloxanthin, an antioxidant residing in the microdomain of *S. aureus* membrane. This photochemistry process is uncovered through transient absorption imaging and quantitated by absorption spectroscopy, Raman spectroscopy, and mass spectrometry. Photolysis of staphyloxanthin transiently elevates the membrane permeability and renders MRSA highly susceptible to hydrogen peroxide attack. Consequently, staphyloxanthin photolysis by low-level 460 nm light eradicates MRSA synergistically with hydrogen peroxide and other reactive oxygen species. The effectiveness of this synergistic therapy is well validated in MRSA planktonic culture, MRSA-infected macrophage cells, stationary-phase MRSA, persisters, *S. aureus* biofilms, and two mice wound infection models. Collectively, our work demonstrates staphyloxanthin photolysis as a new therapeutic platform to treat MRSA infections.

3.1 Introduction

Staphylococcus aureus (*S. aureus*) causes a variety of diseases ranging from skin and soft tissue infections to life-threatening bacteremia[124,125]. Moreover, *S. aureus* has acquired resistance to multiple antibiotic classes that were once effective[126]. A classic example is the emergence of clinical isolates of methicillin-resistant *Staphylococcus aureus* (MRSA) strains in the 1960s that exhibited resistance to β-lactam antibiotics[127,128]. More recently, some MRSA strains have exhibited reduced susceptibility to newer antibiotics such as daptomycin and to last-resort antibiotics such as vancomycin and linezolid[129,130]. Besides the acquired resistance through mutational inactivation, *S. aureus* develops other strategies to undermine the effect of antibiotics, such as residing inside host immune cells[131], forming biofilms, and becoming dormant persisters[132,133]. Those situations pose an appalling challenge to developing new ways to treat MRSA infections.

On the verge of post-antibiotic area, researchers are taking several approaches to tackle MRSA-caused infections. Repurposing existing anticancer, antifungal, anti-inflammatory drugs, has been pursued by harnessing their established feasibility and antibacterial properties[134-136]. Therapeutic application of bacteriophages offers another promising alternative to combat staphylococcal infections[137]. In addition, novel approaches are developed through targeting MRSA-specific virulence factors. More than 90% of all *S. aureus* clinical isolates generate a golden pigment, staphyloxanthin (STX)[138]. STX condenses in the functional membrane microdomain of *S. aureus*[139], endowing *S. aureus* with membrane integrity and excellent antioxidant property[140]. Ever since Nizet and Liu elucidated the pivotal role of STX, the virulence factor which protects *S. aureus* from

neutrophil-based killing[141], stripping this important pigment off MRSA has become a novel therapeutic approach[142,143]. A range of synthetic cholesterol inhibitors have been harnessed to inhibit STX biosynthesis[141,143]. Chen *et al*. found that naftifine, a FDA-approved antifungal drug, blocked the biosynthesis of STX through inhibition of diapophytoene desaturase[144]. Jabra-Rizk *et al*. demonstrated that sesquiterpene farnesol, a natural plant metabolite, effectively suppressed the production of STX through binding the active domain of the dehydrosqualene synthase, thus compromising the membrane integrity[145]. However, administration of exogenous agents only achieved limited efficacy possibly due to off-targeting[146]. Therefore, drug-free approaches to eradicate STX have been pressingly desired.

Here, through label-free transient absorption imaging of non-fluorescent chromophores in *S. aureus*, we accidentally find that STX is prone to photolysis and this photolysis process strongly depends on the excitation wavelength. By absorption spectroscopy, we identify that the optimal wavelength for STX photolysis is around 460 nm. We also unveil that 460 nm light induces STX C=C bond breakdown by employing Raman spectroscopy and mass spectrometry. We then find that STX photolysis transiently elevates the membrane permeability and renders MRSA highly susceptible to reactive oxygen species attack. Based on these findings, we developed a highly effective synergy between STX photolysis and low-concentration hydrogen peroxide, which is well established in eliminating stationary-phase MRSA, MRSA persisters, *S. aureus* biofilms, and MRSA-infected mice wound models. We also find that STX photolysis could assist macrophage cells to eliminate intracellular MRSA, whereas high-concentration antibiotic fails. Our

findings open new opportunities for treating MRSA infections.

3.2 Methods

3.2.1 Portable staphyloxanthin photobleaching apparatus

The apparatus is comprised of three parts: a blue light LED (M470L3, Thorlabs), an adjustable collimator (SM1P25-A, Thorlabs), and a power controller (LEDD1B, Thorlabs). The blue light LED has a central emission wavelength of 460 nm with a full width at half maximum of 30 nm. The beam size is adjustable through the collimator (SM1P25-A, Thorlabs). The maximal power of the blue light LED is 200 mW/cm^2.

3.2.2 Carotenoids extraction from MRSA USA300 and acquisition of absorption spectrum

The pigment extraction protocol was adapted from a previous report[147]. Briefly, 100 µL of bacteria solution supplemented with 1900 µL sterile Tryptic Soy Broth (TSB) was cultured for 24 hours with shaking (speed of 250 rpm) at 37 °C. The suspension was subsequently centrifuged for two minutes at 7,000 rpm, washed once, and re-centrifuged. The pigment was extracted with 200 µL methanol at 55 °C for 20 minutes. Extracts from the CrtM mutant were extracted by the same method. The protocol for the treatment of MRSA USA300 with naftifine was adapted from a published report[144]. Bacteria were cultured with 0.2 mM naftifine for 24 hours at 37°C with the shaking speed of 250 rpm. The extraction procedure was the same as described above. The extracted solutions were subsequently exposed to 460 nm light (90 mW, aperture: 1 cm × 1 cm) at different time intervals (0 min, 5 min, 10 min, 20 min). Absorption spectra of the above solutions were obtained by a spectrometer (SpectraMax, M5).

3.2.3 Mass spectrometry

To study the photobleaching chemistry, we extracted crude STX solution from MRSA and exposed the extract to 460 nm light using the procedure described above. The separation was performed on an Agilent Rapid Res 1200 HPLC system. The HPLC-MS/MS system consisted of a quaternary pump with a vacuum degasser, thermostated column compartment, auto-sampler, data acquisition card, and triple quadrupole (QQQ) mass spectrometer (Agilent Technologies, Palo Alto, CA, USA). An Agilent (ZORBAX) SB-C8 column (particle size: 3.5 μm, length: 50 mm, and internal diameter: 4.6 mm) was used at a flow rate of 0.8 mL/min. The mobile phase A was water with 0.1% formic acid and mobile phase B was acetonitrile with 0.1% formic acid. The gradient increased linearly as follows: 5% B, from one to five min; 95% B from five to six min, and 5% B. Column re-equilibration was 6-10 min, 5% B. The relative concentration of STX was quantified using MS/MS utilizing the Agilent 6460 QQQ mass spectrometer with positive electrospray ionization. Quantitation was based on multiple reaction monitoring. Mass spectra were acquired simultaneously using electrospray ionization in the positive modes over the m/z range of 100 to 1000. Nitrogen was used as the drying flow gas.

In order to understand how STX degrades when exposed to 460 nm light, an Agilent 6545 quadrupole time-of-flight (Q-TOF) (Agilent, Santa Clara, CA, USA) was exploited to conduct the separation and quantification steps. This ultra-performance liquid chromatography (UPLC)-MS/MS utilized an Agilent (ZORBAX) SB-C8 column (particle size: 3.5 μm, length: 50 mm, and internal diameter: 4.6 mm) to conduct the separation at a flow rate of 0.8 mL/min. The relative concentration of STX was quantified using MS/MS

utilizing the Agilent 6545 Q-TOF MS/MS with positive electrospray ionization. The mobile phase was composed of water (A) and acetonitrile (B). The gradient solution with a flow rate of 0.8 mL/min was performed as follows: 85% B, from 0 to 30 min; 95% B, from 30 to 31 min; 85% B, from 31 to 35 min; 85% B, after 35 min. The sample injection volume was 20 μL. The UPLC-MS/MS analysis was performed in positive ion modes in the m/z range of 100-1100.

3.2.4 In vitro assessment of synergy between 460 nm light and H_2O_2

MRSA USA300 was overnight cultured in sterile tryptic soy broth (TSB) in a 37°C incubator with shaking (at 250 rpm) (OD_{600} = 1). Thereafter, an aliquot (20 μL) of the bacterial suspension was transferred onto a glass slide. Samples were exposed to 460 nm light at different time lengths and variable light intensities. For groups treated with H_2O_2, bacteria were collected in phosphate buffered saline (PBS) supplemented with H_2O_2 at different concentrations (0 mM, 1.4 mM, 2.8 mM, 5.5 mM, 11 mM, 22 mM, 44 mM, 88 mM and 176 mM). The solutions were cultured for 30 min. The solution was serially diluted in sterile PBS and transferred to TSB plates in order to enumerate the viable number of MRSA colony-forming-units (CFU). Plates were incubated at 37 °C for 24 hours before counting viable CFU/mL. Data are presented as viable MRSA CFU/mL and percent survival of MRSA CFU/mL in the treated groups.

3.2.5 Checkerboard broth dilution assay

To evaluate the combinatorial behavior between staphyloxanthin photobleaching and hydrogen peroxide, we performed checkerboard broth dilution assays[148] to calculate a

fractional inhibition centration index (FICI). After being exposed to a series of light doses, 0, 15, 30, 60, 120, 240, 480 J/cm^2, MRSA inoculum were transferred to a 96-well plate containing an eight two-fold dilution of hydrogen peroxide starting at 88 mM. Then the plate was cultured at 37°C for 16-20 hours. The optical density at 600 nm (OD_{600}) was recorded to represent the bacteria number. A heat map correlated with OD600 was generated to calculate FICI.

3.2.6 Stationary-phase MRSA and MRSA persister cells

Stationary-phase samples were prepared in the following way: bacteria cells of streaked plate from frozen stock were grown at 37℃, 200 r.p.m. in TSB overnight. Then spin down, wash the pellet with sterile 1×PBS twice. Then the pellet was suspended in 1×PBS.

Persister preparation: As mentioned elsewhere,[149] MRSA USA300 was grown overnight in tryptic soy broth, then diluted in fresh medium and incubated until cells reached logarithmic phase of growth. Bacteria were then exposed to 10×MIC ciprofloxacin for 6 hours. After culturing for 6 hours, spin down and washed the bacteria pellet with sterile 1×PBS twice. Then the washed pellet was resuspended in fresh PBS. Different treatments will be applied by treating the fresh sample with different schemes.

3.2.7 Fluorescence mapping of live and dead S. aureus in biofilm

An overnight culture of *S. aureus* (ATCC 6538) was grown in a 37 °C incubator with shaking (at 250 rpm). Poly-D-lysine (Sigma Aldrich) was applied to coat the surface of glass bottom dishes (35 mm, In Vitro Scientific) overnight. The overnight culture of *S. aureus* was diluted (1:100) in TSB containing 5% glucose and transferred to the glass bottom dishes. The plates were incubated at 37°C for 24-48 hours in order to form mature

biofilm. Thereafter, the media was removed and the surface of the dish was washed gently with sterile water to remove planktonic bacteria. Plates were subsequently treated with 460 nm light alone (200 mW/cm^2, 30 min), H_2O_2 (13.2 mM, 20 minutes) alone, or a combination of 460 nm light and H_2O_2. Groups receiving H_2O_2 were quenched through addition of 0.5 mg/mL catalase (Sigma Aldrich, 50 mM, pH = 7 in potassium buffered solution). After treatment, biofilms were immediately stained with fluorescence dyes, as follows.

To confirm the existence of biofilm on the glass bottom surface, a biofilm matrix stain (SYPRO® Ruby Biofilm Matrix Stain, Invitrogen) was utilized. Biofilms were stained with the live/dead biofilm viability kit (Invitrogen) for 30 minutes to quantify the survival percent of *S. aureus* in the biofilm after treatment. The biofilms were washed with sterile water twice and then imaged using a fluorescence microscope (OLYMPUS BX51, objective: 60×, oil immersion, NA = 1.5). Two different excitation channels (live: FITC; dead: Texas Red) were utilized in order to map the ratio of live versus dead cells within the biofilm. The acquired images were analyzed by ImageJ (National Institute of Health). Statistical analysis was conducted via a two-paired *t*-test through GraphPad Prism 6.0 (GraphPad Software, La Jolla, CA).

3.2.8 Confocal laser scanning microscopy to image intracellular hydrogen peroxide

S. aureus (ATCC 6538) was utilized as the experimental strain. An intracellular hydrogen peroxide kit (Sigma Aldrich) was employed to image the intracellular hydrogen peroxide. The excitation of this dye was through an Olympus FV1000 scanning confocal microscope with the excitation line of 488 nm. A 60 × water immersion objective (Olympus)

was used. For H_2O_2-treated group, overnight cultured *S. aureus* was treated with 0.15% H_2O_2 for 20 min. For 460 nm light plus H_2O_2-treated group, overnight cultured *S. aureus* was treated with 0.15% H_2O_2 for 20 min after 30-min 460 nm light exposure. Then spin down, washed with sterile PBS, repeat twice. Stain the above mentioned samples with the intracellular hydrogen peroxide kit for 30 min. Spin down, washed with sterile PBS, repeat twice of this process. Sandwiched washed samples in between two clean coverslides (VWR). Images were processed by ImageJ (National Institute of Health).

3.2.9 Intracellular MRSA infection model

Murine macrophage cells (J774) were cultured in DulBecco's Modified Eagle Medium (DMEM) supplemented with 10% fetal bovine serum (FBS) at 37 °C with CO_2 (5%). Cells were exposed to MRSA USA400 at a multiplicity of infection of approximately 100:1. 1-hour post-infection, J774 cells were washed with gentamicin (50 μg/mL, for one hour) to kill extracellular MRSA. Vancomycin, at a concentration equal to 2 μg/mL (4 × MIC, MIC: minimal inhibition concentration), was added to six wells. Six wells received 460 nm light treatment twice (six hours between treatments) for two minutes prior to addition of DMEM + 10% FBS. Three wells were left untreated (medium + FBS) and three wells received dimethyl sulfoxide at a volume equal to vancomycin-treated wells. Twelve hours after the second 460 nm light treatment, the test agents were removed; J774 cells were washed with gentamicin (50 μg/mL) and subsequently lysed using 0.1% Triton-X 100. The solution was serially diluted in PBS and transferred to tryptic soy agar plates in order to enumerate the MRSA CFU present inside infected J774 cells. Plates were incubated at 37 ºC for 22 hours before counting viable CFU/mL. Data are presented as $\log_{10}$(MRSA CFU/mL) in infected

J774 cells in relation to the untreated control. The data was analyzed via a two-paired *t*-test, utilizing GraphPad Prism 6.0 (GraphPad Software, La Jolla, CA).

3.2.10 In vivo MRSA wound model

This animal experiment was conducted following protocols approved by Purdue Animal Care and Use Committee (PACUC). To initiate the formation of a skin wound, five groups (N=5) of eight-week-old female BALB/c mice (obtained from Harlan Laboratories, Indianapolis, IN, USA) were disinfected with ethanol (70%) and shaved on the middle of the back (approximately a one-inch by one-inch square region around the injection site) one day prior to infection as described from a reported procedure[150]. To prepare the bacterial inoculum, an aliquot of overnight culture of MRSA USA300 was transferred to fresh tryptic soy broth and shaken at 37 °C until an OD_{600} value of ~1.0 was achieved. The cells were centrifuged, washed once with PBS, re-centrifuged, and then re-suspended in PBS. Mice subsequently received an intradermal injection (40 μL) containing 2.40×10^9 CFU/mL MRSA USA300. An open wound formed at the site of injection for each mouse, ~60 hours post-infection.

Topical treatment was initiated subsequently with each group of mice receiving the following: fusidic acid (2%, using petroleum jelly as the vehicle), 13.2 mM H_2O_2 (0.045%, two-minute exposure), 460 nm light (two-minute exposure, 24 J/cm^2), or a combination of 460 nm light (two-minute exposure, 24 J/cm^2) and 13.2 mM H_2O_2 (two-minute exposure). One group of mice was left untreated (negative control). Each group of mice receiving a particular treatment regimen was housed separately in a ventilated cage with appropriate bedding, food, and water. Mice were checked twice daily during infection and treatment to

ensure no adverse reactions were observed. Mice were treated twice daily (once every 12 hours) for three days, before they were humanely euthanized via CO_2 asphyxiation 12 hours after the last dose was administered. The region around the skin wound was lightly swabbed with ethanol (70%) and excised. The tissue was subsequently homogenized in PBS. The homogenized tissue was then serially diluted in PBS before plating onto mannitol salt agar plates. Plates were incubated for at least 19 hours at 37 °C before viable MRSA CFU/mL were counted for each group. Outlier was removed based upon the Dixon Q Test. Data were analyzed via a two-paired *t*-test, utilizing GraphPad Prism 6.0 (GraphPad Software, La Jolla, CA).

3.2.11 In vivo bioluminescence mice abrasion model

This animal experiment was approved by the Subcommittee on Research Animal Care (IACUC) of Massachusetts General Hospital and were in accordance with National Institutes of Health guidelines. As reported elsewhere,[151] adult female BALB/c mice (Charles River Laboratories, Wilmington, MA, *N*=5), 7-8 weeks old and weighing 16-18 g. The mice were maintained on a 12 h light/dark cycle at a room temperature of 21°C. Before the creation of skin abrasions, mice were anesthetized by i.p. injection of a ketamine-xylazine cocktail and then shaved on the dorsal surfaces using an electric fur clipper. Mouse skin was then scraped using no. 15 scalpel blades until a redden area appeared. This procedure resulted in first degree skin abrasions with most part of the epidermis removed. One drop (100 μL) of overnight cultured bioluminescent MRSA USA300 *LAC::Lux* suspension containing around 10^7 CFU were evenly smeared onto the

mice wounds by using a micropipette. Three hours later, different treatment schemes were applied and the real-time bioluminescence signal from each mouse was acquired.

3.2.12 Photobleaching model

To analyze the time-lapse transient absorption signals, we utilized a mathematical model which was originally used to depict the photobleaching of photosensitizers happening during a photodynamic process[152]:

$$\frac{d[C]}{dt} = -k_1[C][R] \qquad (1)$$

, where t is the duration time, [C] is the concentration of chromophore (e.g., carotenoids in *S. aureus*), $k_1 (k_1 = {}^{1}/_{\tau_1})$ is the rate constant of first-order photobleaching with τ_1 being the first-order photobleaching time constant, [R] is the concentration of active agents (the chromophores which have interaction with light):

$$[R] \sim [R]_0 + k_2[C] \qquad (2)$$

, where k_2 $(k_2 = {}^{1}/_{([C]_0 * \tau_2)})$ is the rate constant of second-order photobleaching with τ_2 being the second-order photobleaching time constant, $[R]_0$ is the initial concentration of the active agent, respectively. The combination of equation (1) and equation (2) leads to:

$$\frac{d[C]}{dt} = -\frac{1}{\tau_1} * [C] - \frac{1}{\tau_2 * [C]_0} * [C]^2 \qquad (3)$$

The solution for equation (3) is:

$$\frac{[C]_t}{[C]_0} = A * \frac{\exp\left(-\frac{t}{\tau_1}\right)}{1 + \frac{\tau_1}{\tau_2} * \left(1 - \exp\left(-\frac{t}{\tau_1}\right)\right.} \qquad (4)$$

, where A is a constant. When first-order photobleaching process pivots (usually happening for low concentration of chromophore and having the involvement of oxygen), $\tau_2 \to \infty$, then equation (4) becomes:

$$\frac{[C]_t}{[C]_0} = A * \exp\left(-\frac{t}{\tau_1}\right) \qquad (5)$$

, which is similar to first-order kinetic reaction. At this occasion, the photobleaching rate is linearly proportional to the concentration of chromophore. When second-order photobleaching process dominates (usually happening for high concentration of chromophore potentially through triplet-triplet annihilation), $\tau_1 \to \infty$, then equation (4) becomes:

$$\frac{[C]_t}{[C]_0} = A * \frac{1}{1 + \frac{t}{\tau_2}} \qquad (6)$$

Under this condition, the photobleaching rate is proportional to the square of chromophore concentration. According to the fitting result, the decaying signal of MRSA under our transient absorption microscopy settings belongs to a second-order photobleaching with $\tau_1 \to \infty$.

3.3 Results

3.3.1 STX photobleaching revealed under a transient absorption microscope

Initially we attempted to differentiate MRSA from methicillin-susceptible *S. aureus* by

transient absorption imaging of their intrinsic chromophores. Intriguingly, once the cultured MRSA was placed under the microscope, the strong signal measured at zero delay between the 520-nm pump and 780-nm probe pulses quickly attenuated over second scale (**Figure 3.1a**). We hypothesized that a specific chromophore in MRSA is prone to photobleaching under the abovementioned settings. To verify this, we fitted the time-course curve with a photobleaching model developed for photosensitizers[152] (**Figure 3.1b**, see Methods):

$$y = y_0 + A * \frac{\exp\left(-\frac{t}{\tau_1}\right)}{1 + \frac{\tau_1}{\tau_2} * \left(1 - \exp\left(-\frac{t}{\tau_1}\right)\right)} \qquad (1)$$

, where t is the duration of light irradiation, y is the signal intensity, y_0 and A are constants, τ_1 and τ_2 are the time constants for the first- and second-order photobleaching, respectively. The first-order bleaching occurs at low concentration of chromophores ($\tau_2 = \infty$). The second-order bleaching takes place when quenching within high-concentration surrounding chromophores dominates ($\tau_1 = \infty$). Derivation of equation (1) is detailed in supplementary information. Strikingly, this photobleaching model fitted well the raw time-course curve ($\tau_1 = \infty, \tau_2$ = 0.15 ± 0.02 s). Moreover, oxygen depletion ($Na_2S_2O_4$: oxygen scavenger) showed negligible effect on the photobleaching speed (τ_2 = 0.14 ± 0.01 s). The same phenomenon was observed in methicillin-susceptible *S. aureus*. To determine whether oxygen plays an essential role during this photobleaching process, we kept the extracted chromophore solution bubbling with nitrogen gas for two hours in order to deplete the oxygen.[153] We found that oxygen depletion didn't affect the photobleaching process. Collectively, these data support a second-order photobleaching process.

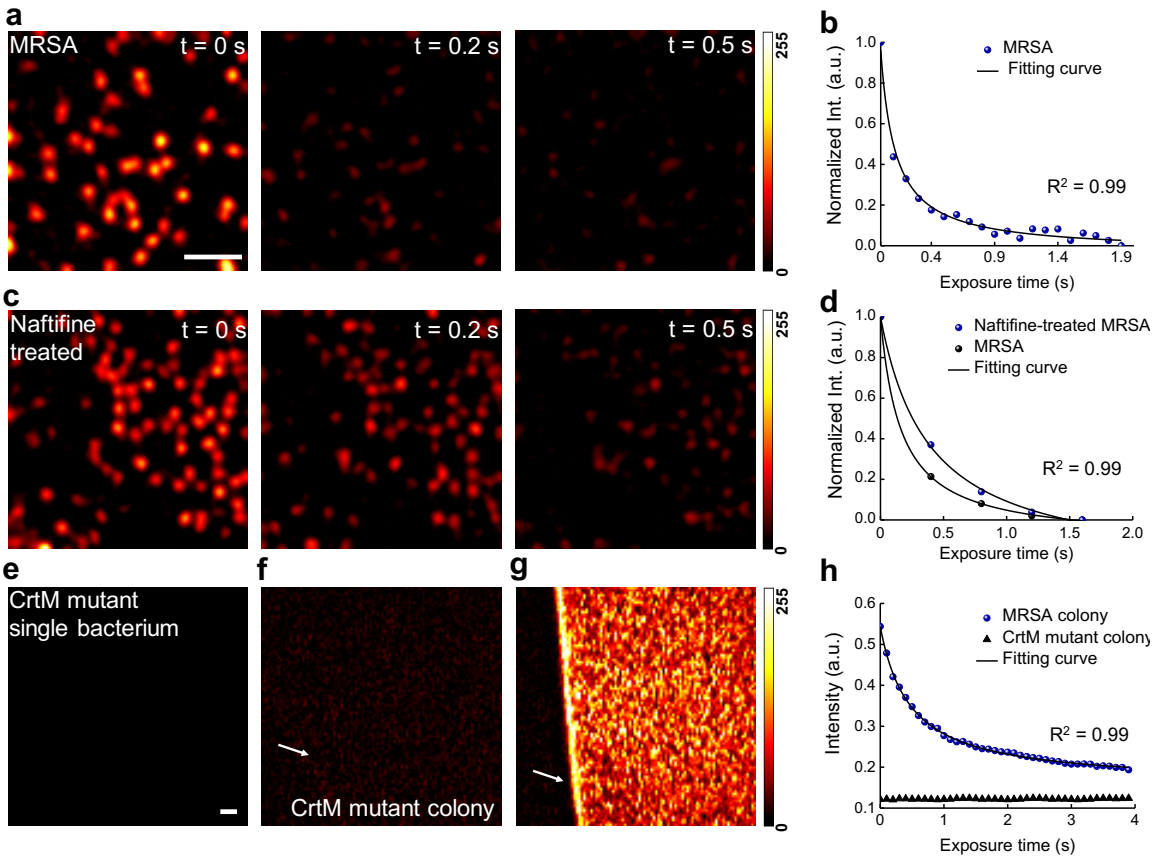

Figure 3.1. Photobleaching of staphyloxanthin in MRSA uncovered by transient absorption microscopy. (a) Pseudo-color time-lapse images of MRSA. Scale bar=5 µm, applies to images in a and c. (b) Representative time-lapse signal (normalized) from MRSA. (c) Pseudo-color time-lapse images of naftifine-treated MRSA. (d) Representative time-lapse signals (normalized) from MRSA and naftifine-treated MRSA. (e-g) Pseudo-color images of CrtM mutant, CrtM mutant colony, MRSA colony at t=0 s, respectively. Scale bar=20 µm, applies to (e-g). (h) Representative raw time-lapse signals from MRSA colony and CrtM mutant colony. White arrows indicate the interface between air and sample. Time-lapse signals were fitted by equation (1). Images were processed from raw data with dynamic range of 0-255 through ImageJ.

Next, we aimed to deduce the specific chromophore inside MRSA that accounts for the observed photobleaching phenomenon. It is known that carotenoids are photosensitive due to the conjugated C=C bonds[154]. Therefore, we hypothesized that STX, the major carotenoid pigment residing in the cell membrane of MRSA, underwent photobleaching in our transient absorption study. To test this hypothesis, we treated MRSA with naftifine to block the synthesis of STX[144]. The treated MRSA exhibited lower signal intensity (**Figure 3.1c**) and slower photobleaching speed (**Figure 3.1d**). Specifically, τ_2 of naftifine-treated

MRSA (0.39 ± 0.07 s) is 2.5 times of that of MRSA (0.15 ± 0.02 s), in consistence with second-order photobleaching. Furthermore, no transient absorption signal was observed in *S. aureus* strain with mutation in dehydrosqualene synthase (CrtM) (**Figure 3.1e**) that is responsible for STX biosynthesis[140]. To avoid the systematic error aroused by single bacterium measurement, we repeated the same analysis using bacterial colonies. It turned out that CrtM mutant colony (**Figure 3.1**, **f** and **h**) only exhibited background induced by cross-phase modulation[155], whereas the MRSA colony showed a sharp contrast against the background (**Figure 3.1g**) and a fast photobleaching decay (**Figure 3.1h**). Taken together, these data confirm that STX in MRSA accounts for the observed photobleaching phenomenon.

3.3.2 Wide-field photobleaching of STX by a portable device

In the transient absorption study, when changing 520-nm pump irradiance while fixing 780-nm probe intensity, both signal intensity and τ_2 changed drastically, whereas the alteration of probe irradiance only affected the transient absorption signal intensity but not τ_2. These findings collectively imply that photobleaching efficacy is highly dependent on the excitation wavelength, which is consistent with the fact that photobleaching is grounded on the absorption of chromophore[156].

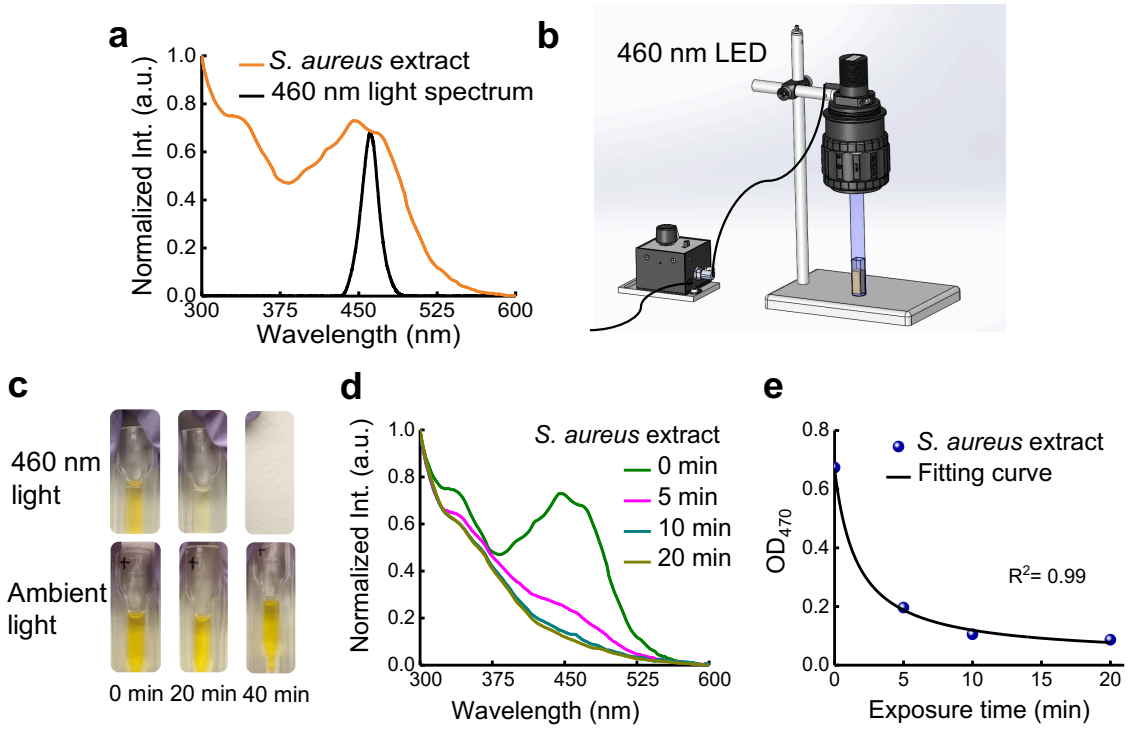

Figure 3.2. Staphyloxanthin is prone to photobleaching under blue light irradiance. (a) Absorption spectrum of crude STX extract (brown) and emission profile of a blue LED (black). (b) Schematic illustration of a portable LED-based wide-field photobleaching device. (c) Pictures of crude STX extract exposed to 460 nm light, and ambient light at different time intervals. (d) Absorption spectra of crude STX extract over different 460 nm light exposure time. (e) OD of crude STX extract at 470 nm adapted from (d) over 460 nm light exposure time. Data points were fitted by equation (1).

To find the optimal wavelength for bleaching STX, we measured the absorption spectrum of crude STX extract from *S. aureus*. The extract showed strong absorption in the window from 400 nm to 500 nm (**Figure 3.2a**). Based on this result, we built a portable device composed of a blue LED with a central emission wavelength at 460 nm for wide-field bleaching STX (**Figure 3.2b**). We exposed the crude STX extract to the 460 nm light (intensity, 90 mW/cm^2) for different time intervals. Remarkably, the distinctive golden color of STX disappeared within 30-min exposure, whereas the control group under ambient light remained unchanged **(Figure 3.2c**). Its absorption within 400-500 nm window decreased dramatically over 460 nm light exposure (**Figure 3.2d**). The optical

density at 470 nm (from **Figure 3.2d**) versus the 460 nm light dose can be well fitted with equation (1) (**Figure 3.2e**). Additionally, naftifine-treated or CrtM-mutant MRSA extracts were insensitive to 460 nm light exposure, indicated by their nearly unchanged absorption spectra. These findings collectively suggest that STX is prone to photobleaching under 460 nm light irradiance.

3.3.3 Mass spectrometry and Raman spectroscopy unveil the photochemistry of STX under 460 nm light irradiance

To understand the chemical nature of this photobleaching process, we investigated the STX degradation products induced by 460 nm light irradiation via mass spectrometry (MS). An abundant peak appears at m/z = 721.5, while a weaker peak at m/z = 819.5 ($[M+H]^+$) is consistent with the molecular weight of STX (Mw = 818.5 g/mol). To find out the relationship between m/z = 721.5 and m/z = 819.5, we gradually increased the collision energy from 0 to 20 eV. In **Figure 3.3a**, the abundance of m/z = 721.5 increases relative to that of m/z = 819.5 with increasing collision energy, indicating that m/z =721.5 is a product ion from m/z = 819.5. When the collision energy was higher than 30 eV, m/z = 241.5, a product of the precursor ion m/z = 721.5, became dominant and presented as a stable marker (**Figure 3a**). Thus, to accurately quantify the amount of STX versus 460 nm light dose, we targeted the peak area in high-performance liquid chromatography (HPLC) chromatograms specifically from ion m/z = 241.5 (**Figure 3.3b**). **Figure 3.3c** depicts the bleaching dynamics of STX induced by 460 nm exposure. 5-min 460 nm light exposure (dose: 27 J/cm^2) decomposed 90% of STX extracted from ~10^9 colony-forming units (CFU ml^{-1}) MRSA, and a dose of 54 J/cm^2 bleached all the STX pigments (data not shown). In contrast

extracts from naftifine-treated and CrtM-mutant *S. aureus* had negligible response to 460 nm light exposure.

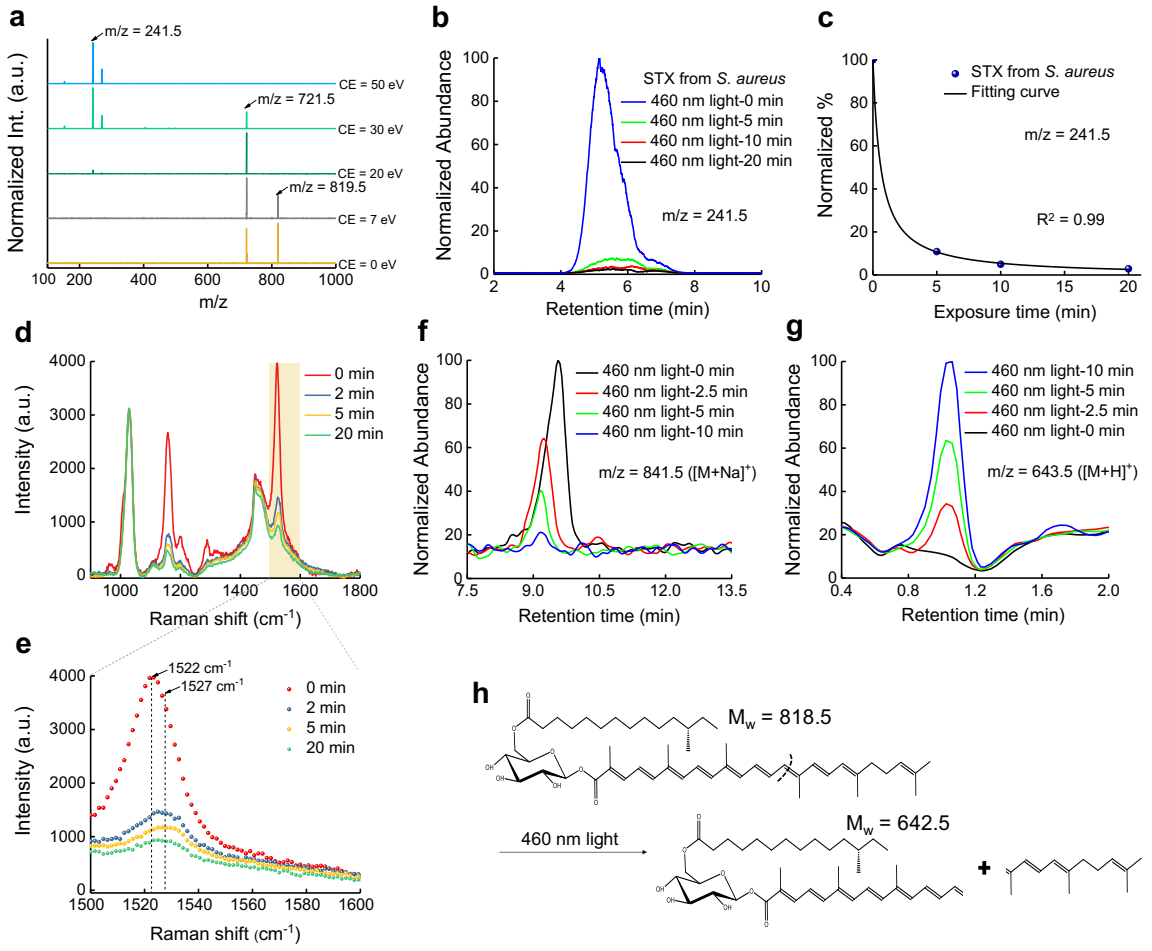

Figure 3.3. Mass spectrometry and Raman spectroscopy unveil the photochemistry of staphyloxanthin under 460 nm light exposure. (a) MS spectra of crude STX extract at different collision energy (CE). Peaks of m/z = 819.5, m/z = 721.5 and m/z = 241.5 are highlighted by black arrows. (b) HPLC chromatograms of STX extracted from concentrated MRSA over 460 nm light exposure at an intensity of 90 mW/cm^2. (c) The amount of STX calculated from (b). Quantification of STX is determined from the peak area of STX in HPLC chromatograms shown in (b). Data points are fitted by equation (1). (d) Raman spectra of crude STX (extracted from concentrated MRSA) under different 460 nm light doses. 460 nm light intensity: 200 mW/cm^2. Raman excitation wavelength: 532 nm, acquisition time: 30 s. (e) Zoomed-in view of (d) in the Raman shift range from 1500 cm^{-1} to 1600 cm^{-1}, Raman shifts at 1522 cm^{-1} and 1527 cm^{-1} are highlighted by black arrows and dashed lines. (f-g) UPLC chromatograms of STX (f) and one of its corresponding products (g) over 460 nm light exposure. (h) Tentative breakdown pathway of STX under 460 nm light irradiance.

Next, we employed Raman spectroscopy to elucidate how 460 nm light irradiance degrades STX. STX exhibited an abundant peak at the Raman shift of 1522 cm^{-1} (**Figure 3.3d**), which was assigned to bacterial carotenoids[157]. As the duration of 460 nm light exposure increases, the Raman intensity at 1522 cm^{-1} dramatically decreases (**Figure 3.3d**). Similar phenomenon was observed in single MRSA. Notably, we found a ~5 cm^{-1} increase in Raman shift after 460 nm light exposure (**Figure 3.3e**), which likely results from a decreased number of conjugated C=C bonds[158] during the photobleaching process. It was worth noting that the protein content (indicated by Raman shift at around 1000 cm^{-1}) remained unchanged during the photobleaching process (**Figure 3.3e**). These findings suggest that 460 nm light irradiance breaks down the STX molecule.

We further utilized time-of-flight MS/MS to quantitate this photolysis process. Different from the *m/z* = 819.5 peak where STX locates in the HPLC chromatograph, STX displays a main peak at *m/z* = 841.5 in the ultra-performance liquid chromatography (UPLC) chromatograms (**Figure 3.3f**), which is an adjunct between STX and Na^+ ($[M+Na]^+$). Degradation of STX would bolster the aggregation of chemical segments. Accordingly, we screened a patch of products after STX degradation. In particular, the intensity of the peak at *m/z* = 643.5 corresponding to an adjunct between a STX segment with H^+ ($[M+H]^+$) significantly increased as 460 nm light exposure elongated (**Figure 3.3g**). **Figure 3.3h** suggests a potential mechanism of how this segment could be formed from breakdown of the C=C bond in STX after 460 nm light exposure. These findings underline that STX can be photolyzed by 460 nm light. We note that the interpretation of other products necessitates further in-depth analysis.

3.3.4 STX photolysis alone is not sufficient to eradicate MRSA

Given that STX is critical to the 8integrity of *S. aureus* cell membrane[140], we wondered whether photolysis of STX could eliminate MRSA. Blue light at 405 nm and 470 nm have been used to kill MRSA, as reviewed by Wang *et al*[159]. However, the efficacy is limited and the molecular mechanism remains elusive. We have established above that STX is the molecular target of blue light irradiation. Accordingly, we found that increasing 460 nm light dose steadily decreased the level of MRSA CFU ml^{-1} (**Figure 3.4a**). Moreover, MRSA was more sensitive to 460 nm light exposure than the CrtM mutant. Nevertheless, the killing efficiency saturates at a level of 216 J/cm^2 (**Figure 3.4a**). To investigate the reason, we continuously monitored the growth of MRSA in fresh medium after 10-min 460 nm light exposure. Remarkably, MRSA exposed to 460 nm light was able to recover and multiply after being cultured in medium (**Figure 3.4b**). We also measured CFU ml^{-1} of 460 nm light-exposed MRSA after being cultured in fresh medium for 30 min. It seems that 460 nm light puts MRSA in a 'traumatized' state other than a death form, and the traumatized MRSA could recover and multiply quickly in the fresh medium (**Figure 3.4c**). Since STX is enriched in membrane microdomain and is essential for membrane integrity,[140] we conducted a membrane permeability assay[160] before and after STX photolysis. We found that the membrane permeability from 460 nm light-exposed MRSA significantly increased compared to control group (**Figures 3.4**, **d** and **e**). However, light-exposed MRSA is able to recover the integrity of cell membrane after being cultured in fresh medium within 30 min (**Figures 3.4**, **d** and **e**). Together, these observations suggest that STX photolysis alone is not sufficient to kill MRSA completely.

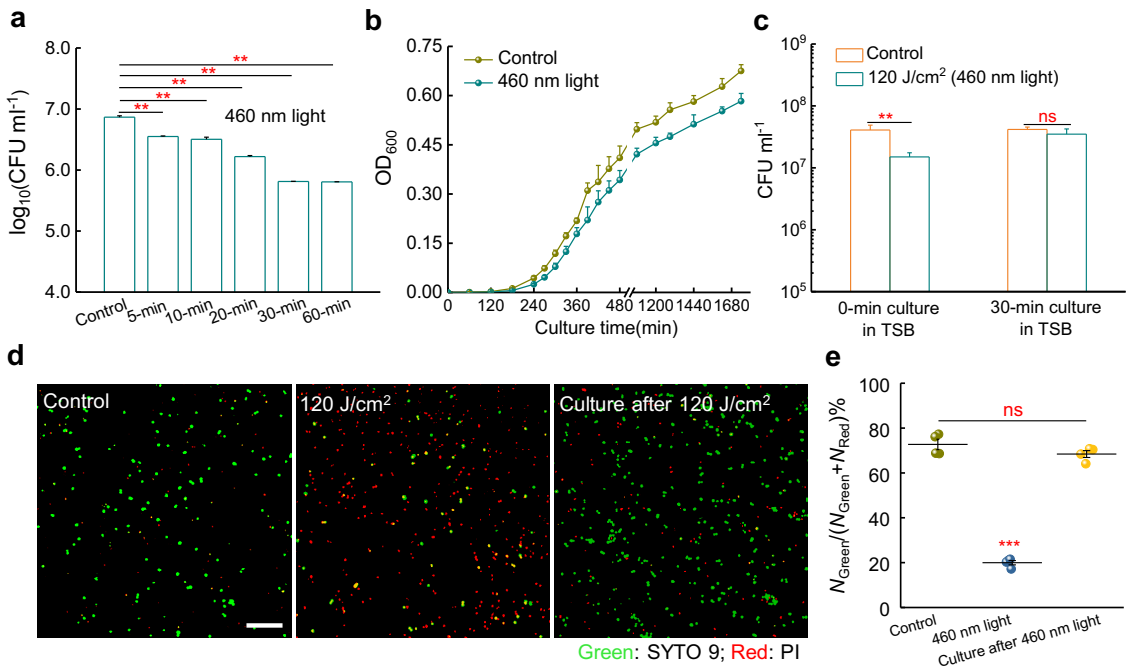

Figure 3.4. Staphyloxanthin photolysis transiently elevates MRSA membrane permeability and is unable to eradicate MRSA completely. (a) Log change in MRSA colony-forming units (CFU ml^{-1}) after treatment with 460 nm light at different doses. Intensity: 60 mW/cm^2, *N*=3. (b) Growth curves of MRSA after no treatment (control) or treatment with 120-J/cm^2 460 nm light irradiance. *N*=6. (c) MRSA CFU ml^{-1} after no treatment (control) or treatment with 120-J/cm^2 460 nm light irradiance, and 30-min culture in TSB medium after 120-J/cm^2 460 nm light irradiance. *N*=3. (d) Confocal laser scanning imaging of membrane permeability after no treatment (control) or treatment with 120-J/cm^2 460 nm light, and 30-min culture in TSB medium after 120-J/cm^2 460 nm light irradiance. Scalar bar=10 μm. Green: intact membrane; Red: damaged membrane. (e) Statistical analysis of cell membrane permeability for (d). N_{Green}, N_{Red} are the number of MRSA with intact membrane, and damaged membrane, respectively. *N*=4. Error bars show standard error of the mean (SEM). Unpaired two-tailed *t*-test (*: $p < 0.001$, **: $p < 0.01$, ns: not significant).**

3.3.5 STX photolysis and hydrogen peroxide attack synergistically eradicate planktonic MRSA

We then asked whether STX photolysis could transiently enhance cellular uptake of hydrogen peroxide, one of the most common reactive oxygen species.[161] We performed confocal laser scanning fluorescence imaging of *S. aureus* with a fluorescent probe (see Methods) to image intracellular hydrogen peroxide. It turned out that after 460 nm light exposure, H_2O_2-treated MRSA exhibited a much stronger fluorescence intensity than H_2O_2-alone treated MRSA or untreated MRSA (**Figures 3.5**, **a** and **b**). No significant

difference was found between H_2O_2-alone treated MRSA and untreated MRSA (**Figure 3.5b**), indicating untreated MRSA has the capability to neutralize H_2O_2. This evidence proves that STX photolysis enhances the entry of hydrogen peroxide into the bacteria, which may cause intensified toxicity to MRSA.

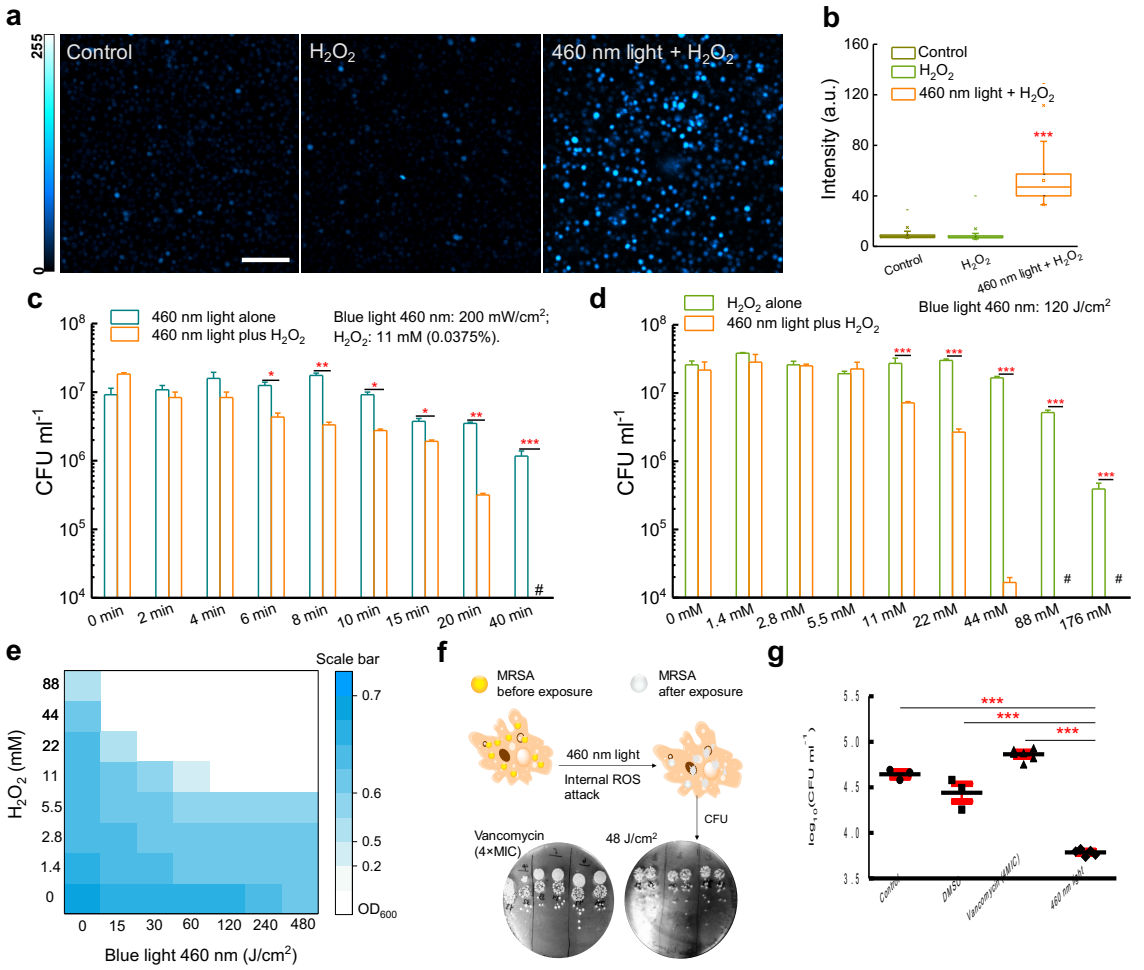

Figure 3.5. Staphyloxanthin photolysis and reactive oxygen species synergistically eliminate planktonic MRSA and intracellular MRSA. (a) Fluorescence images from confocal laser scanning imaging of intracellular H_2O_2 after no treatment (control), 0.15% H_2O_2, or 460 nm light combined with 0.15% H_2O_2. Scalar bar=10 μm. (b) Box chart analysis of fluorescence intensity in (a). (c) MRSA CFU ml^{-1} after treatment with 460 nm light alone, and treatment with H_2O_2 plus 460 nm light. *N*=3. (d) MRSA CFU ml^{-1} after treatment with H_2O_2 alone, and treatment with 460 nm light plus H_2O_2. *N*=3. (e) Checkerboard broth microdilution assays showing the dose-dependent potentiation of H_2O_2 by 460 nm light irradiation against MRSA USA300. (f) Schematic illustrating the utilization of 460 nm light to treat intracellular MRSA. Pictures of spread plates from vancomycin (4×MIC) and 460 nm light-treated groups are shown. (g) Log CFU ml^{-1} results of intracellular MRSA after no treatment or treatment with vancomycin (4×MIC), and 460 nm light (48 J/cm^2). *N*=3-6. Error bars show SEM. Unpaired two-tailed *t*-test (*: $p < 0.001$, **: $p < 0.01$, ns: not significant).**

To examine the bactericidal effect of STX photolysis when combined with hydrogen peroxide, we measured the viability of MRSA exposed to H_2O_2 after 460 nm light exposure. When MRSA was treated with 460 nm light (dose: 108 J/cm^2) followed by increasing concentrations of H_2O_2, a significant reduction ($p < 0.001$) in CFU ml^{-1} was obtained (**Figure 3.5c**). Strikingly, 480-J/cm^2 460 nm light exposure combined with 0.0375% of H_2O_2 (culture time: 30 min) eradicated 10^7 MRSA CFU ml^{-1} completely (**Figure 3.5c**). Therefore, we hypothesized that 460 nm light and H_2O_2 work synergistically to eradicate MRSA. To verify this synergistic effect, we performed the same measurements at various 460 nm light doses while fixing the concentration of H_2O_2 (**Figure 3.5d**). Then we calculated a fractional bactericidal concentration index (FBCI)[162,163], which is widely used in the pharmaceutical research, to evaluate the combinational behavior between two agents. FBCI was calculated by using FBC that stands for fractional bactericidal concentration and MBC which defines the minimum bactericidal concentration. FBC of drug A = MBC of drug A in combination with drug B divided by MBC of drug A alone, FBC of drug B = MBC of drug B in combination with drug A divided by MBC of drug B alone. The FBCI = FBC of drug A + FBC of drug B. A FBCI of ≤ 0.5 is considered to demonstrate synergy, while a FBCI of 1.0 defines an additive effect. A FBCI > 2 defines antagonism. As shown in **Figure 3.5c** and **3.5d**, 44 mM of H_2O_2 along with 120 J/cm^2 (20 min) eliminates around 99.9% the MRSA USA300. Since 200 mW/cm^2 460 nm light did not eradicate all the MRSA USA300 after 40-min exposure time (480 J/cm^2), we have

$$\text{FBC of drug A (blue light)} < \frac{120\ \text{J/cm}^2}{480\ \text{J/cm}^2} = 0.25$$

Since we found that 176 mM H_2O_2 isn't able to eliminate 99.9% of the bacteria, we

have

FBC of drug B (H_2O_2) < $\frac{44\ \text{mM}}{176\ \text{mM}} = 0.25$

Therefore, FBCI = FBC of blue light + FBC of H_2O_2 < 0.25 + 0.25 = 0.5. This result indicates that STX photobleaching works synergistically with hydrogen peroxide to eliminate MRSA USA300.

Next, we conducted a checkerboard broth microdilution assay[148] to calculate the fractional inhibitory concentration index (FICI), which is another commonly used index to evaluate the combinational behavior. In this assay, FICI is calculated by using FIC which stands for fractional inhibitory concentration and MIC which defines minimal inhibitory concentration. FIC of drug A = MIC of drug A in combination with drug B divided by MIC of drug A alone, FIC of drug B = MIC of drug B in combination with drug A divided by MIC of drug B alone, and FICI index = FIC of drug A+FIC of drug B. A FICI of ≤ 0.5 is considered to demonstrate synergy. A FICI of 1.0 is defined as additive. Antagonism is defined as a FICI > 2.0. From **Figure 3.5e**, we can calculate the range of FICI:

FICI < $\frac{30\ \text{J/cm}^2}{480\ \text{J/cm}^2} + \frac{22\ \text{mM}}{88\ \text{mM}} = 0.31$.

This data further confirms the synergy between STX photobleaching and H_2O_2 in treating MRSA USA300. Noteworthy, this treatment did not affect other species of staphylococci, such as *Staphylococcus epidermidis*, that lack the carotenoids.

3.3.6 STX photolysis and reactive oxygen species (ROS) attack synergistically eliminate intracellular MRSA

Studies dating back to the 1970s have demonstrated that MRSA is able to invade and

survive inside mammalian cells, particularly within macrophages[131]. Though macrophages secrete small effector molecules, including ROS, bacteria including MRSA are capable of neutralizing these effector molecules by producing antioxidants such as STX[147]. Meanwhile, antibiotics are generally ineffective at clearing intracellular MRSA in large part due to the shield of phagocytic membrane, which poses an alarming threat to the host cells[131]. As we have demonstrated that STX photolysis plus H_2O_2 kill MRSA synergistically, we wondered whether 460 nm light could synergize with the ROS inside macrophage cells to eliminate intracellular MRSA (illustrated in **Figure 3.5f**). To evaluate this point, we first infected macrophage cells with MRSA for one hour. Then, the infected macrophages were exposed to 2-min 460 nm light (48 J/cm^2) twice over a 6-hour interval. Treated macrophages were subsequently lysed to enumerate CFU ml^{-1} of MRSA (spread plates shown in **Figure 3.5f**). **Figure 3.5g** compiled the statistical analysis of CFU ml^{-1} from different groups. Compared to control group, one-log$_{10}$ reduction in CFU ml^{-1} was found in the 460 nm light-treated group. In contrast, high-concentration vancomycin (5× MIC) was unable to eliminate intracellular MRSA (**Figures 3.5**, **f** and **g**). Additionally, we found that fresh whole blood could eradicate most of MRSA after STX photolysis by blue light. These findings collectively suggest STX photolysis could assist macrophage cells to eradicate intracellular MRSA.

3.3.7 STX photolysis and hydrogen peroxide efficiently eradicate stationary-phase MRSA, persisters, and S. aureus in biofilms

Besides residing inside host immune cells, *S. aureus* is capable of entering the stationary phase or becoming multidrug-tolerant persisters[164] to undermine the

effectiveness of antibiotics. Persisters could escape the effects of antibiotics without having genetic change[165]. Moreover, persisters appear to be a major cause of chronic infections since those cells remain less sensitive to antibiotics[165]. To investigate whether STX photolysis could potentiate low-concentration H_2O_2 to eradicate persister cells, logarithmic-phase MRSA USA300 were incubated with 10×MIC ciprofloxacin for 6 hours to kill active cells in order to generate persister cells[149]. Stationary phase MRSA was obtained by culturing MRSA in medium for 24 hours. Then, different treatments subsequently were employed accordingly. It turned out that STX photolysis combined with low-concentration H_2O_2 reduced CFU ml^{-1} by around two orders of magnitude compared to other groups in the case of both stationary-phase MRSA (**Figure 3.6a**) and persisters (**Figure 3.6b**). This effectiveness provides clues to treat chronic infections.

S. aureus could also form recalcitrant biofilms to evade antibiotics[166]. Due to the difficulties for antibiotics to penetrate the biofilm matrix termed as extracellular polymeric substances[166], bacterial biofilms present a significant source of treatment failure and recurring infections[166]. Compared to antibiotics, an unparalleled advantage of our photolysis therapy lies in the fact that photons can readily penetrate through a cell membrane or a biofilm, or even a layer of tissue. To explore whether STX photolysis combined with H_2O_2 could eradicate *S. aureus* inside a biofilm, we grew biofilms on the bottom of a poly-lysine-coated glass dish and then applied 460 nm light or daptomycin (positive control) to treat these biofilms. Then we stained the treated biofilms with live/dead fluorescence probes (supplementary information), and conducted confocal laser scanning microscopy to examine the efficacy of the above treatments. **Figure 3.6c** shows

that 460 nm light alone (dose: 360 J/cm^2) traumatized *S. aureus* by 80%. **Figure 3.6d** shows that 460 nm light (dose: 360 J/cm^2) plus H_2O_2 (0.045%, 20-min culture time) reduced *S. aureus* CFU ml^{-1} by 92%. Notably, daptomycin (5×MIC, 24-hour culture time) only eliminated *S. aureus* CFU ml^{-1} by 70% (**Figure 3.6d**). These results imply an effective way to eradicate *S. aureus* biofilms grown on a medical implant or a host tissue.

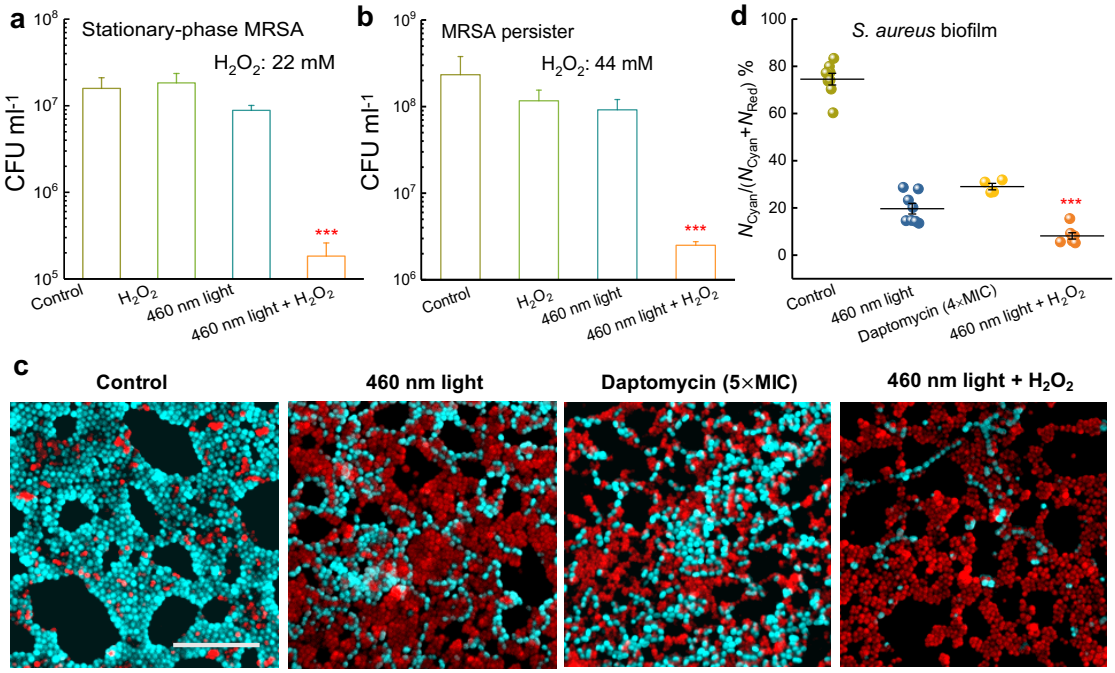

Figure 3.6. Staphyloxanthin photolysis and H_2O_2 effectively eliminate stationary-phase MRSA, persisters, and *S. aureus* inside a biofilm. (a) CFU ml^{-1} of stationary-phase MRSA after various treatments. Dose: H_2O_2, 22 mM, 460 nm light, 120 J/cm^2. *N*=3. (b) CFU ml^{-1} of MRSA persisters after various treatments. Dose: H_2O_2, 44 mM, 460 nm light, 120 J/cm^2. *N*=3. (c) Fluorescence images of *S. aureus* with intact (cyan) and damaged cell membrane (red) inside a biofilm after various treatments. Scale bar=10 µm. 460 nm light: 30-min exposure, 360 J/cm^2. H_2O_2: 0.045%, 20-min culture, then quenched by 0.5 mg/mL catalase solution. (d) Statistical analysis of survival percent of *S. aureus* inside the biofilms. Survival percent= $N_{Cyan}/(N_{Cyan}+N_{Red})$, where N_{Cyan} and N_{Red} represent the number of *S. aureus* with intact and damaged cell membrane, respectively. Error bars show SEM from at least from three replicates. Unpaired two-tailed *t*-test (*: $p < 0.001$), *** indicates significant difference from the other three groups.**

3.3.8 STX photolysis and H_2O_2 effectively reduce MRSA burden in two MRSA-induced mice wound models

The promising results obtained from the above *in vitro* studies led us to evaluate the

efficacy of STX photolysis in a MRSA-infected animal model. Skin infections such as diabetic foot ulceration and surgical site infections[167] are common causes of morbidity in healthcare settings. Notably, *S. aureus* accounts for 40% of these infections[168]. To optimize the parameters for the *in vivo* experiment, we first proved that 2-min 460 nm light exposure (dose: 24 J/cm^2) could cause significant reduction in survival percent of MRSA. Then, two times higher antimicrobial efficiency was obtained when cultured with H_2O_2 (20-min culture time, 0.045%) subsequently. Furthermore, 5-min culture with H_2O_2 after 2-min 460 nm light exposure (dose: 24 J/cm^2) effectively eliminated MRSA by 60%. Notably, the 460 nm light dose applied to treat mouse wound infection was well below the ANSI safety limit for skin exposure[169]. These parameters were used to apply our photolysis treatment to a MRSA-infected animal model.

To induce skin lesions in mice (5 groups; 5 mice per group), we severely irritated mice skin by an intradermal injection containing 10^8 CFU of MRSA USA300 (**Figure 3.7a**), the leading source of *S. aureus* induced skin and soft tissue infections in North America[170]. Sixty hours post injection, wound formed at the site of infection (**Figure 3.7b**, top). Topical treatments were subsequently administered to each group, twice daily for three consecutive days. Wounds of all the treated groups appeared healthier compared to the control group (**Figure 3.7b**, middle). Then, mice were humanely euthanized, and wound tissues were aseptically removed in order to quantify the burden of MRSA in wounds. We further examined the physiological condition of the wounds. The untreated, fusidic acid-treated (positive control), and 460 nm light-treated groups all showed the formation of pus below the wound, in which dead tissues, bacteria, macrophages and neutrophils dwell[171]. This

symptom suggests that mice immune system fought against the bacteria residing inside the wound tissue. In contrast, mice receiving only H_2O_2 or 460 nm light plus H_2O_2 treatment exhibited clean wounds that were free of purulent material, swelling, and redness around the edge of the wound (**Figure 3.7b, bottom**).

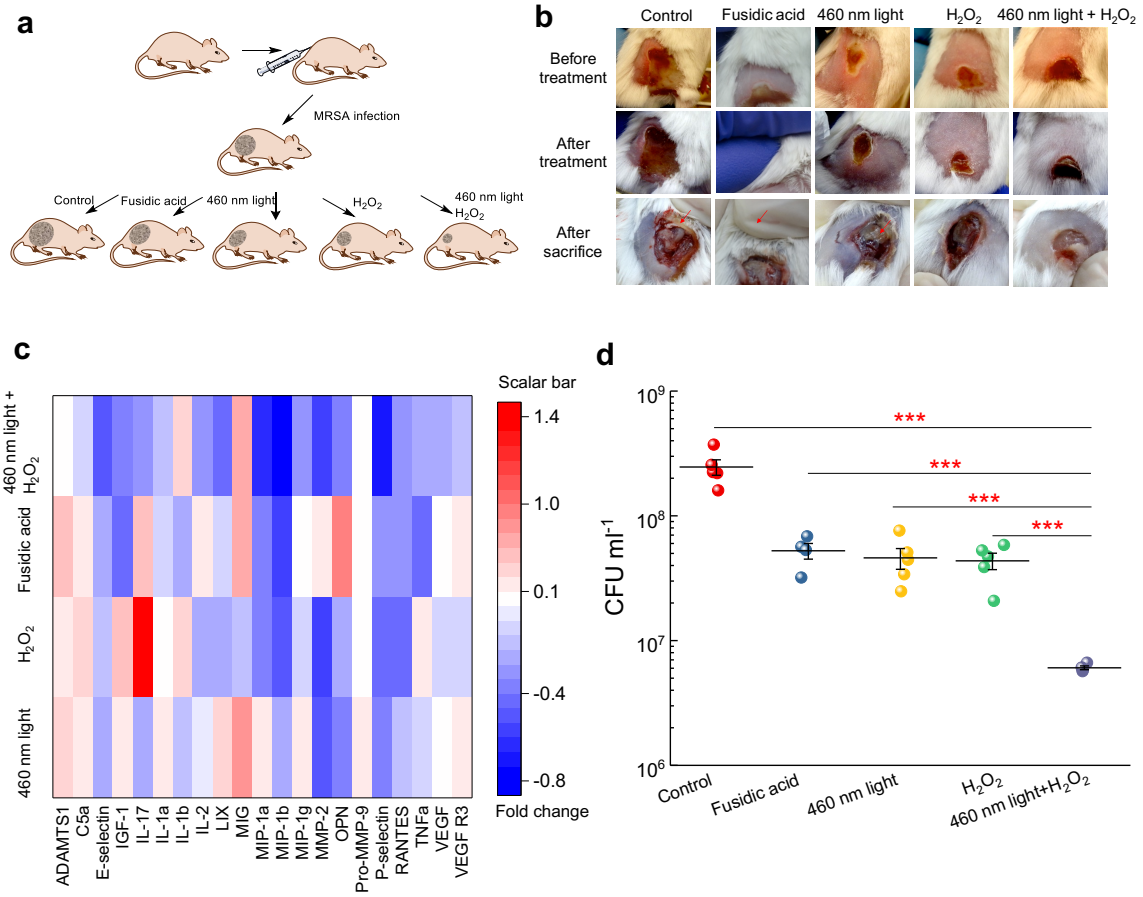

Figure 3.7. Staphyloxanthin photolysis and H_2O_2 effectively reduce MRSA burden in a MRSA-infected mouse wound model. (a) Schematic of experiment design (not drawn to scale). (b) Pictures of mice wounds of five different groups taken before treatment, after treatment and after sacrifice. Red arrows indicate pus formation. (c) Heat map of key pro-inflammatory cytokines and markers in the tissue homogenate samples obtained from mice treated with 460 nm light, H_2O_2, 460 nm light plus H_2O_2, or fusidic acid. Red box indicates upregulation; blue box indicates downregulation; white indicates no significant change. Scalar bar represents fold change compared to the untreated group. (d) MRSA CFU ml^{-1} after no treatment (control) or three-consecutive-day treatment with 2% fusidic acid (petroleum jelly as vehicle), 460 nm light, H_2O_2, and 460 nm light plus H_2O_2. Dose: 460 nm light, 24 J/cm^2, H_2O_2, 0.045%. Error bars show the SEM from five replicates. Outlier was removed through Dixon's Q test. Unpaired two-tailed *t*-test (*: $p < 0.001$).**

To quantify the anti-inflammatory effect, we evaluated a panel of cytokines present in

the supernatant of homogenized tissues extracted from the wounds of mice. By analyzing the skin homogenate collected from the MRSA mice wound model, we found the highest percent of negative fold change from around 200 kinds of cytokines in the 460 nm light plus H_2O_2-treated group compared to the other groups. Noteworthy, the 460 nm light plus H_2O_2-treated group demonstrated the highest ratio of decreased expression of these pro-inflammatory cytokines (**Figure 3.7c**). Specifically, a significant decrease was observed in the 460 nm light plus H_2O_2-treated group regarding to key pro-inflammatory cytokines (TNF-α, IL-1α, IL-2, IL-17, MIP-1α, MIP-1β, LIX) compared with the other groups. Furthermore, there was decreased expression of vascular endothelial growth factor receptor 3 (VEGF R3) in samples obtained from the 460 nm light plus H_2O_2-treated group. This marker is overexpressed in chronic inflammatory wounds, thus resulting in impaired wound reconstruction[172]. These results support a significantly decreased inflammation in the wounds of mice treated with 460 nm light plus H_2O_2, which may suggest that few amounts of MRSA exist in the wound tissue.

To quantify the burden of MRSA in wounds, wound tissues were homogenized, and inoculated onto mannitol salt agar plates (*S. aureus* specific) for CFU counting. The results showed that the 460 nm light plus H_2O_2-treated group exhibited significant MRSA reduction compared to all other groups (**Figure 3.7d**). Remarkably, the 460 nm light plus H_2O_2-treated group showed more than 1.5-$\log_{10}$ reduction of CFU ml^{-1} compared to the untreated group, and more than one-$\log_{10}$ reduction compared to the fusidic acid-treated group (**Figure 3.7d**). Together, these results demonstrate the 460 nm light sensitizes MRSA in a skin infection to H_2O_2, and provides a more effective treatment than antibiotics.

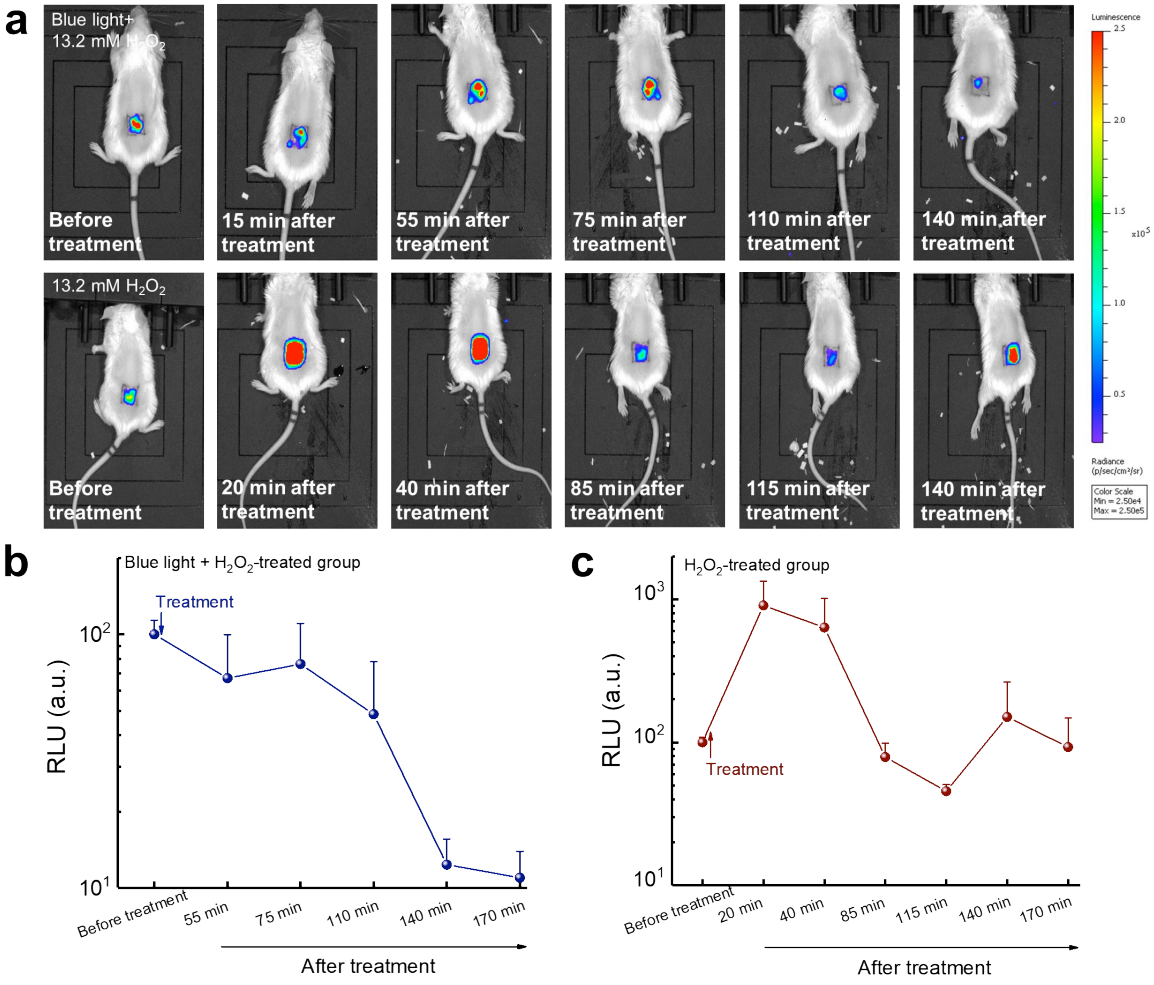

Figure 3.8. ***In vivo*** **bioluminescence imaging of MRSA-infected mice abrasion model under the indicated treatments. (a) Representative bioluminescence images of MRSA-infected mice at different time points after the treatments. Blue light: 460 nm, 120 J/cm^2 (10-min irradiation). H_2O_2: 13.2 mM. (b-c) Quantitative analysis of the bioluminescence signal of MRSA USA300 inside the mice wound after treatment by 460 nm light plus H_2O_2 (b) and treatment by H_2O_2 (c), respectively. *N*=5. Error bars show the SEM.**

To confirm the therapeutic effectiveness of our phototherapy, we further utilized a bioluminescent MRSA USA300 strain for *in vivo* monitoring of MRSA burden in a mouse abrasion model (see Methods). The bioluminescence signal from this luminescent MRSA strain is proportional to the number of live bacteria, thus allowing real-time monitoring the therapeutic efficacy. After being infected for 3 hours, the mice wounds were applied with hydrogen peroxide and 460 nm light plus hydrogen peroxide, respectively. Noteworthy,

we found that MRSA burden in the synergy-treated group has one-log reduction after treatment (**Figures 3.8**, **a** and **b**). In the group of hydrogen peroxide-treated group, MRSA burden reduced at the beginning. However, it rapidly recurred back (**Figures 3.8**, **a** and **c**). The synergy between STX photolysis and H_2O_2, as shown here, implies a new way to effectively clean patients' wounds or surgical room sterilization.

3.4 Conclusion

Through label-free transient absorption imaging of chromophores in MRSA, we find that STX, the golden pigment inside *S. aureus*, is prone to photolysis, especially in the blue light region. We further find that STX photolysis transiently elevates membrane permeability for small molecules. Based on these findings, efficient elimination of MRSA is achieved by combining STX photolysis with subsequent ROS attack both *in vitro* and *in vivo*. STX photolysis combined with low-concentration hydrogen peroxide efficiently inactivates slow-growing stationary-phase cells and MRSA persisters. Owing to the advantageous light penetration capability compared to antibiotics, STX photolysis could not only assist macrophage cells to eliminate intracellular MRSA, but also reduce the number of sessile bacteria inside biofilms when combined with hydrogen peroxide. Effectiveness of this synergistic treatment is demonstrated in two mice wound infection models. These findings suggest a new way for treating *S. aureus*-caused infections in clinic, e.g., diabetic ulcerations. Noting that pigmentation is a hallmark of multiple pathogenic microbes,[173] our work shows the exciting potential of treating multidrug-resistant bacteria by exploiting the unique photochemistry and photophysics of their intrinsic pigments.

CHAPTER 4 PHOTO-DISASSEMBLY OF MEMBRANE MICRODOMAINS REVIVES CONVENTIONAL ANTIBIOTICS AGAINST MRSA

This is work currently under review (Jie Hui, Pu-Ting Dong*..., and Ji-Xin Cheng). And it has been uploaded to bioRxiv. Jie Hui proposed the idea of pulsed laser therapy. Jie and Pu-Ting worked together on the experiments. Lijia contributed to the synergy between STX photolysis and daptomycin.*

Confronted with the rapid evolution and dissemination of antibiotic resistance, there is an urgent need to develop alternative treatment strategies for drug-resistant pathogens. Here, we present an unconventional approach to restore the susceptibility of methicillin-resistant *S. aureus* (MRSA) to a broad spectrum of conventional antibiotics via photo-disassembly of functional membrane microdomains. The photo-disassembly of microdomains is based on effective photolysis of staphyloxanthin, the golden carotenoid pigment that gives its name. Upon pulsed laser treatment, cell membranes are found severely disorganized and malfunctioned to defense antibiotics, as unveiled by membrane permeabilization, membrane fluidification, and detachment of membrane protein, PBP2a. Consequently, our photolysis approach increases susceptibility and inhibits development of resistance to a broad spectrum of antibiotics including penicillins, quinolones, tetracyclines, aminoglycosides, lipopeptides, and oxazolidinones.

4.1 Introduction

Antibiotic resistance in human pathogens is one of the biggest public health challenges of our time. One such deadly pathogen is *S. aureus* or particularly methicillin-resistant *S. aureus* (MRSA), which causes high morbidity and mortality worldwide. An estimate of 23,000 fatalities occur each year in US due to antibiotic-resistant infections; surprisingly,

nearly half of these deaths (11,285) is due to one bacterial pathogen, MRSA [174]. The prevalence of its antibiotic resistance is consistently challenging our current treatment options via various molecular mechanisms. Particularly, overexpression of *mecA* encoded penicillin-binding protein 2a (PBP2a) in MRSA strains reduces the affinity of most beta-lactams[175,176]; active efflux pumps on cell membranes keep intracellular antibiotic concentration at sublethal level, conferring multi-drug resistance to fluoroquinolones and tetracyclines [177,178]; remodeling of membrane composition, e.g. phospholipids, reduces the binding thus the effectiveness of daptomycin, a last-resort antibiotic [179]. Moreover, the development of new antibiotics is currently unable to keep pace with the emergence of resistant bacteria, thus likely leading us to a post-antibiotic era [180]. To tackle this grand challenge, alternative treatment strategies are urgently required.

Grounded on the increasing understanding of virulence factors in disease progression and host defense, anti-virulence strategies have arisen in the past decade as an alternative [181-183]. In *S. aureus*, staphyloxanthin (STX), the yellow carotenoid pigment that gives its name, is a key virulence factor [184]. This pigment is expressed for *S. aureus* pathogenesis and used as an antioxidant to neutralize reactive oxygen species (ROS) produced by the host immune system [185]. Recent studies on cell membrane organization further suggest that STX and its derivatives condense as the constituent lipids of functional membrane microdomains (FMM), endowing membrane integrity and providing a platform to facilitate protein-protein oligomerization and interaction, including PBP2a, to further promote cell virulence and antibiotic resistance [186]. Therefore, blocking STX biosynthesis pathways has become an innovative therapeutic approach. Thus far, cholesterol-lowering drugs,

including compound BPH-652 and statins, have shown capability of inhibiting *S. aureus* virulence by targeting the enzymatic activity, e.g. dehydrosqualene synthase (CrtM), along the pathway for STX biosynthesis [186,187]. However, these drugs suffer from off-target issues, as human and *S. aureus* share the same pathway for biosynthesis of presqualene diphosphate, an intermediate used to produce downstream cholesterol or STX. Additionally, anti-fungal drug, naftifine, was recently repurposed to block STX expression and sensitize *S. aureus* to immune clearance [144]. Despite these advances, all of these are still drug-based approaches to inhibit STX virulence, which require additional treatment time, accompany with serious side effects, show weak activities, and have higher risk for resistance development by targeting a single upstream biosynthetic enzyme, which will eventually prevent their clinical utilization.

In this study, we unveil that staphyloxanthin is the molecular target of photons within the entire blue wavelength range, demonstrating an unconventional way to deplete STX photochemically. Grounded on the STX photolysis kinetics, a short-pulsed blue laser was further identified to strip off this pigment with high efficiency and speed in wide field. In contrast to drug-based approaches, this photonic approach depletes the final product, STX, swiftly in a drug-free manner. More significantly, this disruption, enabled by the pulsed laser, fundamentally disorganizes and further malfunctions FMM as unveiled by increased membrane fluidity, ample membrane permeability, and PBP2a protein detachment, simultaneously and immediately after exposure. These membrane damages inhibit PBP2a deactivation of penicillins and facilitate the intracellular delivery and membrane insertion of conventional antibiotics, specific to their mechanisms of action. As a result, photo-

disassembly of FMM restores the susceptibility and inhibits resistance development to a broad spectrum of conventional antibiotics against MRSA. Additionally, this work further deciphers the structural and functional properties of STX-enriched membrane microdomains for antibiotic resistance, thus providing a strategy to tackle antibiotic resistance by targeting STX virulence.

4.2 Methods

4.2.1 Nanosecond pulsed laser and LED systems

The nanosecond pulsed laser system was composed of a nanosecond pulsed laser source (Opolette HE355 LD, OPOTEK Inc.), a 1 mm-core multimode fiber for light delivery (NA=0.22, OPOTEK Inc.), and a custom-built handheld device. Key specifications of the laser source: tunable wavelength range, 410-2400 nm; pulse repetition rate, 20 Hz; maximum pulse energy at 460 nm, 8 mJ; pulse duration, 5 nanoseconds (ns); spectral linewidth, 4-6 cm^{-1}; pulse-pulse stability, <5%. Within the handheld device, a collimation lens (LB1471-A, Thorlabs) was applied to expand the output beam with a diameter of 1 cm. This device was mounted on a stable optical table for experiments shown in Fig. 1a. After collimation by all these optical components, this system provides a final maximum output of 120 mW (6 mJ in pulse energy). Within the illumination area, photon density follows a near-Gaussian distribution. With the diameter of sample droplet at around 5 mm, the photon density over the sample droplet in this study was assumed uniform.

The continuous-wave LED system applied in this study was composed of a blue light LED (M470L3, Thorlabs), an adjustable collimation adapter (SM2F32-A, Thorlabs), and a power controller (LEDD1B, Thorlabs). The output of the blue light LED is centered at

465 nm with bandwidth of 25 nm and maximum power of 650 mW. The output power of the LED system was adjustable, and its beam size was controlled through the collimator and an iris. In order to compare with nanosecond pulsed laser, the output power of the LED was set to 120 mW and used to illuminate an area of 1 cm in diameter.

4.2.2 Bacterial strains and growth conditions

Methicillin-resistant *S. aureus* (MRSA USA 300, NRS 384), *S. aureus* ΔCrtM mutant, vancomycin-resistant *S. aureus* (VRSA 9, NR-46419), Methicillin-resistant *S. aureus* (MRSA USA 500, NRS 385).

Log-phase and stationary-phase bacterial inoculum preparation: colonies from streaked plate of frozen bacterial stock were inoculated in sterile tryptic soy broth (TSB, 22092, Sigma Aldrich) medium and grown in an orbital incubator (12960-946, VWR) with a shaking speed of 200 rpm for 2-3 hours at 37 ℃ for log-phase bacteria (~10^7 cells/ml). Before each experiment, bacterial cells were spun down and then the harvested bacteria pellets were washed with 1×phosphate-buffered saline (PBS) twice and then resuspended in 1×PBS at its original concentration. Stationary-phases bacterial solution were prepared following the same procedure except that bacteria inoculum was cultured to three days.

4.2.3 Antibiotics and chemicals

Antibiotics used in this study: daptomycin (103060-53-3, Acros Organics), oxacillin (28221, Sigma Aldrich), gentamicin (G1914, Sigma Aldrich), tobramycin (T4014, Sigma Aldrich), ciprofloxacin (17850, Sigma Aldrich), ofloxacin (O8757, Sigma Aldrich), linezolid (PZ0014, Sigma Aldrich), tetracycline (87128, Sigma Aldrich), ramoplanin

(R1781, Sigma Aldrich), vancomycin (V2002, Sigma Aldrich). 10 mg/ml stocks of all compounds were made in 1×PBS or DMSO (W387520, Sigma Aldrich) or sterile water. For treatments with daptomycin, sterile medium or buffer was supplemented with $CaCl_2$ (C79-500, Fisher Scientific) with final working concentration of 50 μg/ml.

Fluorescent dyes used in this study: SYTOX green (S7020, Thermo Fisher Scientific), Texas red-X, succinimidyl ester, single isomer (T20175, Thermo Fisher Scientific), FITC-dextran (FD4, FD70, FD500, Sigma Aldrich). $DiIC_{18}$ (1,1'-Dioctadecyl-3,3,3',3'-Tetramethylindocarbocyanine Perchlorate, D282, Thermo Fisher Scientific). BODIPY FL, STP ester, sodium salt (B10006, Thermo Fisher Scientific).

4.2.4 Resonance Raman spectroscopy

STX was quantified by its Raman peak amplitude at 1161 cm^{-1} measured by resonance Raman spectroscopy (1221, LABRAM HR EVO, Horiba) with a 40×objective (Olympus) and an excitation wavelength of 532 nm. Samples (either from bacterial colony or STX extract solution) were sandwiched between two glass cover slides (48393-230, VWR international) with a spatial distance of ~80 μm. To study staphyloxanthin photolysis kinetics, the same samples were measured after each laser treatment.

4.2.5 SYTOX green membrane permeability assay

Briefly, 1 ml of stationary-phase MRSA (~108 cells/ml) was spun down, got rid of the supernatant, and resuspended with 100 μl of sterile 1×PBS. 5 μl of the above solution was then exposed into laser beam with different treatment time (laser power, 120 mW; illumination area, 1 cm in diameter). After treatment, MRSA solution was collected into

985 µl of sterile water, as SYTOX green shows best performance in buffers without phosphate. Subsequently, 10 µl of stock SYTOX green solution (5 mM in DMSO) was supplemented before aliquoting into a 96-well plate. The fluorescence emission intensity at 525 nm (excitation at 488 nm) was monitored by a plate reader (SpectraMax i3x, Molecular Devices) for more than 2 hours with a 5-min interval at room temperature. To further visualize the uptake of SYTOX green under a laser scanning confocal fluorescence microscopy, MRSA cells were further prepared following these steps: spin down MRSA pellets, get rid of the supernatant, wash the pellets with sterile water twice, and fix them with 10% formalin (HT501128-4L, Sigma Aldrich). All experiments were conducted in duplicate or triplicate.

4.2.6 FITC-dextran membrane permeability assay

To estimate how large a molecule can diffuse into the damaged membrane, we applied dextran conjugated with fluorescein isothiocyanate (FITC-dextran) with variable molecular weight/Stokes radius (FD4-FD500, Sigma Aldrich) and monitored their insertion before and after laser treatment. Briefly, 1 ml of stationary-phase MRSA (~10^8 cells/ml) was spun down, got rid of the supernatant, and resuspended with 100 µl of sterile 1×PBS. 5 µl of the above solution was exposed to pulsed laser with different treatment time. After laser treatment, bacterial solution was collected into 985 µl of sterile pre-warmed TSB, supplemented with 10 µl of FITC-dextran (1 mg/ml), and incubated for 30 min at 37°C. The integrated fluorescence signal from an aliquot of the bacterial solution with or without laser treatment was measured through a plate reader with excitation of 488 nm and emission of 520 nm, respectively. Meanwhile, after incubation, the bacterial

solution was spun down, got rid of the supernatant, washed with pre-warmed TSB twice, and fixed with 10% formalin. Structured illumination microscopy was conducted to quantify FITC-dextran uptake and its distribution on cell membrane with an excitation wavelength of 488 nm. Quantitative analysis of fluorescence emission intensity from individual MRSA cells was performed among groups with different laser treatment time.

4.2.7 Gentamicin-Texas red intracellular uptake assay

To study laser-mediated intracellular uptake of gentamicin (a representative of aminoglycoside), gentamicin was conjugated with a fluorescent dye, Texas-red, to form gentamicin-Texas red. Briefly, 10 mg of gentamicin was dissolved into 1 ml of 0.1 M sodium bicarbonate buffer (S8761-500ML, Sigma Aldrich). 10 mg/ml of Texas red-X succinimidyl ester (T6134, Thermo Fisher Scientific) was added to the gentamicin solution slowly drop by drop. Then the mixed solution was stirred at room temperature for 1 hour. Gentamicin-Texas red was purified through sufficient dialysis against 0.1 M sodium bicarbonate buffer in a dialysis sack (Slide-A-Lyzer G2 Dialysis Cassettes, 2K MWCo, 15 mL, 87719, Thermao Fisher Scientific), and harvested through lyophilization (Labconco). Next, 1 ml of stationary-phase MRSA (~10^8 cells/ml) was spun down, got rid of the supernatant, and suspended with 100 µl of sterile 1×PBS. 5 µl of the above solution was exposed to pulsed laser for different treatment time (1 cm diameter illumination area, 120 mW). After treatment, bacterial droplet was collected into 985 µl of sterile 1×PBS, and then add 10 µl of 1 mg/ml Gentamicin-Texas red. Mixed solution was incubated at 37°C for 30 min with a shaking speed of 200 rpm. After incubation, MRSA pellets were harvested through washing with sterile 1×PBS twice and then fixed with 10% formalin.

Visualization of gentamicin-Texas red on bacterial cells was achieved through a confocal laser scanning microscope (FV 3000, Olympus) with the excitation wavelength of 514 nm. Quantitative analysis of fluorescence emission intensity from individual MRSA cells was conducted and allocated among groups with different laser treatment time.

4.2.8 Ciprofloxacin intracellular uptake assay

To understand how laser treatment affects the uptake of ciprofloxacin (a representative of fluoroquinolone), we adopted a protocol published elsewhere [188]. Briefly, 1 ml of stationary-phase MRSA (~10^8 cells/ml) was spun down, got rid of the supernatant, and suspended with 100 µl of sterile 1×PBS. 5 µl of the above solution was exposed to pulsed laser for different treatment time (1 cm diameter illumination area, 120 mW). After treatment, bacterial droplet was collected into 994 µl of sterile 1×PBS, and then added 1 µl of 10 mg/ml of ciprofloxacin (17850-5G-F, Sigma Aldrich), then incubated for 30 min at 37°C with a shaking speed of 200 rpm. After incubation, MRSA pellets were washed twice by 2 ml of ice-cold PBS. Then ciprofloxacin was extracted using 1 ml of glycine (G8898, Sigma Aldrich)-HCl buffer at pH=3 for 2 hours. The amount of ciprofloxacin was estimated and quantified by measuring the fluorescence intensity via a plate reader with an excited wavelength of 275 nm and emission wavelength of 410 nm.

4.2.9 DiIC_{18} membrane fluidity assay

$DiIC_{18}$ is a fluorescent dye that displays affinity for membrane areas with increased fluidity due to its short hydrocarbon tail [189]. In our protocol, briefly, 1 ml of stationary-phase MRSA (~10^8 cells/ml) were spun down, got rid of the supernatant, and suspended

with 100 µl of pre-warmed TSB supplemented with 1% DMSO. 5 µl of the above solution was exposed to pulsed laser for different treatment time. After treatment, bacterial droplets (with 2.5, 5, 10 min treatment time) were collected into 985 µl of pre-warmed TSB supplemented with 1% DMSO. 10 µl of $DiIC_{18}$ (stock:10 mg/ml in DMSO) were added to the above solution, and incubated for 30 min at 37°C. After incubation, harvested MRSA pellets were washed with pre-warmed TSB supplemented with 1% DMSO for four times, then sandwiched the concentrated bacterial samples between a poly-prep cover slides (P0425, Sigma Aldrich) and a thin cover glass (48404-457, VWR international). A confocal laser scanning microscope (FV3000, Olympus) was applied to visualize and quantify $DiIC_{18}$ uptake at an excitation wavelength of 561nm and via a 100×oil immersion objective (NA = 1.35, Olympus).

4.2.10 Daptomycin-BODIPY membrane fluidity assay

To study how the membrane fluidity change affects the insertion of membrane-targeting antibiotics, we applied daptomycin-BODIPY membrane insertion assay detailed as below. Firstly, we conjugated daptomycin with a fluorescent dye, BODIPY STP ester (B10006, Thermo Fisher Scientific). Briefly, 10 mg of daptomycin (103060-53-3, Acros Organics) was dissolved into 1 ml of 0.1 M sodium bicarbonate solution. Then 100 µl of BODIPY STP ester (B10006, Thermo Fisher Scientific, stock: 1 mg/ml in DMSO) was added to the daptomycin solution drop by drop. Then the mixed solution reacted under stirring at room temperature for 1 hour. Afterwards, the solution was under overnight dialysis against extensive 0.1 M sodium bicarbonate solution. After dialysis, the mixed solution was lyophilized. To further label MRSA cell membrane with daptomycin-

BODIPY, 1 ml of stationary-phase MRSA (~10^8 cells/ml) was spun down, got rid of the supernatant, and suspended with 100 µl of sterile 1×PBS. 5 µl of the above solution was exposed to pulsed laser with different treatment time. After treatment, bacterial droplets were collected into 985 µl of sterile pre-warned TSB medium containing 150 µg/ml of $CaCl_2$. 10 µl of daptomycin-BODIPY (stock: 3 mg/ml in 1×PBS) was added to the above solution, and incubated for 30 min at 37°C. After incubation, harvested MRSA pellets were washed with 1×PBS twice, and fixed with 10% formalin. Confocal laser scanning microscope (FV3000, Olympus) was conducted to quantify daptomycin-BODIPY distribution and its signal intensity at an excitation wavelength of 488 nm. Quantitative analysis of the signal from individual MRSA cells was performed among groups with different laser treatment time.

4.2.11 PBP2a immunofluorescence assay

Basically, 1 ml of stationary-phase MRSA (~10^8 cells/ml) was spun down, got rid of the supernatant, and suspended with 100 µl of sterile 1×PBS. 5 µl of the above solution was exposed to pulsed laser for different treatment time. After treatment, bacterial droplets were collected into 980 µl of sterile 1×PBS, and 20 µl of a primary antibody (Rabbit Anti-PBP2a, RayBiotech, 130-10073-20, 10 µg/ml) targeting PBP2a was added to the above solution. Then the mixed solution was incubated for 30 min at 37°C with a shaking speed of 200 rpm. After incubation, MRSA pellets were washed twice with sterile 1×PBS. As the last wash, MRSA pellets were suspended with 990 µl of 1×PBS. Then 10 µl of secondary antibody (Goat anti-Rabbit Cy5, Abcam, ab97077, 0.5 mg/ml) was added to the above solution, incubated for another 30 min at 37°C with a shaking speed of 200 rpm. After

incubation, MRSA pellets were washed with sterile 1×PBS twice and fixed with 10% formalin. Immunofluorescence experiment was conducted by a confocal laser scanning microscope at an excitation wavelength of 650 nm. Quantitative analysis of signal intensity and its distribution from individual MRSA cells was performed among groups with different laser treatment time.

4.2.12 PBP2a Western blotting assay

Briefly, 3 ml of stationary-phase MRSA (~10^8 cells/ml) was spun down and suspended with 100 µl of 1×PBS. 20 µl of the mixed solution was aliquoted to a centrifuge tube (89166-280, VWR international), and then exposed to pulsed laser with different treatment time (control, 5 min, 10 min, 20 min). After exposure, the four tubes containing MRSA solution were spun down at a speed of 13,000×g for 10 min at 4°C. Then the supernatants were collected into four new sterile tubes. To extract proteins from MRSA pellets, after removing the supernatant, MRSA pellets were suspended with 100 µl of lysis buffer (96.8 µl of RIPA, 1 µl 500 mM DTT, 1 µl of 10% Triton-X, 1 µl of protease inhibitor, and 1 µl of phosphorylase inhibitor). Then the mixed solutions were sonicated by a sonication probe (Cole-Parmer) at 4°C. Released proteins were harvested from the supernatants by centrifuging at 13,000×g for 10 min at 4°C. Electrophoresis separation of the proteins from both MRSA pellets and supernatants was conducted on a 12% SDS-PAGE gel (stacking gel: 4%) at a voltage of 50 V for 30 min followed by 100 V for 1 hour in 1×running buffer (1610772, Bio-Rad). After separation of the proteins, gels were transferred to a PVDF membrane (1620184, Bio-Rad) at a current of 150 mA overnight at 4°C in 1×transfer buffer (1610771, Bio-Rad). After transferring, PVDF membrane was harvested and put into a

clean plastic reservoir containing 5% milk solution (1706404, Bio-Rad). Then the plastic reservoir was placed on a rocking shaker for 30 min. After blocking, the PVDF membrane was further labelled with primary antibody (Rabbit anti-PBP2a, 1:500 dilution in 5% milk solution) for 2 hours in a rotary shaker. Then the PVDF membrane was washed with 1×washing buffer three times with each time for 5 min on the rotary shaker. Afterwards, the PVDF membrane was conjugated with a fluorescent secondary antibody (*Eu*-anti-Rabbit, Molecular Devices, 1:1000 dilution in 5% milk solution) for 1 hour on the rotary shaker and then washed with 1×washing buffer three times with each time for 5 min on the rotary shaker. Lastly, the protein-antibody-antibody fluorophore complex was detected through a plate reader at an excitation wavelength of 340 nm.

4.2.13 Membrane computational method

The Coarse-Grained (CG) simulations were performed using the MARTINI forcefield. The parameters for the cardiolipin were taken from the MARTINI database [190]. For PBP2a, only the transmembrane helix was included in this simulation as we focus on the membrane properties in the current work. The saturated and unsaturated tail of the STX lipid were modeled by “C1” and “C4” bead type, respectively following other lipid parameters within the MARTINI model. The head group of the STX lipid is a glucose for which the MARTINI parameters were taken from the database. The bond and angle parameters for the CG beads of the STX tails were determined using structural information obtained from atomistic simulations. A single STX lipid in solution was simulated using the all atom CHARMM27 [191] forcefield and the TIP3P [192] water model. The equilibrium bond length and angle for the STX tail CG beads were obtained from the positions of the mass centers

of the corresponding groups in atomistic simulations. The bond force constants for both the saturated and unsaturated tails and the angle force constants for the saturated tail were taken as same as for the other lipids in the MARTINI model. However, since every other bond in the unsaturated tail is a C=C bond, the tail is expected to be very rigid. So, the angle force constants for the unsaturated tail were taken to be higher ($200\ kJ/mol - rad^2$) than the angle force constants for the saturated tail ($25\ kJ/mol - rad^2$). To model STX following its photolysis, the long unsaturated tail was truncated, as suggested by the complete loss of C=C vibrational peak in the Raman spectra after STX photolysis. The transmembrane helix of the PBP2a protein was generated using the Chimera software [193]. The CG parameters for the peptide were generated using a script provided in the MARTINI database. We built a bilayer (~17× $17\ nm^2$) of randomly mixed STX, cardiolipin and peptides (400:200:36). The built system was then solvated using the MARTINI water model; 10% anti-freezing beads were also added to avoid any artificial water freezing. Sodium and chlorine ions were then added to maintain 150 mM salt concentration. Each system (with full and truncated STX lipids, respectively) was equilibrated and simulated under the constant pressure and constant temperature ensemble for 10 μs. All simulations were conducted using the GROMACS program [194].

The RDF or the pair correlation function, $g(r)$, between molecule type A and molecule type B is calculated using the following equation

$$g(r) = \frac{1}{< \rho_B >} \frac{1}{N_A} \sum_{i}^{N_A} \sum_{j}^{N_B} \frac{\delta(r_{ij} - r)}{4\pi r^2}$$

Here, N_A and N_B are the number of molecules of type A and type B, respectively. ρ_B denotes the density of molecule type B in a sphere of radius r_m around the molecule type A and $< \rho_B >$ is the average of ρ_B calculated over all type A molecules. The r_m was taken to be ~6 nm which is half of the shortest box dimension.

The area expansion modulus K_A of the membrane was calculated using the following equation:

$$K_A = \frac{k_B T < A >}{< \delta A^2 >}$$

Here k_B, T, and A are the Boltzmann constant, absolute temperature and the membrane surface area, respectively; $< \delta A^2 >$ represents the fluctuation in the surface area, which was calculated as $< \delta A^2 > = < (A - < A >)^2 >$, where $< A >$ is the mean value of the surface area averaged over ~5 μs simulation. The thermal fluctuations in the membrane surface area is less in a tightly packed membrane. Thus, a higher value of K_A represents a more tightly packed membrane.

4.2.14 Serial passage assay for resistance development

To understand whether laser treatment could cause genotypic or phenotypic change in MRSA, and whether STX photolysis could reduce the resistance development for conventional antibiotics, a serial passage study for each treatment scenario was conducted. The initial generation (Day 1) used in this study was stationary-phase MRSA. The sample was prepared, washed and resuspended in 1×PBS at its original concentration. An aliquot (5 μl) of the MRSA suspension was transferred onto a glass cover slide as a droplet of ~5 mm in diameter with or without 10 min laser treatment (1 cm diameter illumination area,

120 mW). The droplets were then collected and resuspended into 5 ml of TSB medium (1:1000 dilution) with an estimated cell concentration of 10^5 CFU/ml. To study resistance development or selection induced by laser treatment alone, three groups were included: a group without laser treatment (SP0), a group with laser treatment (SPL1), and another independent group with laser treatment as a duplicate (SPL2). To study resistance development induced by antibiotic treatment alone and laser plus antibiotic treatment, three groups were included for each antibiotic: antibiotic alone-treated group (SPA0), laser plus antibiotic-treated group (SPLA1), and another laser plus antibiotic-treated group as another independent serial passage (SPLA2). For SP0, SPL1, and SPL2, 200 µl of bacterial suspension was directly transferred to each well of a 96-well plate, with three replicates conducted for each group. For SPA0, SPLA1, and SPLA2, 200 µl of bacterial suspension was transferred into the first dilution row of a 96-well plate with supplemented antibiotics at a desired starting concentration, whereas 100 µl of bacterial suspension was transferred to the rest dilution rows. After twelve two-fold serial dilution, 100 µl of bacterial suspension was added into each well to make a 200 µl of final volume for each well, thus, as an example, supplementing 5.12 µl of 10 mg/ml ofloxacin solution into 200 µl of bacterial culture in the first dilution row makes a starting concentration of 128 µg/ml. Three replicates were applied for each group. These well plates were incubated in a shaker at 37 °C and 200 rpm for 18 hours followed by OD_{600} measurement by a plate reader. After MICs recording for each group, the well plates were continuously incubated in the shaker for 3 days in total. On Day 4, 200 µl of bacterial sample from each group was collected, washed, and resuspended in 1×PBS at its original concentration used as new inoculum for

the next passage following the same protocol as described above. Samples for SPA0, SPLA1, and SPLA2 groups were collected from wells supplemented with sub-MIC antibiotic. Samples for SP0, SPL1, and SPL2 groups were also collected from the well plates. The left bacterial suspension for each group was stored in 25% glycerol at -80 °C for subsequent analysis and experiments. Serial passage for all groups were performed for 50 days with 16 generations in total.

Raman spectroscopy was then applied to monitor STX expression level in groups of interest after the entire serial passage experiment. The protocol is detailed as below: 100 µl of ~400 µl stored bacterial culture was collected, spun down with the supernatant being removed, then resuspended into 5 µl 1×PBS as high-concentration bacterial solution (20 times concentrated). An aliquot (1 µl) was transferred and then sandwiched between two glass cover slides for STX quantification by resonance Raman spectroscopy.

4.3 Results

4.3.1 Pulsed blue laser photolysis of staphyloxanthin

In order to test the hypothesis that STX is the molecular target of photons in the entire blue range, we directly exposed high-concentration stationary-phase MRSA colony to a wavelength-tunable laser beam in a wide-field illumination configuration as shown in **Figure. 4.1a**. Strikingly, the distinctive golden color of MRSA colony fades quickly over time when the wavelengths were tuned into the blue (400-490 nm) wavelength range (e.g. the images of MRSA colony with 460 nm illumination wavelength in **Figure. 4.1a**). As the golden colony color is originated from STX pigment, such color-fading phenomenon suggests that STX is subject to photolysis (molecular structure of STX shown in **Figure.**

4.1a). In order to further validate this point, we applied resonance Raman spectroscopy to quantify STX content in MRSA cells by taking advantage of its high sensitivity, molecular specificity, and linear concentration dependence [195]. STX in MRSA shows three characteristic Raman peaks around 1008 (methyl rocking), 1161 (C-C stretch), and 1525 cm^{-1} (C=C stretch), respectively, corresponding to their specific molecular vibrational modes (**Figure. 4.1b**). With increased laser treatment time, we observed dramatically decreased peak amplitude for all three Raman bands, suggesting the cleavage of both C-C and C=C bonds that constitutes the polyene chain of STX (**Figure. 4.1b**). As a result, the unsaturated tail of STX, the nine conjugated C=C double bonds, is decomposed or truncated, as confirmed by mass spectrometry [196]. In contrast, when we blocked STX biosynthesis in *S. aureus* by knocking down CrtM, namely *S. aureus* ΔCrtM, its colony turns colorless and shows no detectable peaks for all three Raman bands, confirming that these Raman bands are exclusively from STX (**Figure. 4.1c**). With fixed laser power and dosage (50 mW, 5 min exposure time), MRSA colonies were further illuminated at different laser wavelengths and STX photolysis efficiency calculated using the Raman peak amplitude at 1161 cm^{-1} before and after illumination. The results in **Figure. 4.1d** indicate that STX is subject to effective photolysis in the entire blue wavelength range (400-490 nm) with significantly reduced efficiency when above 500 nm. This efficiency curve matches the absorption spectrum of STX as photolysis is grounded on the absorption of chromophore. The effective STX photolysis induces significant absorption change, which is directly reflected on the absorption spectra of MRSA bacterial solution. By compromising the STX photolysis efficiency and optical penetration, 460-480 nm is the

preferable optical window (460 nm illumination wavelength was applied in the following studies). Notably, STX photolysis behavior is not only limited to MRSA, but broadly shown on vancomycin-resistant *S. aureus* (VRSA) and other clinically isolated multi-drug resistant *S. aureus* strains, as more than 90% of all *S. aureus* human clinical isolates generate this golden pigment [197]. Collectively, these results suggest that STX is the molecular target of photons or lasers in the entire blue range.

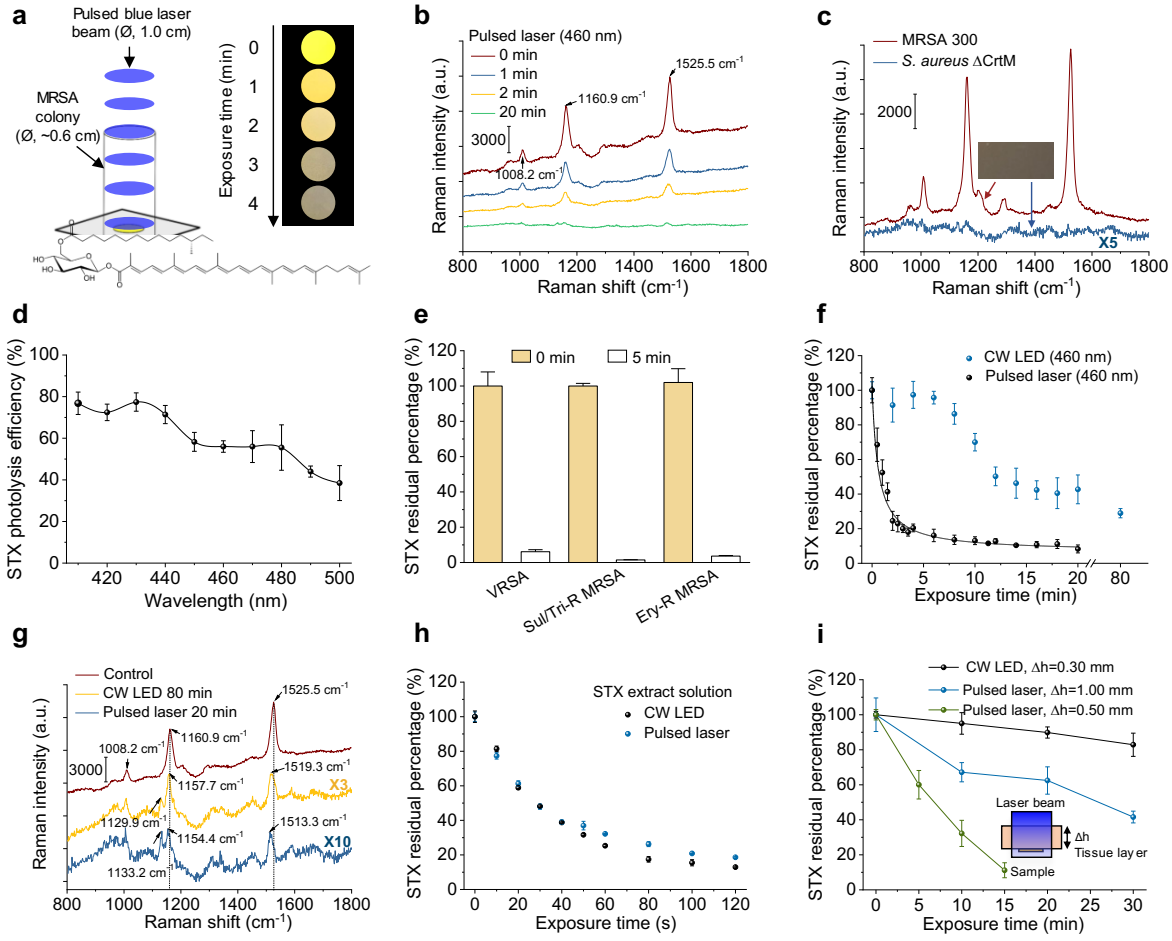

Figure 4.1. Photophysics and photochemistry of pulsed laser photolysis of STX. (a) (Left) Schematic of MRSA colony (or MRSA solution or STX extract solution) treated by nanosecond pulsed laser in a wide-field illumination configuration. (Right) Digital images of MRSA colony over laser treatment time to show golden color fading phenomenon. Image were recorded with sample placed on a transparent glass cover slide over a black paper. (Bottom) STX molecular structure. Ø refers diameter of bacterial colony. (b) Resonance Raman spectroscopy of MRSA colony over 460 nm nanosecond pulsed laser treatment time (measured on the same colony). Numbers indicate major Raman peak positions. (c) Resonance Raman spectroscopy of MRSA and *S. aureus* ΔCrtM

colonies. The images show the color of spun-down cells. (d) Spectroscopic study of STX photolysis efficiency with nanosecond pulsed laser power of 50 mW and treatment time of 5 min. STX photolysis efficiency is quantified by Raman peak amplitude at 1161 cm^{-1}. (e) Raman quantification of STX abundance in multidrug-resistant *S. aureus* cells before and after 5 min laser treatment (460 nm). Bacterial strains include vancomycin-resistance *S. aureus* (VRSA), sulfamethoxazole/trimethoprim-resistant MRSA (Sul/Tri-R MRSA), and erythromycin-resistant MRSA (Ery-R MRSA). (f) STX photolysis kinetics of MRSA colony by nanosecond pulsed laser and CW LED under the same illumination power, area, and center wavelength (460 nm). Solid black curve is the fitting result by a second-order photobleaching model. (g) Resonance Raman spectroscopy of STX in MRSA colony with or without long time-treatment by nanosecond pulsed laser and CW LED at 460 nm highlighting STX photolysis induced Raman peak shifts and the generation of new Raman peak. Numbers indicate Raman peak positions before and after light treatment. (h) STX photolysis kinetics of STX solution by nanosecond pulsed laser and CW LED under the same illumination power, area, and center wavelength (460 nm). STX solution were extracted directly from MRSA cells. (i) STX photolysis kinetics of MRSA colony placed beneath a tissue layer with various thickness by nanosecond pulsed laser and CW LED under the same illumination power, area, and center wavelength (460 nm). The inset shows the schematic of experimental scheme. Δh indicates the thickness of tissue layer. CW, continuous wave. The cells used were all cultured to reach 3-day stationary phase. N=3 for all the above measurements.

4.3.2 Photo-disassembly of FMM: membrane permeabilization

STX is known acting as the constituent lipid of FMM, which are embedded in the lipid bilayer of virulent *S. aureus* strains and implicated in maintenance of membrane integrity. Therefore, we hypothesize that STX photolysis disrupts membrane integrity by increasing membrane permeability, thus facilitating the intracellular accumulation of small-molecule dyes or antibiotics via passive diffusion (**Figure. 4.2a**). To prove this point, membrane permeability with or without laser treatment was evaluated in real time by SYTOX green (600 Da), a fluorescent dye for nucleic acids stain of cells only with compromised membrane. With increased laser treatment time, a significantly larger and faster uptake of SYTOX green is observed, indicating severely compromised cell membranes; whereas cells without laser treatment show negligible uptake, which validates the role of STX on membrane integrity (**Figure. 4.2b**). These results were further confirmed by confocal fluorescence imaging and statistical analysis of signal intensity for individual cells. From **Figures. 4.2, c-d**, significantly brighter fluorescence signal from the entire cell population is observed over laser treatment time, indicating different levels of membrane permeability.

After 10 min laser treatment, such damaged membranes are unable to recover even with 2 hours culturing. In contrast, for *S. aureus* with ΔCrtM (nonpigmented mutant) and log-phase MRSA, no significant difference in SYTOX green uptake is shown between laser treated vs the untreated (**Figure. 4.2e**).

Based on these findings, we further hypothesize that increased membrane permeability induced by STX photolysis would allow passive diffusion of small-molecule antibiotics that target intracellular activities. To demonstrate this point, we used the aminoglycoside, gentamicin, as an example. Gentamicin was firstly conjugated with a fluorescent dye, Texas red, and then imaged via confocal fluorescence microscopy after co-culturing with cells. As expected, cells with laser treatment accumulate significantly more gentamicin molecules than untreated, from either single cell (**Figures. 4.2, f-g**) or the entire cell population. The uptake of ciprofloxacin, another small-molecule antibiotic that belongs to fluoroquinolone class, can be directly detected via its endogenous fluorescent nature. Compared to the untreated cells, increased fluorescence signal is shown on cells with laser treatment (**Figure. 4.2h**). These results further confirm that small-molecule antibiotics can diffuse into the cell via permeable membrane induced by laser treatment.

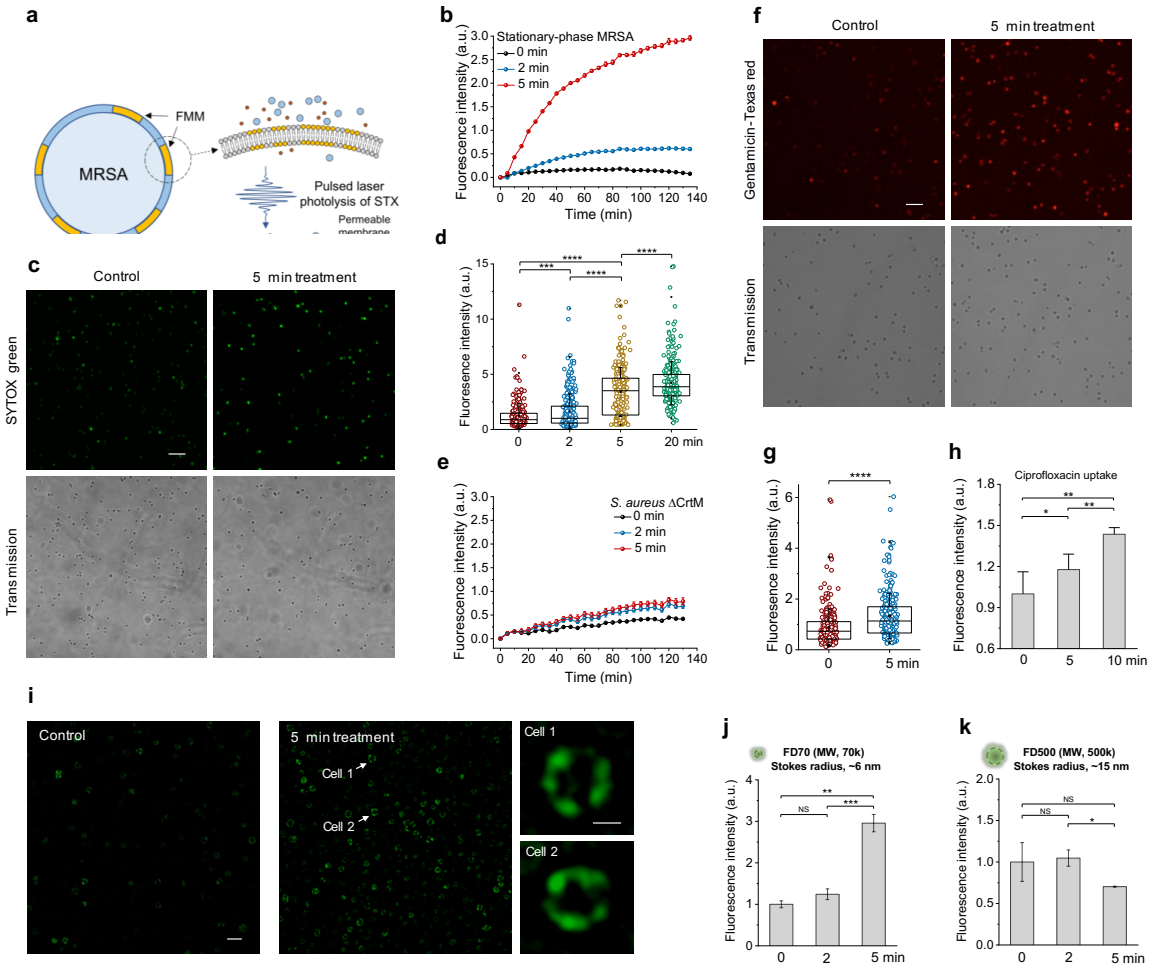

Figure 4.2. First mechanism for photo-disassembly of membrane microdomains: membrane permeabilization. (a) Schematic of membrane permeability mechanism via pulsed laser photolysis of STX. (b) Real-time intracellular uptake kinetics of SYTOX green by stationary-phase MRSA with or without pulsed laser treatment. (c) Confocal fluorescence images of intracellular uptake of SYTOX green by stationary-phase MRSA cells with or without pulsed laser treatment. (Top) fluorescence images. (Bottom) corresponding transmission images. (d) Statistical analysis of fluorescence signal from MRSA cells in (c) from each treated group with N ≥ 300 per group. (e) Real-time intracellular uptake kinetics of SYTOX green by stationary-phase *S. aureus* ΔCrtM with or without pulsed laser treatment. (f) Confocal fluorescence images of intracellular uptake of gentamicin-Texas red by stationary-phase MRSA cells with or without pulsed laser treatment. (Top) fluorescence images. (Bottom) Corresponding transmission images. (g) Statistical analysis of fluorescence signal of MRSA cells in (f) from each treated group with N ≥ 300 per group. (h) Fluorescence detection of ciprofloxacin uptake by stationary-phase MRSA with or without pulsed laser treatment. (i) Structured illumination microscopic images of FD500 uptake by stationary-phase MRSA cells with or without pulsed laser treatment. Insets shows representative images of FD500 distribution on single cell after 5 min laser treatment. Fluorescence detection of (j) FD70 and (k) FD500 uptake by stationary-phase MRSA with or without pulsed laser treatment. MW, molecular weight. Scale bar, 5 μm for (c, f, i) and 0.5 μm for zoom-in images in (i). N=3 for all the above measurements.

To estimate how large a molecule can diffuse into the damaged membrane, we applied dextran labeled fluorescein isothiocyanate (FITC-dextran) with variable molecular weight/Stokes radius and monitored its insertion before and after laser treatment. For FD70 with molecular weight of 70k Da and Stokes radius of 6 nm, longer laser treatment time yields increased fluorescence signal either at individual cell level (**Figure. 4.2i**) or from total cell population (**Figure. 4.2j**). Laser treatment over 5 min leads to ample insertion of FD 70 (**Figure. 4.2j**). Super-resolution imaging of individual cells further shows that these dyes are primarily inserted and concentrated within FMM (**Figure. 4.2i**, zoom-in images). In contrast, when FD500 with molecular weight of 500k Da and Stokes radius of 15 nm was applied, no uptake is shown, indicating an upper limit on molecular Stoke radius of 30 nm level (**Figure. 4.2k**). These results suggest that after effective STX photolysis, FMM becomes porous, allowing molecules with Stokes radius up to nanometer level to diffuse through or insert into the membrane.

4.3.3 Photo-disassembly of FMM: membrane fluidification

After effective STX photolysis, its products no longer maintain the chemical structure and properties of STX. The unsaturated tail of STX is truncated as unveiled by Raman spectroscopy results; the polarity of its products becomes significantly higher than that of STX as suggested by liquid chromatography results[196]. As a result, these products spontaneously tend to disperse or detach from their original membrane organization. These behaviors profoundly disrupt the lipid packing within the microdomain, thus changing the membrane fluidity and subsequently facilitating the insertion of membrane targeting antibiotics, e.g. daptomycin. To test this hypothesis, we evaluated the membrane fluidity

with or without laser treatment by $DiIC_{18}$, a fluorescent dye that displays affinity for membrane areas with increased fluidity due to its short hydrocarbon tail [189](**Fig. 4.3a**). As shown in **Figures. 4.3, b-c**, significantly more $DiIC_{18}$ is shown up as foci in log-phase MRSA when compared to the stationary-phase, as membrane in stationary phase becomes more rigid than that in log phase, partially due to the presence of rigid STX [198]. After laser treatment, the foci number on each cell is significantly increased when compared with that of stationary-phase cells without laser treatment. Notably, 70% of cells in stationary phase show no detectable fluorescence signal, whereas this portion drops dramatically to 35% after 2.5 min laser treatment. The ample uptake indicates that laser treatment renders membrane more fluid due to the depletion of rigid unsaturated STX tail and the subsequent loose packing of lipid bilayer.

The increased membrane rigidity by STX overexpression promotes the bacterial resistance against daptomycin, a cationic antimicrobial peptide, by reducing its membrane binding and subsequent membrane disruption [198-200]. Therefore, we further hypothesize that increased membrane fluidity after STX photolysis facilitates the insertion of daptomycin. To prove this point, we first labeled daptomycin with BODIPY ester, then imaged cellular uptake of daptomycin with or without laser treatment. From **Figures. 4.3, e-f**, significantly more daptomycin uptake is shown for laser-treated groups when compared to the untreated groups; longer treatment yields higher uptake.

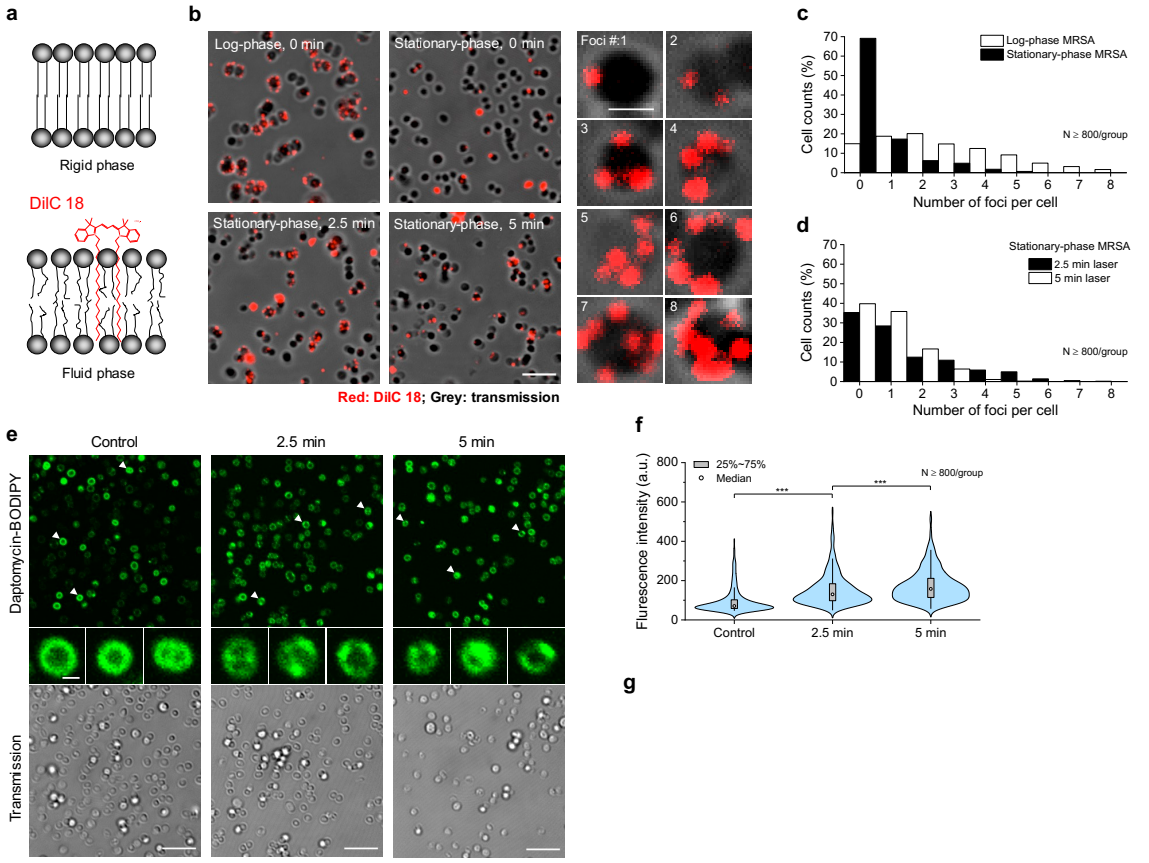

Figure 4.3. Second mechanism for photo-disassembly of membrane microdomains: membrane fluidification. (a) Schematic of membrane insertion of $DiIC_{18}$ induced by gel/rigid-to-liquid/fluid phase change. (b) (Left and middle columns) fluorescence images of $DiIC_{18}$ foci formation for groups including log-phase MRSA and stationary-phase MRSA with or without laser treatment. (Right column) zoom-in fluorescence images of MRSA cells with different foci number on each cell. Fluorescence from $DiIC_{18}$, red; transmission, grey. Scale bar, 5 µm for (left and middle columns) and 1 µm for (right column). Statistical analysis of foci number on cells from each group in (b): (c) log-phase and stationary-phase MRSA without laser treatment; (d) stationary-phase MRSA with different laser treatment time. N ≥ 800/group. (e) (Top row) fluorescence images of daptomycin-BODIPY on stationary-phase MRSA with or without laser treatment. (Middle row) representative zoom-in images of the upper row. (Bottom row) corresponding transmission channels. Scale bar, 5 µm for (top and bottom row) and 0.5 µm for (middle row). (f) Statistical analysis of fluorescence signal intensity from MRSA cells in (e) with or without laser treatment with N ≥ 800. (g) Schematic of antibiotic membrane insertion mechanism via pulsed laser photolysis of STX.

More interestingly, daptomycin distribution between laser treated and untreated groups are quite different; for the untreated, daptomycin distributes evenly on the cell membrane, whereas, aggregates or domain-like structures with bright signal are found on cells after laser treatment (representative zoom-in images in the middle row in **Figure. 4.3e**). These aggregates most likely form within FMM due to the promoted insertion and

oligomerization of daptomycin. Collectively, these results provide evidences to support the ample increase of membrane fluidity after STX photolysis, thus potentiate antibiotic lipopeptides to insert and oligomerize within the domains and further disrupt cell membrane as illustrated in **Figure. 4.3g**.

4.3.4 Photo-disassembly of FMM: transmembrane detachment

To demonstrate how STX photolysis further malfunctions membrane proteins that are co-localized within STX-enriched FMM, we chose penicillin-binding protein 2a, PBP2a, as an example. MRSA acquires resistance to beta-lactam antibiotics through expression of PBP2a, a protein [175] that primarily anchors within FMM through its transmembrane helix and hides its targeting site inaccessible by beta-lactam antibiotics (**Figure. 4.4a**). Considering the relative structural organization of STX and PBP2a, we hypothesize that PBP2a protein complex can be disassembled and unanchored from cell membrane upon effective STX photolysis. To validate this point, we first resolved the structural distribution of PBP2a under a structured illumination microscopy via immunostaining with anti-PBP2a antibodies both for laser-treated (**Figures. 4.4, b-c**) and the untreated (**Figures. 4.4, d-e**). For the untreated, we observed bright fluorescence signal from all stationary-phase MRSA cells due to ample PBP2a expression. These proteins are accumulated discretely within small membrane domains as visualized in both 3-D (**Figure. 4.4b**) and 2-D along various depths (**Figure. 4.4c**). Three to four foci on average is found on each cell, indicating the prevalence of microdomain formation when cells reach their stationary phase. Once treated with pulsed laser, dramatically decreased signal intensity and altered signal distribution are observed on each individual cell (**Figures. 4.4, d-e**). Laser-treated cells have around 2

times lower signal intensity when compared with the untreated, thus indicating a large portion of PBP2a proteins are detached from cell membrane (**Figure. 4.4f**). The left PBP2a proteins are dispersed laterally with its dispersion quantified by coefficient of variation, which is significantly higher than that of the untreated (**Figure. 4.4g**). Such detachment and dispersion lead to significantly reduced contrast between FMM and its neighboring lipid bilayer (**Figure. 4.4e**). Western blotting results further confirms the PBP2a detachment mechanism, as increased amount of PBP2a is found in supernatant over laser treatment time, whereas decreased amount found in MRSA pellets (**Figure. 4.4h**). Taken together, photolysis of the constituent lipids leads to disassembly and detachment of PBP2a from FMM, thus disables MRSA's defense to penicillins as illustrated in **Fig. 4.4i**. Additionally, as PBP2a is primarily utilized to catalyze cell-wall crosslinking, their detachment further affects cell wall synthesis and potentially cell viability.

To further investigate the membrane phase and its mechanical properties, we built a coarse-grained membrane model that contains STX, cardiolipin lipids, and transmembrane helixes of PBP2a proteins and performed microsecond-scale molecular dynamics simulations. At the initial simulation configuration, STX, cardiolipin lipids and peptides randomly disperse in the built bilayer. During 10 μs simulation, these molecules spontaneously self-assemble to a microphase separated system containing well distinguishable STX and cardiolipin microdomains, despite cardiolipin being a charged lipid; PBP2a peptides localize to the center of STX domains or the vicinity of STX/cardiolipin domain interface (**Figure. 4.4j**). The formation of microdomain is primarily driven by the preferable interactions among lipid tails of similar saturation or

unsaturation nature, as in current system all four tails of cardiolipin are saturated, whereas STX lipid has a long unsaturated tail.

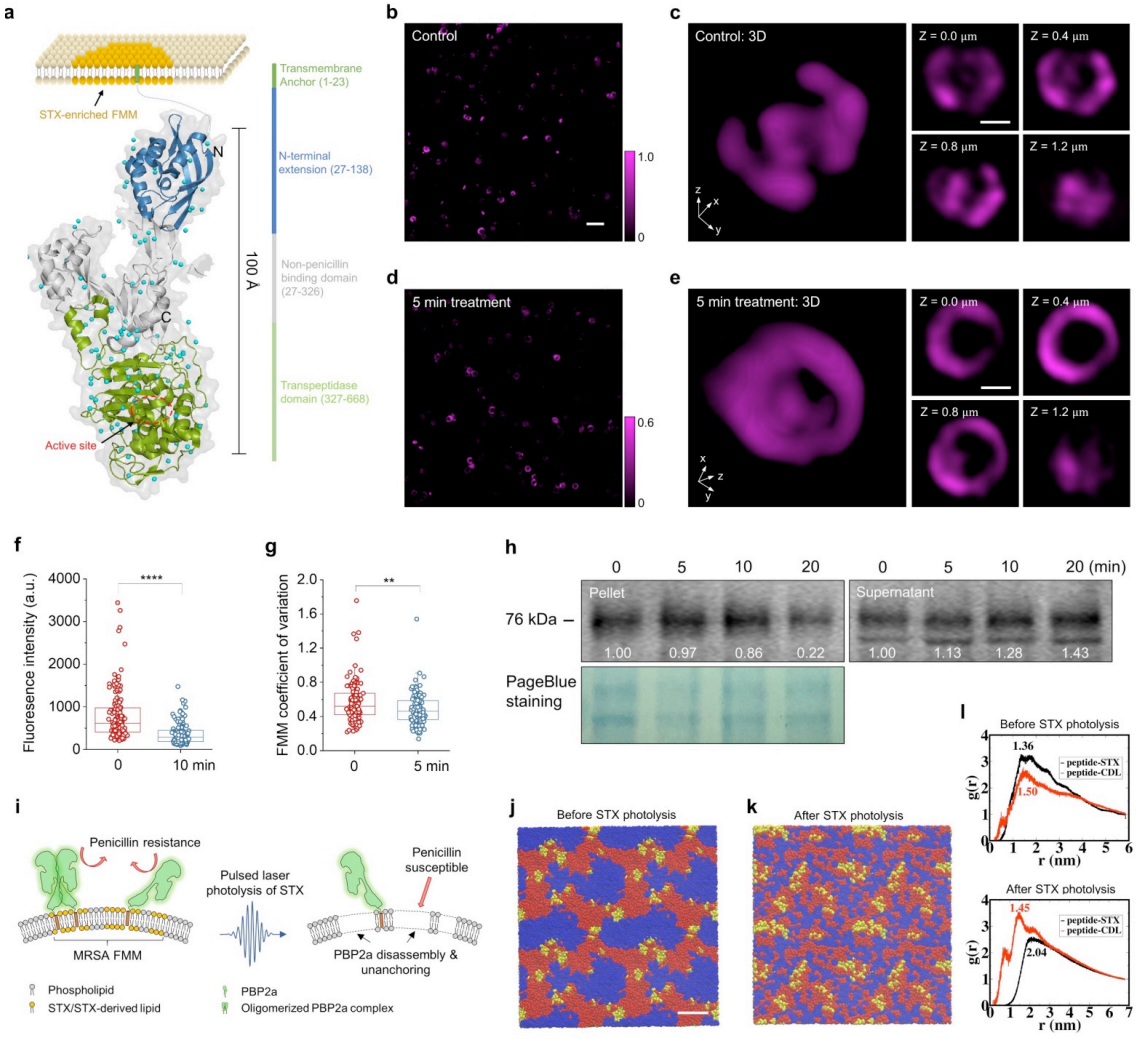

Figure 4.4. Third mechanism for photo-disassembly of membrane microdomains: membrane protein detachment. (a) Schematic of PBP2a protein structure and location relative to STX enriched membrane microdomain. (b, c) SIM images of PBP2a via immunostaining on MRSA cells in (b) 2-D and (c) 3-D. Intensity color bar applies to (b, c). (d, e) SIM images of PBP2a immunostaining on MRSA cells in (d) 2-D and (e) 3-D after 5 min laser treatment. Intensity color bar applies to (d, e). Scale bar, 2.0 μm for (b, d) and 0.5 μm for (c, e). (f) Statistical analysis of signal intensity from MRSA cells with or without laser treatment with N ≥ 100. (g) Statistical analysis of PBP2 coefficient of variation on MRSA cells with or without laser treatment with N ≥ 100. (h) Western blot of PBP2a on MRSA pellets and its supernatant for groups with different laser treatment time. Numbers indicate the integrated signal intensity. Page-blue staining of the same samples was used as a loading control. (i) Schematic of PBP2a disassembly and detachment mechanism via pulsed laser photolysis of STX. (j) Self-assembled microphase separated domain structures of modeled membrane after 10 μs molecular dynamics simulation. Full-length STX lipids, red; cardiolipin lipids, blue; PBP2a peptides, yellow. (k) Final configuration of modeled membrane with

truncated STX after 10μs molecular dynamics simulation. Color scheme also applies to (j). Water and ions are made invisible for clarity for (j, k). Scale bar, 5 nm for (j, k). (l) RDFs of PBP2a peptides relative to the full-length STX and cardiolipins (upper panel) and truncated STX and cardiolipins (lower panel). Numbers on the plot indicate the locations of the first peak for each RDF.

This result is consistent with lipid domain formation commonly found for systems with a mixture of saturated and unsaturated lipids such as DOPC/DPPC, DOPC/DPPG, DOPG/DPPC and many others [201]. To quantify the relative position and abundance of PBP2a peptides relative to STX and cardiolipin lipids, the radial distribution functions (RDFs), $g(r)$, of PBP2a peptides were calculated. **Figure. 4.4l** (upper panel) shows that the RDF peak of PBP2a peptide to STX is higher and located at smaller distance when compared to that of PBP2a peptide to cardiolipin, indicating that PBP2a peptides preferentially interact with STX lipids over cardiolipin, due likely to the better packing between the rigid fully unsaturated STX tail and the PBP2a transmembrane helix. Our Raman spectroscopy results suggest that photolysis of STX leads to the loss of its rigid and unsaturated tail, the conjugated C=C chain. Thus, to mimic the scenario after STX photolysis, we repeated our simulations by replacing full-length STX with truncated STX with its unsaturated tail removed from the model. Interestingly, the truncated STX lipids no longer form microdomains. As a result, all the lipids and PBP2a peptides are randomly dispersed (**Figure. 4.4k**). Moreover, the RDF of PBP2a peptide to cardiolipin now features a higher peak at a smaller distance than that of PBP2a peptide to STX, suggesting that the PBP2a proteins prefer to interact with cardiolipins over truncated STX (**Figure. 4.4l**, lower panel). The different phase features before and after STX photolysis also lead to different membrane mechanics. For example, the calculated area expansion modulus (K_A) of the membrane after microdomain formation is $\sim 58\ k_B T/nm^2$, which is significantly higher

than the value of $\sim 42\ k_B T/nm^2$ with truncated STX, cardiolipins and peptides randomly dispersed after STX photolysis. This suggests that following the truncation of the unsaturated STX tail, the membrane loses the microphase separated domain structure and becomes more loosely packed, which in turn likely reduces the affinity of PBP2a protein to the membrane. Collectively, our simulations provide a plausible rational for the STX photolysis induced membrane remodeling, including the loss of functional domains, the increase of membrane permeability and fluidity, and the detachment of PBP2a from the membrane.

4.3.5 Restoration of conventional antibiotics

With cell membrane catastrophically damaged via STX photolysis, we further reasoned that both cell growth and cell viability are severely compromised by laser treatment alone. To test this point, time-killing assay in phosphate-buffered saline was firstly performed on stationary-phase cells with or without laser treatment. Compared with the untreated, laser-treated cells are killed quickly and efficiently due to their disassembled FMM and incapacity for recovery (**Figure. 4.5a**). The killing efficiency shows strong illumination dosage/time dependence; 16 min laser treatment yields nearly 5-log killing when compared to the untreated. In contrast, *S. aureus* ΔCrtM shows relatively negligible killing by laser treatment (**Figure. 4.5b**). These results confirm that STX photolysis induced membrane disruption is the underlying eradication mechanism. Additionally, its recovery ability after laser treatment was assessed via a post-exposure effect assay, similar to post-antibiotic effect [202], as an important way to establish the optimal dosing regimen. The post-exposure effect of stationary-phase MRSA, depending on STX expression condition and laser

treatment time, reaches up to 6-9 hours, due primarily to the membrane disruption mechanisms (**Figure. 4.5c**), whereas no significant post-exposure effect observed for log-phase MRSA or *S. aureus* ΔCrtM (**Fig. 4.5d**). This post-exposure effect indicates a very slow recovery for stationary-phase cells after laser treatment thus fewer doses required for patients, which is superior than the post-antibiotic effect of most antibiotics including oxacillin, ofloxacin, and gentamicin (< 1 hour post-antibiotic effect for all three antibiotics). More significantly, STX photolysis-induced FMM disassembly can pave a new approach to sensitize these bacteria to conventional antibiotics, even by antibiotics presumed to have no activity against MRSA, such as penicillins.

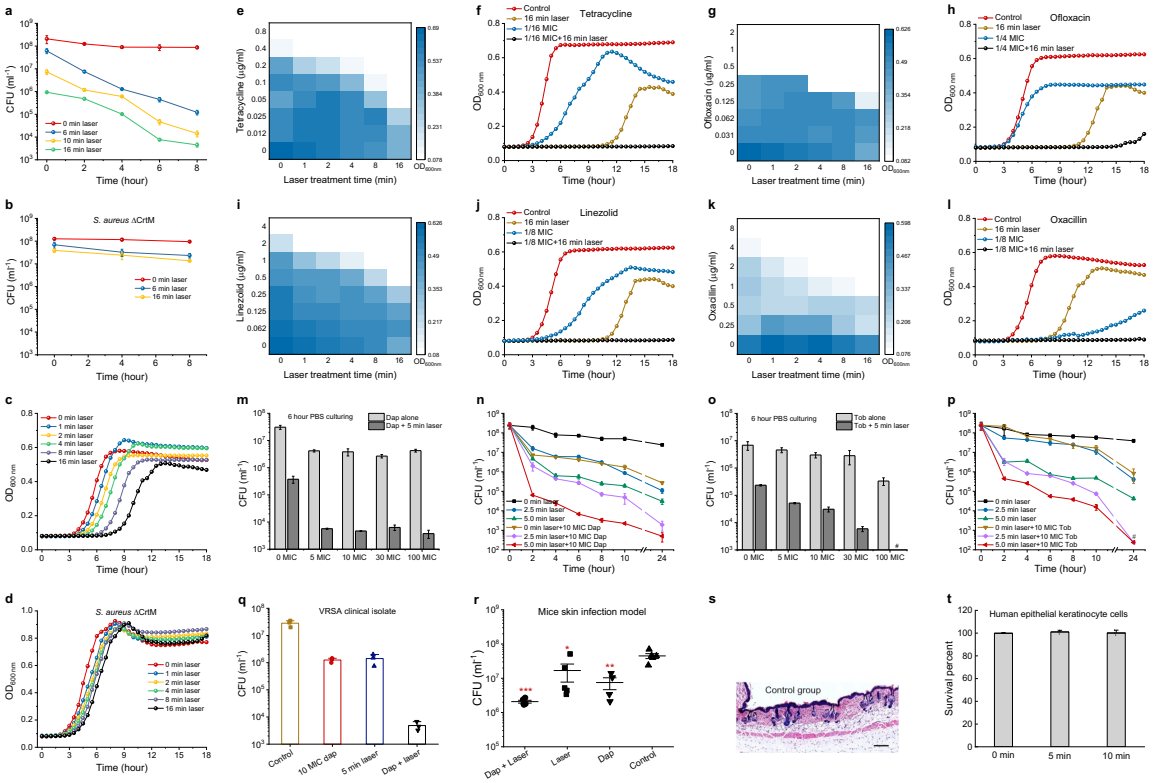

Figure 4.5. Photo-disassembly of membrane microdomains restores a broad spectrum of conventional antibiotics. Time-dependent killing of stationary-phase (a) MRSA and (b) *S. aureus* ΔCrtM cells in phosphate-buffered saline after different laser treatment time. Post-exposure effect of stationary-phase (c) MRSA and (d) *S. aureus* ΔCrtM after different laser treatment time. (e-l) Checkerboard assay results for synergy evaluation between laser treatment and different classes of antibiotics: (e, f) tetracycline, (g, h) ofloxacin, (i, j) linezolid, and (k, l) oxacillin.

(f, h, j, l) Selected cell growth curves acquired from corresponding checkerboard assay results of each antibiotic. (m) Viability of stationary-phase MRSA after laser treatment alone or in combination with daptomycin with different concentrations followed by 6-hour incubation in phosphate-buffered saline. (n) Time-dependent killing of stationary-phase MRSA in phosphate-buffered saline after laser treatment alone or in combination with 10 MIC daptomycin. (o) Viability of stationary-phase MRSA after laser treatment alone or in combination with gentamicin with different concentrations followed by 6-hour incubation in phosphate-buffered saline. (p) Time-dependent killing of stationary-phase MRSA in phosphate-buffered saline after laser treatment alone or in combination with 10 MIC gentamicin. (q) Time-dependent killing of stationary-phase vancomycin-resistant *S. aureus* (VRSA) strain in phosphate-buffered saline for four different treatment groups. (r) Efficiency of laser treatment alone or in combination with daptomycin on MRSA-caused mice skin infection model. (s) Hematoxylin and eosin stained histology evaluation of phototoxicity on mice skin. The mice used and treatment procedure applied were the same as that of (r) but without MRSA infection on the skin. (t) Viability of human keratinocyte cells over different laser treatment time to evaluate phototoxicity. *N*=5 for CFU enumeration for *in vivo* mice study. Dap, daptomycin; Tob, tobramycin. *N*=3 for the rest CFU enumeration, for checkerboard assay of each antibiotic and for phototoxicity evaluation on both human cells and *in vivo* mice.

To demonstrate the laser treatment-mediated synergism with antibiotics, we first applied the checkerboard assay as a screening method. Interestingly, synergism is identified between laser treatment and several major classes of antibiotics for MRSA growth inhibition (**Figures. 4.5, e-l**). Using tetracycline as an example, the lowest concentration needed to completely inhibit MRSA growth within 18 hours is steadily decreased by elongated laser treatment time; 16 min laser treatment enables a 16-fold reduction, where 2-fold change or larger is regarded as synergy based on fractional inhibitory concentration index (FICI) (**Figures. 4.5, e-f**). The similar results are found for quinolones: ofloxacin and ciprofloxacin (**Figures. 4.5, g-h**) and oxazolidinone: linezolid (**Figures. 4.5, i-j**) with 2-fold, 8-fold reduction respectively. Notably, tetracyclines, oxazolidinones and quinolones all target intracellular activities; therefore, they have to penetrate through the membrane barrier in order to be functional. These growth inhibition results further validate our hypothesis that photo-disassembly of FMM renders membrane permeable to allow passive diffusion of small-molecule antibiotics inside cells, thus increasing their effectiveness against MRSA. Due to the disassembly and detachment of PBP2a proteins on cell membrane, laser treatment further re-sensitizes MRSA to penicillin:

oxacillin with its concentration as low as 1 μg/ml, 8-fold lower than that of oxacillin-treated alone (**Figures. 4.5, k-l**). In contrast, when vancomycin, an antibiotic that inhibits cell wall biosynthesis, was tested, no synergism is shown. For bactericidal antibiotics, time-killing assay was then applied as the screening method. Due to laser-mediated membrane insertion and further disruption, 10-minimum inhibitory concentration (MIC) daptomycin is found capable of eradicating stationary-phase/dormant MRSA cells synergistically with only 5 min laser treatment (e.g. more than 3.5-log reduction after 6 hours), whereas antibiotics alone show very limited killing even at 100 MIC (e.g. 1-log reduction after 6 hours) (**Figures. 4.5, m-n**). The similar synergistic killing is observed for aminoglycoside: tobramycin (**Figures. 4.5, o-p**) due to its passive diffusion via laser-mediated permeable membrane. The synergistic therapy between 10 MIC daptomycin and laser treatment are also effective in eradicating VRSA and multidrug-resistant MRSA clinical isolates (**Figure. 4.5q**). Additionally, the synergy with laser treatment for MRSA killing is not only limited to conventional antibiotics; laser treatment facilitates human whole blood by killing stationary-phase MRSA for 3 $\log_{10}$; ROS-producing agents e.g. hydrogen peroxide (at 220 μM low concentration) synergizes with laser treatment and kills stationary-phase MRSA by 4 log within 2 hours, whereas hydrogen peroxide alone shows minor killing even at 22 mM high concentration. In these cases, besides membrane disruption mechanisms, the depleted antioxidant function of STX contributes to ROS-based killing, consistent with previous findings [185].

To determine the clinical relevance of the synergistic therapy between laser treatment and conventional antibiotics, the last-resort antibiotic, daptomycin, was used as the

example and further applied on *in vivo* mice skin infection models. To compare the efficacy of different treatment schemes, four groups (control group,10 mg/ml daptomycin-treated group, 10 min laser-treated group, and 10 mg/ml daptomycin plus 10 min laser-treated group) were applied following a 4-day treatment protocol. After the treatment regimen, infected tissue for each mouse was collected with bacterial load quantified via colony-forming unit (CFU) enumeration. The CFU statistical results for each treatment group (**Figure. 4.5r**) suggest that laser alone-treated group and daptomycin alone-treated group enable 58% and 81% cell killing, respectively; whereas daptomycin plus laser treatment kills around 95% of MRSA in infected skin area. Additionally, the wound areas treated by laser plus daptomycin appear healthier and show the trend of recovery when compared to other groups, as these wound areas show significantly less purulent material, swelling and redness around the edge of the wound. To further evaluate the potential phototoxicity in *in vivo* model, we followed the same treatment protocol as mice skin infection model except removing the MRSA injection step. After the treatment, the skin regions of interest were collected and analyzed via hematoxylin and eosin stained histology slides (representative images shown in **Figure. 4.5s**). As expected, no phototoxicity induced structure change is observed in the laser-treated group. Additionally, the viability of human epithelial keratinocyte cells is also not affected by laser treatment, even under high laser dosage (**Figure. 4.5t**). Notably, laser dosage applied in these studies is below the ANSI safety limit for human skin exposure at 460 nm[203].

4.3.6 Inhibition of antibiotic resistance development

To study MRSA response to our phototherapy, we monitored STX expression level during 48-day serial passage study for 10 min laser alone-treated group. Over the course of 48-day passage, steadily decreased STX expression is observed for laser alone-treated group, as resonance Raman peaks for STX drops over serial passage (**Figures. 4.6, a-b**); on 30^{th} and 45^{th} day for two independent replicates, STX abundance drops below the detection limit (**Figure. 4.6b**); the color of the spun-down cells for both replicates turn to purely white on 48^{th} day whereas the color of the untreated kept golden (**Figure. 4.6c**). Plate inoculation results further confirm that there is no single colony expressing STX pigment for both replicates after 48-day passage. These results suggest that STX virulence can be eliminated by serial laser treatment without any resistance development. When compared with the original MRSA, the susceptibility of this new phenotype to different antibiotics shows no change or only minor change after serial treatment (**Figure. 4.6d**).

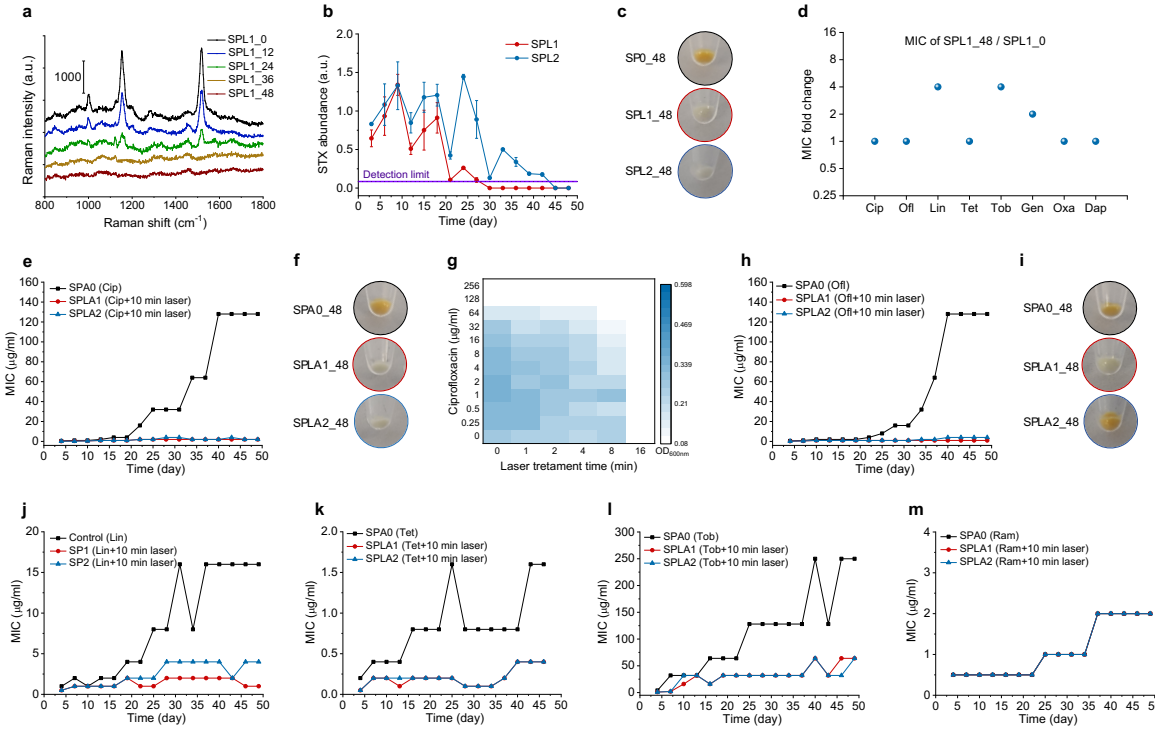

Figure 4.6. Photo-disassembly of membrane microdomains inhibits resistance development to conventional antibiotics. (a) Representative resonance Raman spectroscopy of STX in stationary-phase MRSA cells at different time checkpoints for the group treated with 10 min laser alone over 48-day serial passage. (b) STX abundance in stationary-phase MRSA cells over 48-day serial passage for groups with or without 10 min laser alone quantified via Raman peak amplitude at 1161 cm^{-1}. (c) Images of spun-down cells in (b) after 48-day serially passage showing STX pigmentation. (d) MIC fold change of SPL1 for different classes of antibiotics after 48-day serial passage. (e, h, j, k, l, m) Resistance acquisition over 48-day serial passage in the presence of sub-MIC levels of antibiotics with or without 10 min laser treatment: (e) ciprofloxacin, (h) ofloxacin, (j) linezolid, (k) tetracycline (L) tobramycin, (m) ramoplanin. (f, i) Images of spun-down cells from (e) and (h), respectively, after 48-day serially passage showing STX pigmentation. (g) Checkerboard assay of SPA0_48 showing that 16 min laser treatment completely eliminated cell growth. *N*=3 for checkerboard assay study, Raman spectra, and STX quantification. SPO, serial passage without any treatment; SPL1 and SPL2, serial passage in independent duplicate with laser treatment alone; SPA0, serial passage with sub-MIC antibiotic treatment alone; SPLA1 and SPLA2, serial passage in independent duplicate with 10 min laser plus sub-MIC antibiotic treatment. The numbers after these abbreviations denote serially passage days.

The development of resistance for different antibiotics with or without 10 min laser treatment was studied in parallel by monitoring MICs for each group in the presence of corresponding antibiotic at sub-MIC level over the course of 48-day passage. Strikingly, with the presence of laser treatment, ciprofloxacin-treated group shows no resistance over the entire passage study, as its MIC is kept ≤ 2 μg/ml, whereas the MIC of ciprofloxacin

alone-treated group has reached 128 μg/ml, 256-fold increase relative to its starting MIC (**Figure. 4.6e**). Its spun-down cells turn purely white for both replicates (**Figure. 4.6f**); plate inoculation results show that one replicate has no STX expression and the other with mixture of golden and white colonies, consistent with STX expression level monitored through resonance Raman spectroscopy. These results suggest that STX virulence is closely related to ciprofloxacin resistance development via overexpression of efflux pumps [204]; depletion of STX completely inhibits ciprofloxacin resistance. Therefore, it is highly possible that efflux pump proteins are also co-localized within STX-enriched FMM; STX photolysis malfunctions these efflux pumps while allowing passive diffusion of ciprofloxacin into the cells. Interestingly, using checkerboard assay on the ciprofloxacin-resistant MRSA (MIC: 128 μg/ml), we found that 16 min laser treatment alone completely inhibits the growth of these cells (**Figure. 4.6g**). This phenomenon suggests that the survival of ciprofloxacin-resistant MRSA relies heavily on STX expression to promote efflux pumps. To further explore this class of antibiotics, ofloxacin was investigated in the serial passage study. Similar results are achieved as shown in **Figures. 4.6, h-i**. After a 48-day serial passage, MIC of ofloxacin alone-treated group reaches 128 μg/ml, whereas ofloxacin plus laser-treated replicates have MICs of 1 and 4 μg/ml, respectively. Based on plate inoculation results, one replicate has pure white colonies and the other had a mixture of white and golden colonies. These results suggest STX photolysis not only increases the susceptibility of MRSA to fluoroquinolones, but also inhibits its resistance development. Subsequently, laser treatment-mediated resistance inhibition is also found for other antibiotic classes previous found to synergize with STX photolysis, including linezolid,

tetracycline, and tobramycin (**Figures. 4.6, j-l**). Delayed resistance development is shown for oxacillin and gentamicin during early serial passages. In contrast, decreased resistance development is not shown for ramoplanin, a drug that targets cell wall biosynthesis (**Figure. 4.6m**), as it is not closely related to the membrane disruption mechanisms. Collectively these results further unveil the causality between STX virulence and antibiotic resistance, as well as demonstrating a way to inhibit resistance development to several major classes of antibiotics via photo-disassembly of FMM.

4.4 Discussion and Conclusion

Current antimicrobial development pipeline has failed to meet the growing needs of new and effective antibiotics to fight bacterial infections [180]. Here, we demonstrate an unconventional phototherapy approach to combat MRSA antibiotic resistance by targeting its STX virulence factor. This approach fundamentally relies on the interaction between photons and its endogenous chromophores. Although antimicrobial effect of blue light has been documented for decades [205-207], the underlying mechanism is still a mystery and its treatment efficacy is limited, hampering its clinical applications. Here, we show that STX is the molecular target of photons and subject to photolysis in the entire blue range. This finding directly challenges the traditionally well accepted hypothesis of blue light-sensitive endogenous porphyrins, meanwhile, profoundly opens new opportunities in this field. The detailed study of STX photochemistry and its photolysis kinetics further suggest a short-pulsed laser to nonlinearly accelerate STX photolysis efficiency, speed, and depth, that are beyond the reach of low-level light sources.

We further show that STX photolysis disorganizes and malfunctions membrane for antibiotic defense in three distinct aspects. First, the disruption renders membrane permeable to antibiotic that target intracellular activities e.g. fluoroquinolones and aminoglycosides. Second, membrane becomes more fluid that facilitates the membrane insertion of membrane targeting antibiotic, e.g. daptomycin. Third, proteins, e.g. PBP2a, that anchors within in the FMM is detached and malfunctioned to defense penicillins. These membrane damage mechanisms demonstrate a novel approach to revive a broad spectrum of conventional antibiotic to combat MRSA. Noteworthy, this approach is fundamentally different from photodynamic therapy [208], as it relies on endogenous STX to disrupt cell membrane, thus specifically targeting *S. aureus*, instead of using externally administrated photosensitizer-induced ROS for unselective bacterial eradication.

STX-targeted phototherapy has shown promising potential as a novel treatment platform. Future studies can examine synergies with other classes of antibiotics, as well as the host innate immune system, and/or other reactive oxygen species. For example, disassembly of FMM could be further extended to revive chloramphenicol, as its resistance primarily due to the overexpression of *norA*-encoded multidrug-resistance efflux pumps within the microdomains [209]. As STX has the antioxidant function to shield MRSA from attacks by ROS, effective STX photolysis could further render MRSA susceptible to oxidative host killing including macrophage cells and neutrophils [196]. Similar to daptomycin, the modulation on cell membrane fluidity via laser treatment can facilitate non-oxidative host defense of cationic antimicrobial peptides [198]. Moreover, this platform can be further exploited to screen lead compounds, particularly for those with intracellular

targets.

Targeting MRSA STX virulence by photons exemplifies the approach that utilizes the photochemistry between photons and endogenous chromophores to develop a phototherapy platform for bacterial infections. Carotenoids that has structural and functional similarity broadly present in many other bacterial and fungal species [200], thus can be photochemically decomposed or modulated in a similar manner. Notably, pigmentation is a hallmark for many pathogenic microbes; these pigments similarly promote microbial virulence and exhibits pro-inflammatory or cytotoxic properties [173]. Therefore, these pigments could be the targets of photons via either photochemistry or photothermal approach. Several bacterial enzymes that regulate their virulence are also found sensitive to photons [210]. Therefore, phototherapy approaches based on these specific photon-chromophore interactions could be further explored along this direction.

CHAPTER 5 PHOTOINACTIVATION OF CATALASE REVIVES ANTIMICROBIAL AGENTS AGAINST BROAD-SPECTRUM BACTERIA

This work is currently at the stage of manuscript under preparation (Pu-Ting Dong et al., 2019). Pu-Ting and Yifan made the accidental discovery that bacterial catalase could be photoinactivated. Pu-Ting conducted all the experiments. Jie contributed to the biofilm experiment. Sebastian and Pu-Ting conducted the in vitro evaluation of photoinactivation of catalase combined with H_2O_2 and antibiotics.

Antibiotic resistance kills an estimated 700,000 people each year worldwide, and study predicts that this number could rise to 10 million by 2050 if efforts are not made to curtail resistance[211]. Yet, the pace of resistance acquisition from mutation in pathogens is faster than clinical introduction of new antibiotics. This severe situation calls for an urgent need of developing unconventional ways to combat the resistance. It was known that a lethal effect of antibiotics is through the generation of ROS inside the cells. Catalase, the ubiquitous key defense enzyme existing in most of the aerobic pathogens, is utilized to scavenge hydrogen peroxide, thus preventing downstream oxidative damage. Accidentally, we found that catalase, can be photoinactivated by blue light region, especially around 410 nm light. Photoinactivation of catalase significantly renders broad-spectrum pathogens highly susceptible to ROS-generating antibiotics or immune cells attack. Our discovery and developed therapeutics provide a new avenue for treating infection caused by drug-resistant pathogens.

5.1 Introduction

The rapidly increasing emergence of anti-microbial resistance is leading to the end of a period termed “the antibiotic era”. Bacteria replicate very rapidly and a mutation that helps a microprobe survive in the presence of an anti-microbial drug will become

predominant throughout the microbial population. What is more, the pace of resistance acquisition from mutation in pathogens is faster than clinical introduction of new antibiotics or anti-fungal drugs. The current proposal aims to deal with this severe situation by developing a novel biophotonics strategy that effectively sensitizes resistant pathogens to conventional anti-microbial agents.

Besides STX, we have been searching for a molecule target applicable to various pathogens. We notice that hydrogen peroxide (H_2O_2) is continuously produced inside bacteria from autoxidation of redox enzyme, and it diffuses quickly into the intracellular environment, causing acutely detrimental effect to bacteria (e.g. lipid peroxidation, DNA and protein damage)[212] because of the Fenton reaction:

$$Fe^{2+} + H_2O_2 \rightarrow Fe^{3+} + .OH + OH^-$$

$$Fe^{3+} + H_2O_2 \rightarrow Fe^{2+} + .OOH + H^+$$

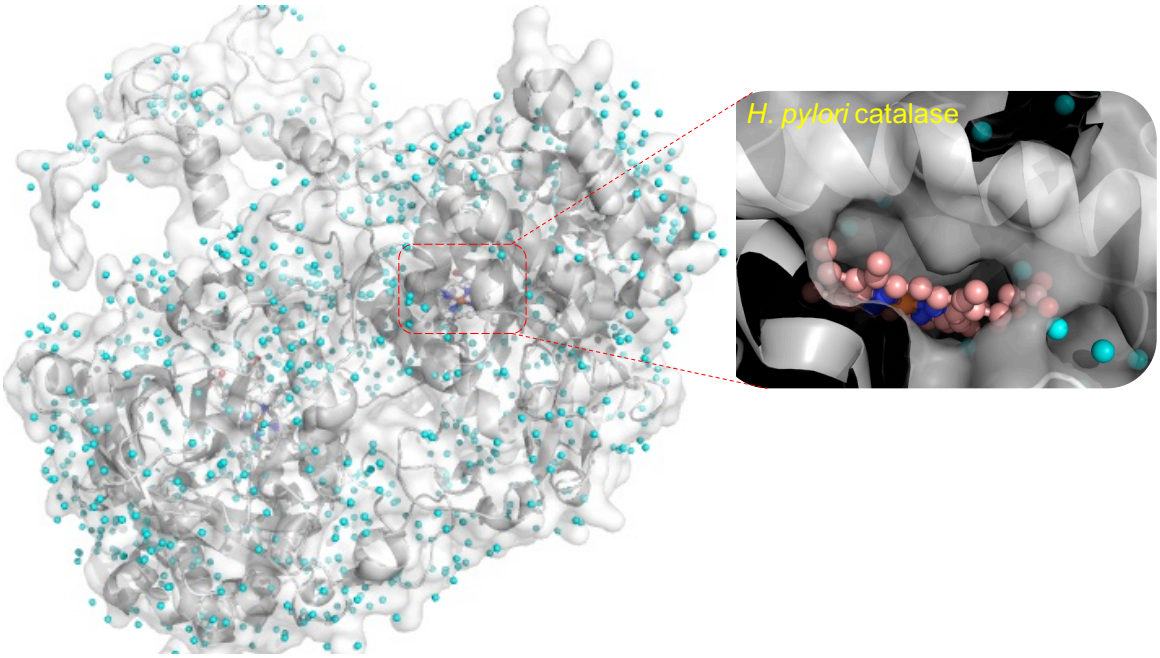

Figure 5.1 Protein structure of *Helicobacter pylori* (*H. pylori*) catalase and its zoomed-in visualization of active cite through PyMOL simulation. The structure of *H. pylori* catalase is from protein data bank (1QWL). Cyan ball: water molecule; blue ball: oxygen atom; pink ball: carbon atom.

Bacteria have evolved to develop scavenging enzymes to degrade intracellular H_2O_2 to maintain an intracellular nanomolar concentration. Heme-containing catalase (**Figure 5.1**) is one of the most important key defense enzymes which selectively scavenge H_2O_2. Most bacteria use catalase to convert excess H_2O_2 into water and O_2 to maintain the H_2O_2 concentration to be below 20 nM [212]. Accidentally, we found that catalase could be efficiently inactivated by the blue light region, especially around 410 nm. This phenomenon was observed from bacterial catalase as well. Subsequently, we almost achieved total eradication of broad-spectrum catalase-positive pathogens by synergizing photoinactivation of catalase and low-concentration H_2O_2. On the contrary, we didn't obverse the enhanced killing effect of H_2O_2 for the catalase-negative *Enterococcus* strains.

For a big class of anti-bacterial and anti-fungal drugs, a lethal effect is through the generation of ROS inside cells [213-217]. The intracellular H_2O_2 and superoxide concentration after treatment of ampicillin or norfloxacin increased [218]. At this stage, catalase plays an important role in getting rid of intracellular H_2O_2, maintaining cellular homeostasis. Thus, photoinactivation of catalase exacerbates the antimicrobial effects of those ROS-generating antibiotics. And we indeed observed this enhancement from planktonic stationary-phase bacteria.

We also demonstrated that photoinactivation of catalase assists our immune cells to eliminate the intracellular pathogens. Neutrophils are highly motile phagocytic cells that serve as the first line of defense of the innate immune system [219]. These cells play an essential role in providing resistance to bacterial and fungal infections through releasing ROS burst (e.g., superoxide, hydroxyl radicals, and singlet oxygen[220]). However,

pathogens elaborate array of strategies to invade and survive inside neutrophils or macrophages, thus acting as the 'Trojan horses' responsible for further dissemination and recurrent infections[131]. Catalase, which is encoded by gene, katA, confers indispensable resistance to the antimicrobial agents released by immune cells[221]. We indeed found that photoinactivation of catalase assists macrophage cells to reduce the intracellular bacterial burden. In summary, our findings provide a novel approach for reviving conventional antimicrobial agents in the battle against drug-resistant pathogens.

5.2 Methods

5.2.1 Bacterial strains

Enterococcus faecalis NR-31970, *Enterococcus faecalis* HM-325, *Escherichia coli* BW 25113, *Escherichia coli* ATCC 25922. *Klebsiella pneumoniae* ATCC BAA 1706. *Klebsiella pneumoniae* ATCC BAA 1705. *Salmonella enterica* ATCC 70720. *Salmonella enterica* ATCC 13076. *Acinetobacter baumannii* ATCC BAA 1605. *Acinetobacter baumannii* ATCC BAA-747. *Pseudomonas aeruginosa* ATCC 47085 (PAO-1). *Pseudomonas aeruginosa* 1133. *Pseudomonas aeruginosa* ATCC 15442. *Pseudomonas aeruginosa* ATCC 9027.

5.2.2 Quantitation of catalase by Amplex red catalase kit

Quantification of catalase both from the pure catalase solution and bacteria was achieved by a fluorescent amplex red catalase kit. Basically, 25 µl of analyte were incubated with 25 µl (40 µM of H_2O_2) for 30 min at room temperature. Then 50 µl of working solution (100 µM Amplex Red reagent containing 0.4 U/ml horseradish

peroxidase) were added to the abovementioned mixture, and the subsequent mixture were incubated for another 30-60 min in the dark. After that, the fluorescence was recorded at an emission of 590 nm when excited at 560 nm.

5.2.3 Resonance Raman spectrum of dried catalase film

Catalase was measured by its Raman peaks at around 1300-1700 cm^{-1} measured by resonance Raman spectroscopy (1221, LABRAM HR EVO, Horiba) with a 40×objective (Olympus) and an excitation wavelength of 532 nm. Samples (dried 'coffee ring' were sandwiched between two glass cover slides (48393-230, VWR international) with a spatial distance of ~80 μm. To study the photoinactivation (by a continuous-wave LED) study, the same samples were measured after each laser irradiation.

5.2.4 CFU experiments to test the potential synergy between photoinactivation of catalase and H_2O_2

Overnight-cultured bacteria was centrifuged, and then discarded the supernatant, suspended with the same amount of PBS. For each bacterial strain, we will have four groups: untreated one, ns-410 nm-treated group, H_2O_2 (22 or 44 mM)-treated group, ns-410 nm plus H_2O_2 (22 or 44 mM)-treated group. Dose for ns-410 nm exposure was 15 J/cm^2. H_2O_2 was incubated with bacteria for 30 min at 37°C with the shaking speed of 200 rpm. After incubation, bacterial burden from each group was serial diluted, inoculated onto TSA plates, then counted by enumeration of these plates.

5.2.4 CFU experiments to test the potential synergy between photoinactivation of catalase and ROS-generating antibiotics

Overnight-cultured bacteria was centrifuged, and then discarded the supernatant, suspended with the same amount of fresh TSB. Then prior to any treatments, the above solution was incubated with antibiotics (10 μg/ml) for 1 hour. For each bacterial strain, we will have four groups: untreated one, ns-410 nm-treated group, antibiotic (2 μg/ml)-treated group, ns-410 nm plus antibiotic (2 μg/ml)-treated group. Dose for ns-410 nm exposure was 15 J/cm^2. Antibiotic was incubated with bacteria for up to 6 hours at 37°C with the shaking speed of 200 rpm. At each time interval, bacterial burden from each group was serial diluted, inoculated onto TSA plates, then counted by enumeration of these plates.

5.2.5 Confocal imaging of intracellular bacteria assay

As described elsewhere[222], murine macrophage cells (RAW 264.7) were cultured in DMEM supplemented with 10% FBS at 37 °C with CO_2 (5%). Cells were exposed to MRSA USA300 or *Salmonella enterica* (with/without ns-410 nm exposure) at a multiplicity of infection (MOI) of approximately 100:1 at serum-free DMEM medium. 1 or 2-hour post-infection, RAW 264.7 cells were washed with gentamicin (50 μg/mL, for one hour) to kill extracellular bacteria in DMEM + 10% FBS. After that, RAW 264.7 cells were washed with gentamicin (50 μg/mL) and subsequently lysed using 0.1% Triton-X 100 for 3 min. After membrane permeabilization, infected RAW 264.7 cells were stained with Live/Dead stain for 15 min, then samples were fixed in 10% formalin for 10 min prior confocal imaging.

5.3 Results

5.3.1 Pulsed blue light effectively inactivates pure catalase and catalase from bacteria

Pure catalase solution (bovine liver catalase, 3 mg/ml in the PBS) were prepared in PBS, then we adopted the protocol published elsewhere[223] to examine the effect of 410-nm exposure on the absorption spectrum of catalase solution. Catalase shows a pronounced absorption at around 410 nm, and its absorption at this wavelength gradually decreases as the 410-nm exposure elongates (**Figure 5.2a**). This suggests that the secondary structure of catalase might be changed, especially in the active heme-containing domain. Besides this, we also investigated this photoinactivation effect by an Amplex Red Catalase kit at different wavelengths (**Figure 5.2b**). It turned out that the photoinactivation trend is similar to the absorption spectrum of catalase, with the 410 nm being the most effective, where 5-min explore depleted ~70% active catalase.

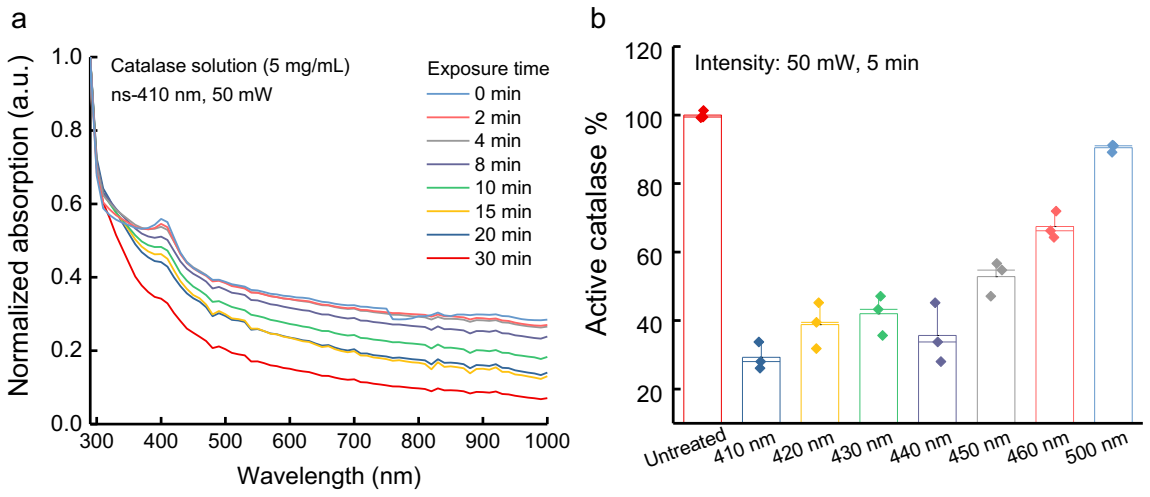

Figure 5.2. Effect of ns-410 nm exposure on pure catalase solution. (a). Absorption spectra of pure catalase solution under ns-410 nm exposure. Catalase solution: 3 mg/ml, filtered with a 0.2 μm filter. (b). Percent of remaining active catalase after different treatment schemes (different wavelengths under the same dosage). Quantification of catalase was obtained by an Amplex Red Catalase kit. Data: Mean±standard deviation (*N*=3).

Since most of the aerobic bacteria and facultative anaerobes express catalase[212], we asked whether one could photoinactivate catalase in situ from the catalase-positive bacteria. We chose *MRSA USA300* and *P. aeruginosa* (PAO-1) as the representative for Gram-positive and Gram-negative bacteria, respectively. Noteworthy, catalase from both *MRSA USA300* (**Figure 5.3a**) and *P. aeruginosa* (**Figure 5.3b**) were photoinactivated by blue light exposure region, especially 410-nm exposure. It was also worthy notifying that the dose we utilized were around 15 J/cm2, well below the ANSI safety limit, and the specimens were stationary-phase cultured bacteria (~10^8 cells/ml).

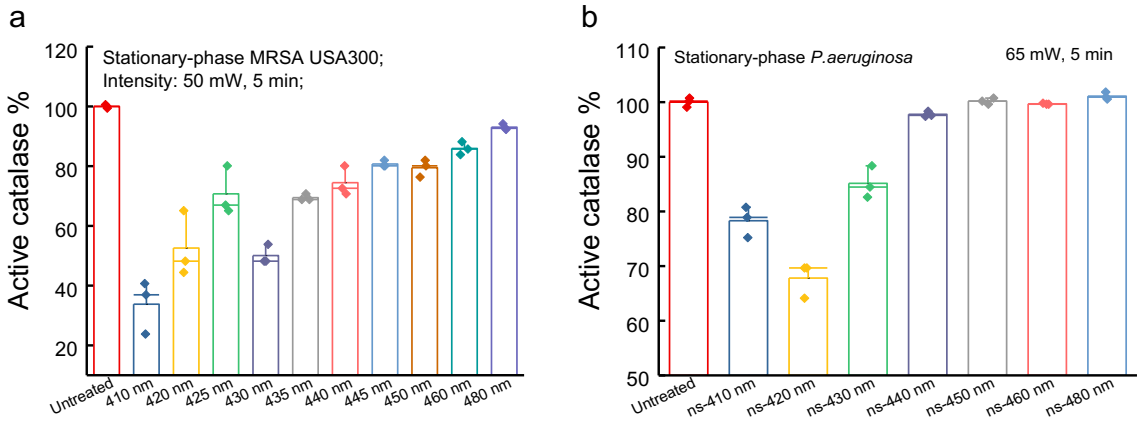

Figure 5.3. Effect of ns-410 nm exposure on active catalase percents from MRSA USA300 and *P. aeruginosa*. (a-b). Percent of active catalase remained inside MRSA USA300 (a) and *P. aeruginosa* (b) after different treatment schemes (different wavelengths under the same dosage). Quantification of catalase was obtained by an Amplex Red Catalase kit. Data: Mean±standard deviation (*N*=3).

To further understand how 410 nm exposure could cause the structural change of catalase, we also performed Resonant Raman spectroscopy to capture the Raman signature of dried catalase film. Apparently, 410 nm exposure significantly drops the Raman intensity at 750 cm^{-1}, and the Raman bands ranging from 1300 cm^{-1} to 1700 cm^{-1}, which are typical vibrational bands of heme ring from catalase[224]. This further consolidates the

fact that 410 nm exposure could cause structural change of catalase.

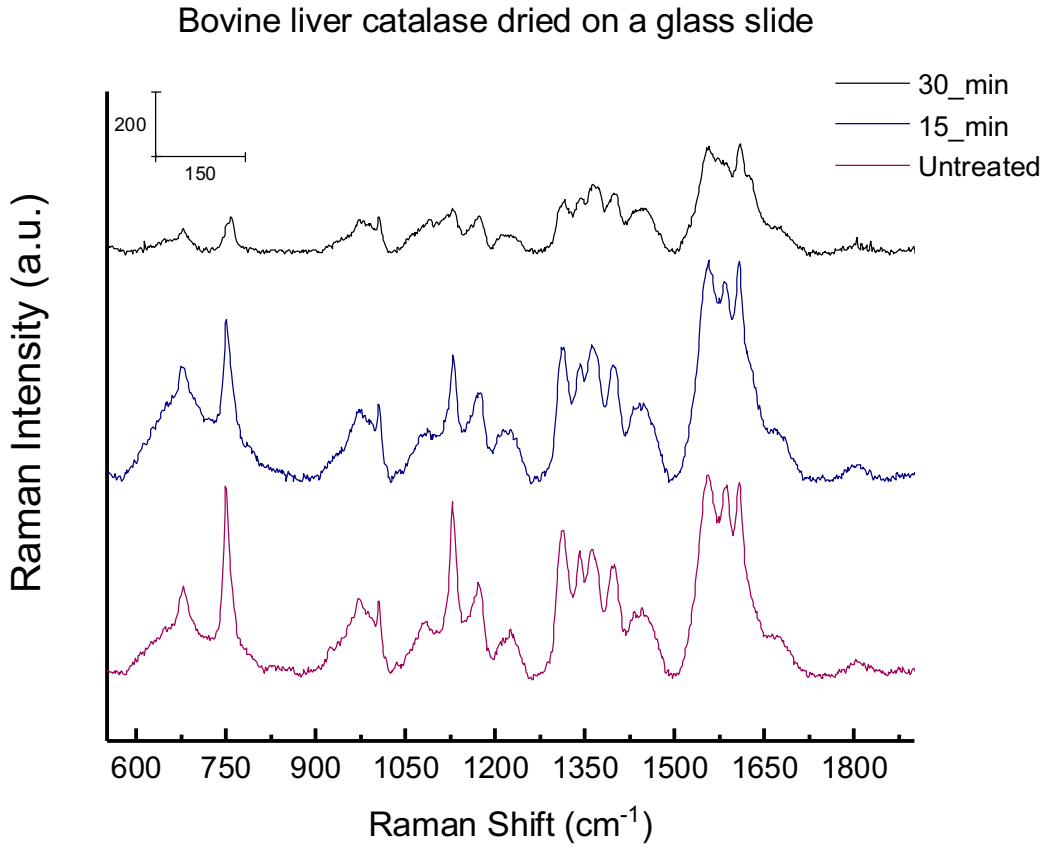

Figure 5.4. Resonant Raman spectra of bovine liver catalase powder with and without 410 nm exposure. 410 nm intensity: 250 mW/cm2. Raman spectrum acquisition time: 25 s. 532 nm excitation. Data: Mean±SD from five spectra.

In addition, we compared the efficacy between ns-410 nm and CW-410 nm on the capability to inactivate catalase. It turned out that It turned out that ns-410 nm is significantly more effective both in the pure solution form (**Figure 5.5a**), or from MRSA USA300 (**Figure 5.5b**) and *P. aeruginosa* (**Figure 5.5c**) compared to CW-410 nm. Moreover, ns-410 exposure eliminates the necessity of heating issue during future clinical study. Thus, for the future photoinactivation of catalase against bacteria study, we plan to utilize ns-410 nm.

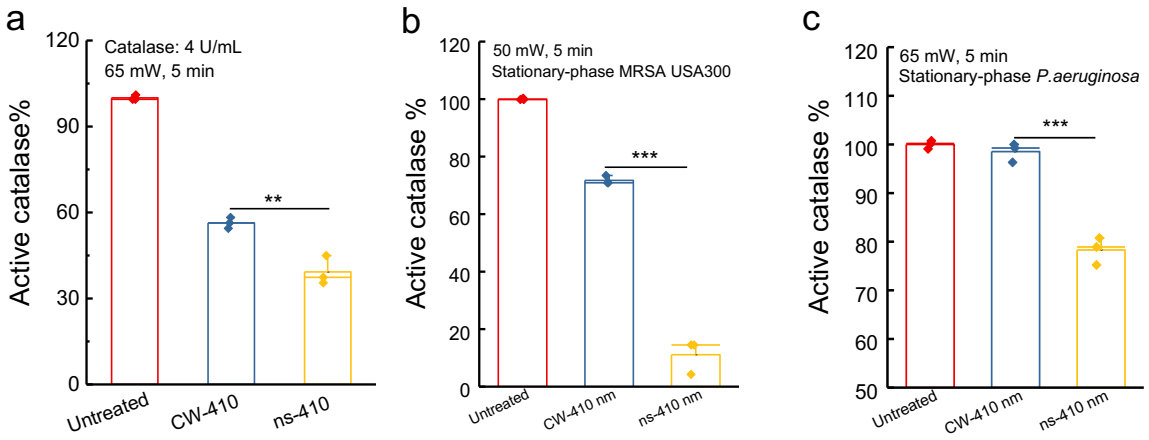

Figure 5.5. Comparison between ns-410 nm and CW-410 nm exposure on the catalase photoinactivation effect from pure catalase solution (a), catalase from MRSA USA300 (b), and catalase from *P. aeruginosa* (c). Quantification of catalase was obtained by an Amplex Red Catalase kit. Data: Mean±standard deviation (*N*=3). Student unpaired *t*-test, ***: $p<0.001$; **: $p < 0.01$.

5.3.2 Photo-inactivation of catalase sensitizes broad-spectrum bacteria to low-concentration H_2O_2

Catalase is an essential detoxifying enzyme in bacteria encountering various endogenous or exogenous stress[225]. Specially, when the gene encoding the expression of catalase is mutant, pathogens were more susceptible to the environmental stress[226]. We asked whether exogenous addition of low-concentration H_2O_2 could eliminate those 'traumatized' pathogens. As shown in **Figure 5.6**, photoinactivation of catalase (15 J/cm^2) alone didn't reduce the MRSA burden (**Figure 5.6a**), *P. aeruginosa* (**Figure 5.6b**) burden, and *Salmonella enterica* (**Figure 5.6c**) significantly. Moreover, low-concentration H_2O_2 (22 mM) didn't exert any significant antimicrobial effect against both MRSA and *P. aeruginosa* (**Figure 5.6**). However, subsequent administration of low-concentration H_2O_2 after photoinactivation of catalase significantly reduce the MRSA and *P. aeruginosa* burden ($\geq$ 3-$\log_{10}$ reduction, **Figure 5.6**). Interestingly, the bacterial killing trend versus irradiance wavelength is similar as that of photoinactivation of catalase versus exposure

wavelength. Noteworthy, low-concentration H_2O_2 combined with 410 nm exposure (15 J/cm^2) achieved total eradication of *P. aeruginosa* (**Figure 5.6b**).

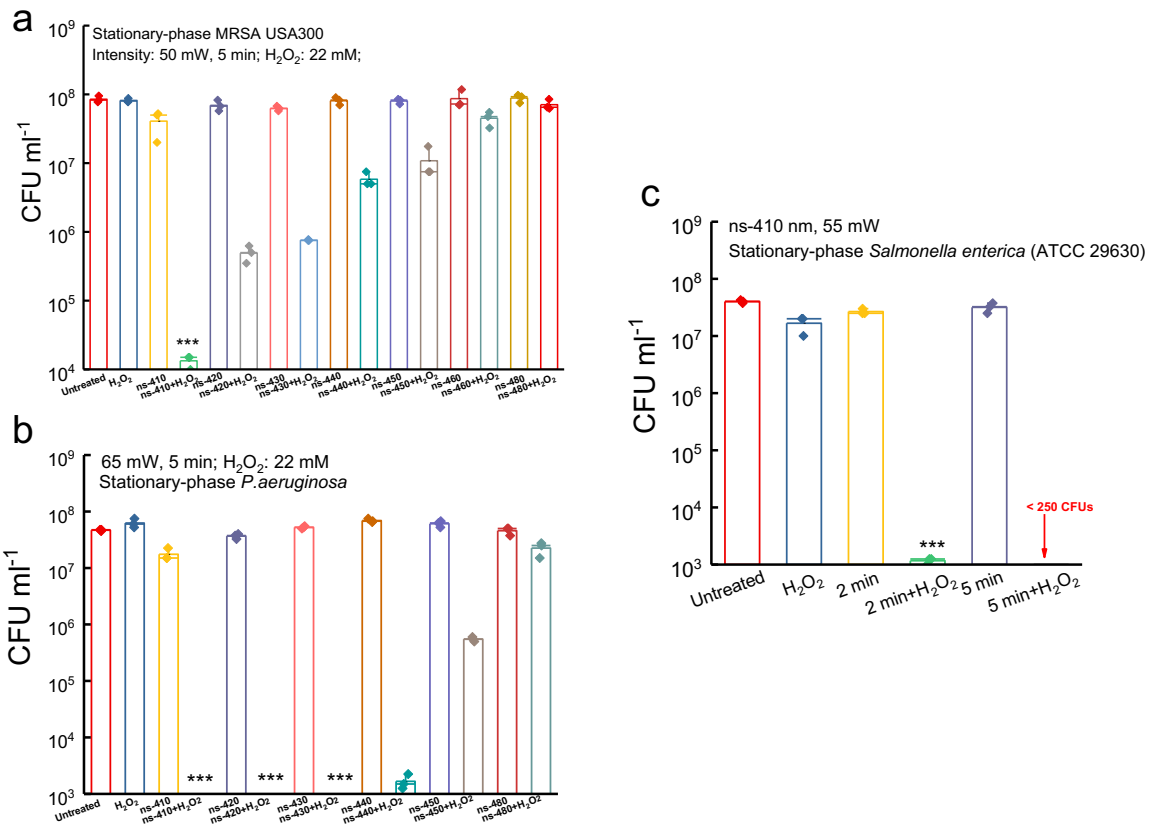

Figure 5.6. CFU ml^{-1} of stationary-phase MRSA USA300 (a), *P. aeruginosa* (b), and *Salmonella enterica* (c) under the treatment of 22 mM H_2O_2 with/without the combination with various light exposure. Data: Mean±standard deviation (*N*=3). Student unpaired *t*-test, ***: $p<0.001$; **: $p < 0.01$. 250 CFUs: limit of detection.

5.3.3 Photoinactivation of catalase revives conventional antibiotics against broad-spectrum bacteria

Besides H_2O_2, we also tried whether photoinactivation of catalase could synergize with conventional antibiotics, especially these who could generate the downstream intracellular ROS. Take tobramycin, a representative of aminoglycoside, as an example. We learned that tobramycin could induce downstream ROS burst[214], thus we tried to combine photoinactivation of catalase and tobramycin together to see whether we could observe an

enhanced effect.

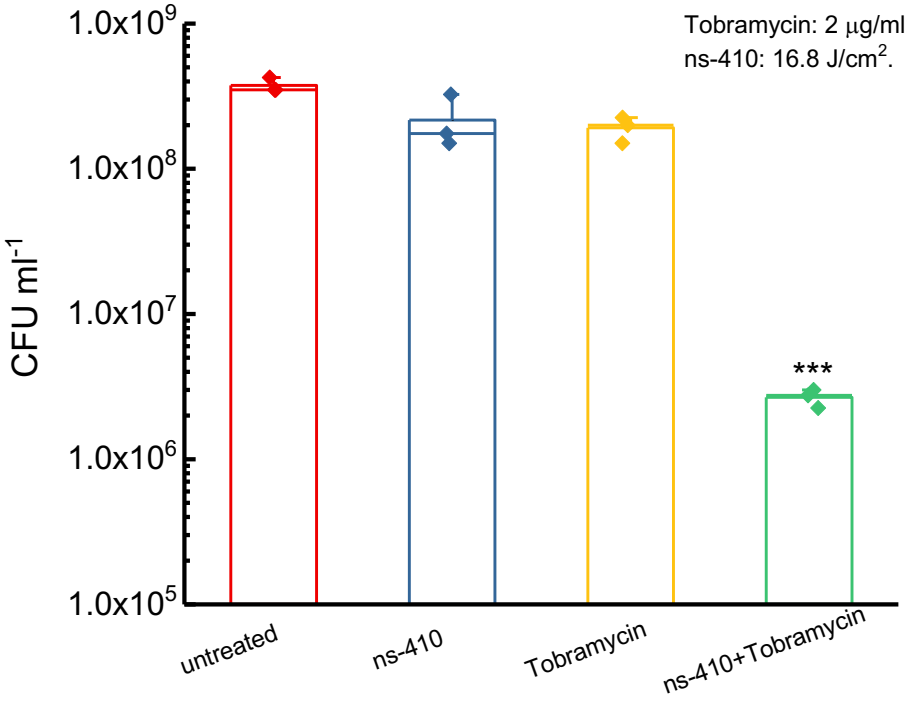

Figure 5.7. CFU ml^{-1} of *E. coli* BW25113 under different treatment schemes. Tobramycin: 2 μg/ml, 4-hour incubation. ***: p<0.001, student unpaired t-test.

Interestingly, we indeed observed enhanced killing effect in the combination-treated group (**Figure 5.7**). More than 100 times enhancement suggests that photoinactivation of catalase indeed accelerates the antimicrobial effect of ROS-generating antibiotics. As a control, we tested the same treatment schemes on a catalase-negative *Enterococcus* strain, *Enterococcus faecalis* NR-31970, we didn't observe any enhanced killing effect at all (**Figure 5.8**). Altogether, this indicates that photoinactivation of catalase helps to revive traditional antibiotics against catalase-positive pathogens.

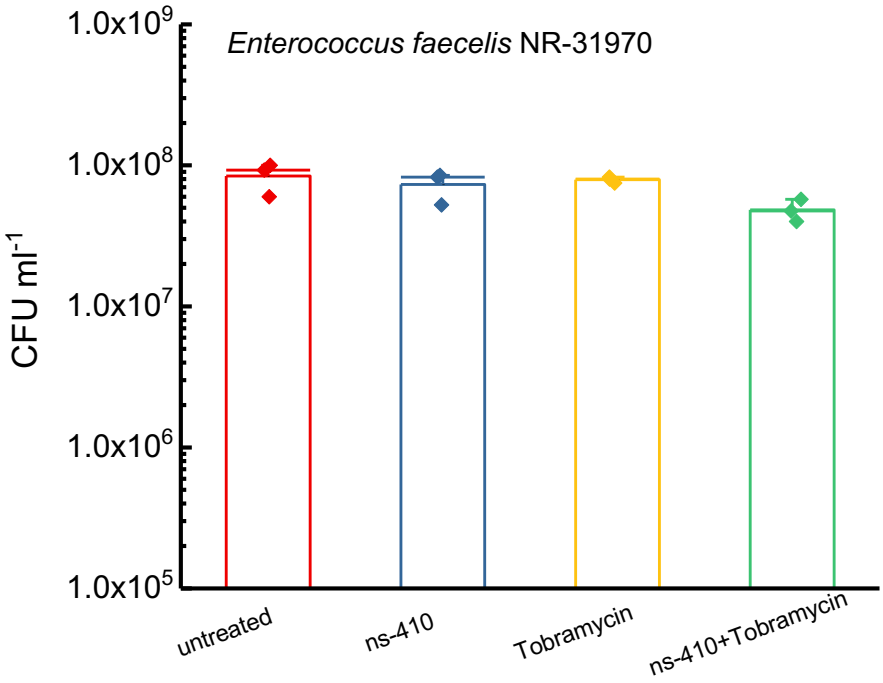

Figure 5.8 CFU ml^{-1} of *Enterococcus faecalis NR-31970* under different treatment schemes. Tobramycin: 2 µg/ml, 4-hour incubation.

5.3.4 Photoinactivation of catalase assists macrophage cells against intracellular pathogens

Neutrophils and macrophage cells are highly essential phagocytic cells that serve as the first line of defense of the innate immune system[219]. These cells play an important role in providing resistance to bacterial and fungal infections through the release of the ROS burst (e.g., superoxide, hydroxyl radicals, and singlet oxygen[220]). However, pathogens have developed array of strategies to invade and survive inside neutrophils or macrophages, thus acting as the 'Trojan horses' responsible for further dissemination and recurrent infections[131]. Catalase, which is encoded by gene, *katA*, confers indispensable resistance to the antimicrobial agents released by immune cells[221]. Based on these facts, we made the hypothesis that photoinactivation of catalase could assist immune cells against intracellular

pathogens. To test the potential assistance effect, we utilized a fluorescent Live/Dead assay to visualize the intracellular live/dead bacteria after ns-410 nm exposure. It turned out We indeed observed a higher percent of dead MRSA intracellularly (**Figure 5.9**).

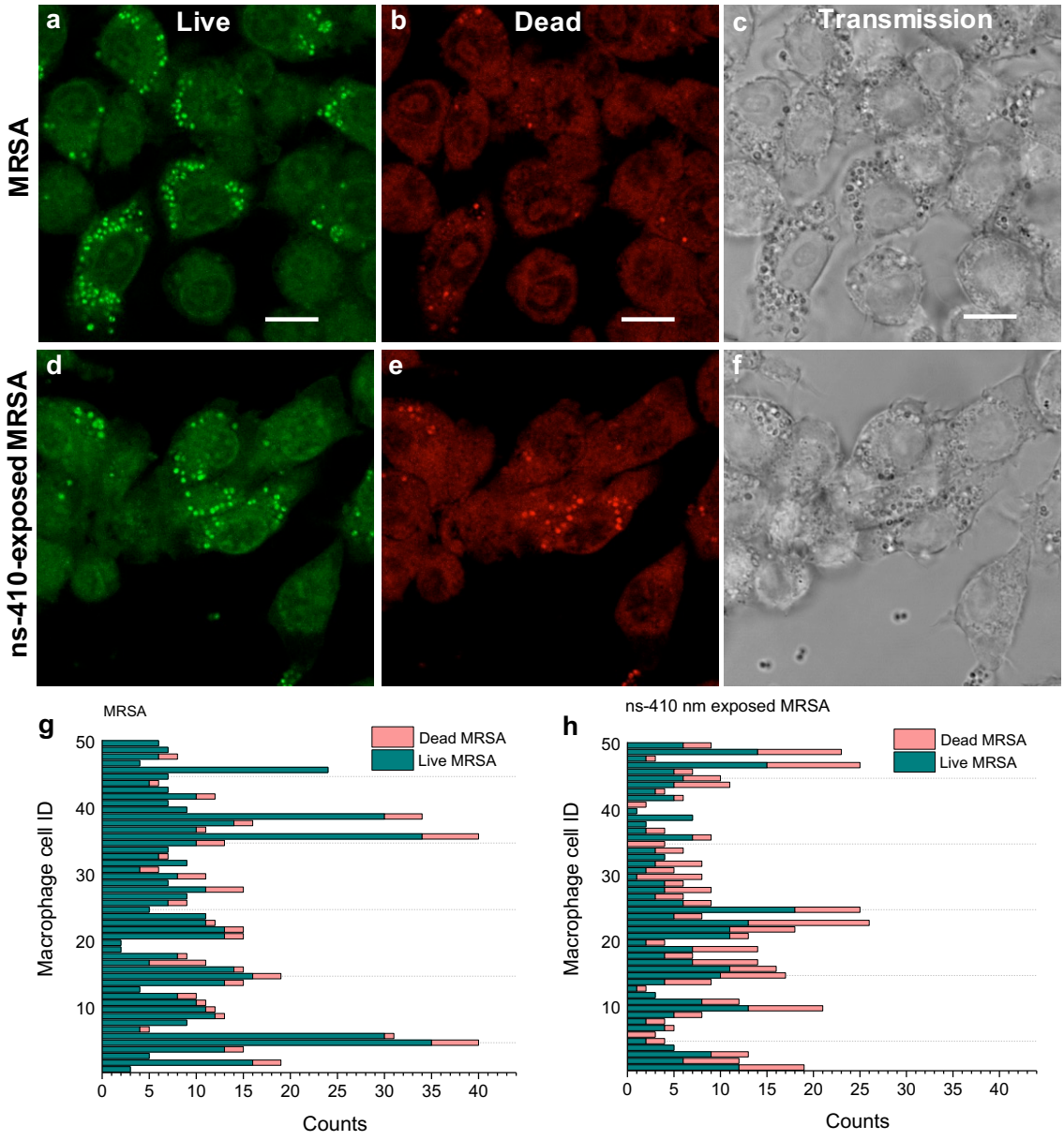

Figure 5.9. Confocal laser scanning microscopy of intracellular MRSA. (a-c). Fluorescence images of intracellular live MRSA (a), and dead MRSA (b), along with the transmission images (c) after MRSA infecting RAW 264.7 macrophage cells for 1 hour. (d-f). Fluorescence images of intracellular live MRSA (d), and dead MRSA (e), along with the transmission images (f) after ns-410 exposed MRSA infecting RAW 264.7 macrophage cells for 1 hour. (g-h). Quantitative analysis of live/dead MRSA from the above two groups. Scalar bar=10 μm.

5.4 Future work and Conclusion

Catalase is an essential detoxifying enzyme in bacteria encountering various endogenous or exogenous stress[225]. Specially, when the gene encoding the expression of catalase is mutant, pathogens were more susceptible to the environmental stress[226]. Accidentally, we found photoinactivation of catalase significantly boosts low-concentration H_2O_2, ROS-generating antibiotics, and immune cells against broad-spectrum bacteria, including the notorious drug-resistant gram-negative bacteria. Further work is needed to evaluate the above synergistic therapy in bacterial biofilm model, bacterial mice infection model. In a summary, our discovery reported here present an effective and novel approach to eliminate broad-spectrum bacteria.

CHAPTER 6 PHOTOINACTIVATION OF CATALASE REVIVES ANTIFUNGAL AGENTS AGAINST BROAD SPECTRUM PATHOGENIC FUNGI

This work is at the stage of manuscript under preparation (Pu-Ting Dong et al, 2019). Pu-Ting, Yuewei, Zeina, and Jie did the in vitro evaluation of antifungal effect between photoinactivation of catalase and H_2O_2, antifungal drugs.

Since most of the pathogenic fungi have catalase as well, especially for the recently emerging *Candida auris* (*C. auris*) strains. It was also known that pathogenic fungus usually colonizes on the skin surface first before they evade into deep tissue infections. Moreover, it was known that *C. auris* strains are usually resilient to H_2O_2 vapor. In this chapter, we demonstrated that catalase from various fungal strains could also be inactivated by 410 nm photons, subsequently sensitizing these pathogens to low-concentration H_2O_2, low-concentration antifungal agents, and also immune cells attack. Together, our findings reported here offer an alternative and novel approach to combat fungal infections.

6.1 Introduction

More than 1.5 million people suffer from serious fungal diseases, and nearly a billion people are estimated to have skin, nail and hair fungal infections [227]. Emerging antifungal resistance has been identified in species like multi-drug resistant pathogen *Candida auris* (*C. auris*) [228], most of which are resistant to azole and one-third of which are even resistant to the last-resort antifungal drug, amphotericin B[229]. Thus, alternative treatments are critically needed to treat these resistant strains. It is known that 90% of fungi species have several heme-containing catalases that dismutase H_2O_2 into water and dioxygen[230].

We have shown that photoinactivation of catalase could effectively achieve sufficient eradication of broad-spectrum bacteria in combination with ROS-generating antimicrobial agents. Here in this chapter we indeed found that catalase level from various fungal strains significantly reduced upon blue light irradiation. We further found that there was a significant increase of H_2O_2 inside the photon-treated fungal cells. Consequently, photoinactivation of catalase dramatically sensitized fungi (in more than 20 species) to low-concentration H_2O_2. These preliminary data led to our working hypothesis that integrating photoinactivation of catalase with ROS producing agents is able to kill a wide range of aerobic fungal species by amplifying the ROS oxidative damage.

Since many antifungal drugs kill fungal cells largely due to the downstream oxidative damage[213,215], we also tested the potential enhancement effect between photoinactivation of catalase and amphotericin B (amp B) or other antifungals. We indeed found the potentiation of ROS-producing anti-fungal drugs (fluconazole and amp B) in catalase inactivated fungal cells. Photoinactivation of catalase was found to inhibit the formation of hyphae when macrophage cells phagocytosing *Candida albicans* (*C. albicans*). Altogether, our findings reported here provide a novel approach to combat fungal especially *C. auris* infections in clinic.

6.2 Methods

6.2.1 Chemicals and fungal strains

DMSO (W387520, Sigma Aldrich), amphotericin B (A9528-100 MG, Sigma Aldrich), ergosterol (AC1178100050, 98%, ACROS Organics). YPD broth (Y1375, Sigma Aldrich). YPD agar (Y1500, Sigma Aldrich). PrestoBlue cell viability assay (A13262, Thermo

Fisher Scientific). *Candida albicans* SC5314, the test of fungal strains used see **table 1**.

6.2.2 Quantification of catalase from fungus before and after 410 nm exposure

Quantification of catalase both from the pure catalase solution and fungal solution were achieved by a fluorescent amplex red catalase kit. Basically, 25 μl of analyte were incubated with 25 μl (40 μM of H_2O_2) for 30 min at room temperature. Then 50 μl of working solution (100 μM Amplex Red reagent containing 0.4 U/ml horseradish peroxidase) were added to the abovementioned mixture, and the subsequent mixture were incubated for another 30-60 min in the dark. After that, the fluorescence was recorded at an emission of 590 nm when excited at 560 nm.

6.2.3 CFU test to quantify the treatment efficacy

Quantification of antifungal treatment schemes were achieved as following: overnight cultured fungal specimen was washed by sterile PBS. And log-phase fungal pathogens were prepared by dilution into fresh YPD broth at a ratio of 1:50, and cultured for another 2-3 hours at 30 °C with the shaking speed of 200 rpm. After that, the fungal concentration was adjusted to be around 1×10^8 cells/ml by centrifuging or further dilution with PBS. 10 μl of the above fungal solution was exposed to 410 nm for 5 min (150 mW/cm^2). After that, the exposed sample was collected into 990 μl of sterile PBS, then supplemented with treatment agents. Later, CFU of fungi cells was enumerated by serial dilution and cultured in YPD agar plates for 48 hours.

6.2.4 PrestoBlue viability assay

First log-phase fungal pathogens were prepared by diluting overnight-cultured fungal

pathogens into fresh YPD broth at a ratio of 1:50, and cultured for another 2-3 hours at 30 °C with the shaking speed of 200 rpm. After that, the fungal concentration was adjusted to be around 1×10^8 cells/ml by centrifuging or further dilution with PBS. 10 µl of the above fungal solution was exposed to 410 nm for 5 min (150 mW/cm^2). After that, the exposed sample was collected into 990 µl of sterile PBS, then supplemented with treatment agents. Aliquots were made from the above sample into a 96-well plate, with each well containing 100 µl. Then 100 µl sterile YPD broth and 23 µl of PrestoBlue were added into the same well. Fluorescence signal at 590 nm from each well was recorded in a time-course (up to 18 hours with the interval of 30 min) manner at an excitation of 560 nm. For each strain, in order to know the exact number of fungal pathogens in each well, we also recorded the corresponding fluorescence signals from fungal pathogens with known number however no external treatments.

6.2.5 Macrophage-Candida albicans interaction unveiled by confocal laser scanning microscopy

As described elsewhere[222], murine macrophage cells (RAW 264.7) were cultured in DMEM supplemented with 10% FBS plus penicillin and streptomycin at 37 °C with CO_2 (5%). Cells were exposed to *Candida albicans SC5314* (with/without 410 nm exposure) at a multiplicity of infection (MOI) of approximately 10:1 at serum-free DMEM medium. 1 or 2-hour post-infection, RAW 264.7 cells were washed with gentamicin (50 µg/mL, for one hour) to kill extracellular pathogens in DMEM + 10% FBS. After that, RAW 264.7 cells were washed with gentamicin (50 µg/mL) and subsequently lysed using 0.1% Triton-X 100 for 3 min. After membrane permeabilization, infected RAW 264.7 cells were stained

with Live/Dead stain for 15 min, then samples were fixed in 10% formalin for 10 min. Formalin was washed away prior confocal imaging.

6.3 Results

6.3.1 410 nm exposure reduces intracellular catalase amount

It was known that most of fungal pathogens are catalase-positive[230]. To test whether 410 nm exposure could cause the loss of catalase activity, we utilized the same approach to quantify the intracellular catalase amount by the amplex red catalase kit before and after 410 nm exposure. It turned out that catalase from various fungal pathogens, either log-phase or stationary-phase could be significantly inactivated by 410 nm exposure (**Figure 6.1**).

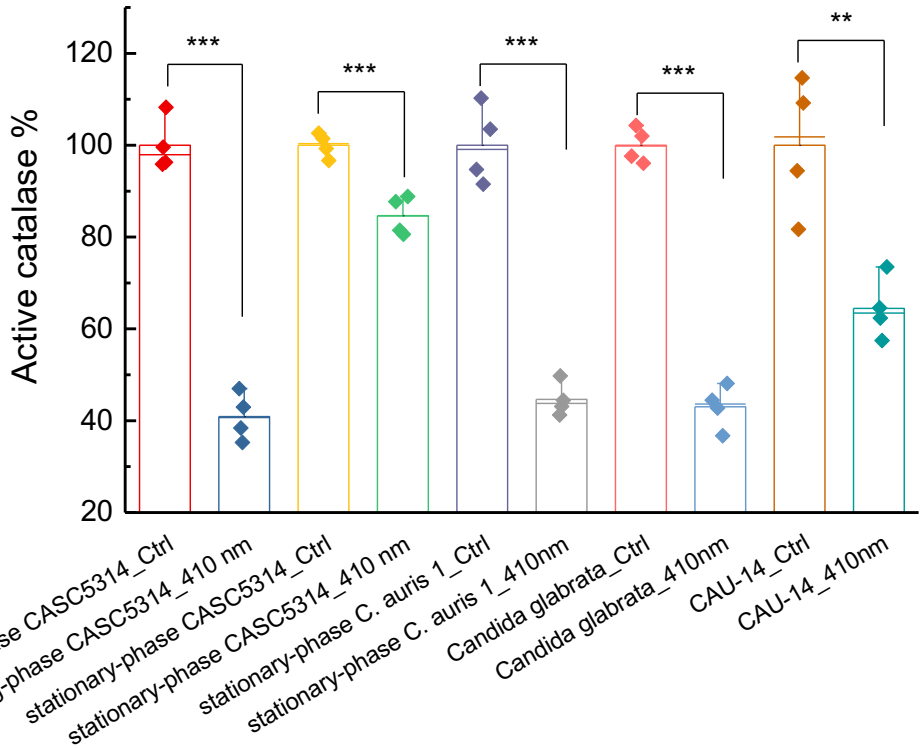

Figure 6.1. Active catalase percent of various fungal strains with or without 410 nm light exposure. Dose: 410 nm, 150 mW/cm^2, 5 min. Fungal concentration: 10^6 cells/ml. CASC5314: wild-type *Candida albicans*.

Noteworthy, catalase from notorious *Candida auris* strain reduced by 60% after only 5-min 410 nm exposure.

6.3.2 Photoinactivation of catalase in combination with H_2O_2 achieved total eradication of C. albicans SC5314 by CFU assay

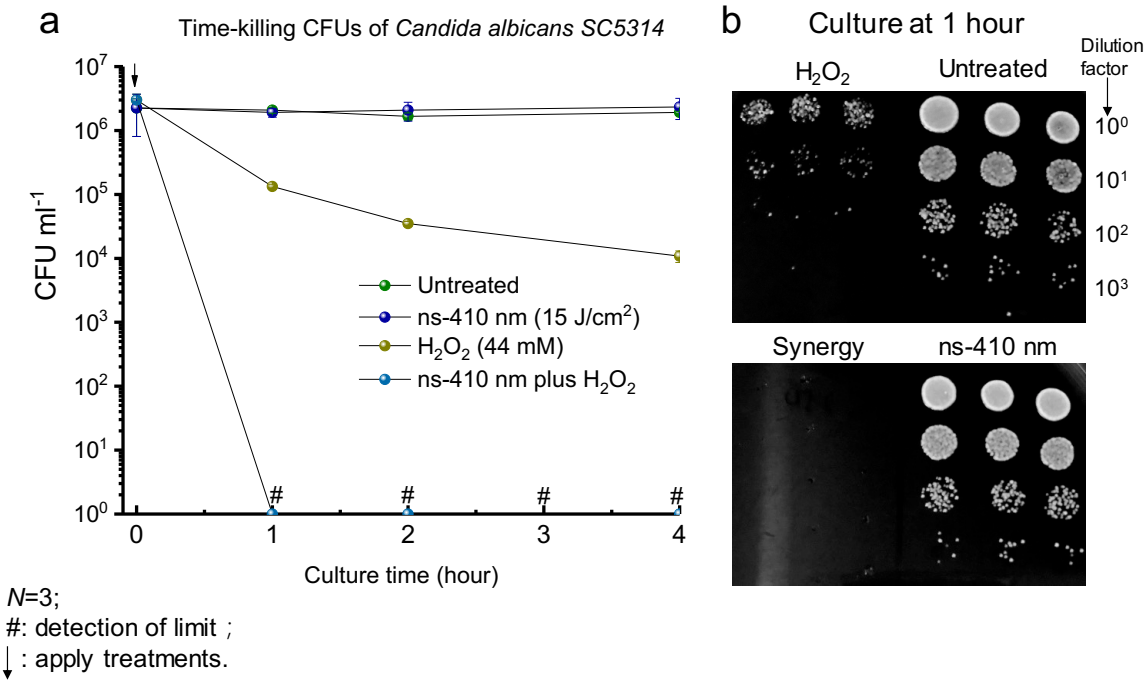

Figure 6.2. CFU results of *CASC5314* after different treatment schemes. (a). Time-killing assay of *CASC5314* after various treatment schemes. (b). Spread plates of *CASC5314* after 1-hour incubation at different treatment schemes.

Since we could effectively inactivate catalase among various fungal strains, we wondered whether photoinactivation of catalase could sensitize them to external H_2O_2 attack. Then we further administrated low-concentration H_2O_2 after 410 nm exposure, and we found that total eradication was achieved after combinational treatments (**Figure 6.2**). Noteworthy, there was more than five orders of magnitude enhancement of the function of H_2O_2 after photoinactivation of catalase (**Figure 6.2**). To further confirm this combinational therapy works as well for other fungal strains, more clinical fungal strains

are needed to confirm the feasibility of this synergistic therapy. Unlike bacteria, fungal cells growth slower, with each colony forming after around 48 hours. Thus, we utilized a high-throughput method, PrestoBlue viability assay, to measure the treatment efficacy.

6.3.3 Photoinactivation of catalase in combination with H_2O_2 achieved efficient eradication of broad-spectrum fungal species by PrestoBlue assay

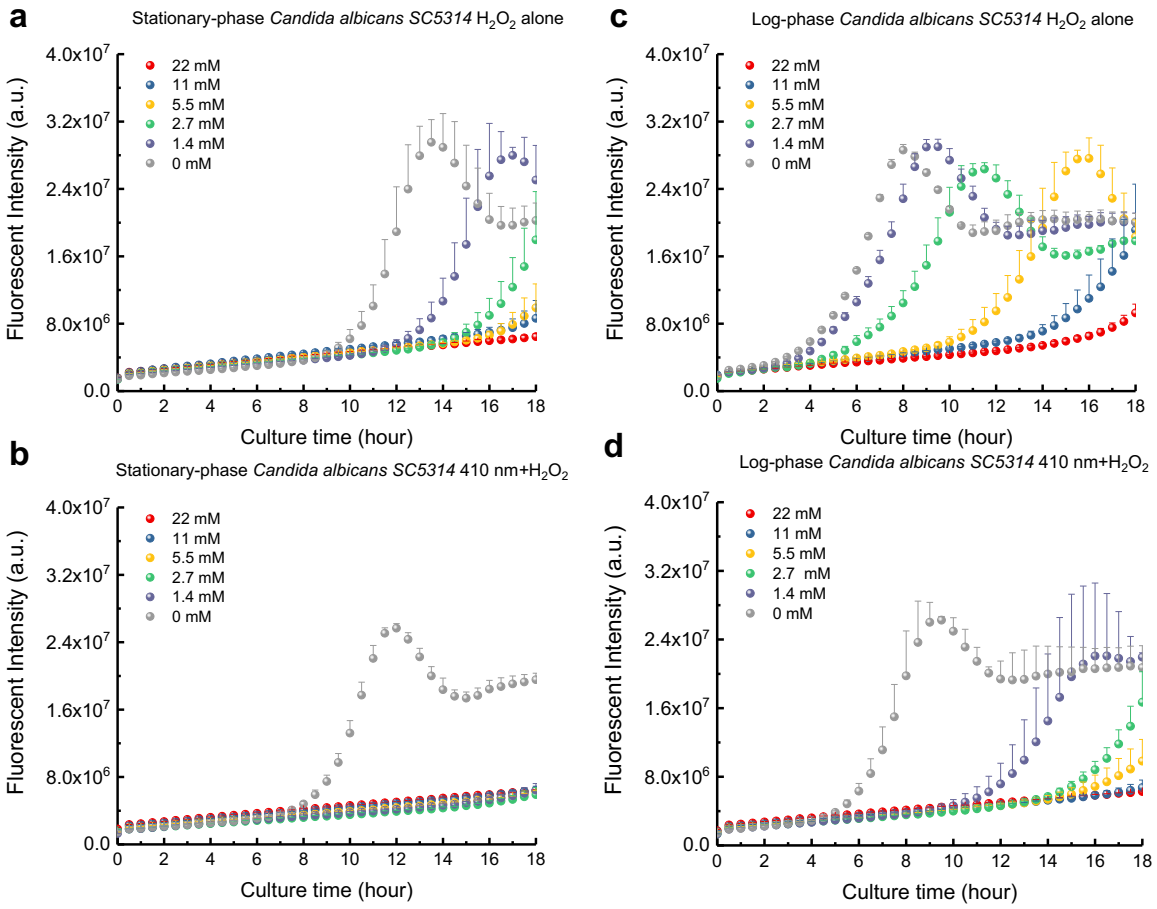

Figure 6.3. Fluorescence signals of PrestoBlue from *CASC5314* under various treatment schemes. (a, c). H_2O_2-alone treated stationary-phase CASC5314 and log-phase *CASC5314*, respectively. (b, d). 410nm plus H_2O_2 treated stationary-phase *CASC5314* and log-phase *CASC5314*, respectively.

As shown in **Figure 6.3**, the utilization of PrestoBlue could achieve the same killing effect as the CFU assay. Interestingly, log-phase and stationary-phase CASC5314 demonstrate different behavior towards the combinational killing, presumably because of the metabolic activity difference between these two states. However, either log-phase or stationary-phase, photoinactivation of catalase always boosts the killing effect of low-concentration H_2O_2. We also tested this synergistic therapy among more than twenty different clinical fungal isolates, and significant killing was consistently found among them.

6.3.4 Candida auris strains are sensitive to 410 nm light exposure

Apart from H_2O_2, we asked whether photoinactivation of catalase could synergize with conventional antifungal agents, such as azoles or amphotericin B (amp B). Similar to some classes of antibiotics, amp B kills fungi partly due to the oxidative damage[213,215]. Therefore, to test our hypothesis, we conducted the PrestoBlue assay after the treatments of photoinactivation of catalase and subsequent addition of amp B against various clinical fungal isolates, including *C. auris* strains.

Interestingly, we found that without the assistance of photoinactivation of catalase, some *C. auris* strains were resilient to amp B (**Figure 6.4**). Nonetheless, with photoinactivation of catalase, we achieved total eradication of *C. auris* strains regardless of the addition of amp B. We tested ten *C. auris* strains and they demonstrated the same behavior. This means *C. auris* strains are exceptionally sensitive to blue light exposure. More studies down to molecular level are needed in order to have a clear understanding of why *C. auris* strains are sensitive to blue light exposure.

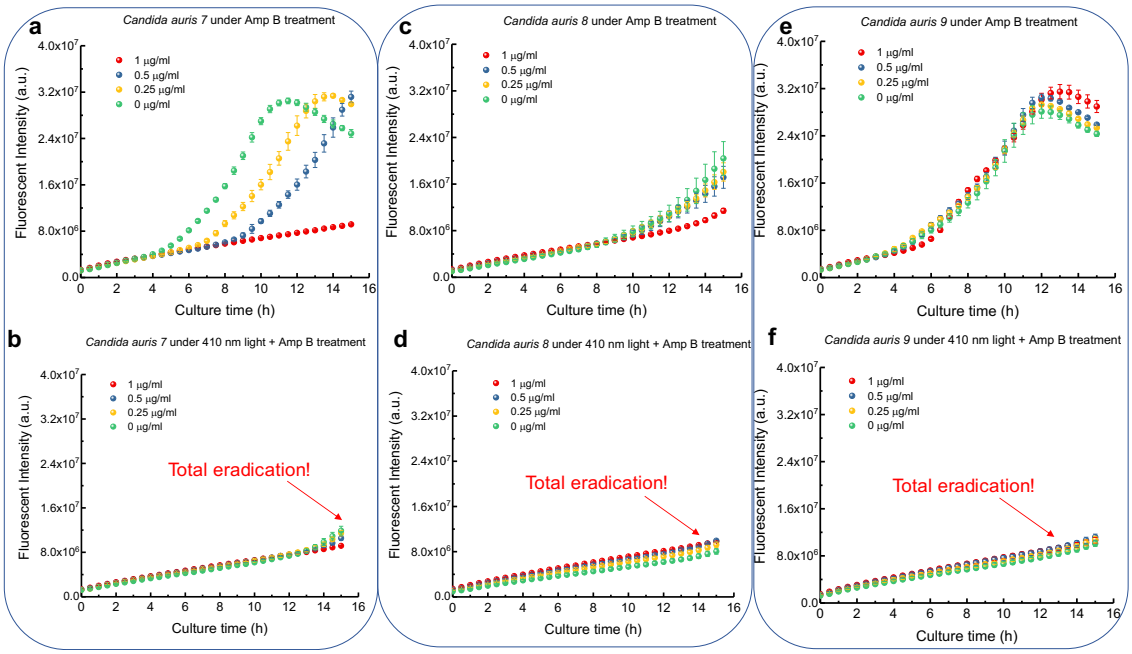

Figure 6.4. Fluorescence signals of PrestoBlue of three different *C. auris* strains under different treatment schemes. (a, c, e). Amp B alone-treated groups. (b, d, f). 410 nm plus amp B-treated groups.

6.3.5 Photoinactivation of catalase inhibits the formation of hyphae of C. albicans, and assists macrophage cells to phagocytose

Besides H_2O_2 and antifungal drugs, our host immune cells play important roles against external evasive pathogens. As we learned that catalase holds an essential role during the battle between *C. albicans* and neutrophils or macrophage cells[231]. Thus, we wondered to know whether photoinactivation of catalase could assist macrophage cells against *C. albicans*. To visualize this effect, we infected RAW 264.7 cells with *C. albicans* and 410 nm-exposed *C. albicans* at a MOI of 10 and labeled with live/dead fluorescence stains.

As shown in **Figure 6.5**, untreated *C. albicans* stay as hyphae form and pierced through macrophage cells. Whereas 410 nm-exposed *C. albicans* remained as dead 'yeast' form intracellularly.

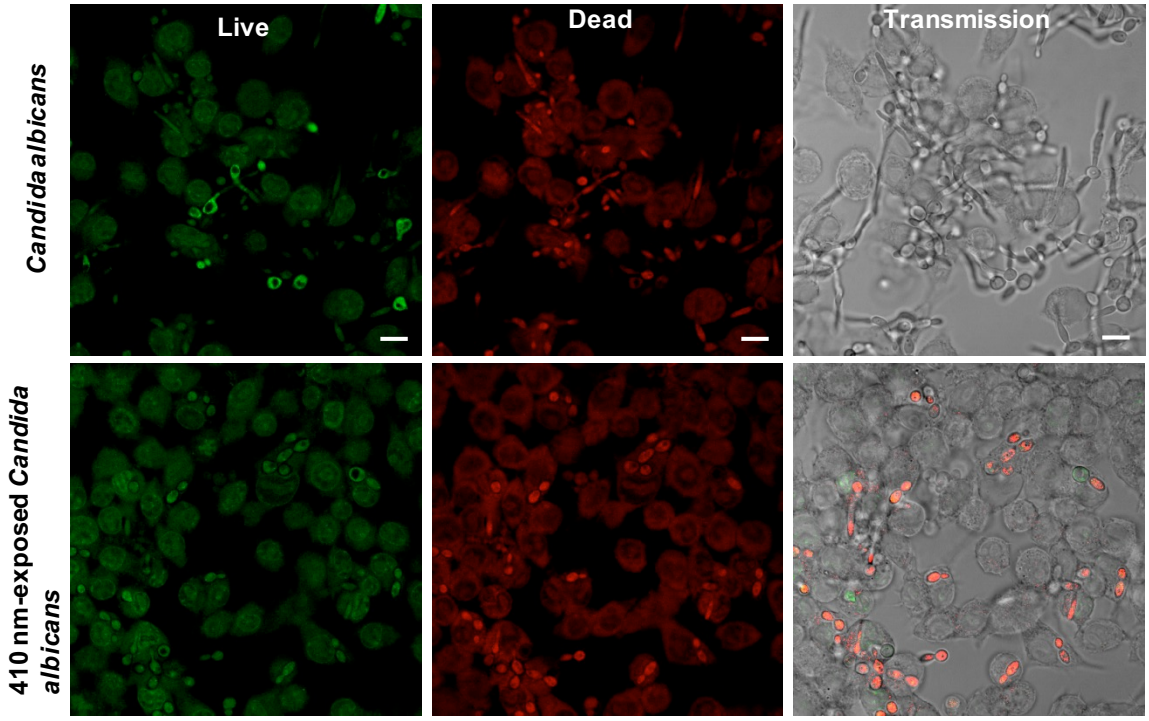

Figure 6.5. Confocal laser scanning imaging of live/dead *C. albicans* after infecting RAW264.7 macrophage cells.

6.4 Future work and Conclusion

Catalase is an essential detoxifying enzyme in fungal cells encountering various endogenous or exogenous stress [232]. Specially, when the gene encoding the expression of catalase is mutant, pathogens were more susceptible to the environmental stress. Accidentally, we found photoinactivation of catalase significantly boosts low-concentration H_2O_2, ROS-generating antibiotics, and immune cells against broad-spectrum bacteria, including the notorious multidrug-resistant *Candida auris* strains. Especially we found that 410 nm exposure significantly inhibited the hyphae formation. Further study is

needed to understand how photoinactivation of catalase could downregulate or upregulate the expression of certain messenger RNAs, such as the expression of secreted aspartic proteases, the virulence factor when hyphae forms [233]. Further work is also needed to evaluate the above synergistic therapy in *Candida albicans* biofilm model, fungal mice infection model. In a summary, our discovery reported here present an effective and novel approach to eliminate broad-spectrum fungus and fungal infections.

CHAPTER 7 DIRECT VISUALIZATION OF AMPHOTERICIN B ORIENTATION IN FUNGAL CELL MEMBRANE BY POLARIZED FINGERPRINT SRS MICROSCOPY

This work is currently under the stage of manuscript in preparation (Pu-Ting Dong et al., 2019). Pu-Ting discovered amphotericin B demonstrated strong stimulated Raman scattering signal from single fungus. Dr. Cheng conceived the idea of imaging amphotericin B by polarized stimulated Raman scattering microscopy. Dr. Mansour provides the broad-spectrum clinical fungal species.

For more than fifty years, amphotericin B (Amp B) has remained the powerful but highly toxic last line for severe and life-threatening systemic fungal infections such as aspergillosis, candidiasis etc. The general understanding of the working mechanism of this drug is 'Amphotericin B acts through pore formation at the cell membrane after binding to ergosterol'. However, sixty years of investigation, the action mechanism of amp B remains unclear. There are two models proposed to illustrate the interaction between amp B and ergosterol in the cell membrane, one is the traditional barrel-stave model, the other is sterol sponge model. Extensive biophysical and structural studies have been utilized to understand the working model, such as UV-visible spectroscopy, fluorescence microscopy, Raman spectroscopy, transmission electron microscopy. However, none of the above methods provide direct visualization of amp B in the cell membrane, moreover, most of methods presented rely on the interaction between amp B and the artificial cell membrane. Thus, there is a need to have a clear understanding of how amp B orientates in the fungus cell membrane. Here, we employed label-free polarized fingerprint stimulated Raman scattering microscopy to visualize amp B in the single fungus cell membrane. And we found that amp B resides in the cell membrane in a highly ordered approach, parallel to the

backbones of phospholipid bilayer, which supports the conventional barrel-stave model. Our findings here provide direct visual evidence of how amp B orients in the cell membrane, thus offering potential guidance of developing novel low-toxicity polyene antifungals.

7.1 Introduction

Nearly a billion people are estimated to have skin, nail and fungal infections ranging from asymptomatic-mild mucocutaneous infections to potentially life-threatening systemic infections[227,234]. Among the pathogenic fungal species, *Aspergillus*, *Candida*, *Cryptococcus* species remain the main fungal species responsible for the majority causes of severe fungal disease[227]. Moreover, *Candida spp* are the fourth most common cause of hospital-acquired systemic infections in the United States with the crude mortality up to 50%[235]. In addition, a novel *Candida* species, *Candida auris* (*C. auris*), the emerging pathogen who has been associated with nosocomial outbreaks on five continents[236]. Noteworthy, some of those *Candida auris* strains are resistant to multiple antifungal classes, resulting in more than 60% mortality[237,238].

For more than fifty years, amphotericin B (amp B) has remained the powerful but highly toxic first line of defense for clinical fungal infections[239] with minimal development of microbial resistance. Understanding how this small molecule kills fungus is thus essential for guiding the development of novel polyene derivatives with resistance-refractory and low-toxicity capability. Extensive research has been harnessed to understand and propose the underlying working mechanism. The first, oldest, and most studied is the ion-channel model proposed by Finkelstein and Holz[240] as shown in **Figure 7.1c**. This

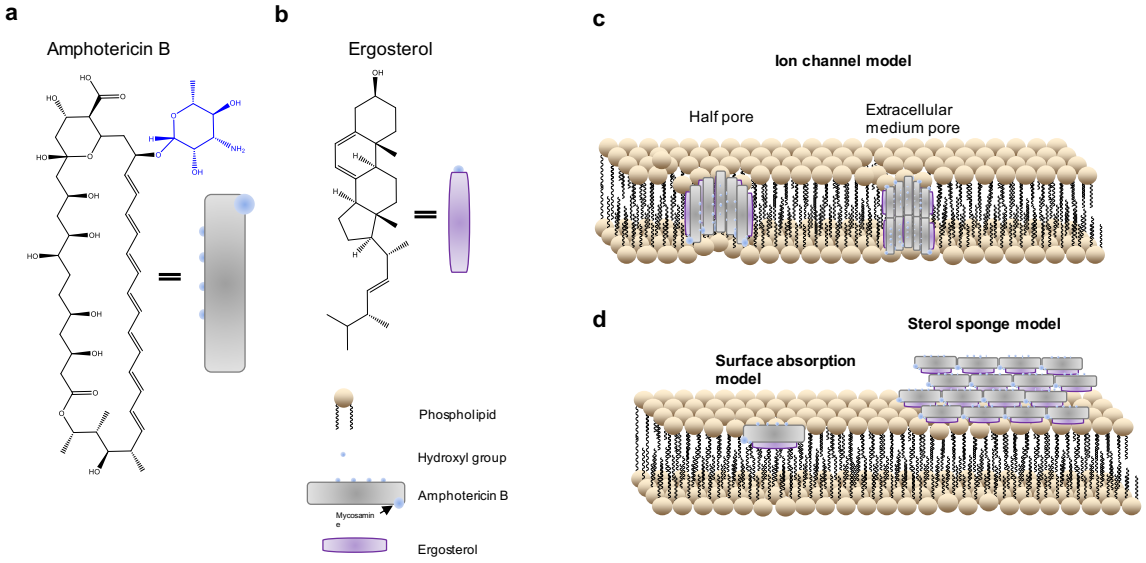

Figure 7.1. Two models proposed to illustrate the working mechanism of amphotericin B. (a-b). Chemical structures of amp B (a) and ergosterol (b), respectively. (c). The ion-channel model, which is called barrel-stave model. (d). The sterol sponge mode.

model is also called barrel-stave model, where amp B molecules aggregate with ergosterol in a way that they form a barrel through a bilayer with its polyhydroxy groups pointing inward and heptaene parts pointing outward. These formed pores are responsible for the leakage of K^+ ions and small organic particles, finally leading to cell death[241]. The second model is based on amp B surface absorption (**Figure 7.1d**) in which antibiotic molecules oriented parallel to the plane lipid surface by sequestering ergosterol to the bilayer surface[242]. The last model is the sterol sponge model (**Figure 7.1d**) where amp B exists as a large aggregate with ergosterol proposed by Burke and coworkers[243]. Among these models, amp B lines parallel to the phospholipid bilayers in the first model. Whereas amp B stays in an orthogonal direction against phospholipid bilayers in the second and third concept.

Extensive studies have been developed to understand the aggregates, such as Circular Dichroism (CD) spectroscopy[244-246], Raman spectroscopy[247], atomic force microscopy[248],

transmission electron microscopy[249], solution NMR spectroscopy[245], computer modeling[250]. Besides these approaches, fluorescence approaches have also been developed to modify the hydroxyl groups and carboxylic groups of amp B aiming at making them fluorescent[245,247]. However, these modifications usually conjugate a bulky fluorophore to amp B, thus potentially affecting its interaction with ergosterol. Therefore, this is an unmet need for alternative approach to achieve direct visualization of amp B in single fungal cell membrane.

Here, through polarization fingerprint stimulated Raman scattering (SRS) microscopy, we achieved direct visualization of amp B in single fungal cell membrane. We further found that amp B exists as a highly ordered form in the cell membrane as the SRS signal of amp B is sensitive to the polarization angle of excitation laser pulses. Compared to the -CH_2 signal at the same polarization condition, we determined that amp B resides in the cell membrane parallel to the phospholipid's bilayer backbones, which supports the traditional barrel-stave model. Our findings reported here provide advanced imaging approach to visualize these polyene antifungals, thus offering potential guidance for developing low toxicity polyene antifungal drugs.

7.2 Methods

7.2.1 Chemicals and fungal strains

DMSO (W387520, Sigma Aldrich), amphotericin B (A9528-100 MG, Sigma Aldrich), ergosterol (AC1178100050, 98%, ACROS Organics). YPD broth (Y1375, Sigma Aldrich). YPD agar (Y1500, Sigma Aldrich). *Candida albicans* SC5314, the test of fungal strains used see **table 1**.

Pathogen	Strain	Number
C. albicans	SC5314	SC5314
C. glabrata	ATCC2001	ATCC2001
C. tropicalis	C22	H3222861
C. parapsilosis	C23	F825987
C. lusitaniae	C30	S1591976
Candida auris	Lung	From MGH--commonly used in MKM lab
Candida haemulonii	CAU-13	AR-0393
Candida duobushaemulonii	CAU-14	AR-0394
Candida haemulonii	CAU-15	AR-0395
Kodameae ohmeri	CAU-16	AR-0396
C. albicans	Ca C13	
C. albicans	Ca C14	
C. glabrata	Cg C1	
C. glabrata	Cg C2	
Candida krusei	CAU-17	AR-0397
C. lusitaniae	CAU-18	AR-0398
Saccharomyces cerevisiae	CAU-19	AR-0399
C. albicans	Ca C15	
C. albicans	Ca C16	
C. albicans	Ca C17	
Candida krusei	CAU-17	AR-0397
C. lusitaniae	CAU-18	AR-0398
Saccharomyces cerevisiae	CAU-19	AR-0399
C. albicans	Ca C15	
C. albicans	Ca C16	
C. albicans	Ca C17	
Candida auris	CAU4	AR-0384
	CAU5	AR-0385
	CAU6	AR-0386
	CAU7	AR-0387
	CAU8	AR-0388
	CAU9	AR-0389

Table 1. Fungal strains utilized for amp B imaging experiments.

7.2.2 Raman spectra of amphotericin B and ergosterol

Ergosterol and amphotericin B (dissolved in DMSO) was measured by its Raman peaks at around 1300-1700 cm^{-1} measured by resonance Raman spectroscopy (1221, LABRAM HR EVO, Horiba) with a 40×objective (Olympus) and an excitation wavelength of 532 nm. Samples (dried 'coffee ring' were sandwiched between two glass cover slides (48393-230, VWR international) with a spatial distance of ~80 μm.

7.2.3 Polarized fingerprint stimulated Raman scattering microscope

As described elsewhere[20,251], hyperspectral SRS images were recorded by a spectral focusing approach. An ultrafast laser system with dual output at 80 MHz (InSight DeepSee, Spectra-Physics) provided pump and Stokes beams. The laser beating frequency was tuned to the C=C fingerprint region between 1400-1700 cm^{-1}. The pump beam was tuned to 895 nm with the Stokes beam at 1040 nm. The Stokes beam was modulated by an acousto-optic modulator at 2.2 MHz. Both pump and Stokes beams are linearly polarized, and the polarization directions of these two beams are controlled by a half-wave plate. A motorized translation stage as employed to scan the delay between the two beams. Both beams were chirped by two or five 12.7-cm SF57 glass rods with the Stokes beam chirped by additional glass rod to match the pulse durations of the both beams. The combined pump and Stokes beams were then sent to a home-build laser-scanning microscope. A 60× water immersion objective (NA=1.2, UPlanApo/IR, Olympus) was used to focus combined light onto sample, and an oil condenser (NA=1.4, U-AAC, Olympus) was used to collect the signal. The stimulated Raman loss signal (from pump beam) was detected by a home-built

photodiode with resonant circuits, which was extracted with a digital lock-in amplifier (Zurich Instrument). Freshly prepared amp B solution and pure ergosterol powder are the standard chemicals to calibrate the Raman shift each time before imaging. For each image showed, the pump powder on the specimen were 10-25 mW and 80 mW, respectively.

7.2.4 Preparation of ghost red blood cell membrane

As described elsewhere[252,253], The erythrocyte ghosts were prepared according to established protocols[253,254]. In brief, the human blood (Boston Children's Hospital Blood Donor Center) was first diluted with PBS at a ratio of 1:20. After three times' washing (3000 rpm centrifuge), the erythrocytes were then exposed to ice-cold 5 mM phosphate buffer (pH 8.0) which caused the erythrocytes to lyse. The samples were kept close to 0°C for 2 minutes (found that the supernatant was deeply red), after which the solution was centrifuged for 15 minutes at 18, 000 g and the supernatant was removed from the pellet. Thereafter the resealing buffer (50 mM NaCl, 5 mM phosphate buffer, pH 8.0) was added to allow for resealing of the membranes. The resealing process lasted 1 hour at room temperature. In order to get rid of all hemoglobin from the cells, we repeated the lysis and resealing procedures twice. When imaged by SRS microscopy, the formed erythrocyte ghost appears as a spherical vesicle.

7.2.5 Amp B-treated log-phase fungal species

Pathogens were cultured overnight by inoculating 1-2 single colonies streaked from frozen stock in sterile YPD broth at 30°C with the shaking speed of 200 rpm. Log-phase growth pathogen was prepared by 1:20 dilution of overnight-cultured fungal pathogens into

fresh YPD, and cultured for 2-3 hour at 30°C. After that, pathogen specimens were centrifuged and supernatant was discarded, then suspended with fresh PBS. The resulting solution were vortexed homogenously, further diluted into PBS with a concentration of 10^6 cells/ml. 3.2 µl of amp B stock (1 mg/ml in DMSO) was added into the above solution to make a final working concentration of 3.2 µg/ml. Then the resulting solution was incubated at 30°C with the shaking speed of 200 rpm for 1 hour. After that, amp-treated fungi were fixed in 10% formalin. Formalin was washed away prior imaging. Fungal specimen was sandwiched between a poly-lysine-coated glass slide and a cover glass.

7.3 Results

7.3.1 Raman spectra of pure ergosterol and amp B

As shown in **Figures 7.2, a and b**, ergosterol has abundant vibrational information in the fingerprint Raman range from 1300 cm^{-1} to 1700 cm^{-1}, where 1602 cm^{-1} (conjugated C=C vibration) is believed to be the standard representative of Raman shifts[255]. Interestingly, amp B has a prominent peak at 1560 cm^{-1} due to the conjugated heptaene structure. Because of electron cloud from the conjugated C=C bonds, the Raman signal at this wavenumber is dominant. Thus, in the following study, we will target this wavenumber specifically for amp B.

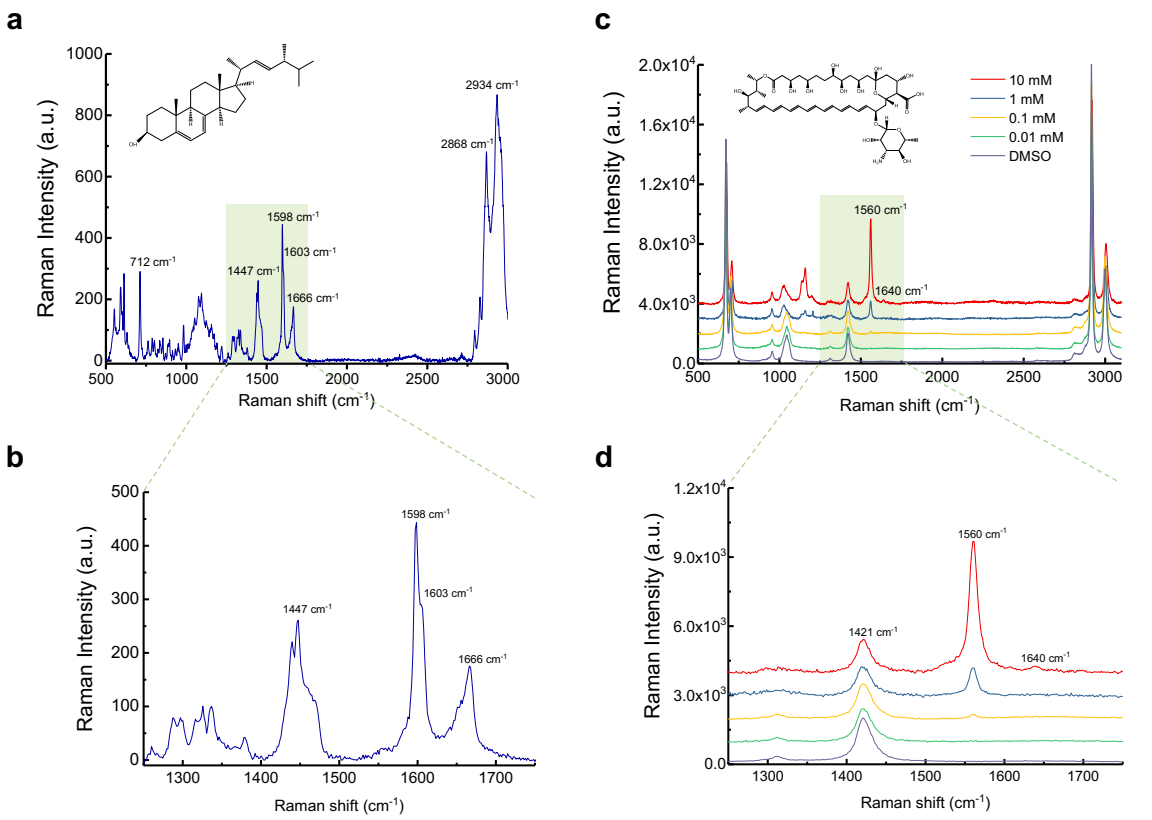

Figure 7.2. Raman spectra of pure ergosterol (a and b) and amp B solution at different concentrations (dissolved in DMSO). Region of interest is highlighted by green-color blank.

7.3.2 Calibration of hyperspectral Stimulated Raman scattering system in the fingerprint window

To achieve mapping of amp B in single fungal cell, first we need to calibrate our hSRS systems with standard chemicals (pure ergosterol and amp B solution) in the spectral window from 1250 cm^{-1} to 1750 cm^{-1}. As shown in **Figure. 7.3**, both ergosterol and amp B (10 mM) exhibited strong Raman signals at step size 40 and 61, respectively (**Figure 7.3a**). Then we combined their step size together with their representative Raman shifts, we built the linear Raman shift calibration curve (**Figure 7.3b**). We also compared the spectral resolution of our hSRS system by chirping with three (**Figure 7.3c**) or six glass

rods (**Figure 7.3d**), it turned out that six-rod chirping could well separate the two major Raman peaks from ergosterol and amp B. Thus, for the following imaging study, we only utilized the six-rod chirping hSRS system.

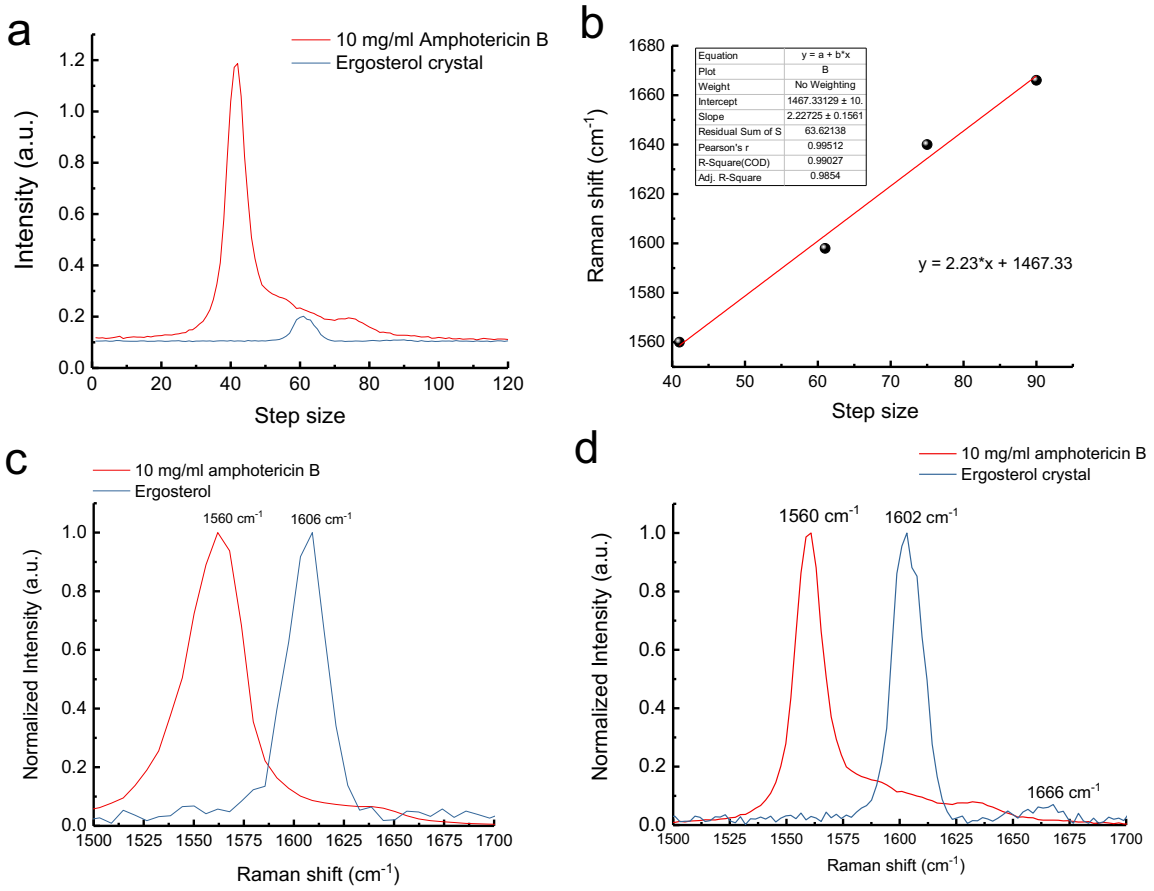

Figure 7.3. Calibration of hyperspectral SRS system with standard chemicals. (a). SRS signal of ergosterol and 10 mM amp B over different step size. (b). Calibration curve of Raman shifts over different step size. (c). SRS spectra of ergosterol and amp B chirping with three SF57 glass rods. (d). SRS spectra of ergosterol and amp B chirping with six SF57 glass rods.

7.3.3 SRS signal of -CH_2 from ghost red blood cell membrane at different laser polarizations

To understand in which direction the pump and Stokes beams are polarized, we utilized a standard procedure to determine it. It was known that the -CH_2 signal of lipids in a ghost

red blood cell membrane is highly ordered as the -CH_2 groups are perpendicular to the backbones of phospholipid bilayers [256]. As shown in **Figure 7.4**, when the laser beams were excited at a horizontal direction, we observed strong -CH signal from the upper and lower parts of ghost cell membrane (**Figure 7.4c**). While when the excited laser beams are in a vertical manner (half wave plates rotated by 45°), the SRS signal was shifted to a left and right approach (**Figure 7.4d**).

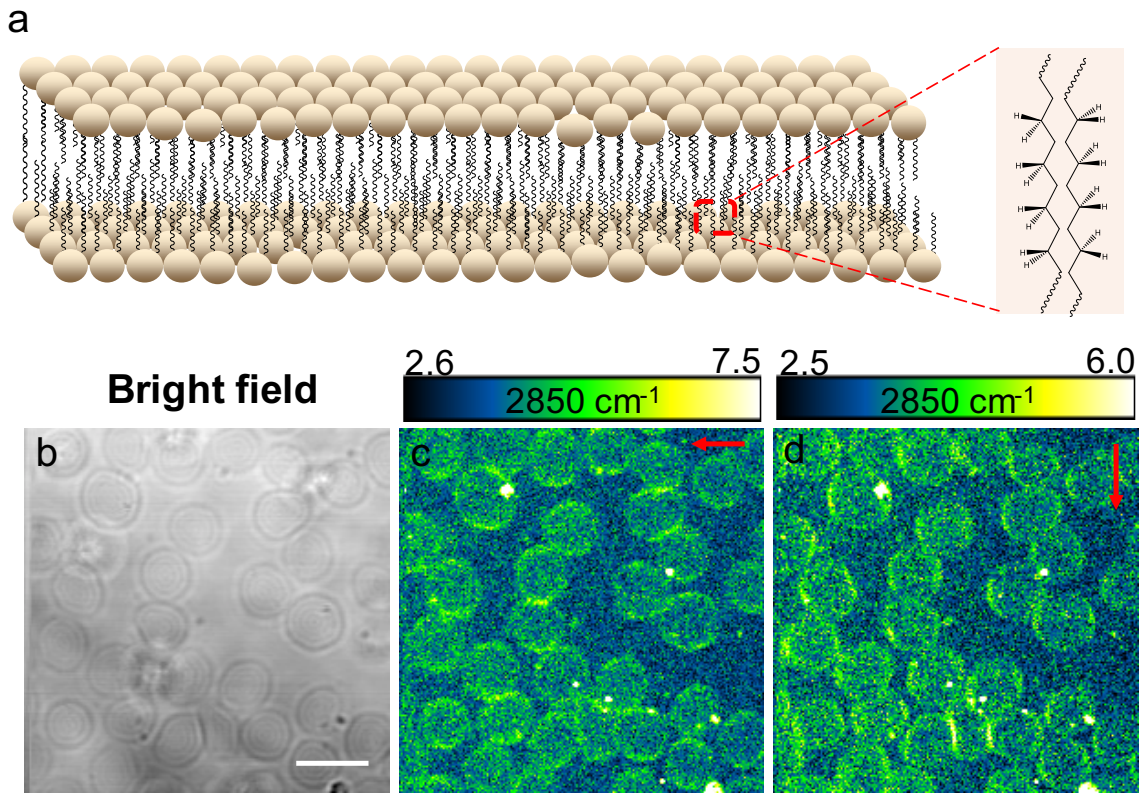

Figure 7.4. SRS signals of -CH_2 at different polarization of excited laser beams. (a). Schematic illustration of phospholipid bilayers and the -CH_2 groups. (b). Transmission image of ghost red blood cell membrane. (c). -CH_2 SRS signal (2850 cm^{-1}) of ghost red blood cell membrane when the excited laser beams are horizontal direction. (d). -CH_2 SRS signal (2850 cm^{-1}) of ghost red blood cell membrane when the excited laser beams are vertical direction. Pump=802 nm, Stokes=1040 nm. Scalar bar=10 µm.

7.3.4 SRS signal of amp B from single fungal cell membrane at different laser polarizations

Next, we were curious how the amp B SRS signal behaves in a single fungal cell membrane when laser beams were excited at the same approach as for the ghost cell membrane. To do this, we switched the beating frequency between pump and Stokes beam

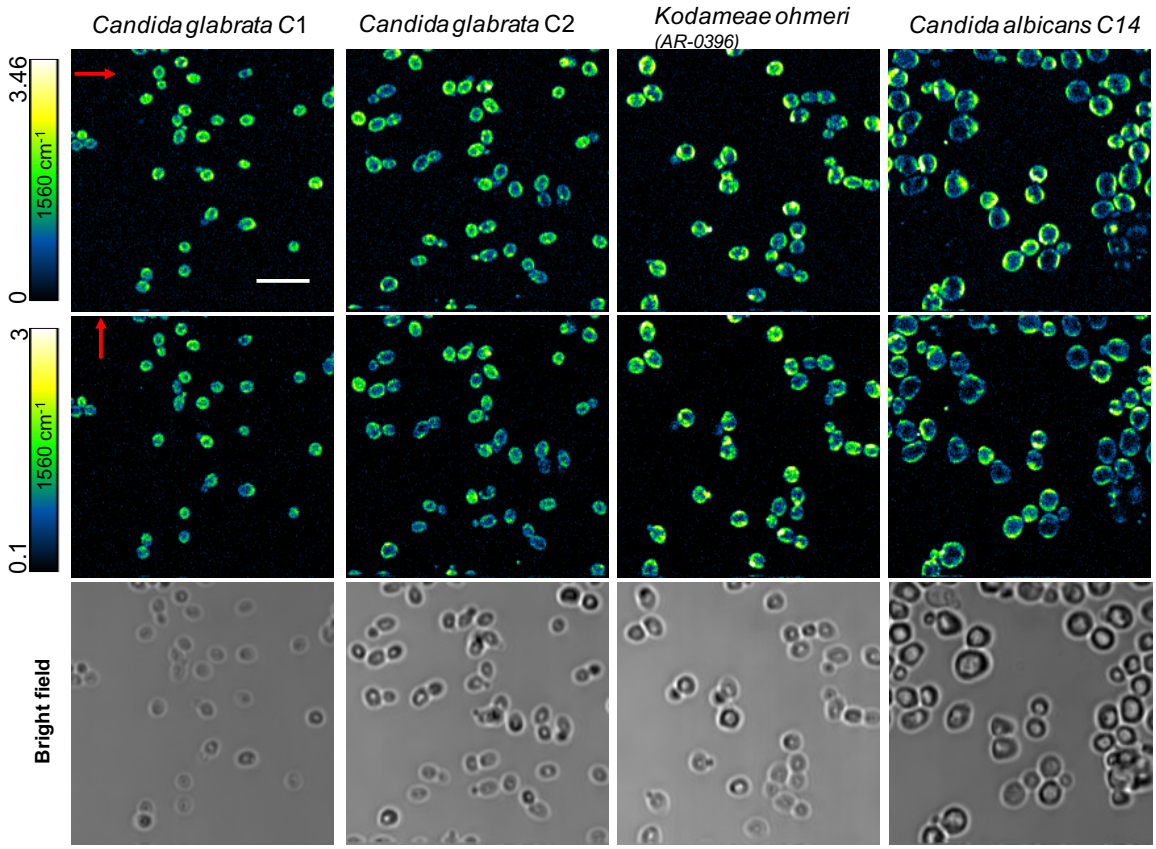

Figure 7.5. SRS signals (1560 cm^{-1}) of amp B from single fungal cell membrane at different polarizations (indicated by the red arrow) of excited laser beams for four different fungal strains. Pump=895 nm, Stokes=1040 nm. Scalar bar=10 µm.

to 1560 cm^{-1}, the representative peak for amp B, and we then recorded the SRS signals of amp B under the excitation of both horizontal and vertical polarized laser beams. It turned out that amp B exists in the cell membrane as a 'hollow core' structure. And the orientation

change of amp B in the cell membrane versus laser polarization behaves in an orthogonal manner compared to that of -CH_2 signal, indicating that the orientation of amp B is parallel to the backbones of phospholipid bilayers. This visual evidence supports the traditional barrel-stave model.

To further confirm this is a universal phenomenon for other fungal species, we also imaged amp B from single *C. auris* as shown in **Figure 7.6**. It turned out that similar phenomenon happened to *Candida auris* species as well. These evidences further consolidate the fact that amp B resides in the cell membrane in a highly ordered manner, parallel to the backbones of phospholipid bilayer, supporting the ion-channel model.

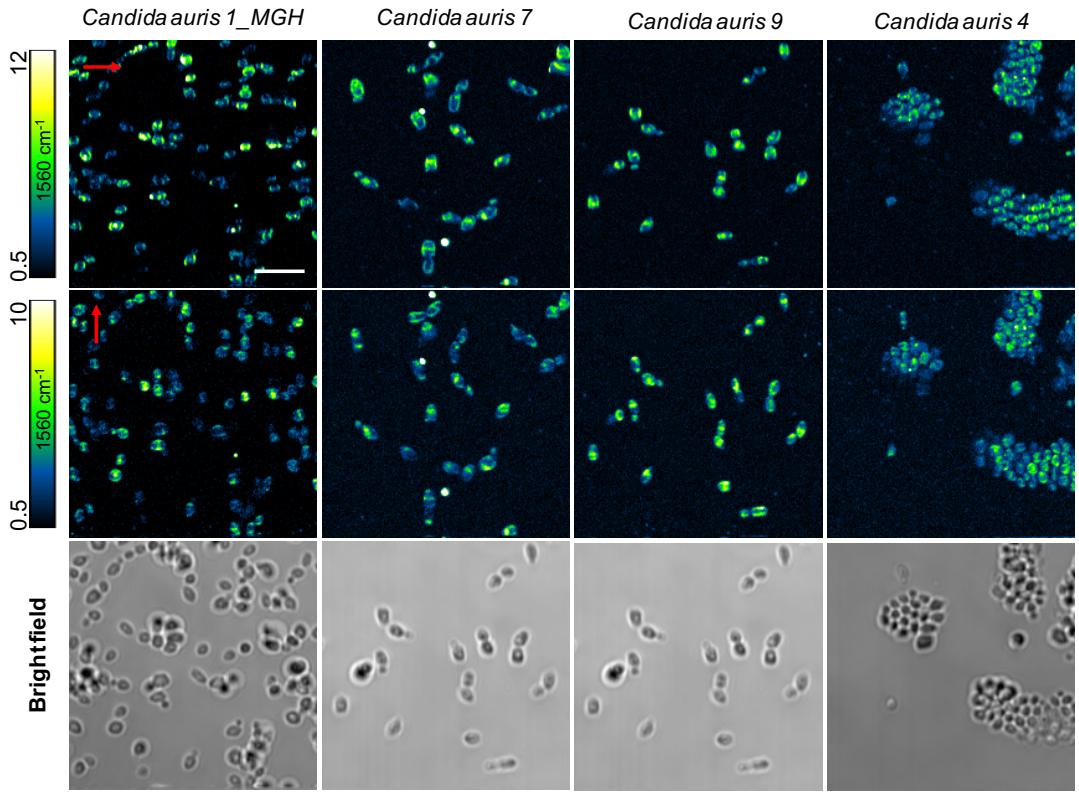

Figure 7.6. SRS signals (1560 cm^{-1}) of amp B from single fungal cell membrane at different polarizations (indicated by the red arrow) of excited laser beams for four different *Candida auris* strains. Pump=895 nm, Stokes=1040 nm. Scalar bar=10 µm.

7.4 Discussion and Conclusion

For more than five decades, the underlying working mechanism of amp B is a mystery. It has shown powerful and resistance-refractory capability even though it is highly toxic. Thus, it is essential to have a better understanding of how this molecule works in the fungal cell membrane. Here, we employed label-free polarized fingerprint stimulated Raman scattering microscopy to visualize amp B in the single fungus cell membrane. And we found that amp B resides in the cell membrane in a highly ordered approach, parallel to the backbones of phospholipid bilayer, which supports the conventional barrel-stave or ion-channel model.

Interestingly, we also found the amp B signal appearing intracellular as droplets, presumably colocalizing with the intracellular lipid droplets. Further imaging evidences are needed to confirm this observation.

We also observed sound signal of ergosterol in a label-free approach in the same spectral window as amp B. And we indeed found C. albicans mutants with low expression of ergosterol exhibits lower SRS signal. This finding might guide us to utilize ergosterol signal as a readout to achieve fast antifungal susceptibility test.

In summary, our findings here provide direct visual evidence of how amp B orients in the cell membrane, thus offering potential guidance of developing novel low-toxicity polyene antifungals.

CHAPTER 8 OUTLOOK

8.1 Label-free imaging intrinsic chromophores for disease diagnosis

We have demonstrated a spectroscopic transient absorption imaging approach that is able to differentiate HbA1c from Hb based on their distinct excited state dynamics. HbA1c fraction inside a single red blood cell is derived quantitatively through phasor analysis. HbA1c fraction distribution of diabetic blood is found apparently different from that of healthy blood. And our technology provides a new way to study heme modification and to derive clinically important information avoid of glucose fluctuation in the bloodstream. For the further future study, a hand-held pump probe pen can be developed to measure the amount of HbA1c *in situ* at hospitals. More chromophores could be further investigated as well for disease diagnosis, such as bilirubin, the broken-down metabolite existing in patients' urine, can be measured as a readout of the healthy condition of patients.

8.2 Targeting intrinsic chromophores for therapeutic purpose

We developed an approach to treat MRSA through photolysis of staphyloxanthin, an antioxidant residing in the microdomain of *S. aureus* membrane. This photochemistry process is uncovered through transient absorption imaging and quantitated by absorption spectroscopy, Raman spectroscopy, and mass spectrometry. Photolysis of staphyloxanthin transiently elevates the membrane permeability, disarms the transmembrane protein like PBP2a, induces considerable membrane fluidity change, thus rendering MRSA highly susceptible to hydrogen peroxide, antibiotics, and immune cells attack. Besides this, we also discovered that through photoinactivation of catalase, another intrinsic chromophore existing in most of the aerobic pathogens (MRSA, *P. aeruginosa*, *Candida albicans* etc.),

we could achieve total eradication of these notorious pathogens. For the future study, a portable and feasible medical device based on the above synergy can be developed to treat clinical infectious disease. More practically, the penetration depth of photons is needed to take into consideration as many pathogens lodge in the deep tissue.

8.3 Label-free imaging of drug to unveil the working mechanism

We employed label-free polarized fingerprint stimulated Raman scattering microscopy to visualize amp B in the single fungus cell membrane. And we found that amp B resides in the cell membrane in a highly ordered approach, parallel to the backbones of phospholipid bilayer, which supports the conventional barrel-stave model. Our findings here provide direct visual evidence of how amp B orients in the cell membrane, thus offering potential guidance of developing novel low-toxicity polyene antifungals. Besides amp B, we could also image other drugs, especially those with polyene or other conjugated groups. This *in situ* uninterruptible Raman-based imaging approach would definitely provide guidance, and visual evidence of how drugs exert its functions to kill the pathogens, and also where the drug lodge inside the pathogen or host cells.

BIBLIOGRAPHY

Pu-Ting Dong received her Ph.D. degree in the January of 2020. Sincerely she acknowledged these important sources during her Ph.D. study. Besides the advanced optical tools and resources provided by Dr. Ji-Xin Cheng. But also, the Boston University Animal Facility at both Charles River campus and medical campus. The imaging facility core at Boston University Charles River campus and Harvard Center for Biological Imaging.

REFERENCES

1 Jacques, S. L. Optical properties of biological tissues: a review. *Physics in Medicine and Biology* **58**, R37-R61, doi:10.1088/0031-9155/58/11/r37 (2013).

2 Tuchin, V. V. *Tissue optics: light scattering methods and instruments for medical diagnosis*. 2nd edition. Bellingham, WA: SPIE (2007).

3 Stover, J. C. *Optical scattering: measurement and analysis*. 3rd edition. Bellingham, WA: SPIE (2012) Vol. 2.

4 Raman, C. V. & Krishnan, K. S. A new type of secondary radiation. *Nature* **121**, 501 (1928).

5 Hahn, D. W. Raman scattering theory. 2007. Available from http://plaza.ufl.edu/dwhahn/Raman%20Scattering%20Theory.pdf

6 Llansola-Portoles, M. J., Pascal, A. A. & Robert, B. Electronic and vibrational properties of carotenoids: from in vitro to in vivo. *Journal of The Royal Society Interface* **14**, 20170504 (2017).

7 Maher, R., Cohen, L., Gallop, J., Le Ru, E. & Etchegoin, P. Temperature-dependent anti-Stokes/Stokes ratios under surface-enhanced Raman scattering conditions. *The Journal of Physical Chemistry B* **110**, 6797-6803 (2006).

8 Kim, Y.-i. *et al.* Endoscopic imaging using surface-enhanced Raman scattering. *European Journal of Nanomedicine*, doi:10.1515/ejnm-2017-0005 (2017).

9 Penney, C., Goldman, L. & Lapp, M. Raman scattering cross sections. *Nature Physical Science* **235**, 110 (1972).

10 Strommen, D. P. & Nakamoto, K. Resonance raman spectroscopy. *Journal of Chemical Education* **54**, 474, doi:10.1021/ed054p474 (1977).

11 Sharma, B., Frontiera, R. R., Henry, A.-I., Ringe, E. & Van Duyne, R. P. SERS: Materials, applications, and the future. *Materials Today* **15**, 16-25 (2012).

12 Premasiri, W. R. *et al.* Characterization of the Surface Enhanced Raman Scattering (SERS) of Bacteria. *The Journal of Physical Chemistry B* **109**, 312-320, doi:10.1021/jp040442n (2005).

13 Camden, J. P. *et al.* Probing the Structure of Single-Molecule Surface-Enhanced Raman Scattering Hot Spots. *Journal of the American Chemical Society* **130**, 12616-12617, doi:10.1021/ja8051427 (2008).

14 Cheng, J.-X. & Xie, X. S. Vibrational spectroscopic imaging of living systems: An emerging platform for biology and medicine. *Science* **350**, aaa8870 (2015).

15 Lee, H. J. & Cheng, J.-X. Imaging chemistry inside living cells by stimulated Raman scattering microscopy. *Methods* **128**, 119-128 (2017).

16 Prince, R. C., Frontiera, R. R. & Potma, E. O. Stimulated Raman scattering: from bulk to nano. *Chemical Reviews* **117**, 5070-5094 (2016).

17 Li, J., Lin, P., Tan, Y. & Cheng, J.-X. Volumetric stimulated Raman scattering imaging of cleared tissues towards three-dimensional chemical histopathology. *Biomedical Optics Express* **10**, 4329-4339, doi:10.1364/boe.10.004329 (2019).

18 Zhang, D. *et al.* Quantitative Vibrational Imaging by Hyperspectral Stimulated Raman Scattering Microscopy and Multivariate Curve Resolution Analysis. *Analytical Chemistry* **85**, 98-106, doi:10.1021/ac3019119 (2013).

19 Mansfield, J. C. *et al.* Label-free Chemically Specific Imaging in Planta with Stimulated Raman Scattering Microscopy. *Analytical Chemistry* **85**, 5055-5063, doi:10.1021/ac400266a (2013).

20 Fu, D., Holtom, G., Freudiger, C., Zhang, X. & Xie, X. S. Hyperspectral Imaging with Stimulated Raman Scattering by Chirped Femtosecond Lasers. *The Journal of Physical Chemistry B* **117**, 4634-4640, doi:10.1021/jp308938t (2013).

21 Fu, D. *et al.* Imaging the intracellular distribution of tyrosine kinase inhibitors in living cells with quantitative hyperspectral stimulated Raman scattering. *Nature Chemistry* **6**, 614 (2014).

22 Wang, K. *et al.* Time-lens based hyperspectral stimulated Raman scattering imaging and quantitative spectral analysis. *Journal of Biophotonics* **6**, 815-820, doi:10.1002/jbio.201300005 (2013).

23 Camp, C. H., Jr. *et al.* High-Speed Coherent Raman Fingerprint Imaging of Biological Tissues. *Nature Photonics* **8**, 627-634, doi:10.1038/nphoton.2014.145 (2014).

24 Ozeki, Y. *et al.* Stimulated Raman hyperspectral imaging based on spectral filtering of broadband fiber laser pulses. *Optics Letters* **37**, 431-433 (2012).

25 Lichtman, J. W. & Conchello, J.-A. Fluorescence microscopy. *Nature Methods* **2**, 910-919, doi:10.1038/nmeth817 (2005).

26 Lakowicz, J. R. *Principles of fluorescence spectroscopy*. (Springer Science & Business Media, 2013).

27 Tsien, R. Y. (Annual Reviews 4139 El Camino Way, PO Box 10139, Palo Alto, CA 94303-0139, USA, 1998).

28 Paddock, S. W. Confocal laser scanning microscopy. *Biotechniques* **27**, 992-1004 (1999).

29 Paddock, S. W. Principles and practices of laser scanning confocal microscopy. *Molecular Biotechnology* **16**, 127-149 (2000).

30 Huang, B., Bates, M. & Zhuang, X. Super-resolution fluorescence microscopy. *Annual Review of Biochemistry* **78**, 993-1016 (2009).

31 Huang, B., Babcock, H. & Zhuang, X. Breaking the diffraction barrier: super-resolution imaging of cells. *Cell* **143**, 1047-1058 (2010).

32 Klar, T. A., Jakobs, S., Dyba, M., Egner, A. & Hell, S. W. Fluorescence microscopy with diffraction resolution barrier broken by stimulated emission. *Proceedings of the National Academy of Sciences of the United States of America* **97**, 8206-8210 (2000).

33 Gustafsson, M. G. L. *et al.* Three-Dimensional Resolution Doubling in Wide-Field Fluorescence Microscopy by Structured Illumination. *Biophysical Journal* **94**, 4957-4970, doi:https://doi.org/10.1529/biophysj.107.120345 (2008).

34 Rust, M. J., Bates, M. & Zhuang, X. Stochastic optical reconstruction microscopy (STORM) provides sub-diffraction-limit image resolution. *Nature Methods* **3**, 793 (2006).

35 Hess, S. T., Girirajan, T. P. & Mason, M. D. Ultra-high resolution imaging by fluorescence photoactivation localization microscopy. *Biophysical Journal* **91**, 4258-4272 (2006).

36 Perez-Arjona, I., de Valcarcel, G. & Roldán, E. Two-photon absorption. *Revista mexicana de física* **49**, 92-101 (2003).

37 Parasassi, T., Gratton, E., Yu, W. M., Wilson, P. & Levi, M. Two-photon fluorescence microscopy of laurdan generalized polarization domains in model and natural membranes. *Biophysical Journal* **72**, 2413-2429 (1997).

38 Yao, J. & Wang, L. V. Photoacoustic microscopy. *Laser & Photonics Reviews* **7**, 758-778, doi:10.1002/lpor.201200060 (2013).

39 Dong, P.-T. & Cheng, J.-X. Pump–probe microscopy: Theory, instrumentation, and applications. *Spectroscopy* **32**, 24-36 (2017).

40 Fischer, M. C., Wilson, J. W., Robles, F. E. & Warren, W. S. Invited Review Article: Pump-probe microscopy. *Review of Scientific Instruments* **87**, 031101 (2016).

41 Chong, S., Min, W. & Xie, X. S. Ground-State Depletion Microscopy: Detection Sensitivity of Single-Molecule Optical Absorption at Room Temperature. *Journal of Physical Chemistry Letters* **1**, 3316-3322, doi:10.1021/jz1014289 (2010).

42 Wang, P. *et al.* Far-field Imaging of Non-fluorescent Species with Sub-diffraction Resolution. *Nature Photonics* **7**, 449-453, doi:10.1038/nphoton.2013.97 (2013).

43 Huang, K.-C. *et al.* High-speed spectroscopic transient absorption imaging of defects in graphene. *Nano Letters* **18**, 1489-1497 (2018).

44 Matthews, T. E., Piletic, I. R., Selim, M. A., Simpson, M. J. & Warren, W. S. Pump-Probe Imaging Differentiates Melanoma from Melanocytic Nevi. *Science Translational Medicine* **3**, 71ra15-71ra15, doi:10.1126/scitranslmed.3001604 (2011).

45 Martin, F. Shedding new light on old art. *Physics World* **26**, 19 (2013).

46 Francis, A. T., Berry, K., Thomas, E. C., Hill, A. H. & Fu, D. In Vitro Quantification of Single Red Blood Cell Oxygen Saturation by Femtosecond Transient Absorption Microscopy. *Journal of Physical Chemistry Letters* **10**, 3312-3317, doi:10.1021/acs.jpclett.9b01116 (2019).

47 Nagai, H. & Kim, Y. H. Cancer prevention from the perspective of global cancer burden patterns. *Journal of Thoracic Disease* **9**, 448 (2017).

48 Liu, C. H. *et al.* "Human breast tissues studied by IR Fourier-transform Raman spectroscopy," in *Conference on Lasers and Electro-Optics*, J. Bufton, A. Glass, T. Hsu, and W. Krupke, eds., Vol. 10 of OSA Technical Digest (Optical Society of America, 1991), paper CWF51.

49 Haka, A. S. *et al.* Diagnosing breast cancer by using Raman spectroscopy. *Proceedings of the National Academy of Sciences of the United States of America* **102**, 12371-12376, doi:10.1073/pnas.0501390102 (2005).

50 Auner, G. W. *et al.* Applications of Raman spectroscopy in cancer diagnosis. *Cancer and Metastasis Reviews* **37**, 691-717 (2018).

51 Brozek-Pluska, B. *et al.* Raman spectroscopy and imaging: applications in human breast cancer diagnosis. *Analyst* **137**, 3773-3780 (2012).

52 Gazi, E. *et al.* Direct evidence of lipid translocation between adipocytes and prostate cancer cells with imaging FTIR microspectroscopy. *Journal of Lipid Research* **48**, 1846-1856 (2007).

53 Milani, A., Basirnejad, M., Shahbazi, S. & Bolhassani, A. Carotenoids: biochemistry, pharmacology and treatment. *British Journal of Pharmacology* **174**, 1290-1324 (2017).

54 Große, C. *et al.* Label-Free Imaging and Spectroscopic Analysis of Intracellular Bacterial Infections. *Analytical Chemistry* **87**, 2137-2142, doi:10.1021/ac503316s (2015).

55 Silge, A. *et al.* Shedding light on host niches: label-free in situ detection of M ycobacterium gordonae via carotenoids in macrophages by Raman microspectroscopy. *Cellular Microbiology* **17**, 832-842 (2015).

56 Robledo, J. A., Murillo, A. M. & Rouzaud, F. Physiological role and potential clinical interest of mycobacterial pigments. *IUBMB Life* **63**, 71-78, doi:10.1002/iub.424 (2011).

57 Mosier-Boss, P. A. Review on SERS of Bacteria. *Biosensors* **7**, 51 (2017).

58 Pahlow, S. *et al.* Isolation and identification of bacteria by means of Raman spectroscopy. *Advanced Drug Delivery Reviews* **89**, 105-120, doi:https://doi.org/10.1016/j.addr.2015.04.006 (2015).

59 Walter, A., März, A., Schumacher, W., Rösch, P. & Popp, J. Towards a fast, high specific and reliable discrimination of bacteria on strain level by means of SERS in a microfluidic device. *Lab on a Chip* **11**, 1013-1021 (2011).

60 Premasiri, W. R. *et al.* The biochemical origins of the surface-enhanced Raman spectra of bacteria: a metabolomics profiling by SERS. *Analytical and Bioanalytical Chemistry* **408**, 4631-4647, doi:10.1007/s00216-016-9540-x (2016).

61 Zhao, X., Li, M. & Xu, Z. Detection of foodborne pathogens by surface enhanced raman spectroscopy. *Frontiers in Microbiology* **9** (2018).

62 Srivastava, S. K. *et al.* Highly sensitive and specific detection of E. coli by a SERS nanobiosensor chip utilizing metallic nanosculptured thin films. *Analyst* **140**, 3201-3209, doi:10.1039/c5an00209e (2015).

63 Doty, K. C. & Lednev, I. K. Raman spectroscopy for forensic purposes: recent applications for serology and gunshot residue analysis. *TrAC Trends in Analytical Chemistry* **103**, 215-222 (2018).

64 Yue, S. *et al.* Cholesteryl ester accumulation induced by PTEN loss and PI3K/AKT activation underlies human prostate cancer aggressiveness. *Cell Metabolism* **19**, 393-406 (2014).

65 Ji, M. *et al.* Detection of human brain tumor infiltration with quantitative stimulated Raman scattering microscopy. *Science Translational Medicine* **7**, 309ra163-309ra163 (2015).

66 Liao, C.-S. *et al.* Spectrometer-free vibrational imaging by retrieving stimulated Raman signal from highly scattered photons. *Science Advances* **1**, e1500738 (2015).

67 Hong, W. *et al.* Antibiotic susceptibility determination within one cell cycle at single-bacterium level by stimulated Raman metabolic imaging. *Analytical Chemistry* **90**, 3737-3743 (2018).

68 Shi, L. *et al.* Optical imaging of metabolic dynamics in animals. *Nature Communications* **9**, 2995 (2018).

69 Baldwin, J. Structure and cooperativity of haemoglobin. *Trends in Biochemical Sciences* **5**, 224-228 (1980).

70 Fu, D., Matthews, T. E., Ye, T., Piletic, I. R. & Warren, W. S. Label-free in vivo optical imaging of microvasculature and oxygenation level. *Journal of Biomedical Optics* **13**, 040503, doi:10.1117/1.2968260 (2008).

71 Min, W. *et al.* Imaging chromophores with undetectable fluorescence by stimulated emission microscopy. *Nature* **461**, 1105-1109, doi:10.1038/nature08438 (2009).

72 Piletic, I. R., Matthews, T. E. & Warren, W. S. Estimation of molar absorptivities and pigment sizes for eumelanin and pheomelanin using femtosecond transient absorption spectroscopy. *The Journal of Chemical Physics* **131**, 181106, doi:10.1063/1.3265861 (2009).

73 Dong, P.-T., Lin, H., Huang, K.-C. & Cheng, J.-X. Label-free quantitation of glycated hemoglobin in single red blood cells by transient absorption microscopy and phasor analysis. *Science Advances* **5**, eaav0561, doi:10.1126/sciadv.aav0561 (2019).

74 Nickerson, H. D. & Dutta, S. Diabetic Complications: Current Challenges and Opportunities. *Journal of Cardiovascular Translational Research* **5**, 375-379, doi:10.1007/s12265-012-9388-1 (2012).

75 Diagnosis and Classification of Diabetes Mellitus. *Diabetes Care* **27**, s5-s10, doi:10.2337/diacare.27.2007.S5 (2004).

76 Thomas, R. L. *et al.* Incidence of diabetic retinopathy in people with type 2 diabetes mellitus attending the Diabetic Retinopathy Screening Service for Wales: retrospective analysis. *BMJ: British Medical Journal* **344**, doi:10.1136/bmj.e874 (2012).

77 E., R. Nephropathy in type 2 diabetes. *Journal of Internal Medicine* **245**, 111-126, doi:doi:10.1046/j.1365-2796.1999.00411.x (1999).

78 Herman, W. H. & Kennedy, L. Underdiagnosis of Peripheral Neuropathy in Type 2 Diabetes. *Diabetes Care* **28**, 1480-1481, doi:10.2337/diacare.28.6.1480 (2005).

79 Malanda, U. L., Bot, S. D. & Nijpels, G. Self-Monitoring of Blood Glucose in Noninsulin-Using Type 2 Diabetic Patients: It is time to face the evidence. *Diabetes Care* **36**, 176-178, doi:10.2337/dc12-0831 (2013).

80 Boland, E. *et al.* Limitations of Conventional Methods of Self-Monitoring of Blood Glucose: Lessons learned from 3 days of continuous glucose sensing in pediatric patients with type 1 diabetes. *Diabetes Care* **24**, 1858-1862, doi:10.2337/diacare.24.11.1858 (2001).

81 Ginsberg, B. H. Factors Affecting Blood Glucose Monitoring: Sources of Errors in Measurement. *Journal of Diabetes Science and Technology (Online)* **3**, 903-913 (2009).

82 Lipska, K. J. *et al.* HbA_{1c} and Risk of Severe Hypoglycemia in Type 2 Diabetes. *Diabetes Care* **36**, 3535-3542, doi:10.2337/dc13-0610 (2013).

83 Florkowski, C. HbA(1c) as a Diagnostic Test for Diabetes Mellitus – Reviewing the Evidence. *The Clinical Biochemist. Reviews* **34**, 75-83 (2013).

84 Sacks, D. B. Hemoglobin A(1c) in Diabetes: Panacea or Pointless? *Diabetes* **62**, 41-43, doi:10.2337/db12-1485 (2013).

85 SAMUEL, R. The Discovery of Glycated Hemoglobin: A Major Event in the Study of Nonenzymatic Chemistry in Biological Systems. *Annals of the New York Academy of Sciences* **1043**, 9-19, doi:doi:10.1196/annals.1333.002 (2005).

86 Cohen, R. M. *et al.* Red cell life span heterogeneity in hematologically normal people is sufficient to alter HbA1c. *Blood* **112**, 4284-4291, doi:10.1182/blood-2008-04-154112 (2008).

87 Sherwani, S. I., Khan, H. A., Ekhzaimy, A., Masood, A. & Sakharkar, M. K. Significance of HbA1c Test in Diagnosis and Prognosis of Diabetic Patients. *Biomarker Insights* **11**, 95-104, doi:10.4137/bmi.s38440 (2016).

88 American Diabetes, A. Standards of Medical Care in Diabetes—2010. *Diabetes Care* **33**, S11-S61 (2010).

89 Weykamp, C., John, W. G. & Mosca, A. A Review of the Challenge in Measuring Hemoglobin A1c. *Journal of Diabetes Science and Technology* **3**, 439-445, doi:10.1177/193229680900300306 (2009).

90 Flückiger, R., Woodtli, T. & Berger, W. Quantitation of glycosylated hemoglobin by boronate affinity chromatography. *Diabetes* **33**, 73-76 (1984).

91 Koval, D., Kašička, V. & Cottet, H. Analysis of glycated hemoglobin A1c by capillary electrophoresis and capillary isoelectric focusing. *Analytical Biochemistry* **413**, 8-15, doi:https://doi.org/10.1016/j.ab.2011.01.048 (2011).

92 Jo, E.-J., Mun, H. & Kim, M.-G. Homogeneous Immunosensor Based on Luminescence Resonance Energy Transfer for Glycated Hemoglobin Detection Using Upconversion Nanoparticles. *Analytical Chemistry* **88**, 2742-2746, doi:10.1021/acs.analchem.5b04255 (2016).

93 Wangoo, N., Kaushal, J., Bhasin, K. K., Mehta, S. K. & Suri, C. R. Zeta potential based colorimetric immunoassay for the direct detection of diabetic marker HbA1c using gold nanoprobes. *Chemical Communications* **46**, 5755-5757, doi:10.1039/c0cc00224k (2010).

94 Syamala Kiran, M. *et al.* Selective Detection of HbA1c Using Surface Enhanced Resonance Raman Spectroscopy. *Analytical Chemistry* **82**, 1342-1348, doi:10.1021/ac902364h (2010).

95 Barman, I. *et al.* Raman Spectroscopy-Based Sensitive and Specific Detection of Glycated Hemoglobin. *Analytical Chemistry* **84**, 2474-2482, doi:10.1021/ac203266a (2012).

96 Kaiser, P., Akerboom, T., Molnar, P. & Reinauer, H. Modified HPLC-Electrospray Ionization/Mass Spectrometry Method for HbA_{1c} Based on IFCC Reference Measurement Procedure. *Clinical Chemistry* **54**, 1018-1022, doi:10.1373/clinchem.2007.100875 (2008).

97 Robles, F. E., Deb, S., Fischer, M. C., Warren, W. S. & Selim, M. A. Label-Free Imaging of Female Genital Tract Melanocytic Lesions With Pump-Probe Microscopy: A Promising Diagnostic Tool. *Journal of Lower Genital Tract Disease* **21**, 137-144, doi:10.1097/lgt.0000000000000290 (2017).

98 Davydova, D. y., Cadena, A., Akimov, D. & Dietzek, B. Transient absorption microscopy: advances in chemical imaging of photoinduced dynamics. *Laser & Photonics Reviews* **10**, 62-81, doi:doi:10.1002/lpor.201500181 (2016).

99 Gao, B., Hartland, G. V. & Huang, L. Transient Absorption Spectroscopy and Imaging of Individual Chirality-Assigned Single-Walled Carbon Nanotubes. *ACS Nano* **6**, 5083-5090, doi:10.1021/nn300753a (2012).

100 Hartland, G. V. Ultrafast studies of single semiconductor and metal nanostructures through transient absorption microscopy. *Chemical Science* **1**, 303-309, doi:10.1039/c0sc00243g (2010).

101 Huang, L. & Cheng, J.-X. Nonlinear Optical Microscopy of Single Nanostructures. *Annual Review of Materials Research* **43**, 213-236, doi:10.1146/annurev-matsci-071312-121652 (2013).

102 Tong, Y., Dan, F. & S., W. W. Nonlinear Absorption Microscopy. *Photochemistry and Photobiology* **85**, 631-645, doi:doi:10.1111/j.1751-1097.2008.00514.x (2009).

103 Chen, A. J. *et al.* Label-Free Imaging of Heme Dynamics in Living Organisms by Transient Absorption Microscopy. *Analytical Chemistry* **90**, 3395-3401, doi:10.1021/acs.analchem.7b05046 (2018).

104 Fu, D., Matthews, T. E., Ye, T., Piletic, I. & Warren, W. S. Label-free in vivo optical imaging of microvasculature and oxygenation level. *Journal of Biomedical Optics* **13**, 040503 (2008).

105 Min, W. *et al.* Imaging chromophores with undetectable fluorescence by stimulated emission microscopy. *Nature* **461**, 1105-1109 (2009).

106 Jung, Y. *et al.* Fast Detection of the Metallic State of Individual Single-Walled Carbon Nanotubes Using a Transient-Absorption Optical Microscope. *Physical Review Letters* **105**, 217401 (2010).

107 Hoelzel, W. *et al.* IFCC Reference System for Measurement of Hemoglobin A_{1c} in Human Blood and the National Standardization Schemes in the United States, Japan, and Sweden: A Method-Comparison Study. *Clinical Chemistry* **50**, 166-174, doi:10.1373/clinchem.2003.024802 (2004).

108 Miedema, K. & Casparie, T. Glycosylated Haemoglobins: Biochemical Evaluation and Clinical Utility. *Annals of Clinical Biochemistry* **21**, 2-15, doi:10.1177/000456328402100102 (1984).

109 Ye, S. *et al.* The impact of the HbA1c level of type 2 diabetics on the structure of haemoglobin. *Scientific Reports* **6**, 33352, doi:10.1038/srep33352 (2016).

110 Evgeny, A. S. *et al.* Formation of hemoglobin photoproduct is responsible for two-photon and single photon-excited fluorescence of red blood cells. *Laser Physics Letters* **15**, 075604 (2018).

111 Mallya, M. *et al.* Absorption Spectroscopy for the Estimation of Glycated Hemoglobin (HbA1c) for the Diagnosis and Management of Diabetes Mellitus: A Pilot Study. *Photomedicine and Laser Surgery* **31**, 219-224, doi:10.1089/pho.2012.3421 (2013).

112 Dong, P.-T. & Cheng, J.-X. Pump–Probe Microscopy: Theory, Instrumentation, and Applications. *Spectroscopy* **32**, 2-11 (2017).

113 Pauling, L. & Coryell, C. D. The Magnetic Properties and Structure of Hemoglobin, Oxyhemoglobin and Carbonmonoxyhemoglobin. *Proceedings of the National Academy of Sciences of the United States of America* **22**, 210-216, doi:10.1073/pnas.22.4.210 (1936).

114 Domingue, S. R., Bartels, R. A., Chicco, A. J. & Wilson, J. W. Transient absorption imaging of hemes with 2-color, independently tunable visible-wavelength ultrafast source. *Biomedical Optics Express* **8**, 2807-2821 (2017).

115 Franzen, S., Kiger, L., Poyart, C. & Martin, J.-L. Heme Photolysis Occurs by Ultrafast Excited State Metal-to-Ring Charge Transfer. *Biophysical Journal* **80**, 2372-2385 (2001).

116 Robles, F. E., Wilson, J. W., Fischer, M. C. & Warren, W. S. Phasor analysis for nonlinear pump-probe microscopy. *Optics Express* **20**, 17082-17092, doi:10.1364/oe.20.017082 (2012).

117 DeFronzo, R. A. *et al.* Type 2 diabetes mellitus. *Nature Reviews. Disease Primers* **1**, 15019, doi:10.1038/nrdp.2015.19 (2015).

118 DeFronzo, R. A. From the Triumvirate to the Ominous Octet: A New Paradigm for the Treatment of Type 2 Diabetes Mellitus. *Diabetes* **58**, 773-795, doi:10.2337/db09-9028 (2009).

119 Haque, K. S. & Siddiqui, M. R. Clinical Significance of Glycated Hemoglobin (HbA1c). *Anwer Khan Modern Medical College Journal* **4**, 3-5 (2013).

120 Stringari, C. *et al.* Phasor approach to fluorescence lifetime microscopy distinguishes different metabolic states of germ cells in a live tissue. *Proceedings of the National Academy of Sciences of the United States of America* **108**, 13582-13587, doi:10.1073/pnas.1108161108 (2011).

121 Digman, M. A., Caiolfa, V. R., Zamai, M. & Gratton, E. The Phasor Approach to Fluorescence Lifetime Imaging Analysis. *Biophysical Journal* **94**, L14-L16, doi:10.1529/biophysj.107.120154 (2008).

122 Fu, D. & Xie, X. S. Reliable cell segmentation based on spectral phasor analysis of hyperspectral stimulated Raman scattering imaging data. *Analytical Chemistry* **86**, 4115-4119 (2014).

123 Dong, P.-T. *et al.* Photolysis of Staphyloxanthin in Methicillin-Resistant Staphylococcus aureus Potentiates Killing by Reactive Oxygen Species. *Advanced Science* **6** (11), 1900030 (2019). doi:10.1002/advs.201900030.

124 Lewis, K. & Strandwitz, P. Microbiology: Antibiotics right under our nose. *Nature* **535**, 501-502 (2016).

125 McAdow, M. *et al.* Preventing *Staphylococcus aureus* sepsis through the inhibition of its agglutination in blood. *PLoS Pathogens* **7**, e1002307 (2011).

126 Geisinger, E. & Isberg, R. R. Interplay between antibiotic resistance and virulence during disease promoted by multidrug-resistant bacteria. *Journal of Infectious Diseases* **215**, S9-S17 (2017).

127 Guignard, B., Entenza, J. M. & Moreillon, P. Beta-lactams against methicillin-resistant *Staphylococcus aureus*. *Current Opinion in Pharmacology* **5**, 479-489 (2005).

128 Tang, S. S., Apisarnthanarak, A. & Hsu, L. Y. Mechanisms of beta-lactam antimicrobial resistance and epidemiology of major community- and healthcare-associated multidrug-resistant bacteria. *Advanced Drug Delivery Reviews* **78**, 3-13 (2014).

129 Baek, J. Y. *et al.* Genetic alterations responsible for reduced susceptibility to vancomycin in community-associated MRSA strains of ST72. *Journal of Antimicrobial Chemotherapy* **72**, 2454-2460 (2017).

130 Smith, J. R. *et al.* Daptomycin in combination with ceftolozane-tazobactam or cefazolin against daptomycin-susceptible and -nonsusceptible *Staphylococcus aureus* in an *in vitro*, hollow-fiber model. *Antimicrobials Agents and Chemotherapy* **60**, 3970-3975 (2016).

131 Lehar, S. M. *et al.* Novel antibody–antibiotic conjugate eliminates intracellular S. aureus. *Nature* **527**, 323-328 (2015).

132 Flemming, H.-C. *et al.* Biofilms: an emergent form of bacterial life. *Nature Reviews. Microbiology* **14**, 563-575, doi:10.1038/nrmicro.2016.94 (2016).

133 Allison, K. R., Brynildsen, M. P. & Collins, J. J. Metabolite-enabled eradication of bacterial persisters by aminoglycosides. *Nature* **473**, 216,

134 Rangel-Vega, A., Bernstein, L. R., Mandujano-Tinoco, E. A., García-Contreras, S. J. & García-Contreras, R. Drug repurposing as an alternative for the treatment of recalcitrant bacterial infections. *Frontiers in Microbiology* **6**, 282, doi:10.3389/fmicb.2015.00282 (2015).

135 Thangamani, S., Younis, W. & Seleem, M. N. Repurposing ebselen for treatment of multidrug-resistant staphylococcal infections. *Scientific Reports* **5**, 11596, doi:10.1038/srep11596 (2015).

136 Kim, W. *et al.* A new class of synthetic retinoid antibiotics effective against bacterial persisters. *Nature* **556**, 103, doi:10.1038/nature26157 (2018).

137 Kaźmierczak, Z., Górski, A. & Dąbrowska, K. Facing Antibiotic Resistance: Staphylococcus aureus Phages as a Medical Tool. *Viruses* **6**, 2551-2570, doi:10.3390/v6072551 (2014).

138 Jorgensen, J. H. *et al. Manual of Clinical Microbiology, Eleventh Edition.* (American Society of Microbiology, 2015).

139 García-Fernández, E. *et al.* Membrane Microdomain Disassembly Inhibits MRSA Antibiotic Resistance. *Cell*, doi:10.1016/j.cell.2017.10.012.

140 Mishra, N. N. *et al.* Carotenoid-related alteration of cell membrane fluidity impacts *Staphylococcus aureus* susceptibility to host defense peptides. *Antimicrobials Agents and Chemotherapy* **55**, 526-531 (2011).

141 Liu, C.-I. *et al.* A Cholesterol Biosynthesis Inhibitor Blocks Staphylococcus aureus Virulence. *Science* **319**, 1391-1394, doi:10.1126/science.1153018 (2008).

142 Gao, P., Davies, J. & Kao, R. Y. T. Dehydrosqualene Desaturase as a Novel Target for Anti-Virulence Therapy against Staphylococcus aureus. *MBio* **8**, doi:10.1128/mBio.01224-17 (2017).

143 Oldfield, E. Targeting Isoprenoid Biosynthesis for Drug Discovery: Bench to Bedside. *Accounts of Chemical Research* **43**, 1216-1226, doi:10.1021/ar100026v (2010).

144 Chen, F. F. *et al.* Small-molecule targeting of a diapophytoene desaturase inhibits *S. aureus* virulence. *Nature Chemical Biology* **12**, 174-179 (2016).

145 Jabra-Rizk, M. A., Meiller, T. F., James, C. E. & Shirtliff, M. E. Effect of Farnesol on Staphylococcus aureus Biofilm Formation and Antimicrobial Susceptibility. *Antimicrobials Agents and Chemotherapy* **50**, 1463-1469, doi:10.1128/aac.50.4.1463-1469.2006 (2006).

146 MacDonald, M. L. *et al.* Identifying off-target effects and hidden phenotypes of drugs in human cells. *Nature Chemical Biology* **2**, 329, doi:10.1038/nchembio790 (2006).

147 Liu, G. Y. *et al.* Staphylococcus aureus golden pigment impairs neutrophil killing and promotes virulence through its antioxidant activity. *The Journal of Experimental Nedicine* **202**, 209-215 (2005).

148 Sopirala, M. M. *et al.* Synergy Testing by Etest, Microdilution Checkerboard, and Time-Kill Methods for Pan-Drug-Resistant *Acinetobacter baumanni*i. *Antimicrobials Agents and Chemotherapy* **54**, 4678-4683, doi:10.1128/aac.00497-10 (2010).

149 Mohamed, M. F., Abdelkhalek, A. & Seleem, M. N. Evaluation of short synthetic antimicrobial peptides for treatment of drug-resistant and intracellular Staphylococcus aureus. *Scientific Reports* **6**, 29707, doi:10.1038/srep29707 (2016).

150 Mohammad, H., Cushman, M. & Seleem, M. N. Antibacterial Evaluation of Synthetic Thiazole Compounds In Vitro and In Vivo in a Methicillin-Resistant Staphylococcus aureus (MRSA) Skin Infection Mouse Model. *PLoS ONE* **10**, e0142321, doi:10.1371/journal.pone.0142321 (2015).

151 Dai, T. *et al.* Blue Light Eliminates Community-Acquired Methicillin-Resistant Staphylococcus aureus in Infected Mouse Skin Abrasions. *Photomedicine and Laser Surgery* **31**, 531-538, doi:10.1089/pho.2012.3365 (2013).

152 Stratonnikov, A. A., Meerovich, G. A. & Loschenov, V. B. in *BiOS 2000 The International Symposium on Biomedical Optics.* 81-91 (International Society for Optics and Photonics).

153 Butler, I. B., Schoonen, M. A. & Rickard, D. T. Removal of dissolved oxygen from water: a comparison of four common techniques. *Talanta* **41**, 211-215 (1994).

154 Kumar, B. N. V., Kampe, B., Rosch, P. & Popp, J. Characterization of carotenoids in soil bacteria and investigation of their photodegradation by UVA radiation via resonance Raman spectroscopy. *Analyst* **140**, 4584-4593 (2015).

155 Min, W. *et al.* Imaging chromophores with undetectable fluorescence by stimulated emission microscopy. *Nature* **461**, 1105-1109 (2009).

156 Galassi, L. *Wavelength dependence of the time course of fluorescence enhancement and photobleaching during irradiation of ethidium bromide-stained nuclei*. Vol. 44 (2000).

157 Silge, A. *et al.* Shedding light on host niches: label-free in situ detection of Mycobacterium gordonae via carotenoids in macrophages by Raman

microspectroscopy. *Cellular Microbiology* **17**, 832-842, doi:doi:10.1111/cmi.12404 (2015).

158 Schaffer, H. E., Chance, R. R., Silbey, R. J., Knoll, K. & Schrock, R. R. Conjugation length dependence of Raman scattering in a series of linear polyenes: Implications for polyacetylene. *The Journal of Chemical Physics* **94**, 4161-4170, doi:10.1063/1.460649 (1991).

159 Wang, Y. *et al.* Antimicrobial blue light inactivation of pathogenic microbes: State of the art. *Drug Resistance Updates* **33-35**, 1-22, doi:https://doi.org/10.1016/j.drup.2017.10.002 (2017).

160 Müller, A. *et al.* Daptomycin inhibits cell envelope synthesis by interfering with fluid membrane microdomains. *Proceedings of the National Academy of Sciences of the United States of America* **113**, E7077-E7086, doi:10.1073/pnas.1611173113 (2016).

161 Gough, D. R. & Cotter, T. G. Hydrogen peroxide: a Jekyll and Hyde signalling molecule. *Cell Death & Disease* **2**, e213, doi:10.1038/cddis.2011.96 (2011).

162 Humphreys, G., Lee, G. L., Percival, S. L. & McBain, A. J. Combinatorial activities of ionic silver and sodium hexametaphosphate against microorganisms associated with chronic wounds. *Journal of Antimicrobial Chemotherapy* **66**, 2556-2561, doi:10.1093/jac/dkr350 (2011).

163 Cottarel, G. & Wierzbowski, J. Combination drugs, an emerging option for antibacterial therapy. *Trends in Biotechnology* **25**, 547-555 (2007).

164 Lewis, K. Persister Cells. *Annual Review of Microbiology* **64**, 357-372, doi:10.1146/annurev.micro.112408.134306 (2010).

165 Wood, T. K., Knabel, S. J. & Kwan, B. W. Bacterial Persister Cell Formation and Dormancy. *Applied and Environmental Microbiology* **79**, 7116-7121, doi:10.1128/aem.02636-13 (2013).

166 Costerton, J. W., Stewart, P. S. & Greenberg, E. P. Bacterial biofilms: A common cause of persistent infections. *Science* **284**, 1318-1322 (1999).

167 Ager, S. & Gould, K. Clinical update on linezolid in the treatment of Gram-positive bacterial infections. *Infection and Drug Resistance* **5**, 87-102 (2012).

168 Weigelt, J. *et al.* Linezolid versus vancomycin in treatment of complicated skin and soft tissue infections. *Antimicrobial Agents and Chemotherapy* **49**, 2260-2266 (2005).

169 *American National Standard for Safe Use of Lasers, ANSI Z136.1.* Laser Institute of America. (2014).

170 Immergluck, L. C. *et al.* Risk of Skin and Soft Tissue Infections among Children Found to be Staphylococcus aureus MRSA USA300 Carriers. *Western Journal of Emergency Medicine* **18**, 201-212, doi:10.5811/westjem.2016.10.30483 (2017).

171 Siqueira, J. F. & Rôças, I. N. Microbiology and Treatment of Acute Apical Abscesses. *Clinical Microbiology Reviews* **26**, 255-273, doi:10.1128/cmr.00082-12 (2013).

172 Paavonen, K., Puolakkainen, P., Jussila, L., Jahkola, T. & Alitalo, K. Vascular endothelial growth factor receptor-3 in lymphangiogenesis in wound healing. *American Journal of Pathology* **156**, 1499-1504 (2000).

173 Liu, G. Y. & Nizet, V. Color me bad: microbial pigments as virulence factors. *Trends in Microbiology* **17**, 406-413 (2009).

174 Centers for Disease Control and Prevention. Active Bacterial Core Surveillance Report (ABCs): Emerging Infections Program Network, Methicillin-Resistant *Staphylococcus aureus* (2011). Available from https://www.cdc.gov/abcs/reports-findings/survreports/mrsa11.html

175 Lim, D. & Strynadka, N. C. Structural basis for the beta lactam resistance of PBP2a from methicillin-resistant Staphylococcus aureus. *Nature Structural Biology* **9**, 870-876, doi:10.1038/nsb858 (2002).

176 Peacock, S. J. & Paterson, G. K. Mechanisms of Methicillin Resistance in Staphylococcus aureus. *Annual Review of Biochemistry* **84**, 577-601, doi:10.1146/annurev-biochem-060614-034516 (2015).

177 Kaatz, G. W., Seo, S. M. & Ruble, C. A. Efflux-Mediated Fluoroquinolone Resistance in Staphylococcus-Aureus. *Antimicrobial Agents and Chemotherapy* **37**, 1086-1094, doi:Doi 10.1128/Aac.37.5.1086 (1993).

178 Li, X. Z. & Nikaido, H. Efflux-Mediated Drug Resistance in Bacteria An Update. *Drugs* **69**, 1555-1623, doi: 10.2165/11317030-000000000-00000 (2009).

179 Bayer, A. S., Schneider, T. & Sahl, H. G. Mechanisms of daptomycin resistance in Staphylococcus aureus: role of the cell membrane and cell wall. *Annals of the New York Academy of Sciences* **1277**, 139-158, doi:10.1111/j.1749-6632.2012.06819.x (2013).

180 Lewis, K. Platforms for antibiotic discovery. *Nature Reviews. Drug Discovery* **12**, 371-387, doi:10.1038/nrd3975 (2013).

181 Clatworthy, A. E., Pierson, E. & Hung, D. T. Targeting virulence: a new paradigm for antimicrobial therapy. *Nature Chemical Biology* **3**, 541-548, doi:10.1038/nchembio.2007.24 (2007).

182 Dickey, S. W., Cheung, G. Y. C. & Otto, M. Different drugs for bad bugs: antivirulence strategies in the age of antibiotic resistance. *Nature Reviews. Drug Discovery* **16**, 457-471, doi:10.1038/nrd.2017.23 (2017).

183 Cegelski, L., Marshall, G. R., Eldridge, G. R. & Hultgren, S. J. The biology and future prospects of antivirulence therapies. *Nature Reviews. Microbiology* **6**, 17-27, doi:10.1038/nrmicro1818 (2008).

184 Marshall, J. H. & Wilmoth, G. J. Pigments of Staphylococcus aureus, a series of triterpenoid carotenoids. *Journal of Bacteriology* **147**, 900-913 (1981).

185 Liu, G. Y. *et al.* Staphylococcus aureus golden pigment impairs neutrophil killing and promotes virulence through its antioxidant activity. *Journal of Experimental Medicine* **202**, 209-215, doi:10.1084/jem.20050846 (2005).

186 Garcia-Fernandez, E. *et al.* Membrane Microdomain Disassembly Inhibits MRSA Antibiotic Resistance. *Cell* **171**, 1354-1367, doi:10.1016/j.cell.2017.10.012 (2017).

187 Liu, C. I. *et al.* A cholesterol biosynthesis inhibitor blocks Staphylococcus aureus virulence. *Science* **319**, 1391-1394, doi:10.1126/science.1153018 (2008).

188 Gutierrez, A. *et al.* Understanding and Sensitizing Density-Dependent Persistence to Quinolone Antibiotics. *Molecular Cell* **68**, 1147-1154.e1143, doi:https://doi.org/10.1016/j.molcel.2017.11.012 (2017).

189 Baumgart, T., Hunt, G., Farkas, E. R., Webb, W. W. & Feigenson, G. W. Fluorescence probe partitioning between L-o/L-d phases in lipid membranes. *Biochimica et Biophysica Acta – Biomembranes* **1768**, 2182-2194, doi:10.1016/j.bbamem.2007.05.012 (2007).

190 Marrink, S. J., Risselada, H. J., Yefimov, S., Tieleman, D. P. & de Vries, A. H. The MARTINI force field: coarse grained model for biomolecular simulations. *Journal of Physical Chemistry. B* **111**, 7812-7824, doi:10.1021/jp071097f (2007).

191 Vanommeslaeghe, K. *et al.* CHARMM general force field: A force field for drug-like molecules compatible with the CHARMM all-atom additive biological force fields. *Journal of Computational Chemistry* **31**, 671-690, doi:10.1002/jcc.21367 (2010).

192 Jorgensen, W. L., Chandrasekhar, J., Madura, J. D., Impey, R. W. & Klein, M. L. Comparison of Simple Potential Functions for Simulating Liquid Water. *Journal of Chemical Physics* **79**, 926-935, doi:Doi 10.1063/1.445869 (1983).

193 Pettersen, E. F. *et al.* UCSF chimera - A visualization system for exploratory research and analysis. *Journal of Computational Chemistry* **25**, 1605-1612, doi:10.1002/jcc.20084 (2004).

194 Abraham, M. J. *et al.* GROMACS: High performance molecular simulations through multi-level parallelism from laptops to supercomputers. *SoftwareX* **1**, 19-25 (2015).

195 Jehlicka, J. *et al.* Potential and limits of Raman spectroscopy for carotenoid detection in microorganisms: implications for astrobiology. *Philosophical Transactions of the Royal Society. A* **372**, doi:ARTN 2014019910.1098/rsta.2014.0199 (2014).

196 Dong, P. T. *et al.* Photolysis of Staphyloxanthin in Methicillin-Resistant Staphylococcus aureus Potentiates Killing by Reactive Oxygen Species. *Advanced Science* **6**, 1900030, doi:ARTN 190003010.1002/advs.201900030 (2019).

197 Kloos, W. E. J., J.H. Staphylococci. in Manual of Clinical Microbiology edn. 4 (eds. Lennette, E.H., Balows, A., Hausler Jr., W.J. & Shadomy, H.J.) 143–153 (American Society for Microbiology, Washington, DC, 1985).

198 Mishra, N. N. *et al.* Carotenoid-related alteration of cell membrane fluidity impacts Staphylococcus aureus susceptibility to host defense peptides. *Antimicrobial Agents and Chemotherapy* **55**, 526-531, doi:10.1128/AAC.00680-10 (2011).

199 Jones, T. *et al.* Failures in clinical treatment of Staphylococcus aureus Infection with daptomycin are associated with alterations in surface charge, membrane phospholipid asymmetry, and drug binding. *Antimicrobial Agents and Chemotherapy* **52**, 269-278, doi:10.1128/AAC.00719-07 (2008).

200 Taylor, R. F. Bacterial triterpenoids. *Microbiological Reviews* **48**, 181-198 (1984).

201 Himeno, H. *et al.* Charge-induced phase separation in lipid membranes. *Soft Matter* **10**, 7959-7967, doi:10.1039/c4sm01089b (2014).

202 MacKenzie, F. M. & Gould, I. M. The post-antibiotic effect. *Journal of Antimicrobial Chemotherapy* **32**, 519-537, doi:10.1093/jac/32.4.519 (1993).

203 American National Standard for Safe Use of Lasers, ANSI Z136.1 (2014).

204 Hooper, D. C. Fluoropuinolone resistance among Gram-positive cocci. *The Lancet. Infectious Diseases* **2**, 530-538, doi: 10.1016/S1473-3099(02)00369-9 (2002).

205 Guffey, J. S. & Wilborn, J. In vitro bactericidal effects of 405-nm and 470-nm blue light. *Photomedicine and Laser Surgery* **24**, 684-688, doi:10.1089/pho.2006.24.684 (2006).

206 Enwemeka, C. S., Williams, D., Enwemeka, S. K., Hollosi, S. & Yens, D. Blue 470-nm light kills methicillin-resistant Staphylococcus aureus (MRSA) in vitro. *Photomedicine and Laser Surgery* **27**, 221-226, doi:10.1089/pho.2008.2413 (2009).

207 Dai, T. *et al.* Blue light eliminates community-acquired methicillin-resistant Staphylococcus aureus in infected mouse skin abrasions. *Photomedicine and Laser Surgery* **31**, 531-538, doi:10.1089/pho.2012.3365 (2013).

208 Hamblin, M. R. & Hasan, T. Photodynamic therapy: a new antimicrobial approach to infectious disease? *Photochemical & Photobiological Sciences* **3**, 436-450, doi:10.1039/b311900a (2004).

209 Piddock, L. J. V. Multidrug-resistance efflux pumps - not just for resistance. *Nature Reviews. Microbiology* **4**, 629-636, doi:10.1038/nrmicro1464 (2006).

210 Swartz, T. E. *et al.* Blue-light-activated histidine kinases: Two-component sensors in bacteria. *Science* **317**, 1090-1093, doi:10.1126/science.1144306 (2007).

211 Willyard, C. J. The drug-resistant bacteria that pose the greatest health threats. *Nature* **543** (7643), 15 https://doi.org/10.1038/nature.2017.21550 (2017).

212 Mishra, S. & Imlay, J. Why do bacteria use so many enzymes to scavenge hydrogen peroxide? *Archives of Biochemistry and Biophysics* **525**, 145-160, doi:10.1016/j.abb.2012.04.014 (2012).

213 Belenky, P., Camacho, D. & Collins, J. J. Fungicidal drugs induce a common oxidative-damage cellular death pathway. *Cell Reports* **3**, 350-358, doi:10.1016/j.celrep.2012.12.021 (2013).

214 Dwyer, D. J. *et al.* Antibiotics induce redox-related physiological alterations as part of their lethality. *Proceedings of the National Academy of Sciences of the United States of America* **111**, E2100-E2109, doi:10.1073/pnas.1401876111 (2014).

215 Sokol-Anderson, M. L., Brajtburg, J. & Medoff, G. Amphotericin B-induced oxidative damage and killing of Candida albicans. *Journal of Infectious Diseases* **154**, 76-83 (1986).

216 Van Acker, H. & Coenye, T. The Role of Reactive Oxygen Species in Antibiotic-Mediated Killing of Bacteria. *Trends in Microbiology* **25**, 456-466, doi:https://doi.org/10.1016/j.tim.2016.12.008 (2017).

217 Van Acker, H. *et al.* The Role of Reactive Oxygen Species in Antibiotic-Induced Cell Death in Burkholderia cepacia Complex Bacteria. *PLoS ONE* **11**, e0159837, doi:10.1371/journal.pone.0159837 (2016).

218 Dwyer, D. J. *et al.* Antibiotics induce redox-related physiological alterations as part of their lethality. *Proceedings of the National Academy of Sciences of the United States of America* **111**, E2100-E2109, doi:10.1073/pnas.1401876111 (2014).

219 Segal, A. W. How neutrophils kill microbes. *Annual Review of Immunology* **23**, 197-223, doi:10.1146/annurev.immunol.23.021704.115653 (2005).

220 Hampton, M. B., Kettle, A. J. & Winterbourn, C. C. Inside the Neutrophil Phagosome: Oxidants, Myeloperoxidase, and Bacterial Killing. *Blood* **92**, 3007-3017 (1998).

221 Flannagan, R., Heit, B. & Heinrichs, D. Antimicrobial mechanisms of macrophages and the immune evasion strategies of Staphylococcus aureus. *Pathogens* **4**, 826-868 (2015).

222 Yang, X., Shi, G., Guo, J., Wang, C. & He, Y. Exosome-encapsulated antibiotic against intracellular infections of methicillin-resistant Staphylococcus aureus. *International Journal of Nanomedicine* **13**, 8095 (2018).

223 Cheng, L., Kellogg III, E. & Packer, L. Photoinactivation of catalase. *Photochemistry and Photobiology* **34**, 125-129 (1981).

224 Chuang, W.-J., Heldt, J. & Van Wart, H. J. Resonance Raman spectra of bovine liver catalase compound II. Similarity of the heme environment to horseradish peroxidase compound II. *Journal of Biological Chemistry* **264**, 14209-14215 (1989).

225 Nakamura, K. *et al.* Microbial resistance in relation to catalase activity to oxidative stress induced by photolysis of hydrogen peroxide. *Microbiology and Immunology* **56**, 48-55 (2012).

226 Mandell, G. L. Catalase, superoxide dismutase, and virulence of Staphylococcus aureus. In vitro and in vivo studies with emphasis on staphylococcal--leukocyte interaction. *Journal of Clinical Investigation* **55**, 561-566, doi:10.1172/jci107963 (1975).

227 Bongomin, F., Gago, S., Oladele, R. & Denning, D. Global and multi-national prevalence of fungal diseases—estimate precision. *Journal of Fungi* **3**, 57 (2017).

228 Schelenz, S. *et al.* First hospital outbreak of the globally emerging Candida auris in a European hospital. *Antimicrobial Resistance & Infection Control* **5**, 35 (2016).

229 Lockhart, S. R. *et al.* Simultaneous emergence of multidrug-resistant Candida auris on 3 continents confirmed by whole-genome sequencing and epidemiological analyses. *Clinical Infectious Diseases* **64**, 134-140 (2016).

230 Hansberg, W., Salas-Lizana, R. & Dominguez, L. Fungal catalases: function, phylogenetic origin and structure. *Archives of Biochemistry and Biophysics* **525**, 170-180 (2012).

231 Pradhan, A. *et al.* Elevated catalase expression in a fungal pathogen is a double-edged sword of iron. *PLoS Pathogens* **13**, e1006405 (2017).

232 Kaloriti, D. *et al.* Mechanisms Underlying the Exquisite Sensitivity of *Candida albicans* to Combinatorial Cationic and Oxidative Stress That Enhances the Potent Fungicidal Activity of Phagocytes. *mBio* **5**, e01334-01314, doi:10.1128/mBio.01334-14 (2014).

233 Jacobsen, I. D. *et al.* Candida albicans dimorphism as a therapeutic target. *Expert Review of Anti-Infective Therapy* **10**, 85-93 (2012).

234 Brown, G. D. *et al.* Hidden killers: human fungal infections. *Science Translational Medicine* **4**, 165rv113-165rv113 (2012).

235 Pfaller, M. & Diekema, D. J. Epidemiology of invasive candidiasis: a persistent public health problem. *Clinical Microbiology Reviews* **20**, 133-163 (2007).

236 Jeffery-Smith, A. *et al. Candida auris*: a Review of the Literature. *Clinical Microbiology Reviews* **31**, e00029-00017, doi:10.1128/CMR.00029-17 %J (2018).

237 Welsh, R. M. *et al.* Survival, Persistence, and Isolation of the Emerging Multidrug-Resistant Pathogenic Yeast *Candida auris* on a Plastic Health Care Surface. *Journal of Clinical Microbiology* **55**, 2996-3005, doi:10.1128/JCM.00921-17 (2017).

238 Pathirana, R. U. *et al.* Fluconazole-Resistant *Candida auris* Is Susceptible to Salivary Histatin 5 Killing and to Intrinsic Host Defenses. *Antimicrobial Agents and Chemotherapy* **62**, e01872-01817, doi:10.1128/AAC.01872-17 (2018).

239 Mora-Duarte, J. *et al.* Comparison of Caspofungin and Amphotericin B for Invasive Candidiasis. *New England Journal of Medicine* **347**, 2020-2029, doi:10.1056/NEJMoa021585 (2002).

240 Finkelstein, A. & Holz, R. J. Aqueous pores created in thin lipid membranes by the polyene antibiotics nystatin and amphotericin B. *Membranes* **2**, 377–408 (1973).

241 Cotero, B. V., Rebolledo-Antúnez, S. & Ortega-Blake, I. On the role of sterol in the formation of the amphotericin B channel. *Biochimica et Biophysica Acta* **1375** (1–2), 43-51 (1998).

242 Mouri, R., Konoki, K., Matsumori, N., Oishi, T. & Murata, M. Complex formation of amphotericin B in sterol-containing membranes as evidenced by surface plasmon resonance. *Biochemistry* **47**, 7807-7815 (2008).

243 Anderson, T. M. *et al.* Amphotericin forms an extramembranous and fungicidal sterol sponge. *Nature Chemical Biology* **10**, 400, doi:10.1038/nchembio.1496 (2014).

244 Bolard, J.. How do the polyene macrolide antibiotics affect the cellular membrane properties? *Biochimca et Biophysica Acta – Reviews on Biomembranes* **864**, 257-304 (1986).

245 Volmer, A. A., Szpilman, A. M. & Carreira, E. M. Synthesis and biological evaluation of amphotericin B derivatives. *Natural Product Reports* **27**, 1329-1349, doi:10.1039/B820743G (2010).

246 Chéron, M. *et al.* Quantitative structure-activity relationships in amphotericin B derivatives. *Biochemical Pharmacology* **37**, 827-836, doi:https://doi.org/10.1016/0006-2952(88)90168-2 (1988).

247 De Kruijff, B. & Demel, R. A. Polyene antibiotic-sterol interactions in membranes of Acholeplasma laidlawii cells and lecithin liposomes. III. Molecular structure of the polyene antibiotic-cholesterol complexes. *Biochimica et Biophysica Acta (BBA) - Biomembranes* **339**, 57-70, doi:https://doi.org/10.1016/0005-2736(74)90332-0 (1974).

248 Milhaud, J., Ponsinet, V., Takashi, M. & Michels, B. Interactions of the drug amphotericin B with phospholipid membranes containing or not ergosterol: new insight into the role of ergosterol. *Biochimica et Biophysica Acta (BBA) - Biomembranes* **1558**, 95-108 (2002).

249 Verkleij, A. *et al.* Freeze-etch electron microscopy of erythrocytes, Acholeplasma laidlawii cells and liposomal membranes after the action of filipin and amphotericin B. *Biochimica et Biophysica Acta* **291**, 577-581 (1973).

250 Baginski, M., Resat, H. & Borowski, E. Comparative molecular dynamics simulations of amphotericin B–cholesterol/ergosterol membrane channels. *Biochimica et Biophysica Acta* **1567**, 63-78, doi:https://doi.org/10.1016/S0005-2736(02)00581-3 (2002).

251 Lee, H. J. *et al.* Electronic Preresonance Stimulated Raman Scattering Imaging of Red-Shifted Proteorhodopsins: Toward Quantitation of the Membrane Potential. *The Journal of Physical Chemistry Letters* **10**, 4374-4381, doi:10.1021/acs.jpclett.9b01337 (2019).

252 Liu, B. *et al.* Label-free spectroscopic detection of membrane potential using stimulated Raman scattering. *Applied Physics Letters* **106**, 173704 (2015).

253 Potma, E. O. & Xie, X. S. Detection of single lipid bilayers with coherent anti-Stokes Raman scattering (CARS) microscopy. *Journal of Raman Spectroscopy* **34**, 642-650, doi:Doi 10.1002/Jrs.1045 (2003).

254 Guck, J. *et al.* The optical stretcher: A novel laser tool to micromanipulate cells. *Biophysical Journal* **81**, 767-784 (2001).

255 Chiu, L.-D., Hullin-Matsuda, F., Kobayashi, T., Torii, H. & Hamaguchi, H.-O On the origin of the 1602 cm–1 Raman band of yeasts; contribution of ergosterol. *Journal of Biophotonics* **5**, 724-728 (2012).

256 Cheng, J.-X., Pautot, S., Weitz, D. A. & Xie, X. S. Ordering of water molecules between phospholipid bilayers visualized by coherent anti-Stokes Raman scattering microscopy. *Proceedings of the National Academy of Sciences of the United States of America* **100**, 9826-9830 (2003).

CURRICULUM VITAE